

①

Measurement of Prompt Photon Production in 1.8 TeV Proton-Antiproton Collisions

Takashi Ino

A dissertation submitted to the Doctoral Program
in Physics, the University of Tsukuba
in partial fulfillment of the requirements for the degree of
Doctor of Philosophy (Science)

June 1996

Abstract

The inclusive production cross section of prompt photons with transverse energies $27 < E_T < 40$ GeV and in pseudorapidity $1.32 < |\eta| < 2.22$ has been measured in proton-antiproton collisions at $\sqrt{s} = 1.8$ TeV. Using the data recorded by the CDF detector during the 1988-1989 TEVATRON collider run, corresponding to an integrated luminosity of 3.8 ± 0.1 pb⁻¹, 3995 prompt photon candidate events are selected in the endplug electromagnetic calorimeter.

From differences in the longitudinal cascade shower profile between a single photon and multi-photons from π^0 and η meson decays, the number of prompt photon events in the candidates is extracted to be 1972 ± 353 . The differences in the shower shape are obtained by a GEANT3 based Monte Carlo detector simulation, which has been carefully studied and found to well reproduce the electromagnetic cascade of electrons at various energies as well as incident angles.

The inclusive production cross section has been obtained to be

$$\sigma = 1.44 \pm 0.09 \text{ (stat.)} \pm 0.27 \text{ (syst.) nb.}$$

The measurement agrees with the next-to-leading order QCD calculation using recent parton distribution functions.

The differential cross section with respect to pseudorapidity has also been measured and found to be in good agreement with the QCD calculation.

The photon event fraction and its dependence on the photon isolation are studied. The isolation dependence of the photon event fraction shows a consistency with the QCD prediction.

Future prospects of prompt photon measurements in the endplug region for the new data, which has been collected during 1992 to 1995, corresponding to roughly 110 pb⁻¹ are also discussed.

Curriculum Vitae

Takashi Ino [REDACTED] He was raised in Chiba by his parents Ken-ichi and Chiyoko Ino until he graduated with a Bachelor of Science degree in 1987 from the Science University of Tokyo at Noda where he started his career in physics with research on amorphous metal. In the same year, he entered the Doctoral Program in Physics, the University of Tsukuba, and started research in high energy physics under the supervision of Prof. Kunitaka Kondo who eventually had supervised the author until the end of his Ph.D. work. In 1988, the author joined the CDF experiment at Fermi National Accelerator Laboratory in Illinois, U.S.A. After receiving his Master of Science degree in 1989, he moved to Fermilab and spent for three years working on the CDF experiment. After the Fermilab years, he worked as a research associate for the Institute of Physics in the University of Tsukuba where he finished his Ph.D. work on prompt photon production in the CDF experiment.

Acknowledgements

I would like to express my greatest appreciation to my advisor, Professor Kunitaka Kondo, for providing me an opportunity to work on the CDF experiment. I am honored to have finished my Ph.D. work under his guidance and encouragement. I have learned much from his enthusiasm and positive attitude toward physics research.

I would also like to thank Stephen Kuhlmann, Robert Blair, Robert Harris, and people of the CDF photon group for valuable suggestions and encouragement. Especially Stephen Kuhlmann, without whom I could not have accomplished this work. I want to thank him again for a lot of his advice.

I am deeply indebted to Shinhong Kim, Mikio Takano, and Masahiko Yokoyama for advice, supports, and discussions with them. They gave me various suggestions as well as shared their knowledge with me.

My many thanks to Koji Takikawa, Shigeyuki Miyashita, Itsuo Nakano, Kiyoshi Yasuoka, Kazuhiko Hara, and Masanori Mishina. They are greatly helpful to me during my thesis work.

I would be grateful to Nobuaki Ohshima, Susumu Igarashi, and Atsushi Taketani who were working for the $D\bar{D}$ experiment during my stay at Fermilab. I had many kinds of discussions with physicists from a non-CDF experiment. They, experienced in high energy physics on various experiments, also gave me precious suggestions. I will never forget people made my life in America happiest, especially the Kunoris. I had a comfortable time at Fermilab with my room mates Luc Demortier and Yoshihiro Seiya who were not only good friends but also good collaborators. Hiroshi Iso, Youhei Morita, Fumihiko Ukegawa, Satoru Ogawa, and Mariko Ninomiya also gave me useful suggestions and taught me physics and mathematics.

The test beam experiment with Yasuo Fukui, Howard Budd, Ryutaro Oishi, Takeshi Chikamatsu, Mark Dickson, Melissa Franklin, Jacobo Konigsberg, Vaia Papadimitriou, Young-Kee Kim, and the CDF Gas Calorimetry Group was unforgettable and provided information indispensable to this work.

I do not know how I can express my gratitude to Makoto Shimojima, Tomohiro Kaneko, Yukihiro Kato, Hisafumi Mitsushio, Nobuyuki Uemura, Eiichiro Hayashi,

Hiroyuki Sato, Tsuyoshi Takada, Housai Nakada, Hirotoshi Toyoda, and Yoko Nanno for useful discussions on physics as well as on private matters.

I am extremely thankful to Carol Picciolo, Kyoko Kunori, Mutsumi Uenishi, and Kazuko Kumashiro for constant supports through their secretary works.

The great success of the CDF experiment is a result of patient and continuous work of the CDF collaboration. I want to thank all the members of the collaboration, including Thomas Baumann, Louis Keeble, Robert B. Mattingly, and Steven Moulding. I wish to tell them "Live long and prosper."

It should be in everyone's mind to thank the Fermilab Accelerator Division, the Computer Division, and the CDF technical staff for their dedicated effort that made the CDF experiment possible.

I finally thank my mother, father, and sister for their warmhearted and endurance support while I worked on this thesis, especially in those years I was three thousand miles over the ocean.

This work was supported by the Ministry of Science, Culture and Education of Japan, the U.S. Department of Energy, the National Science Foundation, the Italian Istituto Nazionale di Fisica Nucleare, and the A. P. Sloan Foundation.

Contents

1	Introduction	1
1.1	Prompt Photon Physics	2
1.2	Parton Distribution Functions	5
1.3	Past, Present, and Future of Prompt Photon Measurement	8
1.4	Overview of the Analysis	9
2	Experimental Apparatus	14
2.1	Fermilab Accelerators	14
2.2	Collider Detector at Fermilab	15
2.3	Detector Components	16
2.3.1	Tracking	16
2.3.2	Calorimeters	17
2.3.3	Muon Detectors	21
2.3.4	Beam-Beam Counter	22
2.4	Data Acquisition System	22
2.5	Trigger System	23
2.5.1	Level 0	23
2.5.2	Level 1	24
2.5.3	Level 2	24
2.5.4	Level 3	25
2.6	Luminosity	25
3	Photon Detection	41
3.1	Electromagnetic Cascade	42

3.1.1	Basic Processes	42
3.1.2	Average Cascade	44
3.1.3	Fluctuations in Cascade	45
3.2	Photon Identification	48
3.2.1	Lateral Shower Profile	48
3.2.2	Longitudinal Shower Profile	49
4	GEANT3 Shower Simulation	61
4.1	GEANT3	61
4.2	Detector Setup in the Simulation	62
5	Event Reconstruction	68
5.1	Calorimeter	69
5.2	Tracking	72
6	Selection Parameters	74
6.1	Electromagnetic Cluster	74
6.2	Other Selection Criteria	78
7	Test Beam Electrons	83
7.1	Two Inch Aluminum Plate	84
7.2	Energy Scan	86
7.3	Position Scan	87
7.3.1	Absolute Energy Scale	88
7.3.2	Non-uniformity	89
7.3.3	Comparisons	89
7.4	Uncertainty of the GEANT3 Simulation	91
8	W Electrons	109
8.1	Event Selection	109
8.2	Monte Carlo Simulation	110
8.3	Estimation of Materials	111

9	Prompt Photons	118
9.1	Event Selection	118
9.2	Simulation	119
9.3	Extraction of Photons	122
9.4	Efficiencies and Uncertainties	123
9.4.1	Level 2 Trigger	123
9.4.2	Isolation	127
9.4.3	E^{had}/E^{EM}	129
9.4.4	$\chi^2_{3\times 3}(\text{old})$ and $\chi^2_{3\times 3}$	130
9.4.5	VTPC Hit Occupancy	131
9.4.6	Vertex	131
9.4.7	Geometrical Acceptance	131
9.4.8	Level 2 Clustering Inefficiency	131
9.4.9	$K_S^0 \rightarrow \pi^0\pi^0$	133
9.4.10	η/π^0 Ratio	134
9.4.11	Electron Contamination	134
9.4.12	Other Uncertainties	136
10	Results and Discussions	165
10.1	Inclusive Cross Section	165
10.2	Differential Cross Section	165
10.2.1	Uncertainty in the Simulation	166
10.2.2	Estimation of Material Thickness	166
10.2.3	Extraction of Photons	168
10.2.4	Efficiencies and Uncertainties	169
10.2.5	Differential Cross Section	169
10.3	Comparison with QCD Predictions	170
10.4	Photon Fraction	171
10.5	Stability of Photon Cross Section	173
11	Future Prospects	189
11.1	Systematic Uncertainty	190

11.2 Precision Measurement	190
11.3 Angular Distribution	191
11.4 Small x Gluons	191
12 Conclusion	196
A Formulation for the Uniformity Estimation	197

List of Tables

1.1	Theoretical calculations of the inclusive cross section for prompt photon production. Errors are statistical since the calculation utilizes the Monte Carlo method.	8
2.1	The calorimeter properties. Energy resolution (σ/E) and position resolution are typical values at 50 GeV.	18
2.2	Material thickness of the endplug electromagnetic calorimeter.	27
2.3	Tower segmentation. "Local (Calorimetry)," "Trigger," "TOWE" represent tower numbers for the calorimeter, the level 2 trigger, and the off-line analysis segmentation. At the trigger level, $\Delta\eta \approx 0.2$ of a tower, and $\Delta\eta \approx 0.09$ for the off-line analysis. Left numbers are for the west module, and right for the east. Numbers in parentheses are the polar angle θ and the corresponding pseudorapidity η at the tower centroids. The φ segmentation is $\Delta\varphi = 5^\circ$ for the local and TOWE tower and 15° for the trigger.	27
3.1	Possible backgrounds. Pure neutral decay (into multi-photons) fraction is also shown.	42
4.1	Material and thickness of the PEM in the GEANT3 simulation.	63
7.1	Absolute energy scale and uniformity for the first segment of the PEM pad.	90
8.1	W selection.	110

8.2	χ_{FSEF}^2 for the W electrons. The aluminum thickness is smeared on an event by event basis with a gaussian function in each simulation. The mean and σ are scanned. The aluminum thickness is limited within 0 cm to $2 \times \text{mean}$	111
9.1	Photon candidate selection.	119
9.2	The number of candidates in the prompt photon sample.	120
9.3	Selection for level 2 trigger study.	124
9.4	Parameters a and b obtained from the fits.	126
9.5	Number of bad towers and geometrical acceptances for Towers in the PEM. Tower number is in the TOWE number. See also Fig. 6.1.	132
9.6	Numbers of clusters in η_{det} ranges with and without requiring the corresponding level 2 clusters.	133
9.7	Efficiencies and systematic uncertainties.	136
10.1	χ_{FSEF}^2 for the W electrons in each η range. The aluminum thickness in the GEANT3 simulation is smeared around the mean with the gaussian σ , where the mean and the σ are scanned. The thickness is limited within 0 cm to $2 \times \text{mean}$. χ_{FSEF}^2 values for the mean thicknesses from 2.5 cm to 3.5 cm are not shown.	167
10.2	Efficiencies and systematic uncertainties in the pseudorapidity ranges of $1.32 < \eta < 1.77$ and $1.77 < \eta < 2.22$	169

List of Figures

1.1	Leading order Feynman diagrams for prompt photon production.	2
1.2	Some of tree level 2 to 2 hard scattering diagrams which can contribute to the bremsstrahlung process.	3
1.3	Feynman diagrams for some of $O(\alpha_s^2)$ three body subprocesses.	4
1.4	Feynman diagrams for some of one-loop graphs contributing to the $O(\alpha_s^2)$ calculation.	5
1.5	Gluon distributions of parton distribution functions, MRS (G), CTEQ 3M, and GRV 94 HO. Distributions of the u quark (valence and sea) are also shown for CTEQ 3M.	11
1.6	Inclusive production cross section for prompt photons of $27 \text{ GeV} < E_T < 40 \text{ GeV}$ in $\sqrt{s} = 1.8 \text{ TeV}$ $\bar{p}p$ collisions with respect to pseudorapidity η . NLO QCD calculations by Owens [7].	12
1.7	Compilation of prompt photon experiments compared to NLO QCD predictions using CTEQ2M parton distributions. Most of the data sets display a steeper dependence on x_T than is predicted by NLO QCD (horizontal line). [J. Huston <i>et al.</i> , Phys. Rev. D 51 , 6139 (1995)]	13
2.1	A schematic view of the Fermilab five stage accelerators providing the world's highest energy.	28
2.2	A perspective view of the CDF detector showing the central detector, the forward and backward detectors.	29
2.3	Cross section through a vertical plane of one half the CDF detector. The detector is symmetric about the midplane and roughly symmetric around the beam axis.	30

2.4	An isometric view of two VTPC modules. They are rotated in φ by 11.3° with respect to each other.	31
2.5	End view of the CTC showing the location of the slots in the aluminum endplate.	32
2.6	Calorimeter towers in one of eight identical η - φ quadrants ($\Delta\varphi = 90^\circ, \eta > 0$). The electromagnetic calorimeter have complete φ coverage out to $\eta = 4.2$	33
2.7	Quadrant of the calorimeter where A, B, C show central, endwall, and endplug, respectively. Towers are numbered from 0 (at 90° in polar direction) to 11 (last tower of endwall modules). Hadronic towers 6,7, and 8 are shared between the central and endwall calorimeters.	34
2.8	Exploded view of a layer of the proportional tube array of the PEM. PC boards with pad patterns and ground plane are shown.	35
2.9	Isometric view of a quadrant showing the projective pad tower structure and longitudinal layers.	36
2.10	Patterns of the outside pickup of electrodes: (a) pads, (b) θ -strips, (c) φ -strips.	37
2.11	The layer of the central muon chambers in one of the central wedges. . .	38
2.12	Elements of the forward muon detector planes.	39
2.13	A beam's-eye view of one of the beam-beam counter planes.	40
3.1	Fractional energy loss per radiation length in lead as a function of electron or positron energy. [Particle Data Group, L. Montanet <i>et al.</i> , Phys. Rev. D 50 , 1260 (1994)]	51
3.2	Energy loss rate in various medium. [Particle Data Group, L. Montanet <i>et al.</i> , Phys. Rev. D 50 , 1260 (1994)]	52

- 3.3 Photon total cross sections as a function of energy in carbon and lead, showing the contributions of different processes. $\sigma_{p.e.}$ atomic photo-effect, $\sigma_{coherent}$ coherent scattering, $\sigma_{incoherent}$ incoherent scattering, κ_n pair production (nuclear field), κ_e pair production (electron field), σ_{nuc} photonuclear absorption. [Particle Data Group, L. Montanet *et al.*, Phys. Rev. D **50**, 1260 (1994)] 53
- 3.4 The average longitudinal profile of cascade showers for 100 GeV electrons incident on the PEM. The circles indicate the measurements, the solid histogram shows the GEANT3 shower simulation, and the curve is a gamma function fit to the measurements. 100 GeV photon induced cascades are also simulated, and the average profile is represented as the dashed histogram. 54
- 3.5 Energy deposits in layers normalized by the incident particle energy, showing fluctuations of 100 GeV electron induced cascades measured by the CDF endplug electromagnetic calorimeter. "Layer 0" measures energy at $t = 2.94 X_0$ in Fig. 3.4. "Layer 1" is $3.52 X_0$, "layer 2" $4.09 X_0$, and so on. Continues on the next page. 55
- 3.6 Distributions of two photon opening angle in $\pi^0 \rightarrow \gamma\gamma$ decays at initial π^0 energies of 50, 75, and 150 GeV. 57
- 3.7 The average profiles of longitudinal cascades induced in the PEM at an incident angle of 20° perpendicular to the chamber planes for single photons, two photons from π^0 decays, and six photons from $\eta \rightarrow 3\pi^0$ decays at a primary particle energy of 87 GeV simulated by GEANT3. Only the multi-photon neutral decay modes are simulated for the mesons. The depth is scaled by the layer number instead of the radiation length. The layer interval corresponds to $0.55 X_0$ at an incident angle of 20° . Detailed description about the GEANT3 simulation is found in the next chapter. . 58

3.8	GEANT3 Monte Carlo simulations for the average longitudinal cascades measured by the cathode pad. Particles are induced in the PEM at an incident angle of 20° perpendicular to the chamber planes for single photons, two photons from π^0 decays, and six photons from η decays at a primary particle energy of 87 GeV. Only the multi-photon neutral decay modes are simulated for the mesons. See Section 2.3.2 for detailed structure of the PEM.	59
3.9	Distributions of first segment energy deposits normalized by the total energy (FSEF). Cascade showers are simulated by GEANT3 under the same conditions in the previous figures.	60
4.1	Geometrical setup of the GEANT3 simulation.	65
4.2	Total amount of material.	66
4.3	Precise structure along the beam direction.	67
5.1	Distribution of event vertices along the beam axis for the prompt photon candidates without the vertex requirement.	73
6.1	PEM fiducial region. Horizontal numbers represent φ towers, and vertical numbers are η in the TOWE numbering (Table 2.3). Blank spaces showing the “fiducial region” of the PEM.	77
6.2	Distributions of $\chi^2_{3 \times 3}(\text{old})$ values for test beam electrons at various energies and incident angles. The incident angle is measured perpendicular to the PEM chambers.	80
6.3	Distributions of $\chi^2_{3 \times 3}$ values for test beam electrons at various energies and incident angles. The incident angle is measured perpendicular to the PEM chambers.	81

6.4	Distributions of VTPC hit occupancies for randomly sampled EM clusters with $E_T \geq 25$ GeV in $1.32 < \eta_{det} < 2.22$, where η_{det} is pseudorapidity measured from the event vertex assumed $z = 0$ cm. (a) with no isolation cut. (b) $E_T^{iso}(0.7) < 3$ GeV required. The peak at $R_{VTPC} = 1$ is considered electrons from heavy quark decays and reduced by limiting energies around the EM cluster. Events between the two peaks are also reduced significantly by the isolation cut compared to the peak at $R_{VTPC} = 0$. . .	82
7.1	MT6 beamline.	92
7.2	Average longitudinal shower profiles for 101 GeV electrons incident at the center of tower 8 ($\theta = 20.24^\circ$) measured by the anode wires. High voltages on layers 30 and 32 are off and removed from the plots. An uncertainty is assumed 5% for the data each layer; statistical errors are negligible. . .	93
7.3	FSEF distributions for 101 GeV electrons incident at the center of tower 8 ($\theta = 20.24^\circ$). Errors for the test beam are statistical only. 2000 electrons are simulated under each condition, and the number of events is normalized to the test beam data.	94
7.4	χ_{LSD}^2 and χ_{FSEF}^2 with respect to aluminum thickness in the GEANT3 simulation. 2000 electrons simulated at each thickness.	95
7.5	Average longitudinal showers for electrons with transverse energies 48, 76, 101, 126, and 157 GeV incident at the center of η tower 5 ($\theta = 26.40^\circ$). The symbols represent the test beam, and curves are the simulations. A uncertainty is assumed 5% for the test beam each layer. The aluminum thickness in the GEANT3 simulation is 8.1 cm.	96
7.6	(a) - (e) χ_{LSD}^2 shown as circles and quadratic fits. (f) Most probable thicknesses from the fits.	97
7.7	Distributions of FSEF for electrons with energies 48, 76, 101, 126, and 157 GeV at the center of η tower 5 ($\theta = 26.40^\circ$). Test beam electrons are shown as crosses, and the histograms are the simulations. The aluminum thickness in the GEANT3 simulation is 8.1 cm.	98

7.8	(a) - (e) χ_{FSEF}^2 shown as circles and quadratic fits. (f) Most probable thicknesses from the fits.	99
7.9	Average longitudinal showers for 101 GeV/c electrons incident at the centers of η towers 3, 6, and 12 ($\theta = 29.29, 24.13, \text{ and } 14.20^\circ$). The symbols represent the test beam, and curves are simulations. An uncertainty is assumed 3% for the test beam data each layer. Dead layers are excluded from averaging. The aluminum thickness in the GEANT3 simulation is 8.1 cm.	100
7.10	Energy deposits in the pad segments to 101 GeV test beam electrons at the center of η 8. No dead layer correction is applied.	101
7.11	Deviations of the averages energy deposits to 101 GeV electrons. The aluminum thicknesses for the simulation are 7.7, 8.1, 8.1, 8.3, and 7.7 cm for $\eta = 3, 5, 6, 8, \text{ and } 12$, respectively, where the simulation best matches to the test beam. Statistical uncertainties are negligible for both test beam data and Monte Carlo.	102
7.12	Ratios of energies measured by the pad and the anode for (a) the sum of all the three depth segments (all 34 layers) and (b) the first segment (first 5 layers). 101 GeV electrons at all the PEM towers in the fiducial region. 100 events collected from each tower.	103
7.13	First segment responses of the pad to 101 GeV electrons. (a) First segment energy for a tower ($\eta = 8, \varphi = 22$). (b) The averages of FSE for 127 same η towers. (c) The standard deviations. (d) The variances. . . .	104
7.14	(a) - (e) χ_{LSD}^2 and quadratic fits. The last five layers are not used for the χ_{LSD}^2 calculation in (a). (f) Most probable thicknesses from the fits. . . .	105
7.15	Distributions of FSEF for the η position scan. 101 GeV electrons are incident at the centers of η towers 3, 5, 6, 8, and 12 ($\theta = 29.29, 26.24, 24.13, 20.24, \text{ and } 14.20^\circ$, respectively). The aluminum thickness in the simulation is 8.1 cm. Note that the test beam is shown in histograms and the Monte Carlo in the symbols since there simulated 2000 electrons for each tower, while the test beam contains 12700 events each.	106

7.16 (a) - (e) χ_{FSEF}^2 and quadratic fits. (f) Most probable thicknesses from the fits.	107
7.17 Estimations of the total amount of materials between the MT5 dipole magnets and the PEM excluding the real two inch aluminum plate placed in front of the detector. The average is shown in the solid line, and the dots represent the error.	108
8.1 Distributions of E , E_T , and $ \eta $ for the 489 W electrons.	113
8.2 FSEF distributions of the W electrons and the simulation. In the GEANT3 simulation, the thickness of the aluminum plate is changed on an event by event basis to reproduce the CTC endplate, calculated from the blue print of the CTC endplate for electron path lengths.	114
8.3 Distribution of the electron path lengths in the CTC endplate ($\times \cos \theta$). The path length is defined as a total aluminum length in the CTC endplate along a trajectory of a particle with θ , φ , and z_{vertex} . The mean and the σ correspond to $0.36 X_0$ and $0.16 X_0$, respectively.	115
8.4 FSEF distributions of the W electrons and simulations. In each simulation, the aluminum thickness is smeared with a gaussian function. The mean is fixed at 6.0 cm, and the σ is scanned.	116
8.5 (a)-(e) FSEF distributions of the W electrons and simulations. In each simulation, the aluminum thickness is smeared with a gaussian function. The σ is fixed at 2.0 cm, and the mean is scanned. (f) χ_{FSEF}^2 values with respect to the mean aluminum thickness.	117
9.1 Distributions of E_T , E , $ \eta $, and FSEF of the photon sample.	137
9.2 FSEF distributions for various isolation thresholds.	138
9.3 FSEF distributions of the GEANT3 simulation for single photons, π^0 's, and η 's. The mean thickness of the aluminum plate is 6.5 cm, and the gaussian σ is 2.0 cm. Only the neutral decay modes are simulated for mesons. Each spectrum is normalized to unity.	139

- 9.4 Fittings to the FSEF distribution of the data with the Monte Carlo spectra of photons and background mesons. Four sets of the Monte Carlo data with different means of the aluminum plate thickness are used. Bins of $FSEF = 0.0 - 0.2$ are used for the χ^2 calculation. 140
- 9.5 The number of photons by the fitting with respect to the mean aluminum thickness. For the nominal thickness (solid vertical line) of 6.24 cm, the number of photons is evaluated 1972. The error (dots) is estimated 353 for ± 0.51 cm, which is the sum of the uncertainties for the GEANT3 simulation, obtained $0.046 X_0$ in Section 7, and for the total amount of materials, obtained 0.31 cm thick aluminum in Section 8. 141
- 9.6 $\eta_{det}-\varphi$ positions for off-line EM clusters with no corresponding level 2 trigger EM clusters. $E_T^{det} > 23$ GeV required for clusters. 142
- 9.7 $\eta_{det}-\varphi$ positions for off-line clusters which passed the “gas photon 23 GeV” trigger. $E_T^{det} > 23$ GeV, $E^{had}/E^{EM} < 0.1$, and $\chi^2(ol) < 20$ required. Four quadrants are overlaid for each east or west to enhance the pattern. Solid lines represent the level 2 trigger tower boundaries, and dashed lines are the off-line towers. 143
- 9.8 The efficiencies for the level 2 trigger “gas photon 23 GeV.” Continues on the next page. 144
- 9.9 The efficiencies for the level 2 trigger “gas photon 23 GeV.” 146
- 9.10 Distributions of E_T in a randomly placed cone of radius 0.7 for minimum bias events, approximating an underlying E_T distribution expected for prompt photon events in (a) the central region of $|\eta| < 0.9$ and (b) the endplug region of $1.32 < |\eta| < 2.22$. Dashed line in (b) show the $E_T^{iso}(0.7)$ distribution for the prompt photon candidates without the isolation cut, and the number of events are normalized to that of minimum bias events. Mean and RMS shown in (b) are for minimum bias events. 147
- 9.11 Distributions of (a) E_T in a cone of radius 0.3, (b) 0.4, and (c) in an annulus between radius 0.3 and 0.4 centered on test beam electrons of 101 GeV incident at the center of η tower 8 (local number), corresponding to $E_T = 35$ GeV. 148

- 9.12 Lateral shower leakage for an EM cluster represented in curves showing (a) η and (b) energy dependences. Note that the typical EM cluster size is $\Delta\eta \times \Delta\varphi \sim 0.1$ 149
- 9.13 (a) E_T in a cone of radius 0.7 due to lateral shower leakage for prompt photon candidates. (b) Underlying E_T with lateral shower leakage. Solid lines represent the nominal value. Dashed lines and dots are the minimum and the maximum, respectively. The mean and RMS are for the nominal. 150
- 9.14 Longitudinal shower profiles for photons and electrons by the GEANT3 simulation. $E = 87$ GeV at $\eta = 1.72$ corresponding to $E_T = 30$ GeV. . . 151
- 9.15 E^{had}/E^{EM} ratios for Monte Carlo photons (line) and electrons (dashed line). (a) $E = 87$ GeV at $\eta = 1.72$ ($E_T = 30$ GeV). (b) $E = 107$ GeV at $\eta = 1.72$ ($E_T = 37$ GeV). 152
- 9.16 (a) θ dependence of the cut " $E^{had}/E^{EM} < 0.05$." (b) Energy dependence of the cut " $E^{had}/E^{EM} < 0.05$." Solid line showing a linear fit, and dashed lines are 1% errors. 153
- 9.17 $\chi^2_{3 \times 3}$ vs energy for the old and the new. Test beam electrons incident at the center of calorimetry tower 5 ($\eta = 1.45$ or $\theta = 26.33^\circ$). Only 12 events with $\chi^2_{3 \times 3}(\text{old}) \geq 20$ and one with $\chi^2_{3 \times 3} \geq 5$ out of 2344 events. See text for details. 154
- 9.18 $\chi^2_{3 \times 3}$ vs η for the old and the new. 101 GeV test beam electrons used. Only one event with $\chi^2_{3 \times 3}(\text{old}) \geq 20$ and one with $\chi^2_{3 \times 3} \geq 5$ out of 3192 events. See text for details. 155
- 9.19 Distributions of VTPC hit occupancy R_{VTPC} for (a) minimum bias events along randomly placed roads between the vertex and the PEM, (b) W electron candidates without the E_T and the VTPC requirements, and (c) EM clusters with the same requirements as the prompt photon candidates except the VTPC cut. 156
- 9.20 Off-line cluster positions for level 2 trigger unbiased clusters with $E_T^{det} > 20$ GeV. No requirement for level 2 trigger EM clusters. Four quadrants are overlaid each east or west for enhancement. Solid lines represent level 2 trigger tower boundaries. 157

- 9.21 Off-line cluster positions for level 2 trigger unbiased clusters with $E_T^{det} > 20$ GeV. The existence of the corresponding level 2 EM clusters required. Four quadrants are overlaid each east or west for enhancement. Solid lines represent level 2 trigger tower boundaries. 158
- 9.22 Off-line cluster positions for level 2 trigger unbiased clusters with $E_T^{det} > 20$ GeV having no corresponding level 2 EM clusters. Four quadrants are overlaid each east or west for enhancement. Solid lines represent level 2 trigger tower boundaries. 159
- 9.23 (a) Distributions of FSEF for K_S^0 's, the total background, and single photons, showing the K_S^0 contribution. The mean thickness of the aluminum plate is 6.5 cm, and the gaussian σ is 2.0 cm for the GEANT3 simulation. Only the neutral decay modes are simulated for mesons. (b) Fitting with the above spectra to the prompt photon candidates. Bins of FSEF = 0.0 – 0.2 are used for a fitting. 160
- 9.24 Distributions of FSEF for the background. η 's and π^0 's are mixed at the production ratios of 0.75 ($1.02 - 1\sigma$), 1.02, and 1.29 ($1.02 + 1\sigma$). 161
- 9.25 Fittings with the FSEF spectra for the background mesons at the η/π^0 production ratios of 0.75 and 1.29. 162
- 9.26 (a) Distributions of FSEF for electrons, the total background, and single photons, showing the electron contamination. The electron spectrum is normalized to the background spectrum at a ratio of 0.04, which is best matched when the prompt photon to background meson ratio is 1. The mean thickness of the aluminum plate is 6.5 cm, and the gaussian σ is 2.0 cm. (b) Distributions of FSEF for the background including electrons at $e^-/b.g. = 3, 4, \text{ and } 5\%$, where the prompt photon to background ratio is assumed 1. 163
- 9.27 Fittings with the electron mixed background. The electron contamination ratio is varied, $e^-/b.g. = 3, 4, \text{ and } 5\%$. Bins of FSEF = 0.0 – 0.2 are used for fittings. 164

10.1	Distributions of FSEF for the prompt photon candidates in two pseudorapidity ranges.	175
10.2	Distributions of FSEF for the W electrons in two pseudorapidity ranges.	176
10.3	(a)-(e) FSEF distributions for the W electrons and the GEANT simulations in $1.32 < \eta < 1.77$. In each simulation, the aluminum thickness is smeared with a gaussian function. The σ is fixed to 2.0 cm, and the mean is scanned. (f) χ^2_{FSEF} values with respect to the mean aluminum thickness.	177
10.4	(a)-(e) FSEF distributions for the W electrons and the GEANT simulations in $1.77 < \eta < 2.22$. In each simulation, the aluminum thickness is smeared with a gaussian function. The σ is fixed to 2.0 cm, and the mean is scanned. (f) χ^2_{FSEF} values with respect to the mean aluminum thickness.	178
10.5	Fittings to the FSEF distribution of the data in $1.32 < \eta < 1.77$ with Monte Carlo spectra of single photons and background mesons. Five sets of Monte Carlo data with the aluminum plate thickness smeared around different means are used. Four of them are shown here. Bins of FSEF = 0.0 – 0.2 are used for fittings.	179
10.6	Fittings to the FSEF distribution of the data in $1.77 < \eta < 2.22$ with Monte Carlo spectra of single photons and background mesons. Four sets of Monte Carlo data with the aluminum plate thickness smeared around different means are used. Bins of FSEF = 0.00 – 0.15 are used for fittings.	180
10.7	Estimations of the nominal numbers of prompt photon events for the low and high η ranges.	181
10.8	Differential cross section for prompt photon production in the endplug and central regions.	182
10.9	Differential cross section for prompt photon production. The next-to-leading order QCD calculation with CTEQ 3M parton distribution function is compared with the measurement. The leading order calculation is also presented.	183
10.10	NLO QCD calculations with PDF sets, CTEQ 3M, MRS (G), and GRV 94 HO.	184

10.11	Estimations of uncertainties in the NLO QCD calculation. (a) The QCD prediction increases with loosening the isolation cut. (b) The QCD prediction increases with decreasing the factor for the renormalization and factorization scales.	185
10.12(a)	The photon fraction with respect to the isolation threshold. (b) The numbers of prompt photon events and neutral meson events with respect to the isolation threshold.	186
10.13	The photon fraction with respect to the isolation threshold for two η ranges.	187
10.14	The prompt photon cross section with respect to the isolation threshold. The cross section is stable for $\lesssim 5$ GeV.	188
11.1	NLO QCD calculations of the differential cross section for prompt photon production with respect to P_T	193
11.2	NLO QCD calculations showing difference in the differential cross section for prompt photon production. The cross section is normalized by CTEQ 3M.	194
11.3	Scatter plot showing an η distribution of prompt photons and the associate jets by the HERWIG Monte Carlo generator.	195

The CDF Collaboration

F. Abe,⁸ D. Amidei,⁴ G. Apollinari,¹¹ M. Atac,⁴ P. Auchincloss,¹⁴ A. R. Baden,⁶
 A. Bamberger,^a A. Barbaro-Galtieri,⁹ V. E. Barnes,¹² F. Bedeschi,¹¹ S. Behrends,²
 S. Belforte,¹¹ G. Bellettini,¹¹ J. Bellinger,¹⁸ J. Bensinger,² A. Beretvas,⁴ J. P. Berge,⁴
 S. Bertolucci,⁵ S. Bhadra,⁷ M. Binkley,⁴ R. Blair,¹ C. Blocker,² A. W. Booth,⁴
 G. Brandenburg,⁶ D. Brown,⁶ E. Buckley,¹⁴ A. Byon,¹² K. L. Byrum,¹⁸ C. Campagnari,³
 M. Campbell,³ R. Carey,⁶ W. Carithers,⁹ D. Carlsmith,¹⁸ J. T. Carroll,⁴ R. Cashmore,^a
 F. Cervelli,¹¹ K. Chadwick,⁴ G. Chiarelli,⁵ W. Chinowsky,⁹ S. Cihangir,⁴ A. G. Clark,⁴
 D. Connor,¹⁰ M. Contreras,² J. Cooper,⁴ M. Cordelli,⁵ D. Crane,⁴ M. Curatolo,⁵ C. Day,⁴
 S. Dell'Agello,¹¹ M. Dell'Orso,¹¹ L. Demortier,² P. F. Derwent,³ T. Devlin,¹⁴
 D. DiBitonto,¹⁵ R. B. Drucker,⁹ J. E. Elias,⁴ R. Ely,⁹ S. Errede,⁷ B. Esposito,⁵ B. Flaughner,¹⁴
 G. W. Foster,⁴ M. Franklin,⁶ J. Freeman,⁴ H. Frisch,³ Y. Fukui,⁸ Y. Funayama,¹⁶
 A. F. Garfinkel,¹² A. Gauthier,⁷ S. Geer,⁶ P. Giannetti,¹¹ N. Giokaris,¹³ P. Giromini,⁵
 L. Gladney,¹⁰ M. Gold,⁹ K. Goulianos,¹³ H. Grassmann,¹¹ C. Grosso-Pilcher,³ C. Haber,⁹
 S. R. Hahn,⁴ R. Handler,¹⁸ K. Hara,¹⁶ R. M. Harris,⁹ J. Hauser,³ T. Hessing,¹⁵
 R. Hollebeek,¹⁰ L. Holloway,⁷ P. Hu,¹⁴ B. Hubbard,⁹ B. T. Huffman,¹² R. Hughes,¹⁰
 P. Hurst,⁷ J. Huth,⁴ M. Incagli,¹¹ T. Ino,¹⁶ H. Iso,¹⁶ H. Jensen,⁴ C. P. Jessop,⁶
 R. P. Johnson,⁴ U. Joshi,⁴ R. W. Kadel,⁴ T. Kamon,¹⁵ S. Kanda,¹⁶ D. A. Kardelis,⁷
 I. Karliner,⁷ E. Kearns,⁶ R. Kephart,⁴ P. Kesten,² R. M. Keup,⁷ H. Keutelian,⁷ S. Kim,¹⁶
 L. Kirsch,² K. Kondo,¹⁶ S. E. Kuhlmann,¹ E. Kuns,¹⁴ A. T. Laasanen,¹² J. I. Lamoureux,¹⁸
 W. Li,¹ T. M. Liss,⁷ N. Lockyer,¹⁰ C. B. Luchini,⁷ P. Maas,⁴ M. Mangano,¹¹ J. P. Marriner,⁴
 R. Markeloff,¹⁸ L. A. Markosky,¹⁸ R. Mattingly,² P. McIntyre,¹⁵ A. Menzione,¹¹ T. Meyer,¹⁵
 S. Mikamo,⁸ M. Miller,³ T. Mimashi,¹⁶ S. Miscetti,⁵ M. Mishina,⁸ S. Miyashita,¹⁶
 Y. Morita,¹⁶ S. Moulding,² A. Mukherjee,⁴ L. F. Nakae,² I. Nakano,¹⁶ C. Nelson,⁴
 C. Newman-Holmes,⁴ J. S. T. Ng,⁶ M. Ninomiya,¹⁶ L. Nodulman,¹ S. Ogawa,¹⁶ R. Paoletti,¹¹
 A. Para,⁴ E. Pare,⁶ J. Patrick,⁴ T. J. Phillips,⁶ R. Plunkett,⁴ L. Pondrom,¹⁸ J. Proudfoot,¹
 G. Punzi,¹¹ D. Quarrie,⁴ K. Ragan,¹⁰ G. Redlinger,³ J. Rhoades,¹⁸ M. Roach,¹⁷ F. Rimondi,^a
 L. Ristori,¹¹ T. Rohaly,¹⁰ A. Roodman,³ A. Sansoni,⁵ R. D. Sard,⁷ A. Savoy-Navarro,^a
 V. Scarpine,⁷ P. Schlabach,⁷ E. E. Schmidt,⁴ M. H. Schub,¹² R. Schwitters,⁶ A. Scribano,¹¹
 S. Segler,⁴ Y. Seiya,¹⁶ M. Sekiguchi,¹⁶ P. Sestini,¹¹ M. Shapiro,⁶ M. Sheaff,¹⁸ M. Shochet,³
 J. Siegrist,⁹ P. Sinervo,¹⁰ J. Skarha,¹⁸ K. Sliwa,¹⁷ D. A. Smith,¹¹ F. D. Snider,³ R. St. Denis,⁶
 A. Stefanini,¹¹ R. L. Swartz, Jr.,⁷ M. Takano,¹⁶ K. Takikawa,¹⁶ S. Tarem,² D. Theriot,⁴
 M. Timko,¹⁵ P. Tipton,⁹ S. Tkaczyk,⁴ A. Tollestrup,⁴ G. Tonelli,¹¹ J. Tonnison,¹²
 W. Trischuk,⁶ Y. Tsay,³ F. Ukegawa,¹⁶ D. Underwood,¹ R. Vidal,⁴ R. G. Wagner,¹
 R. L. Wagner,⁴ J. Walsh,¹⁰ T. Watts,¹⁴ R. Webb,¹⁵ C. Wendt,¹⁸ W. C. Wester, III,⁹
 T. Westhusing,¹¹ S. N. White,¹³ A. B. Wicklund,¹ H. H. Williams,¹⁰ B. L. Winer,⁹ A. Yagil,⁴
 A. Yamashita,¹⁶ K. Yasuoka,¹⁶ G. P. Yeh,⁴ J. Yoh,⁴ M. Yokoyama,¹⁶ J. C. Yun,⁴ F. Zetti¹¹

¹ Argonne National Laboratory, Argonne, Illinois 60439

² Brandeis University, Waltham, Massachusetts 02254

³ University of Chicago, Chicago, Illinois 60637

⁴ Fermi National Accelerator Laboratory, Batavia, Illinois 60510

⁵ Laboratori Nazionali di Frascati, Istituto Nazionale di Fisica Nucleare, Frascati, Italy

⁶ Harvard University, Cambridge, Massachusetts 02138

⁷ University of Illinois, Urbana, Illinois 61801

⁸ National Laboratory for High Energy Physics (KEK), Tsukuba, Ibaraki 305, Japan

⁹ Lawrence Berkeley Laboratory, Berkeley, California 94720

¹⁰ University of Pennsylvania, Philadelphia, Pennsylvania 19104

- ¹¹ *Istituto Nazionale di Fisica Nucleare, University and Scuola Normale Superiore of Pisa, I-56100 Pisa, Italy*
¹² *Purdue University, West Lafayette, Indiana 47907*
¹³ *Rockefeller University, New York, New York 10021*
¹⁴ *Rutgers University, Piscataway, New Jersey 08854*
¹⁵ *Texas A&M University, College Station, Texas 77843*
¹⁶ *University of Tsukuba, Tsukuba, Ibaraki 305, Japan*
¹⁷ *Tufts University, Medford, Massachusetts 02155*
¹⁸ *University of Wisconsin, Madison, Wisconsin 53706*
^a *Visitor*

Chapter

Introduction

Physics with large transverse momenta (P_T) produced in proton-antiproton collisions and looks to new physics such as supersymmetry [1] and grand unification [2] as well as tests for the standard model. The CDF experiment has been carrying out such tests, and high P_T physics, at geographically-separated sites of the $SU(3) \times U(1)$ electroweak gauge model [3] and quantum chromodynamics (QCD) of the $SU(3)$ color gauge theory [4, 5]. In this thesis, we present, for the first time in the CDF experiment, a measurement of prompt photons with transverse energies between 20 GeV and 40 GeV produced in a 10^7 pseudorapidity-range of $1.37 < |\eta| < 1.43$ ($x = -1$ to 1) [6, 7], where η is the pseudorapidity measured from the proton direction) in a $\sqrt{s} = 1.8$ TeV proton-antiproton collision. The data of an integrated luminosity $L = 3.0 \text{ pb}^{-1}$ collected during the 1994-1995 TEVATRON running run at Fermi National Accelerator Laboratory (Fermilab) in Batavia, Illinois, the United States of America are used for the study.

Throughout the literature, the term "prompt photon" is used to indicate a single photon produced from the initial parton within an interval of decay produced central region such as η^0 's and η^{\pm} 's. However, in QCD calculations, a photon emitted in the hard-scattering process, from a jet which is initiated by a quark or a gluon from the hard-scattering vertex, is also included in prompt photons.

Chapter 1

Introduction

Photons with large transverse momentum (P_T) produced in proton-antiproton collisions are keys to new physics such as supersymmetry [1] and quark compositeness [2], as well as tests for the standard model. The CDF experiment has been carrying out such tests, with high P_T photons, as gauge-gauge couplings of the $SU(2)\times U(1)$ electroweak gauge model [3] and quantum chromodynamics (QCD) of the $SU(3)$ color gauge theory [4, 5].

In this thesis, we present, for the first time in the CDF experiment, a measurement of prompt photons with transverse energies between 27 GeV and 40 GeV produced in a high pseudorapidity range of $1.32 < |\eta| < 2.22$ ($\eta = -\ln \tan(\theta/2)$, where θ is the polar angle of photons measured from the proton direction) in $\sqrt{s} = 1.8$ TeV proton-antiproton collisions. The data of an integrated luminosity $\mathcal{L} = 3.8 \text{ pb}^{-1}$ collected during the 1988-1989 TEVATRON collider run at Fermi National Accelerator Laboratory (Fermilab) in Batavia, Illinois, the United States of America are used for the study.

Throughout the literature, the term “prompt photon” is used to indicate a single photon produced from the initial parton collision in contrast to decay particles of neutral mesons such as π^0 's and η 's. However, in QCD calculations, a photon radiated, in the bremsstrahlung process, from a jet which is initiated by a quark or a gluon from the hard collision is also included in prompt photons.

1.1 Prompt Photon Physics

Prompt photon production plays an important role in determining the gluon distribution of the proton and testing perturbative QCD. Compared to jet production processes, there are two advantages in studies of perturbative QCD for prompt photon production.

- In the lowest order, there are only four diagrams for production of prompt photons, Compton and annihilation subprocesses, each with one QCD vertex as shown in Fig. 1.1.
- An energy and a production direction of a photon can be measured more accurately than those of a jet. In the latter case, there are problems of ambiguities in the jet definition and the poorer energy resolution of a detector to hadrons.

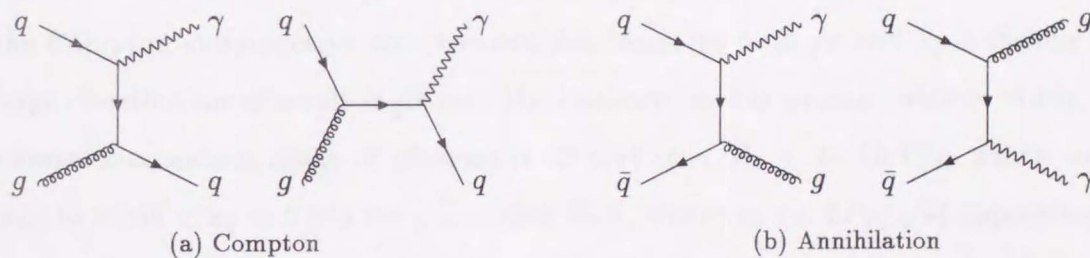


Figure 1.1: Leading order Feynman diagrams for prompt photon production.

In the parton model, the hard scattering is described by the lowest-order subprocesses which, for high- P_T photon production, correspond to two-body scattering. The Born terms for Compton and annihilation subprocesses are

$$\frac{d\sigma}{dt}(gq \rightarrow \gamma q') = \frac{\pi\alpha\alpha_s}{3} \frac{\hat{s}^2 + \hat{u}^2}{-\hat{s}^3\hat{u}},$$

where $\hat{s} = (q + g)^2$, $\hat{t} = (q - q')^2$, $\hat{u} = (g - q')^2$, and

$$\frac{d\sigma}{dt}(q\bar{q} \rightarrow \gamma g) = \frac{8\pi\alpha\alpha_s}{9} \frac{\hat{t}^2 + \hat{u}^2}{\hat{s}^2\hat{t}\hat{u}},$$

where $\hat{s} = (q + \bar{q})^2$, $\hat{t} = (q - g)^2$, and $\hat{u} = (\bar{q} - g)^2$. The corresponding expression for the invariant cross section is

$$E_\gamma \frac{d^3\sigma}{dp_\gamma^3}(A + B \rightarrow \gamma + X) = \sum_{ab} \int dx_a dx_b \phi_{a/A}(x_a) \phi_{b/B}(x_b) \frac{d\sigma}{dt}(ab \rightarrow \gamma c) \delta(\hat{s} + \hat{t} + \hat{u}),$$

where a , b , and c are incoming and outgoing partons. $\phi_{a/A}(x_a)$ represents the probability density for finding parton a in the hadron A , carrying momentum fraction x_a .

For large x , where x represents the parton momentum fraction, the tree level Feynman diagrams dominate prompt photon production. In addition, it is expected that the annihilation subprocesses have a large contribution in proton-antiproton collisions, while the Compton subprocesses are significant in proton-proton collisions because probability densities of “sea” quarks and gluons are small at high x . On the other hand, for small x , the Compton subprocesses are expected dominant for both pp and $\bar{p}p$ collisions due to large distribution of small x gluons. For instance, in our prompt photon study, the transverse momentum range of photons is $27 \text{ GeV}/c < P_T < 40 \text{ GeV}/c$, which corresponds to $0.030 < x_T < 0.044$ for $\sqrt{s} = 1800 \text{ GeV}$, where $x_T (\equiv 2P_T/\sqrt{s})$ approximates the parton momentum fraction. In other words, our study is sensitive to the gluon distribution inside the proton at small x . However, for these small x values, higher order diagrams, especially the bremsstrahlung process, cannot be neglected for prompt photon production. In the bremsstrahlung process, a photon is radiated by a quark or a gluon produced through parton-parton scattering (Fig. 1.2) in the process of hadronization. In

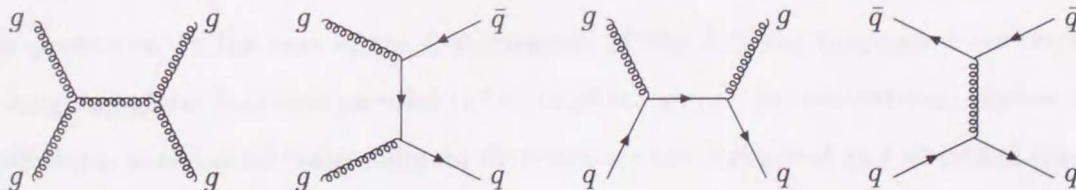


Figure 1.2: Some of tree level 2 to 2 hard scattering diagrams which can contribute to the bremsstrahlung process.

such bremsstrahlung subprocesses, the inclusive invariant cross section can be written

as

$$E_\gamma \frac{d^3\sigma}{dp_\gamma^3}(A + B \rightarrow \gamma + X)$$

$$= \sum_{abcd} \int dx_a dx_b dz_c \phi_{a/A}(x_a) \phi_{b/B}(x_b) \frac{\hat{s}}{z_c^2 \pi} \frac{d\sigma}{d\hat{t}}(ab \rightarrow cd) D_{\gamma/c}(z_c) \delta(\hat{s} + \hat{t} + \hat{u}),$$

where a, b , and c, d are incoming and outgoing partons. Hatted variables are Mandelstam invariants of the partonic subprocess. $D_{\gamma/c}(z_c)$ is the fragmentation function which describes the probability for parton c to radiate a photon with a fractional momentum to the parton of z_c in the final state. $d\sigma/d\hat{t}$ is the partonic differential cross section, and the factor $\hat{s}/(z_c^2\pi)$ is associated with the partonic and hadronic cross sections.

One may consider the $O(\alpha_s^2)$ three body processes. Some of such diagrams are illustrated in Fig. 1.3. However, various collinear singularities appear in calculating

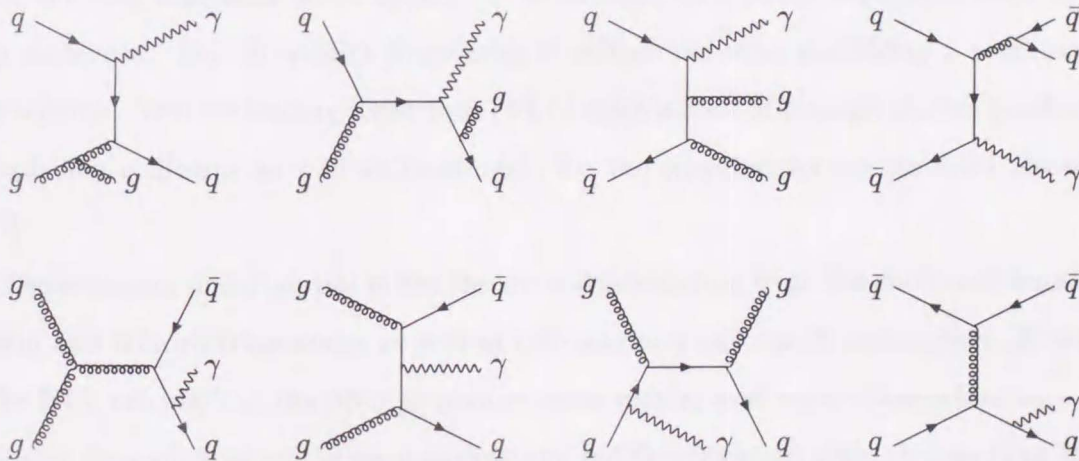


Figure 1.3: Feynman diagrams for some of $O(\alpha_s^2)$ three body subprocesses.

these processes. In the case of the first diagram of Fig. 1.3, the divergence occurs when the outgoing gluon becomes parallel to the incident gluon. In conventional higher order calculations, such initial state collinear divergencies are factorized and absorbed into the initial parton distribution. Similarly, in the last diagram of Fig. 1.3, when the outgoing quark (right-bottom) and photon become parallel, the diagram develops a final state collinear singularity. However, such a contribution has already been included in the bremsstrahlung subprocess, and when calculating, subtraction terms are introduced in order to avoid double counting. Other final parton (quark-gluon, gluon-gluon, quark-

splitting) collinear singularities are factorized and absorbed into the parton-to-parton splitting (fragmentation) function.

In addition, another divergencies occur when one of the final state partons becomes soft. This infrared divergence is cancelled exactly by a corresponding divergence in one-loop interference diagrams. Some of such loop graphs are sketched in Fig. 1.4.

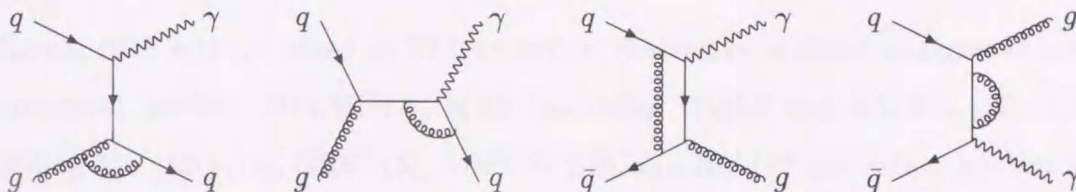


Figure 1.4: Feynman diagrams for some of one-loop graphs contributing to the $O(\alpha_s^2)$ calculation.

In the loop diagrams, there appear the ultraviolet divergency, associated with infinite loop momenta. The ultraviolet singularity is subtracted after specifying a renormalization scheme. Next-to-leading-logarithm (NLL) calculations of prompt photon production in hadronic collisions as well as treatments for the singularities are detailed elsewhere [6, 7].

There remain uncertainties in the theoretical calculation from the choices of renormalization and factorization scales as well as collinear and soft cutoff parameters. However, in the NLL calculation, the prompt photon cross section and other observables show less dramatic dependences on the renormalization and factorization scale choices than in the case where only the leading logarithms are used. It is also found that the collinear and soft cutoffs have almost no effects on the observables in the proper ranges of the parameters [7]. In addition, for comparisons with experimental data, the bremsstrahlung process or the photon fragmentation function gives rise to another uncertainty because of an isolation cut for reconstructing photons in the experiment.

1.2 Parton Distribution Functions

Studies of prompt photon production in hadronic collisions can date back to as early as the middle of the century [8], before the quark era. However, recent development

on prompt photon production shows qualitative understandings both theoretically and experimentally. Especially, evolution of the parton distribution function (PDF) in the last decade is remarkable. Until the late 1980's, the first generation of the PDF sets such as DO [9] and EHLQ [10] had been widely used. Those first generation PDF sets were based on leading order (LO) calculations and are no longer consistent with current data.

Recent PDF sets are based on NLL evolution, derived from global analyses of various experimental results. DFLM [11], MRS (including HMRS and KMRS) [12], CTEQ (including MT [13]) [14], GRV [15], ABFOW [16], and BM [17] are rather modern PDF sets. DFLM and ABFOW are for specific processes; DFLM for neutrino scattering and ABFOW for prompt photon production. Others are for general purposes. However, they differ from each other significantly, even within the same group because of differences in coverage of x and Q^2 , schemes of calculations, treatments of experimental errors, etc. Such differences between some PDF sets are shown in Fig. 1.5. The plot displays the gluon distribution function of today's most up-to-date PDF sets, MRS (G), CTEQ 3M, and GRV 94 HO. As one notices, more than 10% variation is observed in the gluon distribution, especially for lower x .

In Fig. 1.5, the gluon distributions for $0.002 < x < 0.2$ are presented. In our prompt photon study, an x_T range between 0.030 and 0.044 are explored. However, measurements of prompt photons at high rapidity provide us with information on the gluon density for lower x values. Since we concentrate on photons produced in $1.32 < |\eta| < 2.22$ with no restrictions on associate jets, the minimum allowed value of the parton fractional momentum

$$x_{min} = \frac{x_T \cdot e^\eta}{2 - x_T \cdot e^{-\eta}}$$

becomes as low as 0.002. At this small x , a steep rise of the gluon density with decreasing x is expected. However, it is questionable if this rise can be described by the conventional Altarelli-Parisi (or GLAP) evolution equations [18] or by the BFKL dynamics [19]. For much lower values of x , we are expected to enter a new regime where perturbative QCD is no longer valid.

The GLAP evolution starts from a known structure of the proton at $Q^2 = Q_0^2$,

and then the parton distributions can be calculated up to large $\log Q^2$ in perturbative QCD using the Altarelli-Parisi equations. The BFKL equation is effectively the leading $\alpha \log(1/x)$ resummation of soft gluon emissions. It is obtained on solving the equation that the gluon density rises toward small x as

$$x g(x, Q^2) \sim x^{-\lambda},$$

with $\lambda \sim 0.5$.

Recent deep inelastic scattering (DIS) experiments at HERA [20, 21] show such a behavior of the increase in the gluon (or, more correctly, sea quarks via $g \rightarrow q\bar{q}$ transition) density, but with $\lambda \sim 0.3$, which is rather consistent with perturbative QCD predictions using the GLAP evolution equations. However, the BFKL evolution cannot still be ruled out since the structure function $F_2(x, Q^2)$ is predicted [22] as

$$F_2(x, Q^2) = C(x, Q^2) x^{-\lambda} + F_2^{bg}(x, Q^2),$$

where the coefficient $C(x, Q^2)$ of the BFKL contribution and the non-BFKL contribution, $F_2^{bg}(x, Q^2)$, are weakly dependent on x . In the HERA regime of $x \sim 5 \times 10^{-4}$ and $F_2^{bg}(x, Q^2)/C(x, Q^2) \sim 30$ at $Q^2 \sim 15 \text{ GeV}^2$, $F_2(x, Q^2)$ results in the $x^{-0.3}$ behavior [23].

The lepton-hadron collisions provide today's most accurate measurements for the quark distributions. However, the gluon distribution can only be probed via $g \rightarrow q\bar{q}$ transition or in the next-to-leading order (NLO) processes ($e^-g \rightarrow e^-q\bar{q}$). Given the significant role which the gluons play in QCD, it is important to measure the gluon distribution in separate processes such as prompt photon or two jet production in hadron-hadron collisions.

The inclusive production cross section for prompt photons with $27 \text{ GeV} < E_T < 40 \text{ GeV}$ in $1.32 < |\eta| < 2.22$ is calculated up to the NLO processes by Owens [7] using recent PDF sets for $\bar{p}p$ collisions at $\sqrt{s} = 1.8 \text{ TeV}$ as listed in Table 1.1.

The differential cross section $d\sigma/d\eta$ is also computed and shown in Fig. 1.6 for the central ($|\eta| < 0.9$) and endplug ($1.32 < |\eta| < 2.22$) regions.

PDF Set	Cross Section (pb)
MRS (G)	1227 ± 6
CTEQ3M	1259 ± 5
GRV 94 HO	1176 ± 6

Table 1.1: Theoretical calculations of the inclusive cross section for prompt photon production. Errors are statistical since the calculation utilizes the Monte Carlo method.

1.3 Past, Present, and Future of Prompt Photon Measurement

Large transverse momentum production of prompt photons was advocated to result from the parton structure of the proton [24]. Experimental results on prompt photon production had been published by the CERN Intersecting Storage Ring (ISR) experiments in proton-proton collisions at $\sqrt{s} = 30 - 60$ GeV. Later, fixed target and collider experiments of proton-proton and proton-antiproton collisions have explored a wide range of the parton momentum fraction from 0.01 to 0.6. A good systematical study on prompt photon production from various experiments is found in Ref. [25].

Recent results on prompt photon production have shown good qualitative agreements with QCD calculations, except a systematic pattern of excesses toward low E_T . Such trends are observed in both fixed target (E706¹) and collider experiments (R806², UA1, UA2³, CDF [4], DØ⁴) in a wide range of x_T . J. Huston *et al.* [25] have studied, in a noble way, P_T distributions of prompt photon production for the above and other experiments except the DØ measurement (the DØ result on prompt photon production was published after their analysis; however it also suggests the same discrepancy between

¹E706 is a fixed target experiment at Fermilab studying prompt photon and neutral meson production by hadron beams at 500 GeV/c – 800 GeV/c. Results on prompt photon production are found in Ref. [26].

²R806 is an ISR experiment at CERN. A study of prompt photon production is found in Ref. [27]. Other ISR experiments such as CCOR (CERN-Columbia-Oxford-Rockefeller), BCMOR (BNL-CERN-Michigan State-Oxford-Rockefeller), and AFS (Axial Field Spectrometer) collaborations have also studied prompt photon production.

³UA1 and UA2 are CERN $S\bar{p}p$ S collider experiments at $\sqrt{s} = 546$ GeV and 630 GeV. Studies on prompt photon production are found in Refs. [28, 29].

⁴DØ is the other TEVATRON collider experiment at Fermilab with an efficient capability of photon detection in forward region as well as energy measurement. See [30] for recent results on prompt photon production.

the experiment and the theoretical calculation) and found steeper spectra than the NLO QCD prediction. Figure 1.7 summarizes the discrepancies. They concluded that neither global fits with new parton distributions nor improved photon fragmentation functions can resolve the problem since the deviation occurs at different x values for experiments at different energies, and it could be explained by the transverse momentum fraction k_T of the initial partons or by multiple gluon emissions from the initial partons.

The CDF experiment is today about to encounter a new regime of small x where no previous experiments could reach. It has a capability of seeking out the gluon density directly in the lowest order processes as low as $x \sim 0.0003$. It is definitely a challenge for us to explore this new regime, to boldly go where no one has gone before.

1.4 Overview of the Analysis

We review the CDF detector briefly in the next chapter with some details in the main component for our study, as well as the scheme of data taking.

In Chapter 3, the method for prompt photon identification is described. Prompt photons are obtainable only statistically, not on an event by event basis, but as the event fraction in a certain data sample, by comparing systematical differences in the conversion probability and/or the cascade shower shape between the signal and background events. After introducing GEANT3, detector description and shower simulation tool, in Chapter 4, we explain the data reconstruction flow and the event selection criteria in Chapters 5 and 6.

Since shower simulation is very important in this study, it is essential to know how well the GEANT3 simulation reproduces real cascades. In Chapter 7, the reliability of the simulation is estimated by comparing shower simulations with real electron cascades. Electron cascades of the 1990 test beam run at various momenta and incident angles are used for estimations of the systematics. In addition, it is not well known how much of materials exists in the endplug region of the CDF detector. We will estimate the total amount of materials, in Chapter 8, from comparisons of cascade shower shapes between Monte Carlo electrons and the real electrons from W boson decays.

We, at last, reach the data in Chapter 9. The selection of prompt photon candidates,

the statistical extraction of the number of prompt photons, and efficiency estimations are made. Finally, the cross section for prompt photon production is evaluated. In the last chapters, we will discuss the result, comparing it with next-to-leading order QCD calculations, and see future prospects.



Figure 1.2: Gluon distribution of prompt photons. The curves are: NLO (QCD), LO (QCD), and NLO (MC). The x-axis is the number of prompt photons, and the y-axis is the probability $P(n)$.

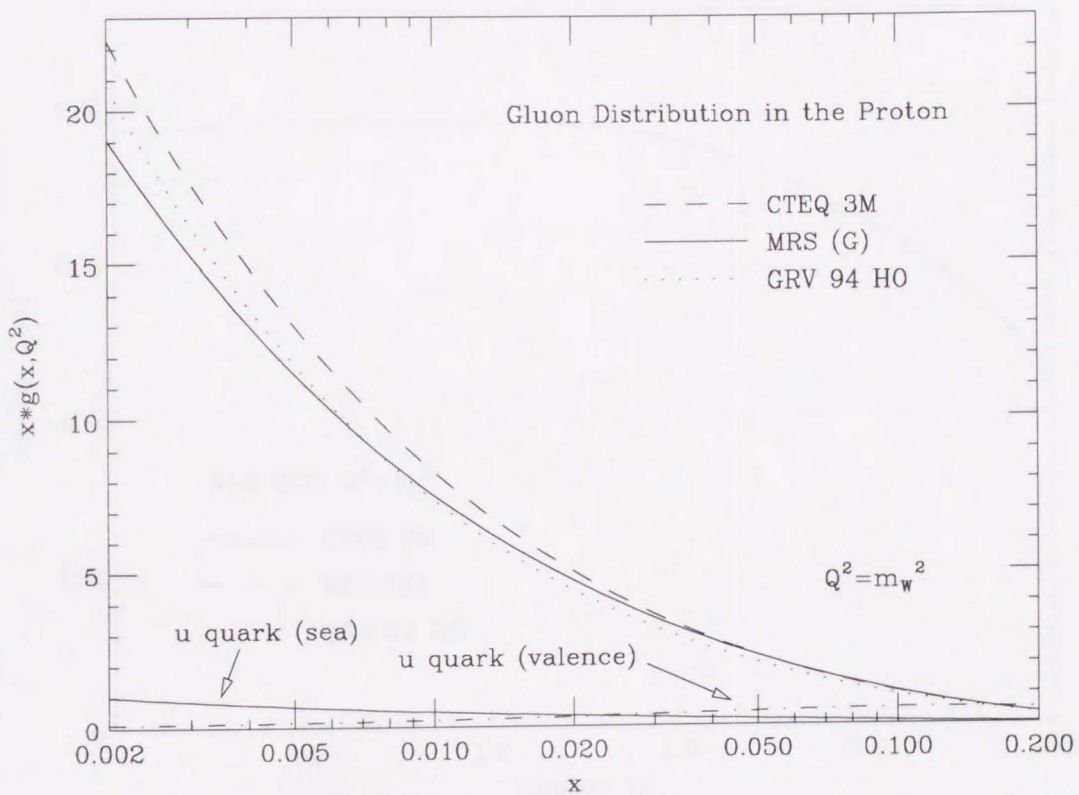


Figure 1.5: Gluon distributions of parton distribution functions, MRS (G), CTEQ 3M, and GRV 94 HO. Distributions of the u quark (valence and sea) are also shown for CTEQ 3M.

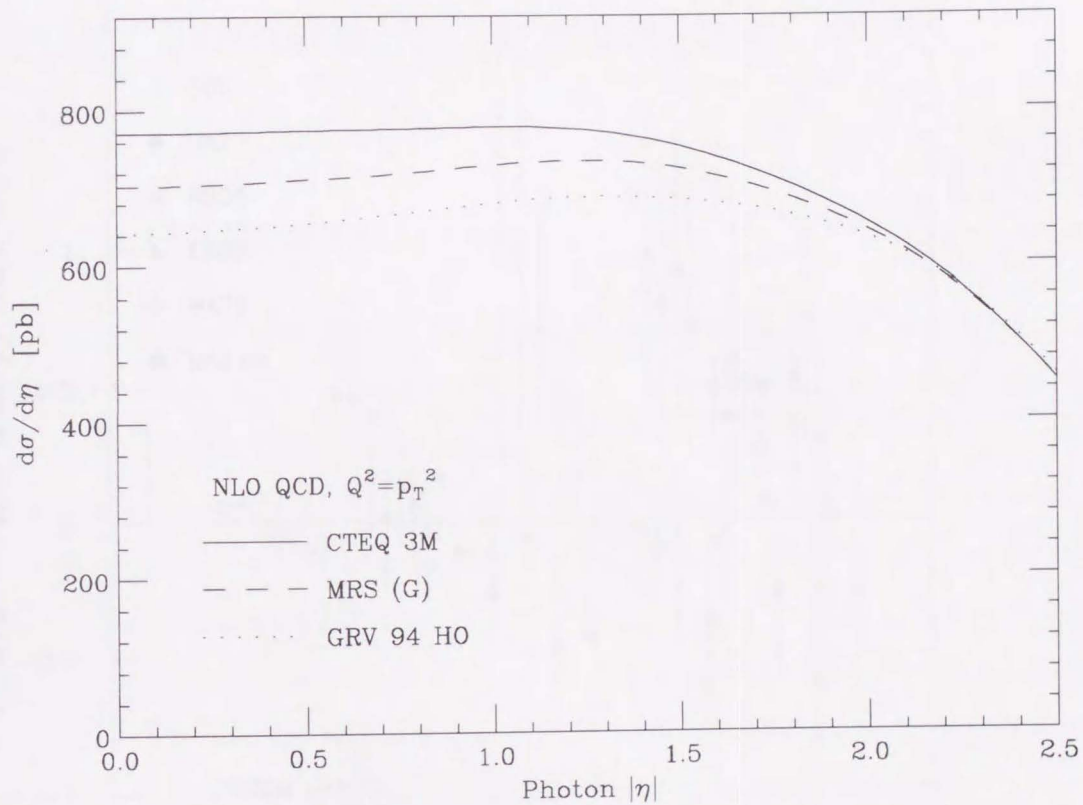


Figure 1.6: Inclusive production cross section for prompt photons of $27 \text{ GeV} < E_T < 40 \text{ GeV}$ in $\sqrt{s} = 1.8 \text{ TeV}$ $\bar{p}p$ collisions with respect to pseudorapidity η . NLO QCD calculations by Owens [7].

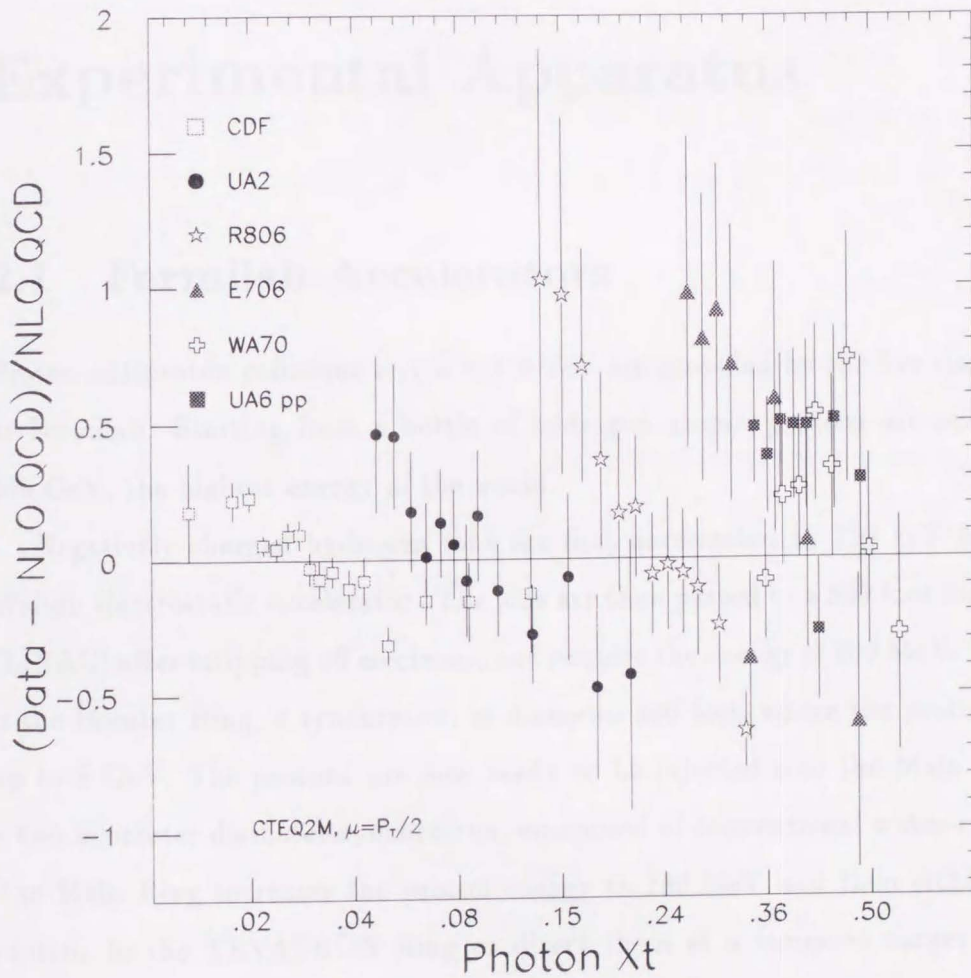


Figure 1.7: Compilation of prompt photon experiments compared to NLO QCD predictions using CTEQ2M parton distributions. Most of the data sets display a steeper dependence on x_T than is predicted by NLO QCD (horizontal line). [J. Huston *et al.*, Phys. Rev. D **51**, 6139 (1995)]

Chapter 2

Experimental Apparatus

2.1 Fermilab Accelerators

Proton-antiproton collisions at $\sqrt{s} = 1.8$ TeV are provided by the five stage accelerators at Fermilab. Starting from a bottle of hydrogen atoms, protons are accelerated up to 900 GeV, the highest energy of the world.

Negatively-charged hydrogen ions are first accelerated to 750 keV by a Cockcroft-Walton electrostatic accelerator. The ions are then passed to a 500 foot linear accelerator (LINAC) after stripping off electrons, and acquire the energy of 200 MeV. The third stage is the Booster Ring, a synchrotron of diameter 500 feet, where the protons are boosted up to 8 GeV. The protons are now ready to be injected into the Main Ring, which is a two kilometer diameter synchrotron, composed of conventional water-cooled magnets. The Main Ring increases the proton energy to 150 GeV and then either transfers the protons to the TEVATRON Ring or direct them at a tungsten target for antiproton production.

The TEVATRON, which is made of a thousand superconducting magnets, accelerates the protons up to 900 GeV in the same tunnel that houses the Main Ring. The Main Ring provides 10^{10} protons per bunch, and 10^4 antiprotons are produced and collected in the Debuncher Ring. The antiprotons are stochastically cooled to 8 GeV and then stored in the Accumulator Ring. The antiprotons are merged into a single beam, cooled further, and stored over a period of hours or even a day until the number reaches 10^{10} . The

accumulated antiprotons are transferred to the Main Ring and then the TEVATRON Ring, accelerated to 150 GeV, and then 900 GeV. The process of the acceleration is illustrated in Fig. 2.1.

Both p and \bar{p} beams circulate in the same magnetic and RF fields which produce helical orbits. Quadrupole magnets are used to focus the beam to a diameter of $\sim 40 \mu\text{m}$ at B0 and D0 collision points, where the CDF (Collider Detector at Fermilab) and the DØ detectors measure the $\bar{p}p$ collisions.

Major achievements of the TEVATRON are not only the beam energy but also its luminosity. A large number of particles in squeezed beam provide a large luminosity. The TEVATRON provided an instantaneous luminosity of $10^{30} \text{ cm}^{-2} \text{ s}^{-1}$ during the 1988-1989 collider run.

2.2 Collider Detector at Fermilab

The CDF detector is a general purpose hybrid detector pursuing research on reactions in proton-antiproton collisions. It consists of a superconducting magnet, beam-beam counters, tracking chambers, electromagnetic and hadron calorimeters, and muon chambers. It is separated into three parts, a central detector which covers $10^\circ < \theta < 170^\circ$ and two identical forward/backward detectors covering $2^\circ < \theta < 10^\circ$ and $170^\circ < \theta < 178^\circ$, where θ is the polar angle measured from the proton beam direction. A perspective view of the CDF detector is shown in Fig. 2.2. Any of the two identical detector modules is specified by its location. Since, at B0 experiment area, protons pass from the west to east, those modules covering $\theta < 90^\circ$ are called the east modules, and the rest the west.

The CDF coordinate system is defined by its origin at the nominal vertex or the center of the detector with the z axis along the proton beam, the y axis pointing vertically upward, and the x axis the north. The azimuthal angle φ and the pseudorapidity η are often used to point a particle's direction or a certain location of the detector in the η - φ plane. The azimuthal φ is measured from the positive x axis to the positive y axis, and the pseudorapidity is defined as $\eta \equiv -\ln(\tan \theta/2)$.

2.3 Detector Components

Particles produced in $\bar{p}p$ collisions traverse the beam pipe, a 5.08 cm diameter Be tube with a wall thickness of 500 μm , the tracking chambers located inside the superconducting solenoidal magnet that generates 1.4 T magnetic field along the proton beam; then, encounter the electromagnetic and hadron calorimeters. Muons passing through the calorimeters are finally detected by the muon chambers. An elevation view of the forward half of the CDF detector is shown in Fig. 2.3. In the following subsections, each detector component is briefly reviewed. A complete description is, however, found in [31].

2.3.1 Tracking

The CDF detector has three separate tracking systems. They are named the vertex time projection chambers (VTPC), the central tracking chamber (CTC), and the central drift tubes (CDT).

The VTPC system consists of 8 separate time projection chamber modules mounted end to end along the beam direction, covering $|z| < 143.5$ cm. Figure 2.4 is a schematic drawing of two octagonal VTPC modules. Each module has two 15 cm long drift regions divided by a high voltage grid. At the end of each drift space, proportional chambers are arranged. Anode sense wires, seen in Fig. 2.4, provide the r - z coordinates, where r is the radial distance from the beam, and cathode pads provide the r - φ coordinates.

The VTPC has coverage of $-3.5 < \eta < 3.5$ for the inner layer and $-2.6 < \eta < 2.6$ for the outer layer. Reconstructed VTPC tracks are mainly used to determine the event vertex, which has an accuracy of ~ 1 mm. The VTPC also gives track information for particles produced at small or large θ , where the CTC does not have its coverage. In the endplug region ($1.32 < |\eta| < 2.22$), the CTC provides 3-dimensional track information only for $|\eta| < 1.8$, and only the VTPC provides track information for the rest of the $|\eta|$ range. It should also be noted that the position resolution of the VTPC for a hit varies 200 μm to 550 μm depending on the hit position, and the two track resolutions are 3 cm for φ , 6 mm for r , and 6 mm/ θ for z , where θ is the polar angle and $\theta < \pi/2$.

The CTC is a cylindrical drift chamber with the radius 1.3 m and the length 3.2 m,

covering $|\eta| < 1$. It contains 9 “superlayers.” Five of them consist of 12 axial sense wires per layer, and the rest four, stereo superlayers; each layer consists of 6 sense wires which are tilted by $\pm 3^\circ$ relative to the beam direction. These 84 layers give track information with its momentum resolution better than $\delta P_T/P_T^2 \leq 0.002$. Figure 2.5 shows an endplate of the chamber.

Outside the CTC is the CDT. The CDT system consists of three layers of 1.27 cm diameter tubes with 3 m length providing additional tracking information. A hit position is determined by the drift time and charge division measurements. Its typical resolution is 2.5 mm in z and 200 μm in the azimuthal direction. The CDT system is also used to identify prompt photons from their conversions into electron pairs in the central region.

2.3.2 Calorimeters

The CDF calorimeters have a projective tower geometry, that is, each tower or calorimeter cell points at the nominal event vertex. The towers are segmented by $\Delta\eta \approx 0.1$, and $\Delta\varphi = 15^\circ$ for $|\eta| < 1.3$ and $\Delta\varphi = 5^\circ$ for $1.1 < |\eta| < 4.2$. Figure 2.6 shows the tower segmentation. There are three electromagnetic calorimeters, central (CEM), endplug (PEM), and forward (FEM), and four hadron calorimeters, central (CHA), endwall (WHA), endplug (PHA), and forward (FHA). In the central and endwall calorimeters, scintillator is used for sampling layers. In the endplug and forward calorimeters, argon-ethane 50-50 filled proportional tube chambers with cathode pad readout are employed for the active medium. As absorber, lead is employed for the electromagnetic calorimeters, and steel for the hadron calorimeters. Each electromagnetic calorimeter is located in front of its corresponding hadron calorimeter, but η coverage are slightly different and listed in Table 2.1 as well as detector properties.

Central

The central electromagnetic and hadron calorimetry system consists of 24×2 “wedge” modules. Each module has 2.5 m width and covers 15° in φ . 24 wedge modules are cylindrically arranged around the solenoidal magnet; two of these modules cover both east and west sides. There is a layer of gas proportional chambers with cathode strip

	Central		Endwall
	EM	Hadron	Hadron
$ \eta $ coverage	0 – 1.1	1 – 0.9	0.7 – 1.3
Tower size, $\Delta\eta \times \Delta\varphi$	$0.11 \times 15^\circ$	$0.11 \times 15^\circ$	$0.11 \times 15^\circ$
Active medium	polystyrene scintillator	acrylic scintillator	acrylic scintillator
Scintillator thickness	0.5 cm	1.0 cm	1.0 cm
Absorber	Pb	Fe	Fe
Number of layers	31	32	15
Energy resolution	2%	11%	14%
Position resolution [cm^2]	0.2×0.2	10×5	10×5

	Endplug		Forward	
	EM	Hadron	EM	Hadron
$ \eta $ coverage	1.1 – 2.4	1.3 – 2.4	2.2 – 4.2	2.3 – 4.2
Tower size, $\Delta\eta \times \Delta\varphi$	$0.09 \times 5^\circ$	$0.09 \times 5^\circ$	$0.1 \times 5^\circ$	$0.1 \times 5^\circ$
Active medium	proportional tube chambers with cathode pad readout		proportional tube chambers with cathode pad readout	
Tube size [cm^2]	0.7×0.7	1.4×0.8	1.0×0.7	1.5×1.0
Absorber	Pb	Fe	Pb	Fe
Number of layers	34	20	30	27
Energy resolution	4%	20%	4%	20%
Position resolution [cm^2]	0.2×0.2	2×2	0.2×0.2	3×3

Table 2.1: The calorimeter properties. Energy resolution (σ/E) and position resolution are typical values at 50 GeV.

readout located at a depth of 6 radiation lengths ($\theta = 90^\circ$) in the CEM. The strips provide high spatial resolution in z for shower cascades, and the anode wire readout measures the $r \times \varphi$ view. Their position resolutions are ± 2 mm or better for 50 GeV electrons. The energy resolution for the CEM is calibrated with electrons from the decays of Z 's and W 's produced in $\bar{p}p$ collisions, combining with CTC track information [32].

$$\left(\frac{\sigma_E}{E}\right)^2 = \left(\frac{13.5\%}{\sqrt{E \sin \theta}}\right)^2 + (1.7\%)^2,$$

where E is in GeV.

A wedge module contains 10 electromagnetic towers, while 9 hadron towers due to

the limited size along the beam direction. For the towers without full depth in the central hadron calorimeter, the endwall hadron calorimeter is mounted to the side. Figure 2.7 shows a cross sectional view of the central and endwall calorimeters along with the endplug calorimeters. As shown in the drawing, the WHA also covers a part of the endplug region. The endwall hadron calorimeter consists of 24×2 modules and has its θ coverage from 30° to 45° and from 135° to 150° . It is attached to the magnet yoke and serve as part of the flux return path.

Endplug

The PEM is a 2.8 m diameter and 50 cm deep cylindrical proportional chamber with 34 sampling layers, covering $10^\circ < \theta < 35^\circ$ and $145^\circ < \theta < 170^\circ$. Each east or west PEM consists of four $\Delta\varphi = 90^\circ$ quadrant modules, all four enclosed in a gas vessel. A sampling layer is composed of a 0.065% calcium and 0.7% tin dosed lead sheet and a chamber of arrayed gas proportional tubes with cathode pad and strip readout as shown in Fig. 2.8. A tube is made of fine grain carbon powder loaded polystyrene and has a square inner cross section of $7 \text{ mm} \times 7 \text{ mm}$ with 0.8 mm thick walls. The cathode pads and strips are etched out of the copper plating clad on G10 panels. The pad surfaces are in contact with one side of the tube array, and on the other side are the strips, however not in all the layers. The material thickness of each layer is listed in Table 2.2.

The cathode pads are segmented by $\Delta\varphi = 5^\circ$ and $\Delta\eta = 0.09$ for $1.41 < |\eta| < 2.4$, and they are longitudinally connected together into three segments in depth. The first depth segment contains the first 5 layers, the second the next 24, and the third the last 5, respectively. Since there is a steel made cover panel in front of the chambers, the first segment starts at a depth of $0.722 X_0$, and the second ranges from $3.292 X_0$ to $15.628 X_0$, where the depth is measured along the z axis. In the full detector setup, however, there exist many more materials in front of the PEM, such as the VTPC cage, the CTC endplate, etc. The total amount of materials between the vertex and the first chamber of the PEM is virtually unknown. A schematic of a quadrant module is shown in Fig. 2.9.

The strips are only inserted in the 6th layer to the 15th. There are two types of strips, θ and φ , and each is alternately arranged, the θ -strips in the even number layers and the

φ -strips in the odd number layers. The θ -strips are 32 arc-shaped strips of $\Delta\eta = 0.02$ stretched by 30° in φ , and the η -strips are 30 radial strips of $\Delta\varphi = 1^\circ$. The coverage of these strips is $1.2 < |\eta| < 1.84$. Each five θ or φ strips are connected together in depth at the same (η, φ) units. Pad and strip geometries of typical chambers are shown in Fig. 2.10.

The anode wires are connected together over a 90° quadrant each layer. This anode readout provides a longitudinal profile of energy depositions in a quadrant of the detector.

With test beam electrons, various characteristics of the detector performance are measured. The energy resolution is obtained as

$$\frac{\sigma_E}{E} = \frac{28\%}{\sqrt{E}}$$

for 20 GeV to 200 GeV electrons. By scanning all the towers with 100 GeV electrons, the tower to tower uniformity is achieved to be 2% or better. Position resolutions by the pad readout are $\Delta\theta = 0.04^\circ - 0.2^\circ$ and $\Delta\varphi = 0.2^\circ - 0.3^\circ$. They are improved to $\Delta\theta = 0.04^\circ$ and $\Delta\varphi = 0.1^\circ$ by the strips. Structures and characteristics about the PEM are detailed in [33].

In the PEM, the calorimeter towers are dealt with differently for the trigger and the off-line analysis. Table 2.3 shows the tower segmentation and numbering for the PEM at the calorimeter, trigger, and off-line analysis levels. Throughout the test, the tower is pointed by the TOWE (off-line analysis level) number unless specified.

The endplug hadron calorimeter (PHA) consists of 20 sampling layers of gas proportional chambers with cathode pad readout, each separated by a 5 cm steel plate. The pad segmentation follows that of the PEM, and each tower is connected for all 20 layers. The gas proportional chambers are divided into 30° sectors in the azimuth, and the anode wires of a layer is connect over a sector. The same resistive plastic tubes as used for the PEM are employed for the proportional chambers in the PHA. Energy resolution is measured with test beam pions for an energy rage of 40 GeV to 200 GeV [34] as

$$\frac{\sigma_E}{E} = \frac{132\%}{\sqrt{E}}.$$

Forward/backward

Forward calorimeters are located approximately 7 m from the interaction point, and they have polar coverage of $2^\circ < \theta < 10^\circ$ and $170^\circ < \theta < 178^\circ$. The forward electromagnetic calorimeter consists of 30 layers of proportional chambers, and each east or west calorimeter is divided into four quadrants. Each layer is composed of a lead sheet and a chamber of gas proportional tubes with cathode readout. The cathode pads are segmented by $\Delta\eta = 0.1$ and $\Delta\varphi = 5^\circ$ and connected longitudinally into towers with two depth segmentation, either of which contains 15 layers. With test beam electrons of momenta from 20 GeV to 200 GeV, the energy resolution is measured to be

$$\frac{\sigma_E}{E} = \frac{25\%}{\sqrt{E}} + 0.5\%.$$

The forward hadron calorimeter (PHA) is also composed of proportional tube chambers and steel plates, covering $2.2 \leq |\eta| \leq 4.2$. Each east or west PHA is segmented into four independent sections, and each section contains 27 sampling layers. The cathode surface of each of the ionization chambers has been segmented into 20 bins in pseudorapidity ($\Delta\eta = 0.1$) and 18 bins in azimuth ($\Delta\varphi = 5^\circ$). The signals from each chamber pad at fixed η and φ are summed together to produce the total energy signal for a given projective tower. Energy resolution is parameterized by

$$\frac{\sigma_E}{E} = 8.6\% + \frac{113\%}{\sqrt{E}} + \frac{283\%}{E},$$

as obtained with test beam pions for 20 GeV to 200 GeV.

2.3.3 Muon Detectors

There are two systems in the CDF detector to measure muons which penetrate the calorimeters; one is in the central region, the other in the forward/backward region.

In the central detector, each wedge contains 4 layers of muon chambers at the end of the hadron calorimeter section, 3.5 m away from the beam line, covering $56^\circ < \theta < 124^\circ$. A cross sectional view of the chambers is shown in Fig. 2.11. The position resolution of the central muon detector (CMU) has been attained to 250 μm per point in the φ

direction by drift time and 1.2 mm per point in the z direction by charge division.

In both forward and backward region, there is a muon spectrometer, each, consisting of large magnetized steel toroids with drift chamber planes and triggering scintillation counters as shown in Fig. 2.3. Each spectrometer contains two 1 m thick steel toroids with the inner and outer diameters are 0.914 m and 7.82 m, respectively. A magnetic field in the toroids ranges from 2.0 T at inner radius to 1.6 T at the outer radius. The forward muon system measures muon position for polar angles between 3° to 16° and 164° to 177° with an accuracy of 5° in the φ direction and $\approx 200 \mu\text{m}$ in the r direction. The momentum resolution is 13%, independent of momentum, for muons with momentum above 8 GeV/c. Figure 2.12 shows an r - φ view of the spectrometer.

2.3.4 Beam-Beam Counter

The beam-beam counter (BBC) is a plane of scintillation counters on the front face of each east or west FEM, providing a “minimum bias trigger” for the detector (Section 2.5). The counters are arranged in a rectangle around the beam pipe as shown in Fig. 2.13, that cover the polar angular region from 0.32° to 4.47° , corresponding to a pseudorapidity range of 3.24 to 5.90. The counters have the timing resolutions less than 200 ps and provide an accurate measurement of the interaction time. It gives a measurement of the event vertex with an accuracy of 4 cm. The BBC also serves as the primary luminosity monitor.

2.4 Data Acquisition System

There are approximately 100,000 electronic channels in the CDF detector. They are photomultiplier tubes, pad/strip/wire chambers, drift chambers, and drift chambers with current division readout. The calorimetry requires a large dynamic range for the electronic readout, extending from a few tens of MeV to many hundreds of GeV. The RABBIT (Redundant Analog Bus Based Information Transfer) system was developed to meet this requirement. It is a crate-based analog front-end system, which consists of 129 crates mounted on the detector, dealing with six tenths of all the electronic channels.

Analog signals being read out from the detector components, RABBIT channels are then digitized in the crates, and they are read out by fast intelligent scanners called MX's, which interface the signals to the Fastbus data acquisition system.

The signals from the drift chambers are shaped at the detector and brought up from the collision hall to commercial Fastbus TDC modules in the counting room. The signals are then read out by a second type of intelligent scanners called the SSP's. Each scanner can buffer four events, and handles approximately 1000 channels.

The data acquisition (DAQ) system is comprised by the Fastbus network with many custom designed modules, that allow for the bandwidth necessary to transmit the data for each event. For a nominal event size of 100k bytes, the DAQ system reads out events at a rate of 20 Hz to 30 Hz into the next stage. A detailed technical description is given in Ref. [35].

2.5 Trigger System

The CDF event trigger system consists of four stages of event processing and reduction of the event rate. In the 1988-1989 run, the TEVATRON was operated with six bunches of protons and of antiprotons providing a typical luminosity of $10^{30} \text{ cm}^{-2} \text{ s}^{-1}$. The beam crossing interval of $3.5 \mu\text{s}$ (286 kHz) and the $\bar{p}p$ inelastic scattering cross section at $\sqrt{s} = 1.8 \text{ TeV}$ of $\sim 50 \text{ mb}$ result in an event rate of $\sim 50 \text{ kHz}$. The trigger system reduces this high rate to manageable level of a few Hz, selecting events of physics interest.

2.5.1 Level 0

The level 0 trigger requires an inelastic collision of a proton and an antiproton, determined by hits in both east and west BBC's within a 15 ns window centered on the beam crossing time. It is also called the "minimum bias trigger." The level 0 trigger initiates the Level 1 trigger to read the signals from the calorimeter and make a decision, and it takes more than $3.5 \mu\text{s}$ to process these. Accordingly, the Level 0 trigger is automatically inhibited for the next beam crossing, once an event is accepted.

2.5.2 Level 1

The Level 1 trigger refers only to the global feature of an event, making a decision based mainly upon energy deposits in the “trigger towers,” the stiff track trigger based on a fast hardware track processor, and the muon triggers [36, 37]. The trigger towers are formed by summing calorimeter tower signals so as to have a size of $\Delta\eta \times \Delta\varphi = 0.2 \times 15^\circ$, and energy deposits being weighted by $\sin\theta$ to represent the transverse energy.

The Level 1 calorimeter triggers require that the transverse energy sum over all towers with E_T being larger than a low threshold (typically 1 GeV) to be greater than a higher threshold (typically 30 GeV – 40 GeV). Both electromagnetic and hadronic energy, or either one, can be summed in a given tower.

The Level 1 trigger reduces the event rate to a few kHz out of ~ 50 kHz at Level 0.

2.5.3 Level 2

The Level 2 trigger performs primitive clustering and track matching between CTC tracks and clusters or muon hits, to see topological features of an event.

Level 2 trigger clusters are identified by a hardware system specialized for this purpose, by searching the 42×24 array of towers in the η - φ plane. First of all, a high threshold (typically 100 GeV) is loaded in a comparator, and the threshold begins to reduce until one or more trigger towers above the threshold appear, at which point the ramp stops, and then these towers are listed as seeds. Each of four nearest neighbor towers around a seed (the diagonal neighbors with different η and different φ are not included) is included in a cluster if one has E_T larger than a lower threshold (typically 1 GeV). The nearest neighbors of the newly selected towers are then searched, and each with E_T larger than the threshold being added, and so on until no more contiguous towers are found. This process is repeated until no new seed towers exist. Once a tower is included in a cluster, it is prohibited from being included in any of the subsequent clusters. Energies of all towers in a cluster are summed to form the total E_T , the E_T -weighted first and second moments of the cluster for both η and φ . Separate sums are kept for hadronic and electromagnetic energies. These are digitized and presented as a list of clusters to a fast hardware Level 2 processor.

During the processing of clusters, the fast hardware track finders are monitoring the selected towers and lists course P_T of tracks corresponding to the coordinate of the towers. Muons are matched to the CTC, and with their momenta also appear in the cluster list.

A Level 2 decision is then made on a selection of photons, electrons, jets, muons, and missing E_T by a programmable processor. Many combination of the above can be programmed in parallel. Since the DAQ system needs an order of 1 ms to read out signals from whole the detector components, an event rate of 100 Hz or less (typically 20 Hz – 30 Hz) is required after the Level 2 trigger. Once the Level 2 trigger is satisfied, the DAQ system starts reading detector signals, and the Level 3 initiates its event selection.

2.5.4 Level 3

The Level 3 system is designed to execute FORTRAN-77 filter algorithms as the last stage of the on-line trigger system and capable of a more sophisticated event selection with high flexibility. It identifies physical objects such as photons and muons in an equivalent way used in the off-line reconstruction (Section 5). Level 3 uses Advanced Computer Program (ACP) [38] 32-bit processors, based on Motorola MC68020 MPU's and MC68881 floating point coprocessors, installed in VME crates with VME bus control and interface modules. In the 1988-1989 run, 60 sets of such processors were used to select events, and they were written onto magnetic tapes at a rate of ~ 1 Hz for off-line analyses.

2.6 Luminosity

The luminosity is measured by monitoring the beam current and profile, or by measuring the cross section for a certain process. The CDF luminosity is calculated from a combination of the above two to achieve an accurate measurement.

The luminosity in a bunched beam collider can be calculated from the intensity, the longitudinal profile, and the transverse size of each bunch. The transverse size is measured by wires flown through the beam, and a resistive wall current monitor [39]

measures the intensity and the longitudinal profile.

The luminosity can also be obtained by measuring the event rate for a certain process of which the cross section is known. The CDF luminosity is measured by the BBC system, counting the event rate of inelastic $\bar{p}p$ collisions.

We start the luminosity calculation with a known cross section. The UA4 experiment has measured the inelastic $\bar{p}p$ cross section to be 38.9 ± 1.8 mb [40]. However, its center of mass energy was 546 GeV, while the TEVATRON is normally operated at $\sqrt{s} = 1800$ GeV. Therefore, the inelastic event rate (R_{BBC}^{546}) was measured by the BBC's along with the accelerator luminosity ($\mathcal{L}_{accel}^{546}$) at a reduced TEVATRON energy down to $\sqrt{s} = 546$ GeV. The luminosity at $\sqrt{s} = 1800$ GeV is, then, calculated with the event rate and the accelerator luminosity at $\sqrt{s} = 1800$ GeV, R_{BBC}^{1800} and $\mathcal{L}_{accel}^{1800}$, by the following equation:

$$\mathcal{L} = \frac{R_{BBC}^{1800}}{\sigma_{BBC}^{1800}},$$

where

$$\begin{aligned} \sigma_{BBC}^{1800} &= \sigma_{BBC}^{546} \cdot \frac{R_{BBC}^{1800}}{R_{BBC}^{546}} \cdot \frac{\mathcal{L}_{accel}^{546}}{\mathcal{L}_{accel}^{1800}} \\ &= 51.15 \pm 1.79 \text{ mb.} \end{aligned}$$

σ_{BBC}^{546} is the BBC effective cross section at $\sqrt{s} = 546$ GeV obtained from the UA4 inelastic cross section with a small correction for CDF due to the difference in the acceptance.

σ_{BBC}^{1800} is the BBC effective cross section at $\sqrt{s} = 1800$ GeV.

The corresponding total integrated luminosity for the 1988-1989 run is acquired to be

$$L = \int \mathcal{L} dt = 3.76 \pm 0.13 \text{ pb}^{-1}.$$

More details on the luminosity measurement are described in [41] and references therein.

	Thickness [mm]	Radiation length
Front cover: steel plate ($z = 173.99 - 175.26$ cm)	12.7	0.722
Each sampling layer ($z = 175.26 - 226.06$ cm)		
Lead sheet	2.69	0.480
Chamber layer		
Cu-clad G10	1.6	0.013
Conductive plastic tube	8.6	0.007
Cu-clad G10	1.6	0.013
Epoxy	0.2	
50 μ m G10 (on 6th to 15th strips)	0.05	
Total of a layer	12.1	0.514

Table 2.2: Material thickness of the endplug electromagnetic calorimeter.

Local (Calorimetry)	Trigger	TOWE
0 (35.24°, 1.147)		19/66 (35.24°, 1.147)
1 (32.62°, 1.229)	15/26 (33.21°, 1.210)	20/65 (31.67°, 1.260)
2 (30.81°, 1.289)		
3 (29.29°, 1.342)		
4 (28.05°, 1.387)	14/27 (27.44°, 1.410)	21/64 (28.65°, 1.365)
5 (26.33°, 1.453)		22/63 (26.33°, 1.453)
6 (24.13°, 1.543)		23/62 (24.13°, 1.543)
7 (22.24°, 1.633)	13/28 (23.05°, 1.590)	24/61 (22.24°, 1.633)
8 (20.24°, 1.723)		25/60 (20.24°, 1.723)
9 (18.53°, 1.813)	12/29 (19.33°, 1.770)	26/59 (18.53°, 1.813)
10 (16.96°, 1.903)		27/58 (16.96°, 1.903)
11 (15.52°, 1.993)	11/30 (16.19°, 1.950)	28/57 (15.52°, 1.993)
12 (14.20°, 2.083)		29/56 (14.20°, 2.083)
13 (12.99°, 2.173)	10/31 (13.55°, 2.130)	30/55 (12.99°, 2.173)
14 (11.88°, 2.263)		31/54 (11.88°, 2.263)
15 (10.80°, 2.359)	9/32 (11.34°, 2.310)	32/53 (10.80°, 2.359)

Table 2.3: Tower segmentation. “Local (Calorimetry),” “Trigger,” “TOWE” represent tower numbers for the calorimeter, the level 2 trigger, and the off-line analysis segmentation. At the trigger level, $\Delta\eta \approx 0.2$ of a tower, and $\Delta\eta \approx 0.09$ for the off-line analysis. Left numbers are for the west module, and right for the east. Numbers in parentheses are the polar angle θ and the corresponding pseudorapidity η at the tower centroids. The φ segmentation is $\Delta\varphi = 5^\circ$ for the local and TOWE tower and 15° for the trigger.

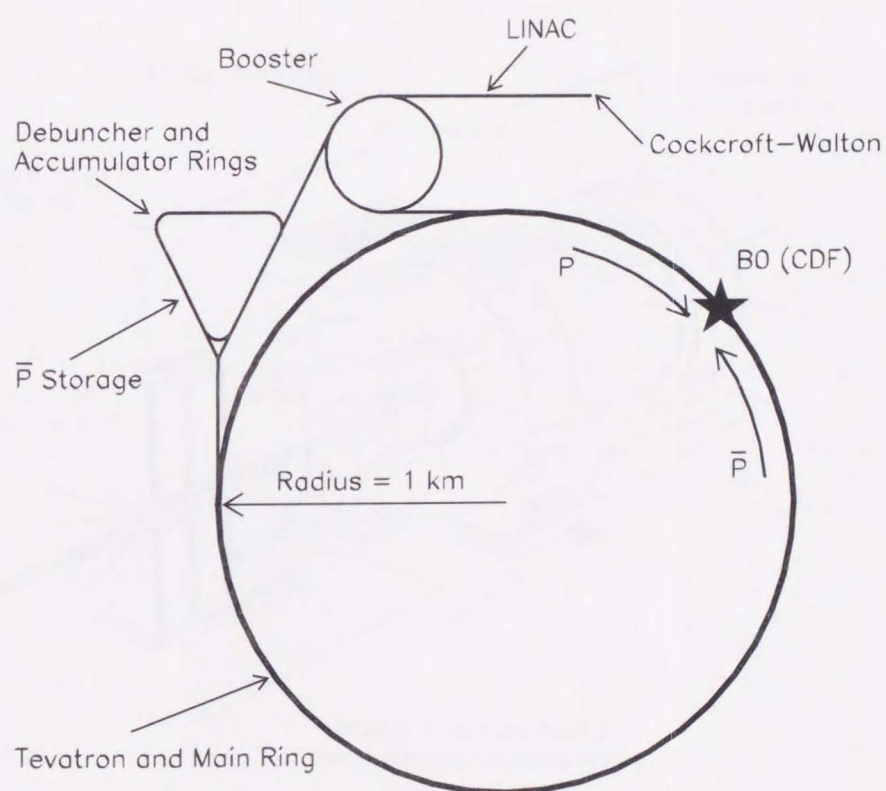


Figure 2.1: A schematic view of the Fermilab five stage accelerators providing the world's highest energy.

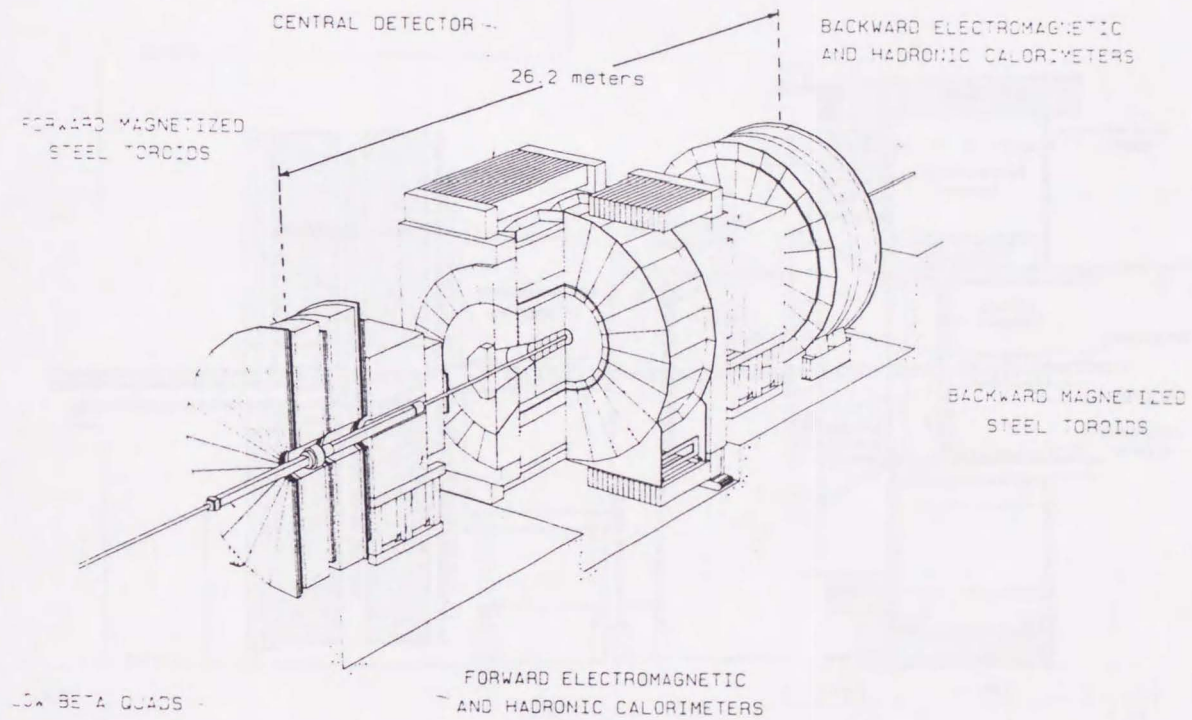


Figure 2.2: A perspective view of the CDF detector showing the central detector, the forward and backward detectors.

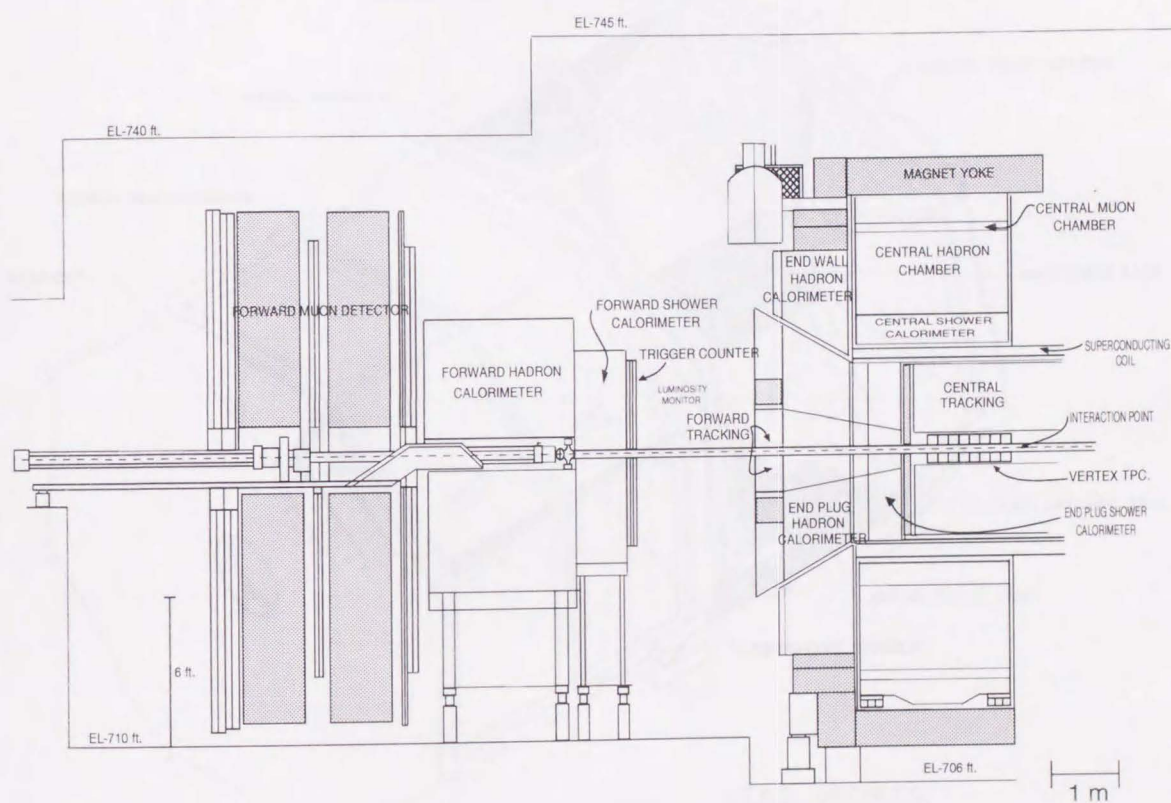


Figure 2.3: Cross section through a vertical plane of one half the CDF detector. The detector is symmetric about the midplane and roughly symmetric around the beam axis.

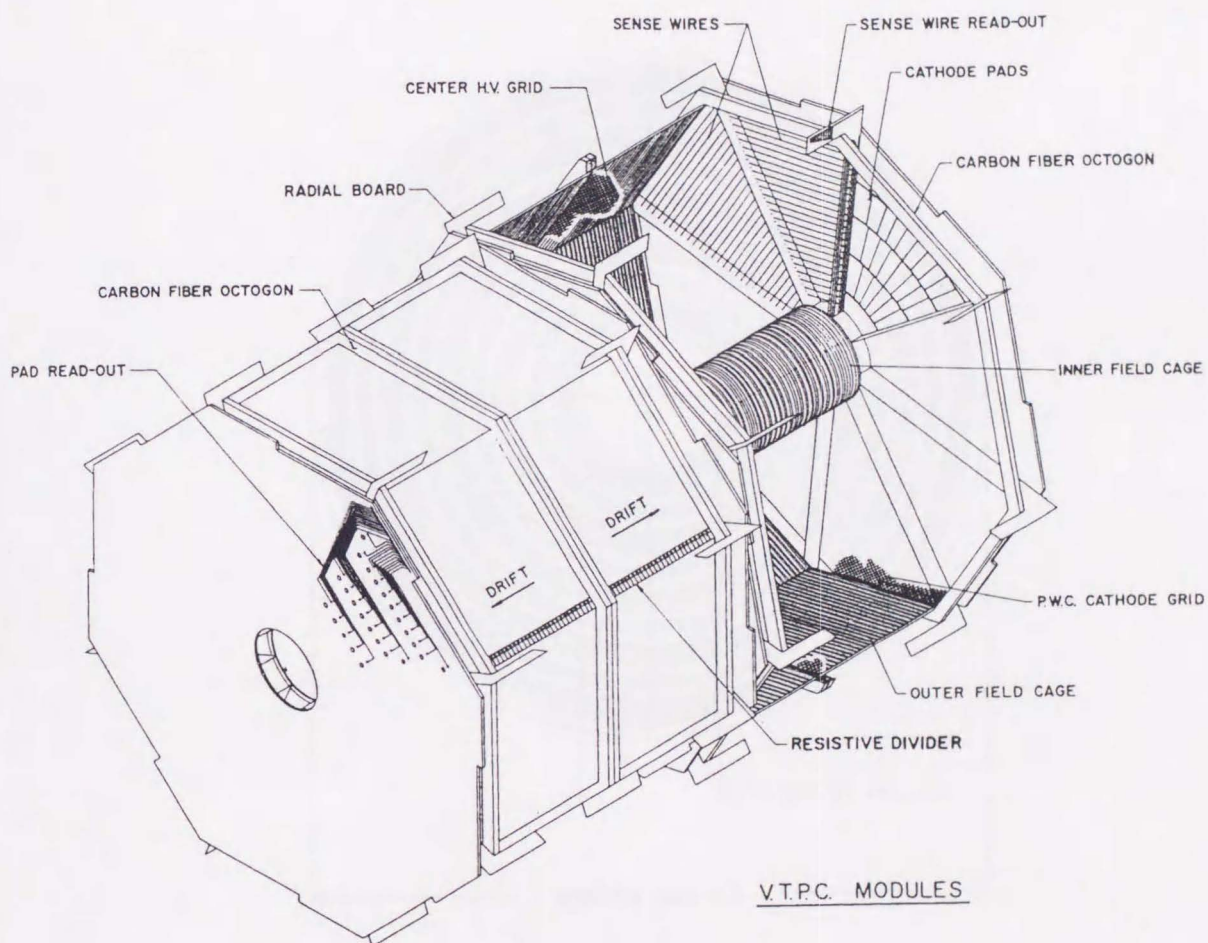


Figure 2.4: An isometric view of two VTPC modules. They are rotated in φ by 11.3° with respect to each other.

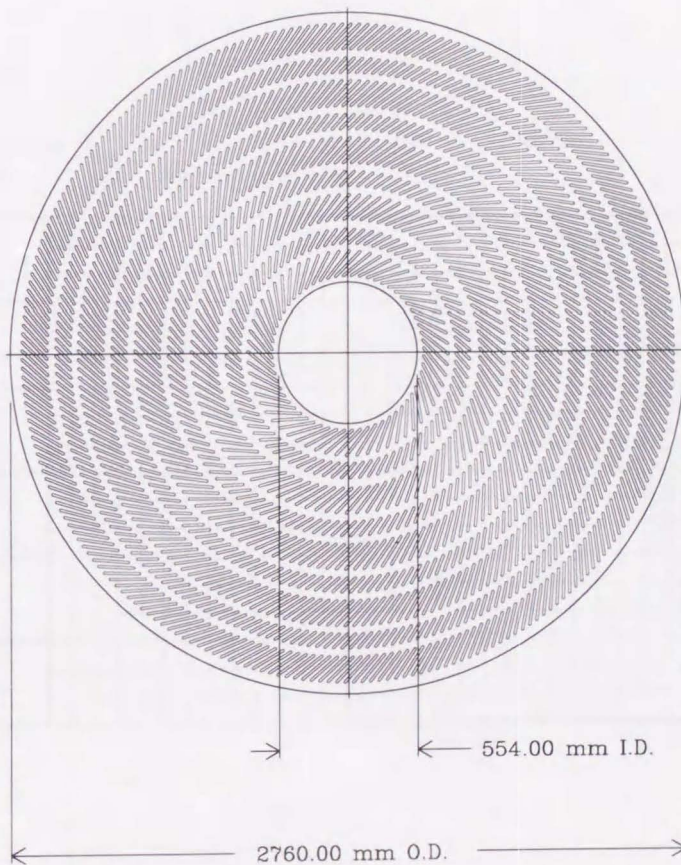


Figure 2.5: End view of the CTC showing the location of the slots in the aluminum endplate.

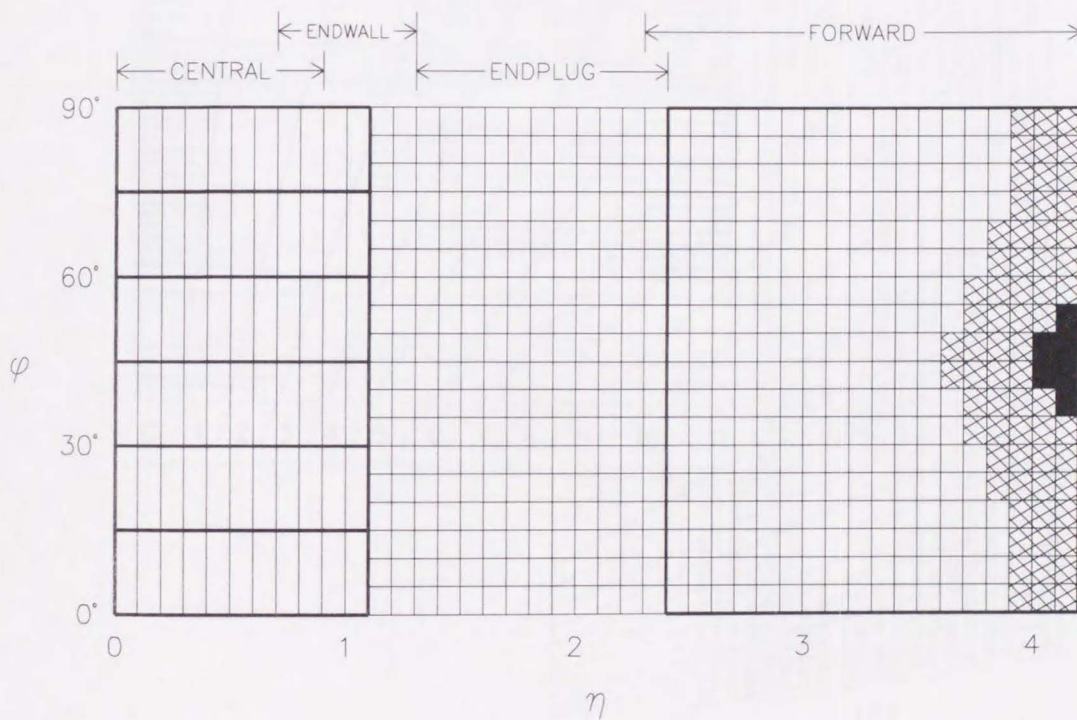


Figure 2.6: Calorimeter towers in one of eight identical η - ϕ quadrants ($\Delta\phi = 90^\circ, \eta > 0$). The electromagnetic calorimeter have complete ϕ coverage out to $\eta = 4.2$.

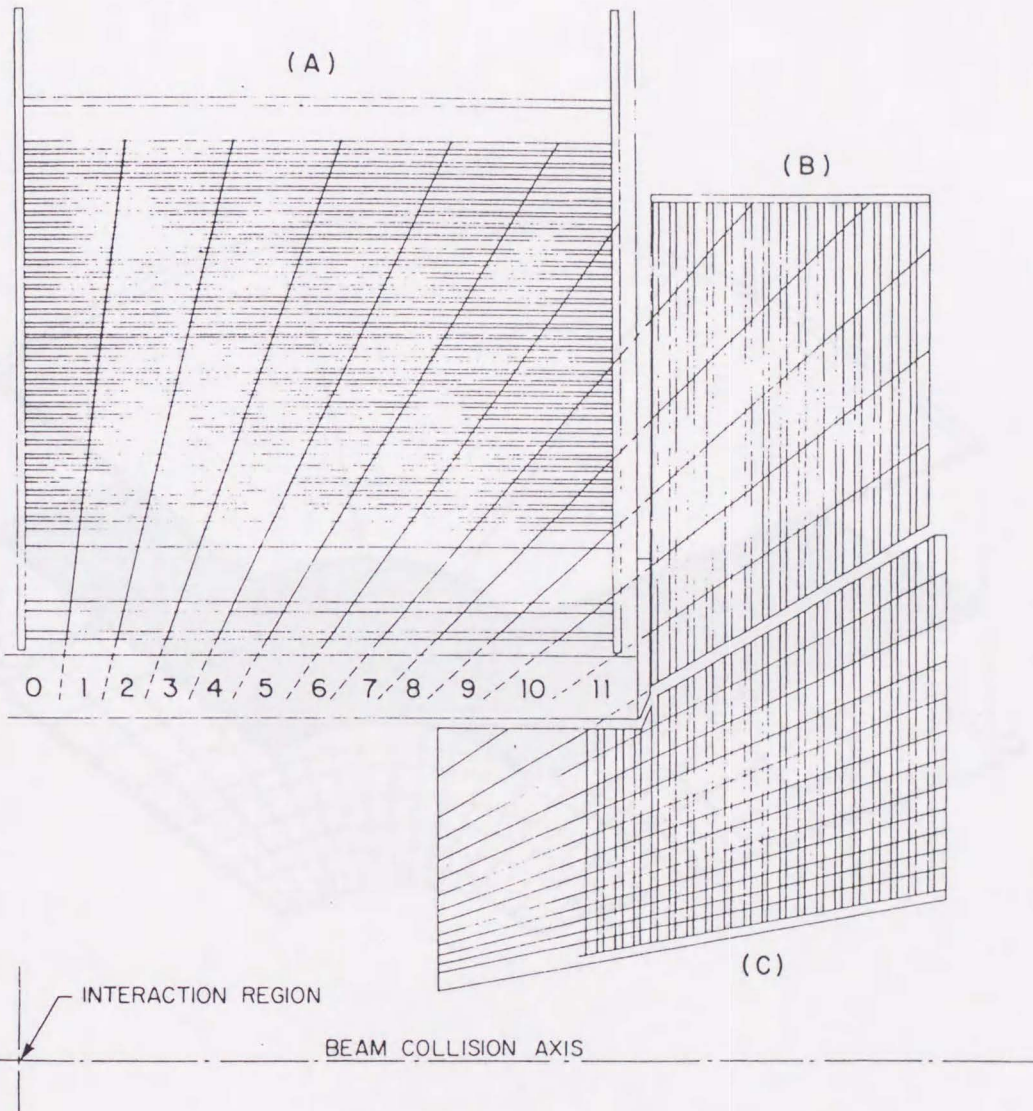


Figure 2.7: Quadrant of the calorimeter where A, B, C show central, endwall, and endplug, respectively. Towers are numbered from 0 (at 90° in polar direction) to 11 (last tower of endwall modules). Hadronic towers 6,7, and 8 are shared between the central and endwall calorimeters.

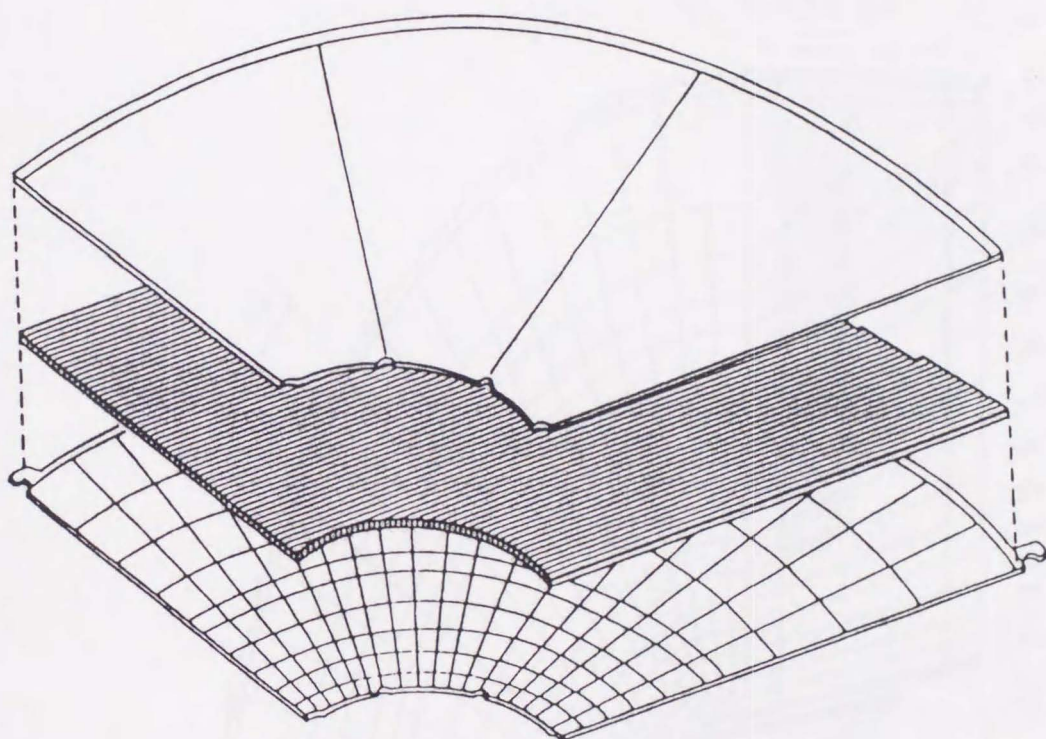


Figure 2.8: Exploded view of a layer of the proportional tube array of the PEM. PC boards with pad patterns and ground plane are shown.

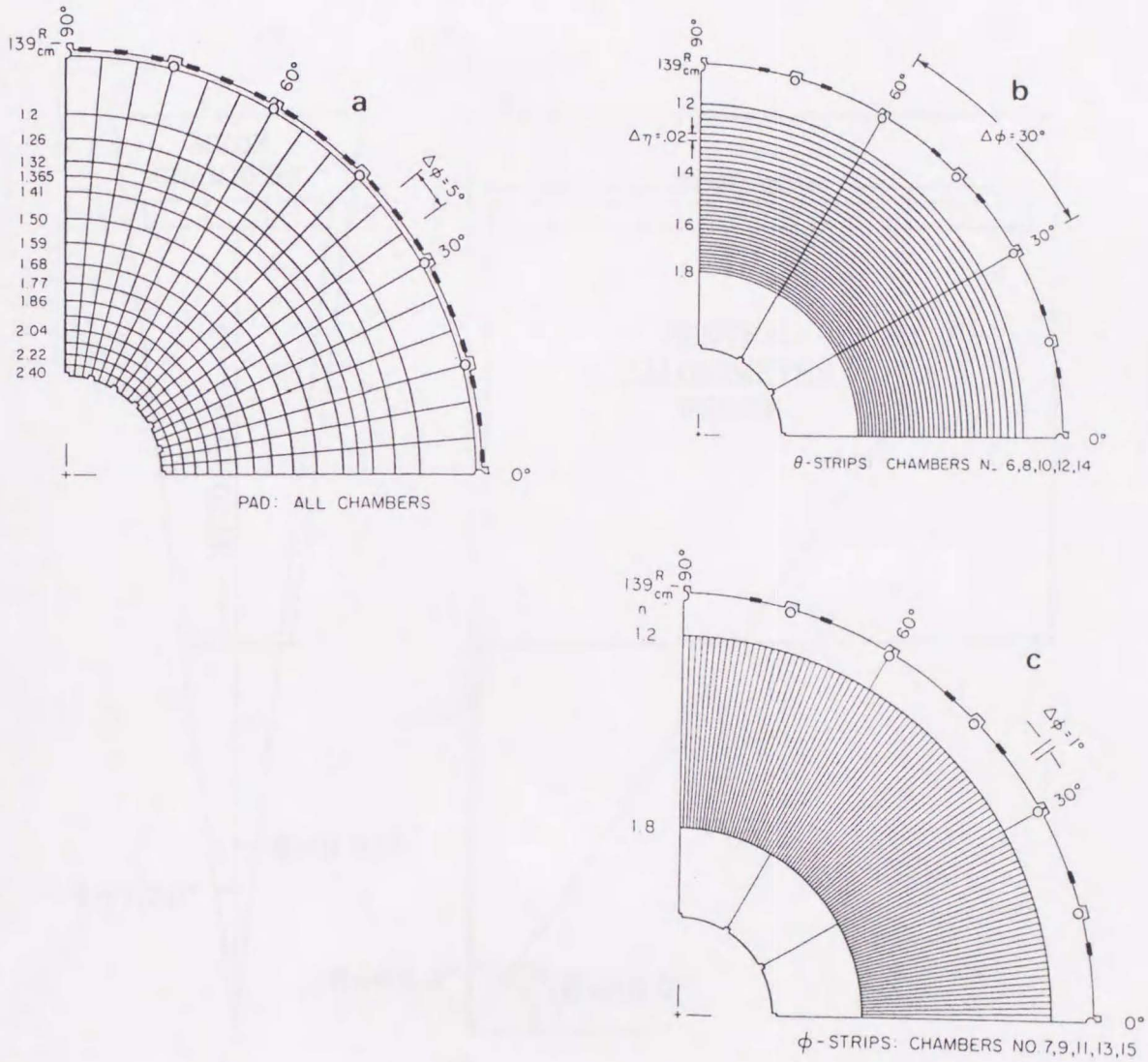


Figure 2.10: Patterns of the outside pickup of electrodes: (a) pads, (b) θ -strips, (c) ϕ -strips.

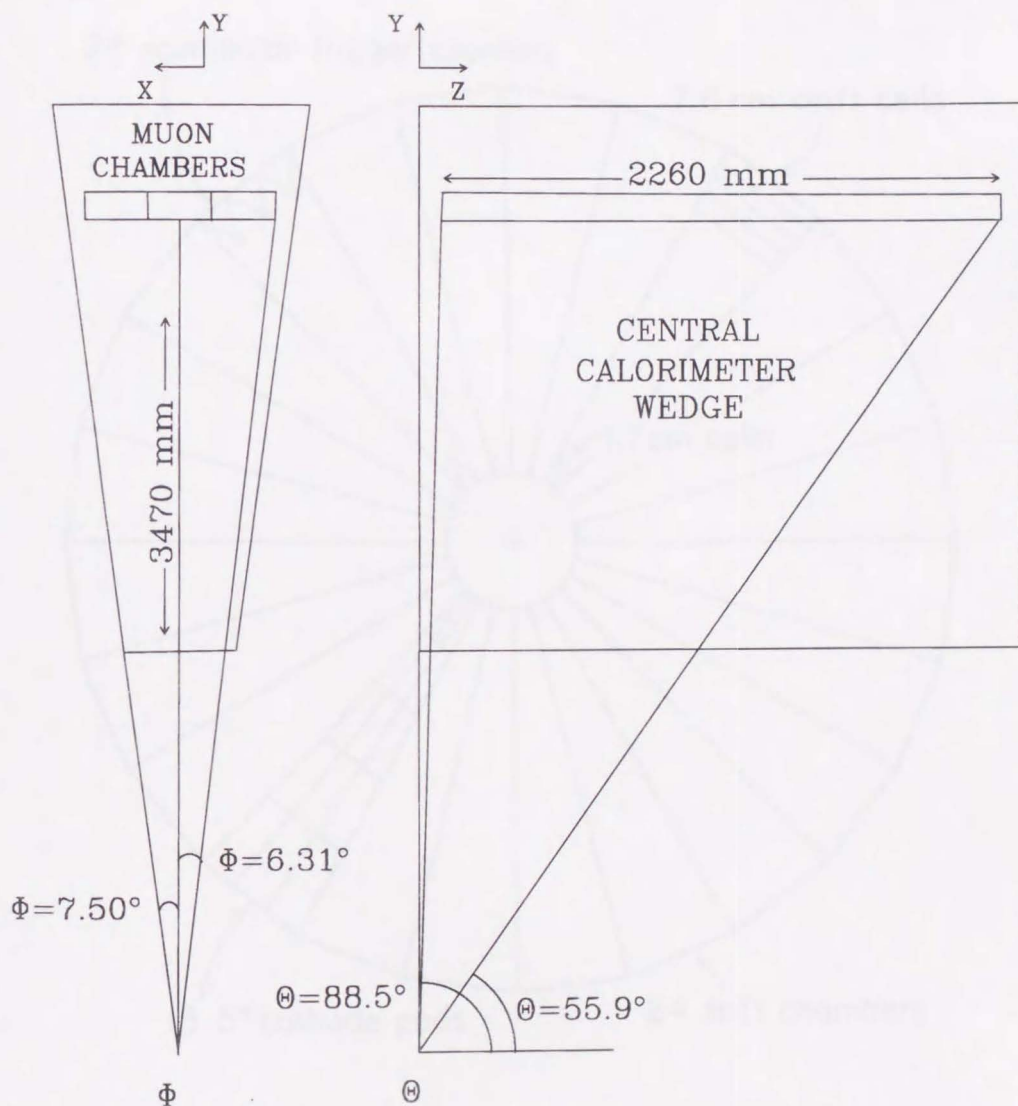


Figure 2.11: The layer of the central muon chambers in one of the central wedges.

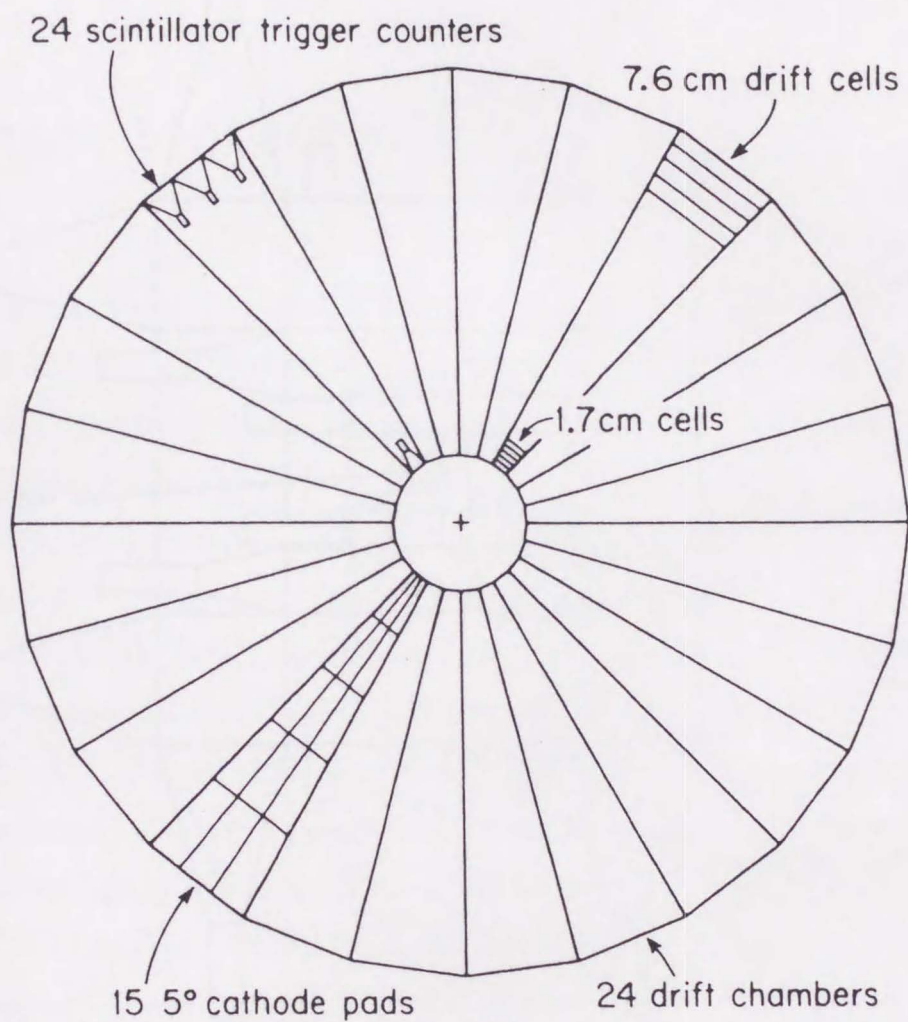


Figure 2.12: Elements of the forward muon detector planes.

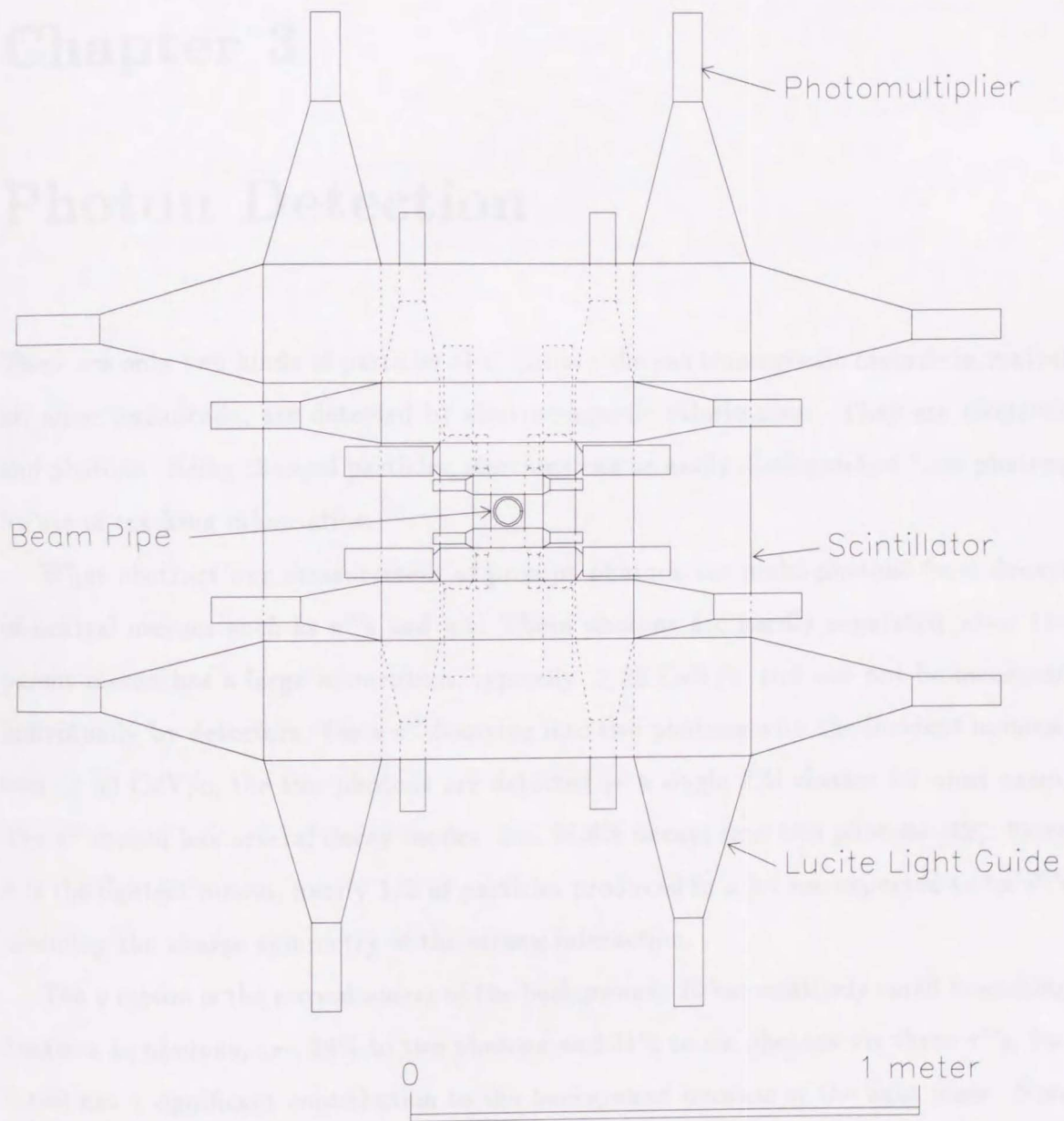


Figure 2.13: A beam's-eye view of one of the beam-beam counter planes.

Chapter 3

Photon Detection

There are only two kinds of particles that initiate the electromagnetic cascade in matter or, more technically, are detected by electromagnetic calorimeters. They are electrons and photons. Being charged particles, electrons can be easily distinguished from photons by use of tracking information.

What obstruct our measurement of prompt photons are multi-photons from decays of neutral mesons such as π^0 's and η 's. These photons are hardly separated when the parent meson has a large momentum, typically $\gtrsim 20$ GeV/c, and can not be measured individually by detectors. For a π^0 decaying into two photons with the incident momentum $\gtrsim 50$ GeV/c, the two photons are detected as a single EM cluster for most cases. The π^0 meson has several decay modes, but 98.8% decays into two photons [42]. Since it is the lightest meson, nearly 1/3 of particles produced in a jet are expected to be π^0 's assuming the charge symmetry of the strong interaction.

The η meson is the second source of the background. It has relatively small branching fractions to photons, i.e., 39% to two photons and 31% to six photons via three π^0 's, but it still has a significant contribution to the background because of the light mass. Note that most of $\eta \rightarrow 3\pi^0 \rightarrow 6\gamma$ decays are observed as single EM clusters (Section 9.2).

There are several other neutral mesons possible to become backgrounds against the prompt photon. See Table 3.1 for such potential background mesons and their neutral decay modes with branching fractions together with those for π^0 and η . Due to the low production rates and small branching fractions, however, their contributions are

Meson	Decay Mode	Branching Ratio [%]	Neutral Decay [%]
π^0	$\gamma\gamma$	98.798 ± 0.032	98.798 ± 0.032
η	$\gamma\gamma$	38.8 ± 0.5	30.8 ± 0.4
η	$\pi^0\pi^0\pi^0$	31.9 ± 0.4	30.8 ± 0.4
ω	$\pi^0\gamma$	8.5 ± 0.5	8.4 ± 0.5
η'	$\pi^0\pi^0\eta$	20.8 ± 1.3	14.2 ± 0.9
η'	$\gamma\gamma$	2.12 ± 0.13	2.12 ± 0.13
ϕ	$\eta\gamma$	1.28 ± 0.06	0.90 ± 0.04
K_S^0	$\pi^0\pi^0$	31.39 ± 0.28	30.6 ± 0.3

Table 3.1: Possible backgrounds. Pure neutral decay (into multi-photons) fraction is also shown.

expected very small. Though any neutral mesons other than π^0 or η are not included in the background, we only consider the $K_S^0 \rightarrow \pi^0\pi^0$ decay and estimate the systematics to the production cross section of prompt photons in Section 9.4. However, it gives still a very small contribution to the background because of the long life time and the relatively small decay fraction to $\pi^0\pi^0$ (31.4%). Since the systematic uncertainty to the prompt photon cross section by the K_S^0 decays will be found negligible compared to other systematics, the other mesons such as ω or η' are not considered as the backgrounds. We also omit K_L^0 decaying to three π^0 's since the life time of K_L^0 is long (5.17×10^{-8} s) enough to penetrate the detector before one decays.

The photon identification is attained by characterizing differences in the shape between single photon induced and multi-photon induced cascades. We start the discussion with the nature of the electromagnetic cascade shower.

3.1 Electromagnetic Cascade

3.1.1 Basic Processes

Electrons (positrons) lose energy in traversing matter in two ways: the ionization energy loss and the process of radiation loss or *bremsstrahlung*. Figure 3.1 shows the energy dependence of the fractional energy loss for electrons by these processes along with other small contributions.

The mean rate of ionization loss of a charged particle is given by the Bethe-Bloch equation,

$$\frac{dE}{dx} = \frac{4\pi N_0 z^2 e^4 Z}{mv^2 A} \left[\log \left(\frac{2mv^2}{I(1-\beta^2)} \right) - \beta^2 \right],$$

where m is the electron mass, z and v are the charge (in units of e) and velocity of the particle, $\beta = v/c$, N_0 is Avogadro's number, Z and A are the atomic number and mass number of the atoms of the medium, and x is the path length in the medium measured in g cm^{-2} . The quantity I is an effective ionization potential, averaged over all electrons, with approximate magnitude $I = 10Z$ eV. It is noted that the equation shows dE/dx being independent of the particle mass. The energy loss rate in various medium is shown in Fig. 3.2.

Since dE/dx increases very slowly, logarithmically with $\gamma = (1 - \beta^2)^{-1/2}$, a high momentum electron loses energy mostly by radiative collisions with the atomic nuclei of the medium. The electron radiates *bremsstrahlung* photons, with the photon spectrum having the approximate form dE'/E' , where E' is the photon energy. Integrated over the spectrum, the total radiation loss of an electron in traversing a thickness dx of medium becomes

$$\left(\frac{dE}{dx} \right)_{rad} = -\frac{E}{X_0},$$

where X_0 is a radiation length. The average energy of a beam of electrons with an initial energy E_0 , after traversing a thickness x of medium, is written

$$\langle E \rangle = E_0 \exp \left(-\frac{x}{X_0} \right).$$

It is useful to define the *critical energy* E_c , where energy losses by the above two processes, the ionization loss and bremsstrahlung, are equal. It is roughly described by

$$E_c \simeq \frac{600}{Z} \text{ MeV}.$$

For example, the critical energy for lead is 6.9 MeV, where $Z = 82$.

In matter, a photon loses energy mostly by the following processes:

- Photoelectric absorption

- Compton scattering
- Pair production

At low energies, the photoelectric effect is dominant, and its cross section varies with photon energy E as $1/E^3$. For a photon of its energy around 1 MeV, the Compton scattering dominates the energy loss, and the cross section changes as $1/E$. At high energies, a photon loses most of the energy by the pair production, with a cross section essentially independent of energy. Figure 3.3 shows contributions to the photon cross section in carbon and lead.

The conversion process of a high energy photon to an e^+e^- pair is closely related to that of electron bremsstrahlung. The attenuation of a beam of high energy ($\gtrsim 1$ GeV) photons at intensity I_0 by pair production in a thickness x of absorber is written as

$$I = I_0 \exp\left(-\frac{7x}{9X_0}\right). \quad (3.1)$$

The intensity is reduced by $1/e$ in a distance of $9X_0/7$, where the $9X_0/7$ is called the *conversion length*.

3.1.2 Average Cascade

When a high energy electron or photon is incident on thick absorber, it initiates an electromagnetic cascade as pair production and bremsstrahlung generate more electrons and photons with lower energies. Electron energies eventually fall below the critical energy, and then dissipate their energies by the ionization process rather than by bremsstrahlung.

The mean longitudinal profile of the energy deposition in an electromagnetic cascade is well described by a gamma distribution:

$$\frac{dE}{dt} = E_0 \frac{b^{\alpha+1}}{\Gamma(\alpha+1)} t^\alpha e^{-bt},$$

$$t = \frac{x}{X_0},$$

where x is the depth in absorber measured from a point at which the cascade starts.

The CDF test beam experiment has found the parameters to have the following

energy dependences:

$$\alpha = 1.91 + 0.484 \ln E \quad \text{and}$$

$$b = 0.582 - 0.014 \ln E,$$

where E is the incident electron energy. The longitudinal profile of the average cascade for 100 GeV electrons incident on the PEM is shown in Fig. 3.4 together with GEANT3 Monte Carlo shower simulations (Chapter 4) for electrons and photons. Due to the conversion length, the photon profile is shifted to the depth compared to the electron profile.

The lateral spread of a shower is mainly due to the multiple Coulomb scattering of the electrons which do not radiate but have a large enough energy to travel far away from the incident axis. In any material, the spread is of order one Molière unit R_M ,

$$R_M = \frac{21 \text{ MeV}}{E_c} X_0.$$

On the average, only 10% of the energy lies outside the cylinder with radius R_M . The lateral distributions of cascades are characterized by a narrow core, and broaden as the shower develops. They are often represented as the sum of two gaussian functions.

3.1.3 Fluctuations in Cascade

It is important to understand shower fluctuations since the cascade is a result of the combined phenomena of bremsstrahlung and the pair production, and large fluctuations, which make an event by event separation of prompt photons from multi-photon background events impossible, are expected in the shower development.

“Sampling fluctuations” are a type of important fluctuations. In a sampling calorimeter, the degraded energy is measured in a number of sensitive layers interspersed by passive absorber. It measures the sum of ionization losses of charged particles traversing the sensitive layers by the following facts:

- The ionization loss of a charge particle is independent of its energy. Thus, the sum of ionization losses is proportional to the number of charged particles traversing

the sensitive layers.

- The number of those charged particles is proportional to the incident energy.

The above are essentially true. The ionization loss increases only logarithmically with $\gamma = (1 - \beta^2)^{-1/2}$ as seen previously. The number of charged particles in the cascade increases with the energy of the initial particle, and the relation can be shown with the following assumptions:

- Each electron with an energy larger than the critical energy undergoes a radiation process at a distance of one radiation length from the place where it has been produced and that, in this process, it loses half of its energy to a secondary photon.
- Each photon undergoes a materialization process at a distance of one radiation length from the place of production, splitting its energy equally between the two secondary electrons.
- Both the Compton effect and the collision loss of electrons with an energy larger than the critical energy is neglected.
- When electron energy becomes smaller than the critical energy, cease to radiate and soon brought to rest by collision losses.

According to the above assumption, a high energy ($E_0 > E_c$) electron incident upon matter will give rise to one electron and one photon of energy $E_0/2$ after one radiation length. In the next radiation length, the secondary electron will produce an electron-photon pair; the secondary photon will produce a electron-positron pair. After t radiation length, the total number of particles will be $N = 2^t$, and the energy of each particle is $E(t) = E_0 2^{-t}$. Thus, the total number of particles at t will increase exponentially, and then drops abruptly to zero. The maximum will occur at

$$t = t_{max} = \frac{\ln(E_0/E_c)}{\ln 2},$$

and at which, the number of particles will be

$$N = N_{max} = \frac{E_0}{E_c}.$$

In the actual case, the number of particles should be different from the above obtained by a consequence of oversimplified assumptions, at least it should be smooth dependence of N on t . However, precise analytic studies in Ref. [8] confirmed the qualitative nature of the above prediction.

Since the number of charged particles in a shower is proportional to energy of the primary particle, one can measure, by assuming N has a nominal distribution, the energy with an RMS error as

$$\left(\frac{\sigma(E)}{E}\right)_{\text{SAMPLING}} \simeq \frac{1}{\sqrt{N}},$$

For an incident energy of $\gtrsim 50$ GeV, the number of particles can be large enough to have a nominal distribution near $t = t_{max}$. However, it is not enough large at $t \ll t_{max}$ or at $t \gg t_{max}$, and the fluctuations are expected much larger. It is important to mention that even if the energy deposit at a fixed depth has a gaussian distribution, the energies deposited at different depths are strongly correlated. As expected, positive fluctuations in the region before the shower maximum correspond to negative fluctuations on the tail, and vice versa.

Another fluctuations called "path length fluctuations" arise in a sampling calorimeter due to the wide spread of electron angles. Especially in a gas calorimeter, like the PEM, these fluctuations are fairly large since the critical energy is small and low energy electrons moving along a sensitive layer leave more energy than those moving perpendicularly to the plane. Back scatterings of low energy electrons by absorber layers make the fluctuations even larger.

Minimum ionizing particles traversing material give an asymmetric distribution of deposited energy, known as the Landau distribution. The large fluctuations are due to the small number of collisions involving large energy transfers. The energy spread due to the "Landou fluctuation" is written by

$$\left(\frac{\sigma(E)}{E}\right)_{\text{LANDAU}} \simeq \frac{1}{\sqrt{N \log(10^4 \cdot x [\text{g cm}^{-2}])}}.$$

In a gas quantameter, $x \simeq 10^{-3} \text{ g cm}^{-2}$, and the equation predicts a widening of the sampling resolution by a factor $\sim \sqrt{2}$.

There are other causes which broaden the error of the energy measurement, such as noises from readout electronics and poor calibrations. The measured fluctuations are expected much larger than the above prediction. Figure 3.5 shows measured fluctuations of 100 GeV electron induced cascades in the CDF endplug electromagnetic calorimeter.

3.2 Photon Identification

The largest fraction of the background against prompt photons is the $\pi^0 \rightarrow \gamma\gamma$ decay. However, we also expect a significant number of η mesons as another primary source of the background since the difference of masses of the two neutral mesons is negligible in $\sqrt{s} = 1.8$ TeV $\bar{p}p$ collisions, and the production rates for both mesons are measured even [4]. Only the branching fractions to neutral modes make the contributions different.

π^0 and η mesons are mostly produced in jets, and accompanied by many other particles nearby (non-isolated). Therefore, a limitation on energy flow around the electromagnetic cluster should dramatically reduce the background events, while prompt photons are isolated and not diminished. However, we still expect a substantial number of the background mesons produced isolated by fluctuations in the jet fragmentation, because of an extremely large production rate of QCD multi-jet events.

When measured as electromagnetic clusters in a detector, these single photons and multi-photons will show very similar characteristics except for small differences in the conversion probability and in the shower shape. Due to large shower fluctuations, they are only distinguishable statistically, that is, one cannot tell which is a prompt photon or a meson individually. One can only tell how many of prompt photon events are contained in a certain sample.

3.2.1 Lateral Shower Profile

Two photons from a π^0 decay can hardly be separated when the initial meson has energy $\gtrsim 50$ GeV. Figure 3.6 shows distributions of the two photon opening angle in $\pi^0 \rightarrow \gamma\gamma$ events at initial π^0 energies of 50, 75, and 100 GeV. Considering the typical energy in our prompt photon measurement of 100 GeV, the two photons are separated by $\sim 0.2^\circ$

or ~ 6 mm at a distance of 2 m from the vertex, where the shower becomes maximum in the PEM. Comparing this with the Molière radius of the PEM, ~ 3.5 cm, it is found that cascades of the two photons are measured as a single shower.

Lateral shower profiles of the two photons, however, should be broader than those of single photons. Such broadening has been studied and used for prompt photon detection in the central region analysis [4]. However, it was found that the two photons from the decay of π^0 are almost always too close to observe a significant broadening of the shower for energies above ~ 50 GeV, and we conclude the lateral shower profile is not useful at higher energies.

In the central photon analysis, lateral shower profiles are measured by the strip and wire chambers, which are ~ 2 m apart from the vertex, located near the shower maximum in the CEM. The PEM is also equipped with strip chambers, located ~ 2 m apart from the vertex, with approximately the same position resolutions of the central strip and wire chambers. Considering these conditions as well as the Molière radii of the same size for both calorimeters, it can be concluded that separating prompt photons of energies over ~ 50 GeV from π^0 background by the lateral shower profile is impossible.

3.2.2 Longitudinal Shower Profile

The average longitudinal cascade of $\pi^0 \rightarrow \gamma\gamma$ events has the shower maximum before that of single photon events with the same primary energy for the following two reasons:

- Each of the two photons from a π^0 decay has approximately a half of the π^0 energy. Note that the shower maximum is at a thickness of about $\log(E_0/E_c)$.
- The conversion probability in Eq. 3.1 is squared by the two photons.

Figure 3.7 shows the average profiles of longitudinal cascade showers for single photons, two photons from π^0 decays, and six photons from $\eta \rightarrow 3\pi^0$ decays at an incident energy of 87 GeV by GEANT3 shower simulations.

Figure 3.7 is presented as measurements by the anode wire readout of the PEM. It is useless, however, unless the photon candidate is extremely isolated since the wires of a sampling plane are ganged over 90° and measures energy deposits in the quadrant. As

mentioned in Section 2.3.2, the cathode pads are segmented by $\Delta\eta \times \Delta\varphi = 0.09 \times 5^\circ$ and capable of measurements of energy deposits in the three depth segments along the beam axis. Figure 3.8 displays the average longitudinal profiles measured by the pad. Pad measurements are less dramatical, but still differences of the energy deposits in the first and third segments are noticeable.

Since fluctuations are important, the energy deposit should be dealt with fluctuations. Figure 3.9 shows distributions of energy deposits in the first segment normalized by the total energy (first segment energy fraction or FSEF). As expected, multi-photons have larger energy fractions than prompt photons. Especially for smaller values of FSEF, the distributions are remarkably different. The “spike” in the first bin of the photon distribution comes from that some photons make only few or no conversions in the first segment.

To extract the cross section for prompt photon production, the distribution of measured FSEF is fit by a linear combination of those for single photons and for multi-photon backgrounds as

$$F_{data} = \varepsilon_\gamma \cdot F_\gamma + (1 - \varepsilon_\gamma) \cdot F_{background},$$

where F_{data} represents the FSEF distribution of the data, F_γ and $F_{background}$ are those for single photons and for background mesons obtained with GEANT3 shower simulations. ε_γ is a free parameter ($0 < \varepsilon_\gamma < 1$) and determined so that the sum of the photon and background distributions reproduces the data. Once F_{data} , F_γ , and $F_{background}$ are each normalized to unity, ε_γ represents the photon fraction in the data.

In evaluating the cross section, we need to study dependences of FSEF spectra on the incident angle and energy, and possible backgrounds other than π^0 and η mesons. The “fitting” method and problems will be detailed in Chapter 9.

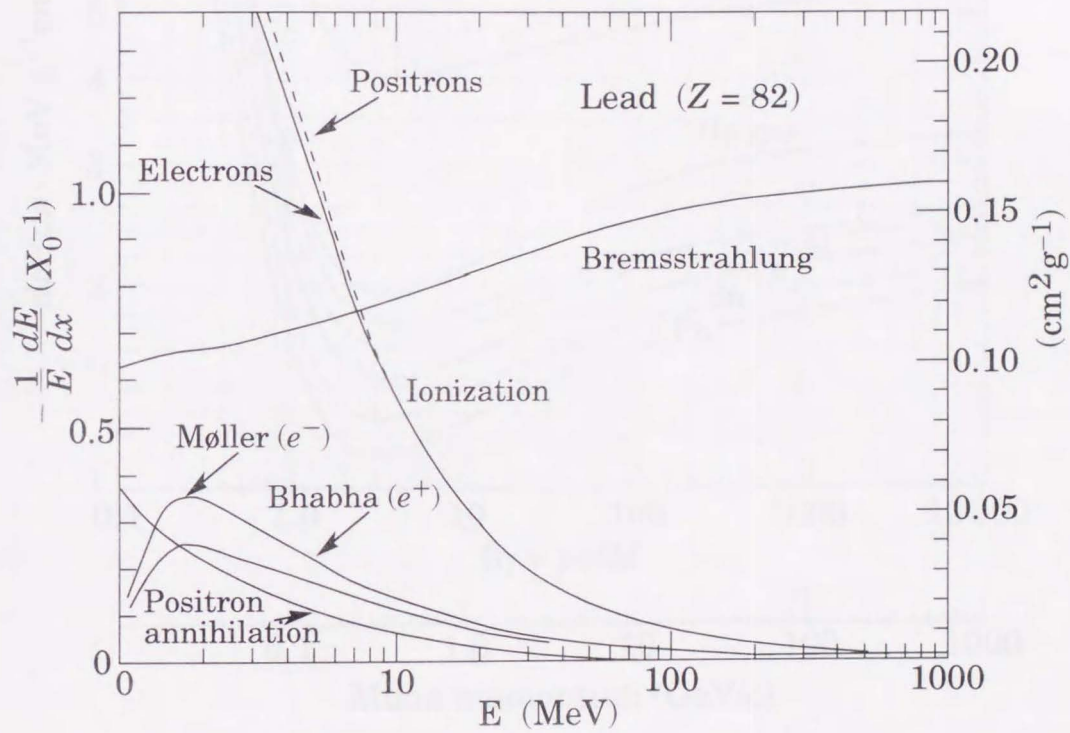


Figure 3.1: Fractional energy loss per radiation length in lead as a function of electron or positron energy. [Particle Data Group, L. Montanet *et al.*, Phys. Rev. D **50**, 1260 (1994)]

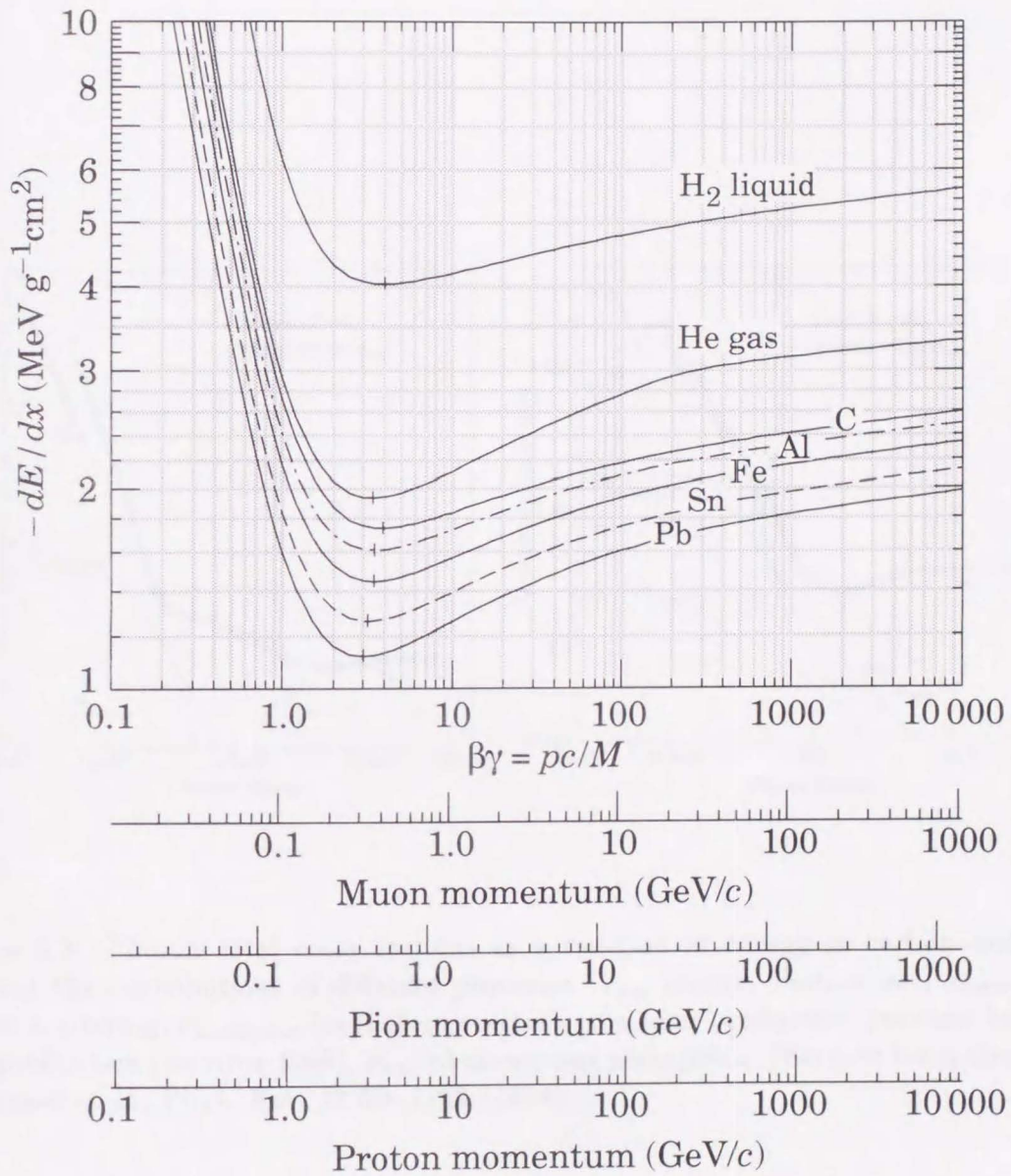


Figure 3.2: Energy loss rate in various medium. [Particle Data Group, L. Montanet *et al.*, Phys. Rev. D **50**, 1260 (1994)]

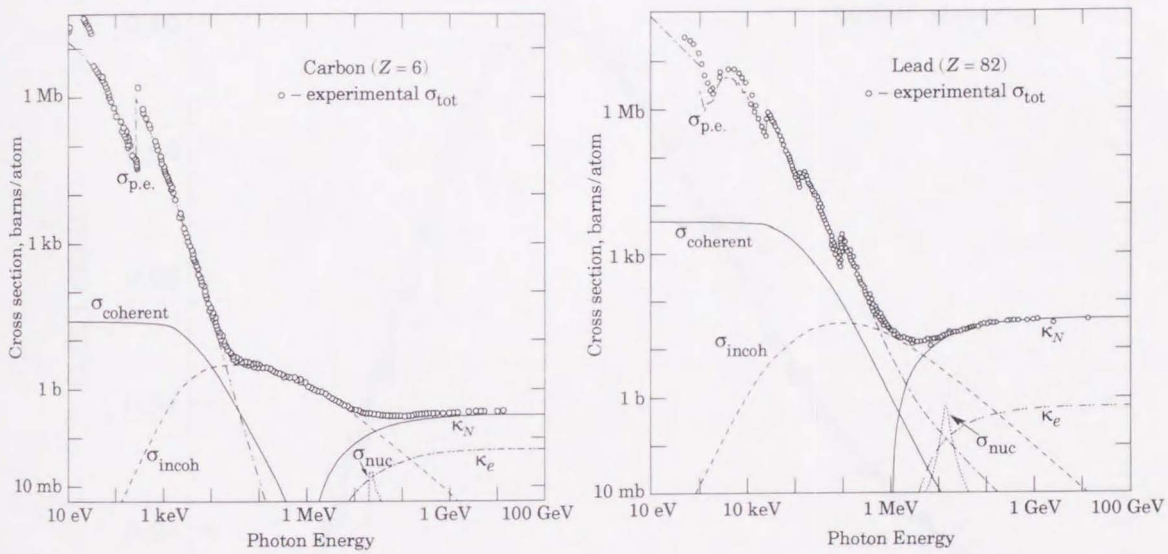


Figure 3.3: Photon total cross sections as a function of energy in carbon and lead, showing the contributions of different processes. $\sigma_{p.e.}$ atomic photo-effect, $\sigma_{coherent}$ coherent scattering, $\sigma_{incoherent}$ incoherent scattering, κ_n pair production (nuclear field), κ_e pair production (electron field), σ_{nuc} photonuclear absorption. [Particle Data Group, L. Montanet *et al.*, Phys. Rev. D **50**, 1260 (1994)]

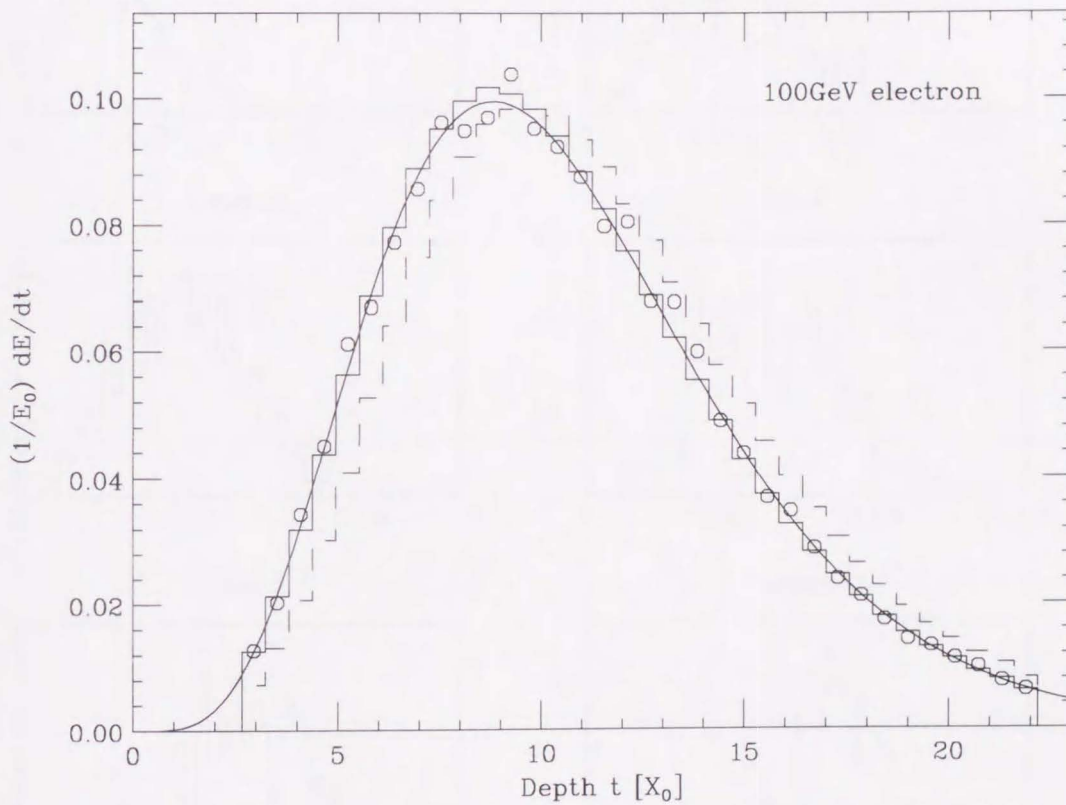


Figure 3.4: The average longitudinal profile of cascade showers for 100 GeV electrons incident on the PEM. The circles indicate the measurements, the solid histogram shows the GEANT3 shower simulation, and the curve is a gamma function fit to the measurements. 100 GeV photon induced cascades are also simulated, and the average profile is represented as the dashed histogram.

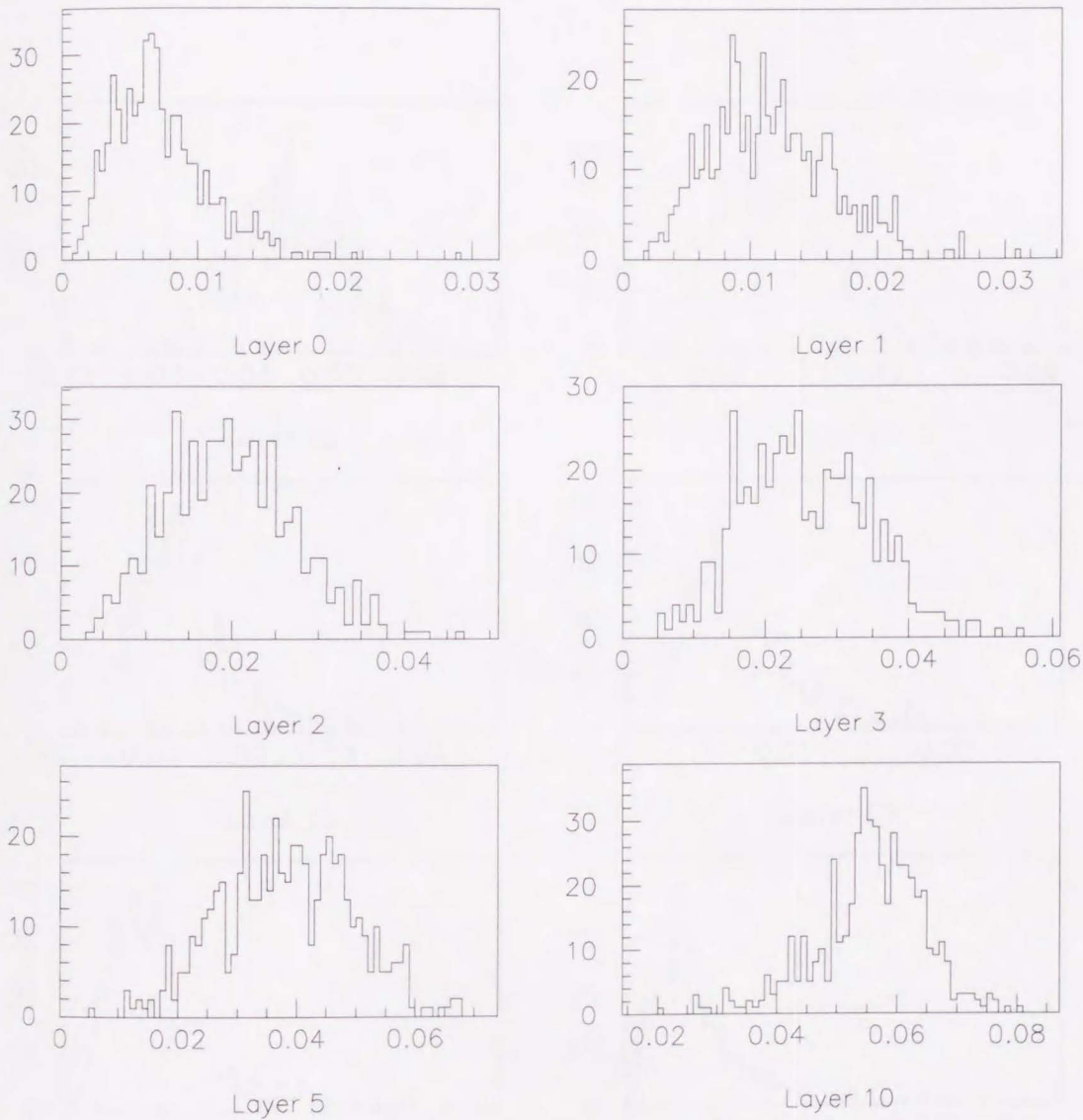
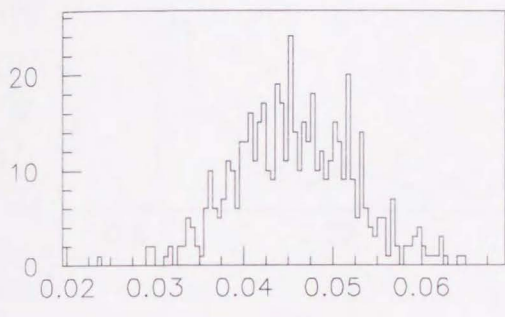
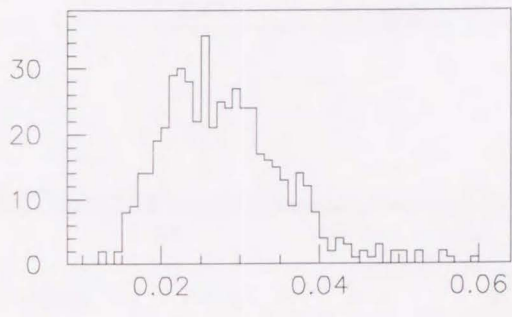


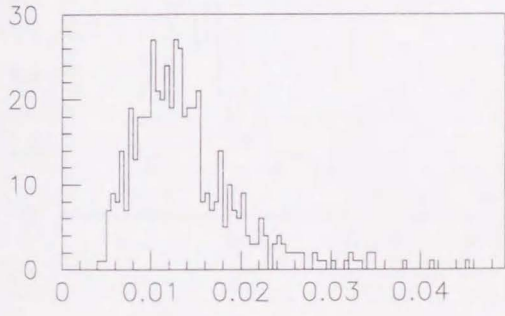
Figure 3.5: Energy deposits in layers normalized by the incident particle energy, showing fluctuations of 100 GeV electron induced cascades measured by the CDF endplug electromagnetic calorimeter. “Layer 0” measures energy at $t = 2.94 X_0$ in Fig. 3.4. “Layer 1” is $3.52 X_0$, “layer 2” $4.09 X_0$, and so on. Continues on the next page.



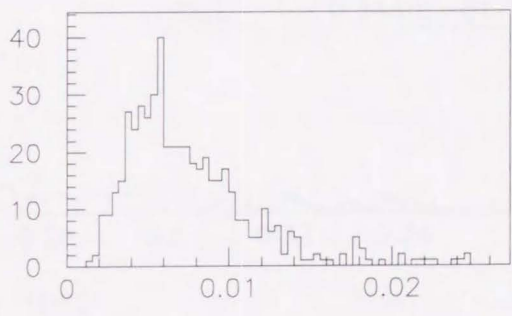
Layer 15



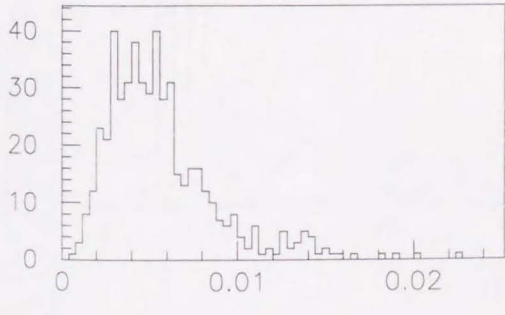
Layer 20



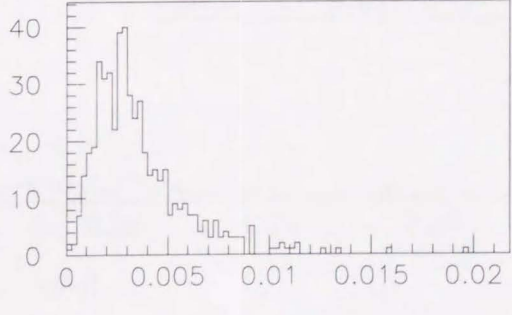
Layer 25



Layer 29



Layer 31



Layer 33

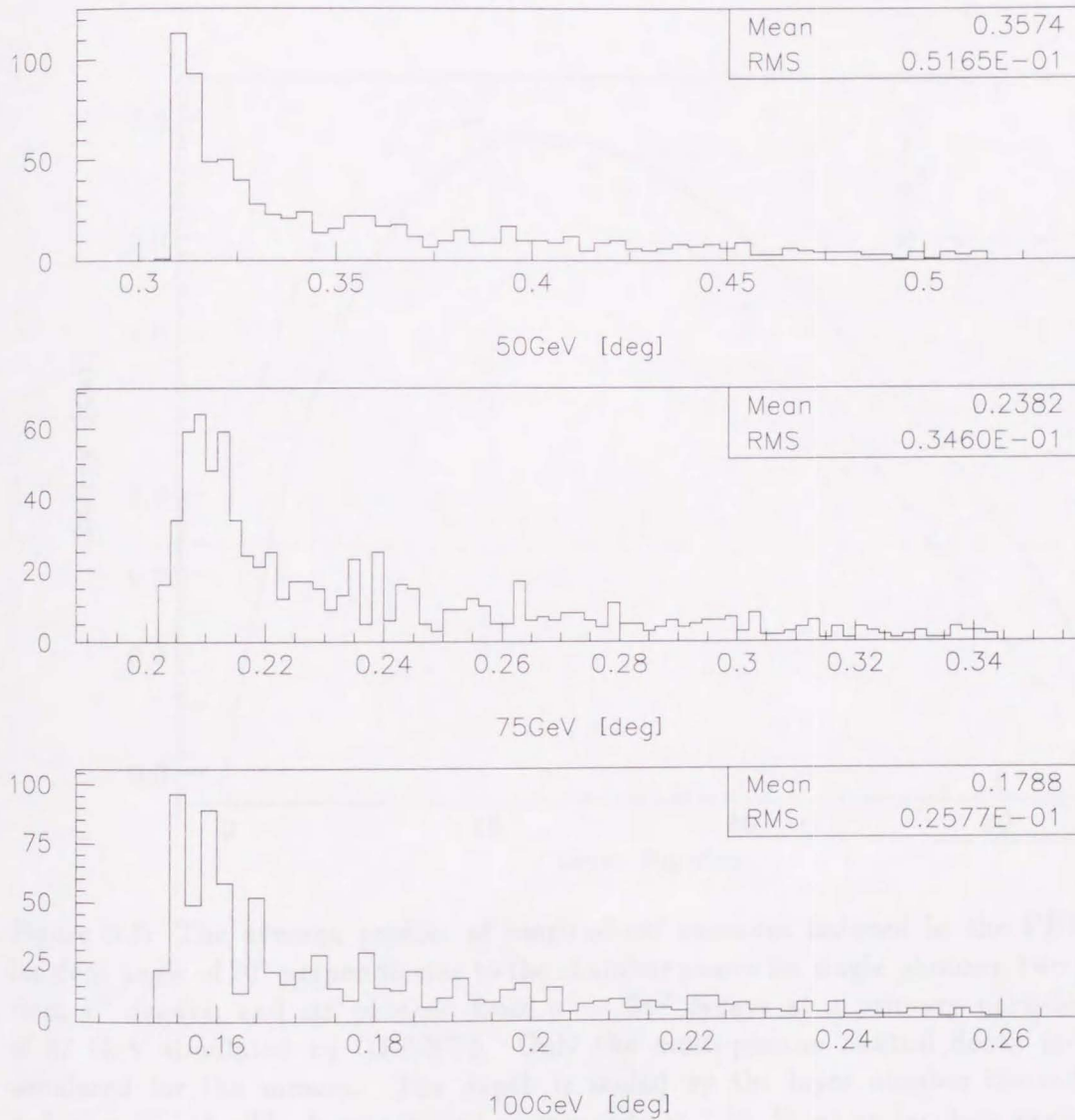


Figure 3.6: Distributions of two photon opening angle in $\pi^0 \rightarrow \gamma\gamma$ decays at initial π^0 energies of 50, 75, and 150 GeV.

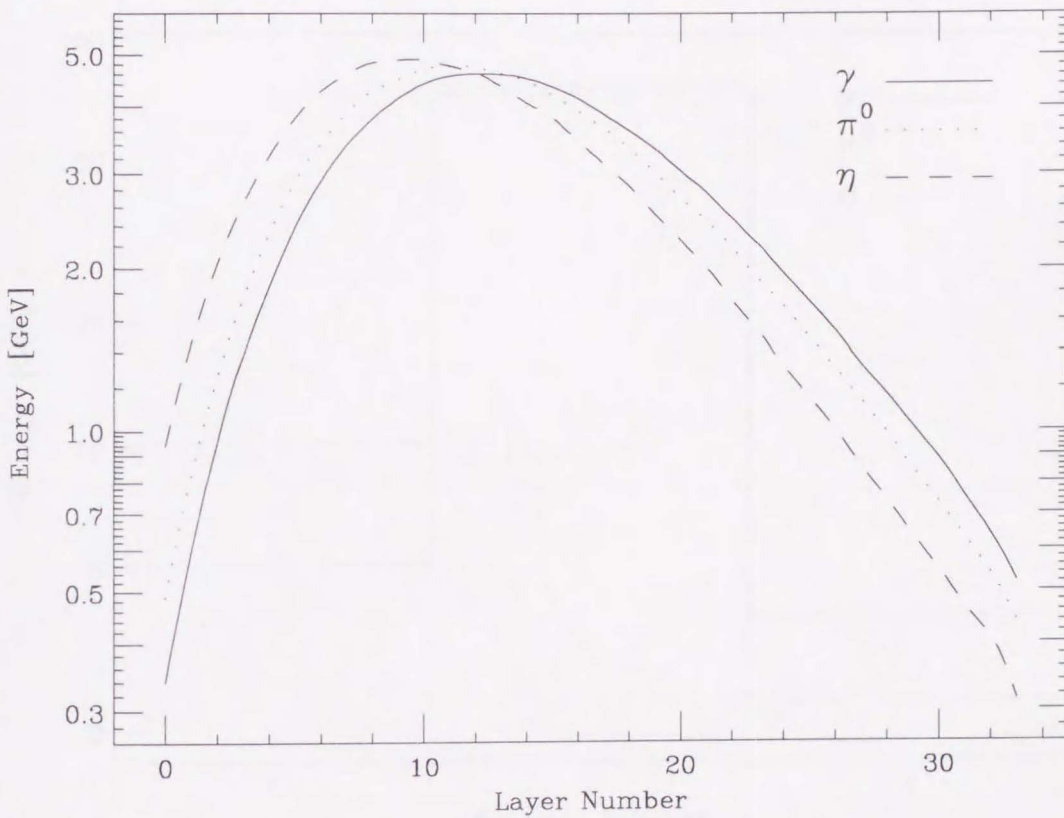


Figure 3.7: The average profiles of longitudinal cascades induced in the PEM at an incident angle of 20° perpendicular to the chamber planes for single photons, two photons from π^0 decays, and six photons from $\eta \rightarrow 3\pi^0$ decays at a primary particle energy of 87 GeV simulated by GEANT3. Only the multi-photon neutral decay modes are simulated for the mesons. The depth is scaled by the layer number instead of the radiation length. The layer interval corresponds to $0.55 X_0$ at an incident angle of 20° . Detailed description about the GEANT3 simulation is found in the next chapter.

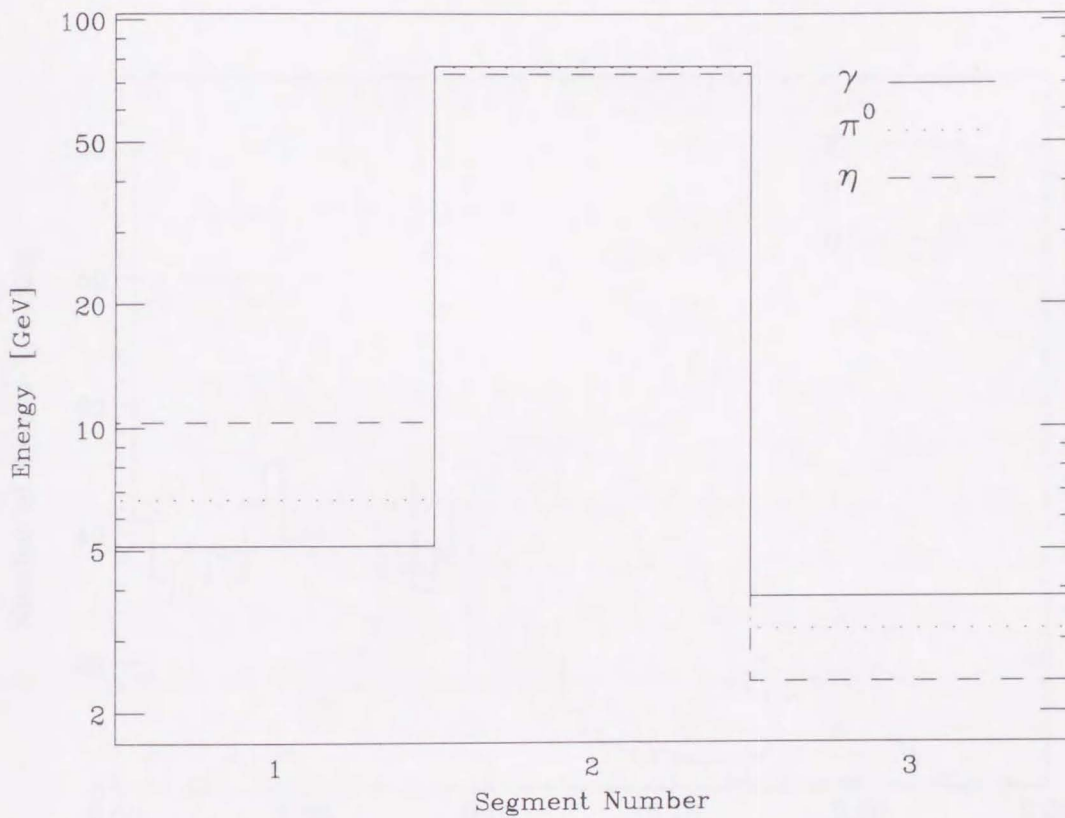


Figure 3.8: GEANT3 Monte Carlo simulations for the average longitudinal cascades measured by the cathode pad. Particles are induced in the PEM at an incident angle of 20° perpendicular to the chamber planes for single photons, two photons from π^0 decays, and six photons from η decays at a primary particle energy of 87 GeV. Only the multi-photon neutral decay modes are simulated for the mesons. See Section 2.3.2 for detailed structure of the PEM.

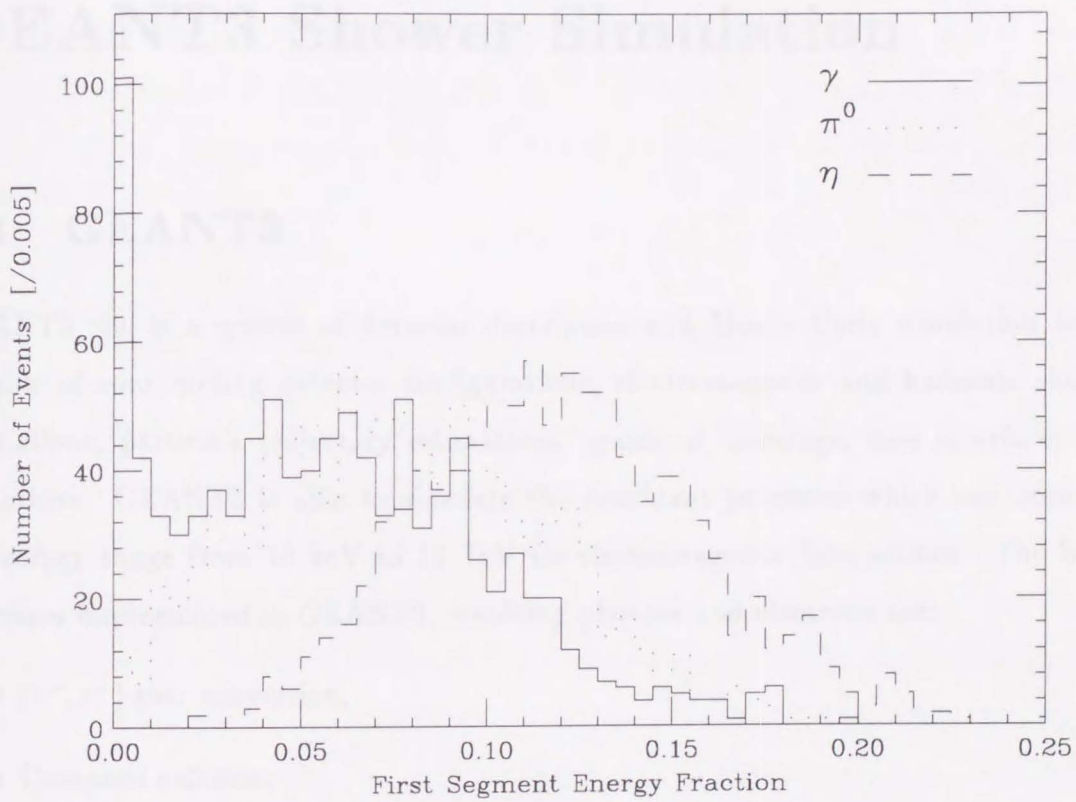


Figure 3.9: Distributions of first segment energy deposits normalized by the total energy (FSEF). Cascade showers are simulated by GEANT3 under the same conditions in the previous figures.

Chapter 4

GEANT3 Shower Simulation

4.1 GEANT3

GEANT3 [49] is a system of detector description and Monte Carlo simulation tools, capable of constructing detector configurations, electromagnetic and hadronic shower simulations, particle's trajectory estimations, graphical drawings, user interface, and the others. GEANT3 is able to simulate the dominant processes which can occur in the energy range from 10 keV to 10 TeV for electromagnetic interactions. The basic processes implemented in GEANT3, involving photons and electrons are:

- (e^+, e^-) pair conversion,
- Compton collision,
- Photoelectric effect,
- Photo fission of heavy elements,
- Layleigh effect,
- Multiple scattering,
- Ionization and δ -ray production,
- Bremsstrahlung,
- Annihilation of positrons,

- Generation of Čerenkov light.

Other processes involving muons or hadrons are also implemented, but not listed here.

By means of systematic fits to the existing data in the world, the cross-sections of the electromagnetic processes are well reproduced, within a few percent, from 10 keV to 100 GeV, both for light (low Z) and heavy materials.

For multiple scattering probabilities, there are many alternatives such as either Molière distribution or gaussian approximation. for multiple scattering probabilities. All the controls are set to the default values [50] for this study except the kinetic energy cuts for photons and electrons. The kinetic energy thresholds are set to the minimum value of 10 keV to reproduce as much shower fluctuations by lower energy particles as possible.

4.2 Detector Setup in the Simulation

In order to obtain (first segment energy fraction (FSEF) distributions for single photons and neutral meson backgrounds, GEANT3 (version 3.1416) is employed for electromagnetic shower simulations. GEANT3 is capable of simulating cascade showers for all the detector components of CDF. It is, however, practically impossible as well as unnecessary to reconstruct a full set of the CDF detector in the GEANT3 simulation because of limited computing speed, memories, etc. Since our interest is the electromagnetic cascade inside the PEM, only the endplug electromagnetic calorimeter has been built in the GEANT3 simulation together with other materials existing between the event vertex and the PEM. The other detector components are not implemented, while the PHA is added only for a special case, i.e., for estimations of cascade leakages from the PEM as described in Section 9.4. The magnetic field is ignored in the simulation.

Figure 4.1 shows the overall geometrical setup in the GEANT3 simulation. Only the PEM is prepared as a single detector. Known inside materials such as the beampipe, VTPC, CTC, and others are replaced by homogeneous matter so that it reproduces the total thickness (in radiation lengths) of the materials. As shown in Fig. 4.1, two cylindrical aluminum blocks are substituted for the beampipe, VTPC with the Faraday cage, and CTC graphite tube with the inner HV cylinder. The total amount of materials for

the design values of the CDF detector and the GEANT3 simulation is shown in Figure 4.2 as a function of the polar angle. The GEANT3 simulation is found to reproduce the design values well for the fiducial region¹ of the PEM.

Another aluminum plate is placed parallel to the PEM surface for simulating the CTC endplate. The real CTC endplate, however, does not have a uniform thickness. It is a two inch thick aluminum plate with many slots bored for wiring as shown in Fig. 2.5. About 30% of the aluminum is removed to allow passage of the wires and insulators through the endplate. In addition, a good deal of cables for the readouts of the VTPC and CTC are laid in a space between the CTC and PEM; a large number of pre-amplifiers are mounted on each end of the CTC (the numbers are not same for the east and west sides); other materials such as wire mounting blocks, connectors, and G10 boards are not added in Fig. 4.2. It is virtually beyond our capability to implement every small materials in the GEANT3 simulation. Hence, the thickness of the aluminum plate in the simulation is not fixed, and we will estimate the total amount of inside detector materials in Chapter 8 by comparing the electron cascades from W decays with simulations for different aluminum thicknesses.

The chamber structure of the PEM is reproduced as precisely as possible with reasonable computing speed. Some of very thin materials are omitted or absorbed in other materials. Figure 4.3 shows the structure of the calorimeter along the beam axis. The material and thickness are detailed in Table 4.1. The fine shape of the conductive plas-

Front cover plate	Fe	12.7 mm	$0.722 X_0$
Each sampling layer:		14.8 mm	$0.507 X_0$
Lead plate	Pb	2.7 mm	$0.482 X_0$
G10	60% SiO ₂ and 40% epoxy (C ₂₁ H ₂₄ O ₄)	1.6 mm	$0.009 X_0$
Plastic	polystyrene ($\{CH_2CH(C_6H_5)\}_n$)	2.9 mm	$0.007 X_0$
Gas	50% Ar and 50% ethane (C ₂ H ₆)	5.7 mm	
Vacuum		0.3 mm	
G10	60% SiO ₂ and 40% epoxy (C ₂₁ H ₂₄ O ₄)	1.6 mm	$0.009 X_0$

Table 4.1: Material and thickness of the PEM in the GEANT3 simulation.

¹The fiducial region is where the detector has a full measurement capability. See Chapter 6 for details.

tic tube is not reproduced. They are built as thin plastic plates which have the same volume. Gas is also filled as thin layers. The copper-clads on G10 boards, the 50 μm G10 boards, and epoxy glue are neglected. Instead, the thickness of the lead plate is increased by 0.01 mm, and a remaining space 0.3 mm thick is kept vacuum. No pad or strip structure is reproduced since we do not use lateral shower shapes for photon identification. The pad structure is, however, implemented only for studies of the meson decays in Section 9.2 and the lateral shower χ^2 cut in Section 9.4.4.

An energy deposit in a sampling layer is the sum of ionization energy loss of electrons and positrons. A conversion factor from the ionization loss to the energy was obtained to be ~ 6300 by a calibration with 100 GeV electrons incident at the center of the PEM.

The GEANT3 simulation is used not only for producing cascades of single photons and mesons but also for electrons. In Chapter 7, electron cascades of the simulation are compared with the observed showers for the test beam electrons to see how much we can rely on the GEANT3 simulation. For simulating test beam electrons, the aluminum pipes surrounding the beam line are removed, while one parallel to the PEM surface is not, since, during the test beam run, an aluminum plate was placed a few centimeters in front of the PEM to simulate the CTC endplate during the test beam run. Details in the test beam setup will be discussed in Chapter 7.

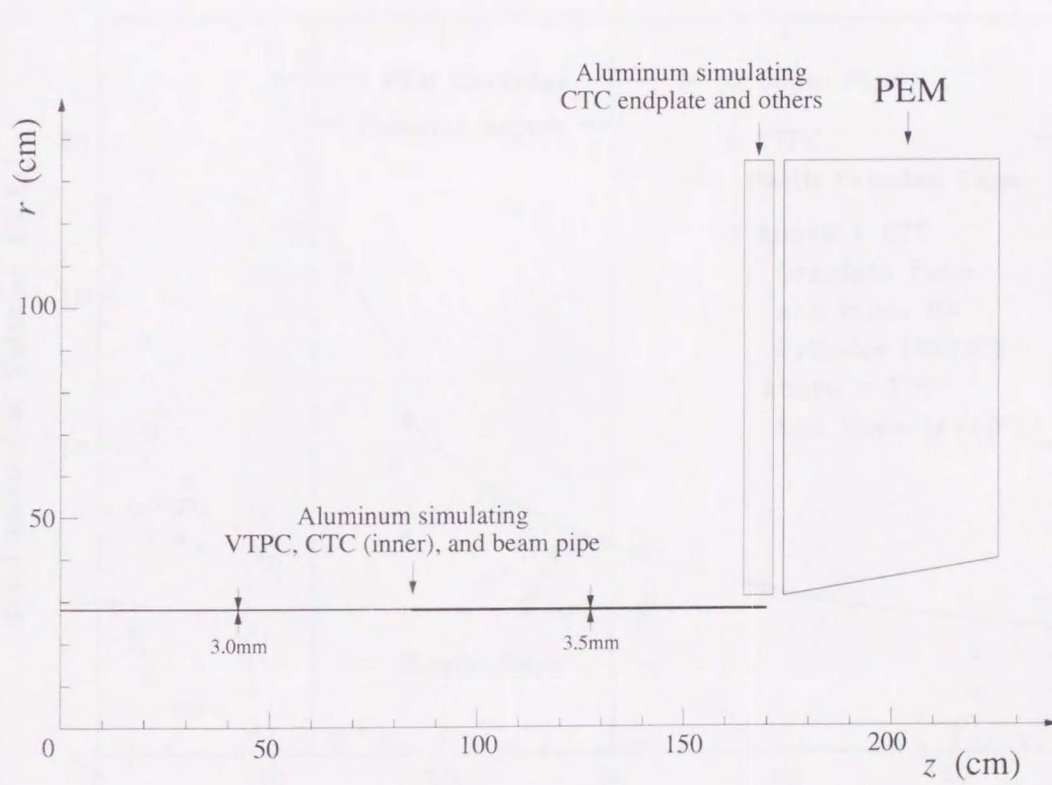


Figure 4.1: Geometrical setup of the GEANT3 simulation.

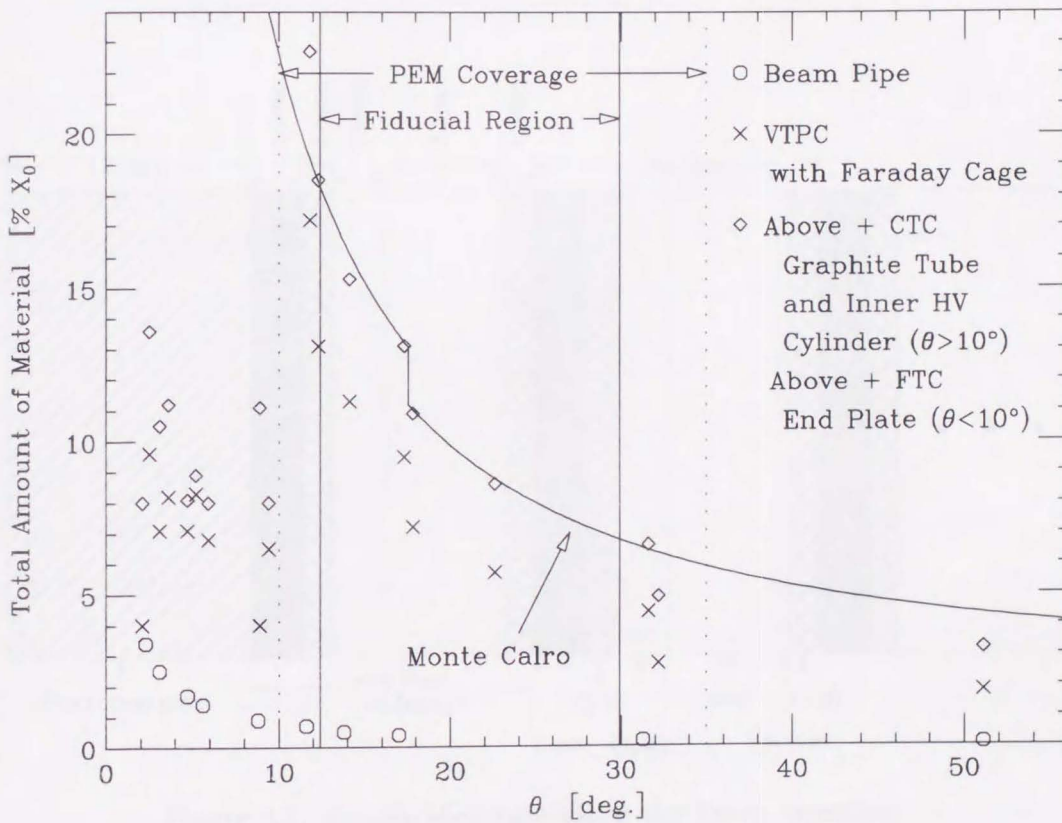


Figure 4.2: Total amount of material.

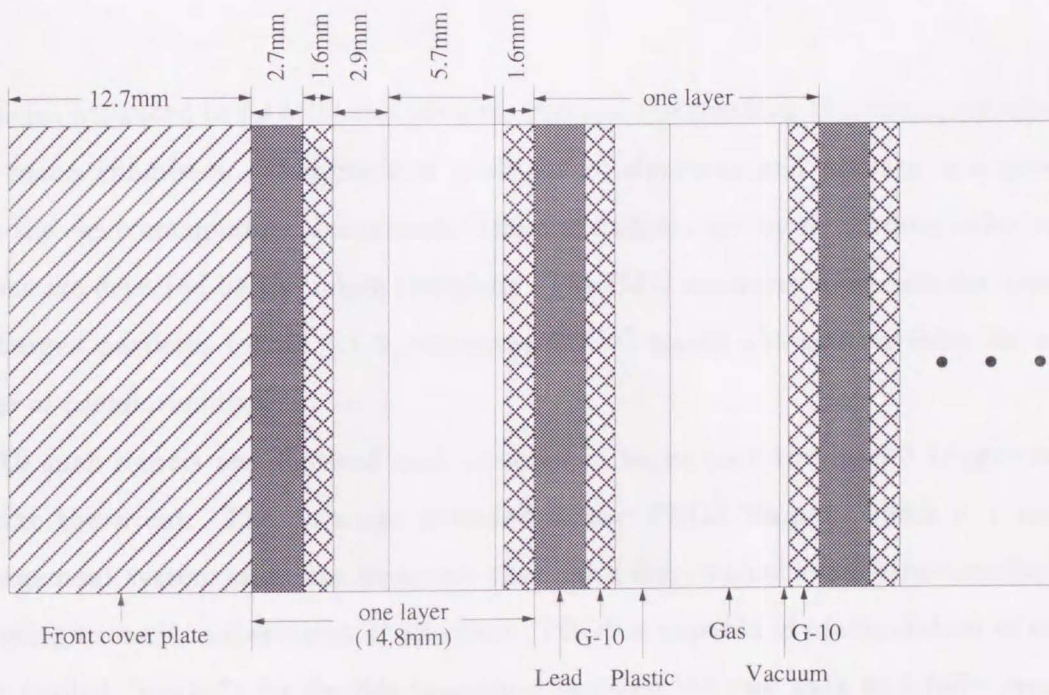


Figure 4.3: Precise structure along the beam direction.

Chapter 5

Event Reconstruction

Particles produced in $\bar{p}p$ collisions traverse through the tracking chambers, calorimeters, and muon chambers. Energies and positions of electrons and photons are measured with the electromagnetic calorimeters. Those of hadrons are by the hadron calorimeters. Muons are detected by the muon chambers. The CTC measures momenta and positions of charged particles for $|\eta| \lesssim 1.8$, while the VTPC tracks charged particles for a wide range of pseudorapidity.

All such signals are digitized and recorded in tapes once the level 3 trigger decides to take the event. The data are recorded in the YBOS format, which is a memory management system and data structure that has a hierarchical event structure for rapid accessing to major subsections of an event. YBOS is capable of manipulation of subsections (called “banks”) for flexible transition between the raw data and fully processed events, and has other features [43]. The raw data (recorded on-line) contains only ADC, FADC, and TDC counts of the various detector components (D banks). They are “reconstructed” to become more physical elements such as energy clusters and tracks by the CDF standard event reconstruction programs, then selected according to the event characteristics, and recorded onto another tapes for individual analysis. This reconstruction process is named the “production.”

The raw data are reconstructed at two stages. At the first stage, raw ADC, FADC, and TDC counts are converted to energies and times, and then stored in the E (elements) banks. At the next stage, tower by tower energies are grouped into clusters, and hit

times of the tracking chambers are converted into positions which are connected and reconstructed as tracks. The cluster energy corresponds to particle or jet energy, and the track corresponds to particle trajectory. Banks containing these properties of calorimetry clusters and reconstructed tracks are called the S (subject) banks. In the following sections, we describe the process of reconstructing events concerning this study from the trigger level [44] to the off-line analysis level.

5.1 Calorimeter

EM Calorimeter and Clusterings

Both photons and electrons initiate electromagnetic cascades in the calorimeters. Since the cascade shower has finite lateral spread, the total energy of an incident particle is obtained by summing energies over several calorimetry towers.

In the level 1 trigger, transverse energy summed over CEM, PEM, and FEM trigger towers with at least 4 GeV is required to be larger than 7 GeV. The transverse energy E_T of a trigger tower is defined as tower energy multiplied by $\sin \theta_{det}$, where θ_{det} is the polar angle from the proton beam line to the tower centroid assuming an event vertex at $z = 0$ cm. This definition is also true at the level 2 trigger stage. However, in the level 3 trigger or in the off-line analysis, E_T is calculated with a reconstructed event vertex and based on the calorimetry tower, not the trigger tower.

In the level 2 trigger, an “EM clustering photon” with $E_T^{EM} \geq 23$ GeV is required. For the PEM, E_T^{EM} is not the sum of all the three depth segments, but the second segment is only used to obtain E_T^{EM} at this stage as well as in the level 1 trigger. Therefore, the tower E_T^{EM} in the level 1 or 2 trigger is corrected by multiplying a factor so as to become consistent with the sum of the three depth segments. The correction factor is calculated from the average longitudinal shower profile to 100 GeV electrons, and obtained to be 1.10 as a ratio of the average energy deposit in the three segments to that in the second segment. However, it is only true for a quadrant with no “dead layers.” A dead layer is an anode wire plane on which the high voltage is reluctantly turned off to avoid leak current. The correction factor includes such ineffectiveness. It

should also include the energy and η dependences since the longitudinal shower profile changes with them. However, it is not implemented in the level 1 or 2 trigger.

Starting with a seed tower of $E_T^{EM} \geq 4$ GeV, a level 2 electromagnetic cluster is formed by adding four adjacent towers if one has at least 3.6 GeV in E_T^{EM} . Then, next four adjacent towers around the joined tower are examined and so on. This procedure is repeated until no new tower is added. $E_T^{EM}/E_T^{total} > 1/1.125$ and the number of trigger towers ≤ 15 are also required for the "EM clustering photon."

In the level 3 trigger, another clustering algorithm EMCLST, which is the same as used in the off-line analysis, is performed based on the calorimetry tower. EMCLST first finds a seed tower with $E_T^{EM} \geq 3$ GeV, then each of the 8 neighboring towers around the seed (daughter towers) is added to the corresponding cluster if one has E_T^{EM} at least 0.1 GeV and equal to or larger than 10% of the seed E_T^{EM} . Next, each of the surrounding 16 towers is examined and added if one has E_T^{EM} at least 0.1 GeV and equal to or larger than 10% of the adjacent daughter tower. For the PEM, the clustering is limited only within 5×5 towers around the seed. E_T^{EM} of a cluster should be at least 7.5 GeV, and E_T^{had}/E_T^{EM} is required to be less than 0.125, where E_T^{had} is a sum of transverse energies in corresponding hadron calorimeter towers of the cluster. In the level 3 trigger, noises from the electronics and discharges [45] are removed by filtering modules. Events passing the level 3 trigger are recorded for the off-line analysis. At this stage, only the raw data are written onto tapes.

Corrections for EM Calorimeter

At the off-line reconstruction stage, event reconstructions are again performed, but this time with various corrections. For the PEM, the following corrections are applied:

- Miscabling correction,
- Gas gain correction,
- Tower map correction,
- Quadrant gain correction,
- Non-linearity correction,

- Dead wire plane correction.

All the above corrections are made when the raw data are converted to the element data except the dead wire plane correction which is applied after EMCLST is performed.

It was found that some of the PEM readout cables were not connected to the corresponding front-end electronics [46]. Some of such mis-connections affected the triggers. Since the clustering algorithms in the level 2 and the level 3 triggers refer to the towers sequentially, some of the mis-labeled towers are neither examined nor added to a cluster. Such towers are not used for the analysis (the miscabling cut).

The gas gain of a proportional counter changes with temperature, pressure, and gas-mixture. The PEM system tracks the gas gain by the monitor tubes mounted in the PEM gas vessel. The latest gas gain constant is set to the triggers at the beginning of every run, and it is not changed during the entire run, which usually continues for several hours to half a day. This gain variation is corrected later in the production.

A tower to tower variation is observed in the pad response of the PEM. This variation is measured to be an order of $\sim 5\%$ with 100 GeV test beam electrons incident at the center of every PEM tower. Thus, we need correction factors, on a tower by tower basis, to get rid of this variation. Defining a standard tower in each quadrant, the correction factors are calculated relatively to the response of the standard tower. This correction leaves a quadrant to quadrant variation, and quadrant to quadrant gain correction factors are obtained using responses to electrons from decays of W and Z bosons [47]. These processes bridge the differences between the test beam and the B0 collider experiments as well as aging of the detector.

It is known that the PEM has a non-linear response against the incident energy due to gain saturation and longitudinal shower leakage. The response is fitted by a quadratic function and corrected accordingly.

Dead layer correction factors are obtained in the same way as in the level 1 and 2 triggers, but this time for all the three depth segments or all the 34 layers. The correction factors are calculated on a quadrant by quadrant basis, with respect to dead layers in the quadrant, and applied to EM clusters.

Jet Clustering

Jet clustering algorithm JETCLU is performed in the level 3 trigger and the production. It first lists towers containing energies at least 1 GeV, then these towers adjacent to each other, either at a corner or on a side, are grouped into pre-clusters. Pre-clusters are formed around the highest E_T tower as transverse energies of towers decrease monotonically to the edge of clusters. Pre-clusters within a cone of a fixed radius in the η - φ plane are added into a cluster. The cluster center is calculated as the energy-weighted average of towers with $E_T \geq 0.1$ GeV. Pre-clusters in a cone around this newly defined cluster center are again added into a cluster. This process is repeated until the set of towers no longer changes. Jets are, however, not referred to in the analysis.

5.2 Tracking

The CTC signal is not used for this study either, since it has only partial coverage for the PEM, while the VTPC has full coverage. There are no requirements for the VTPC at the level 1 or 2 trigger stage. But the level 3 trigger requires the event vertex, which is calculated by reconstructing VTPC tracks from the wire information, to be within $|z| < 200$ cm. There are two steps to reconstruct the event vertex. Track segments are first identified in each chamber octant. Then, the primary vertex location is reconstructed from the intercepts of these track segments and the beam axis. Figure 5.1 shows a distribution of reconstructed event vertices for the prompt photon candidates with no vertex requirement (Chapter 9). No other VTPC information is required at the production stage.

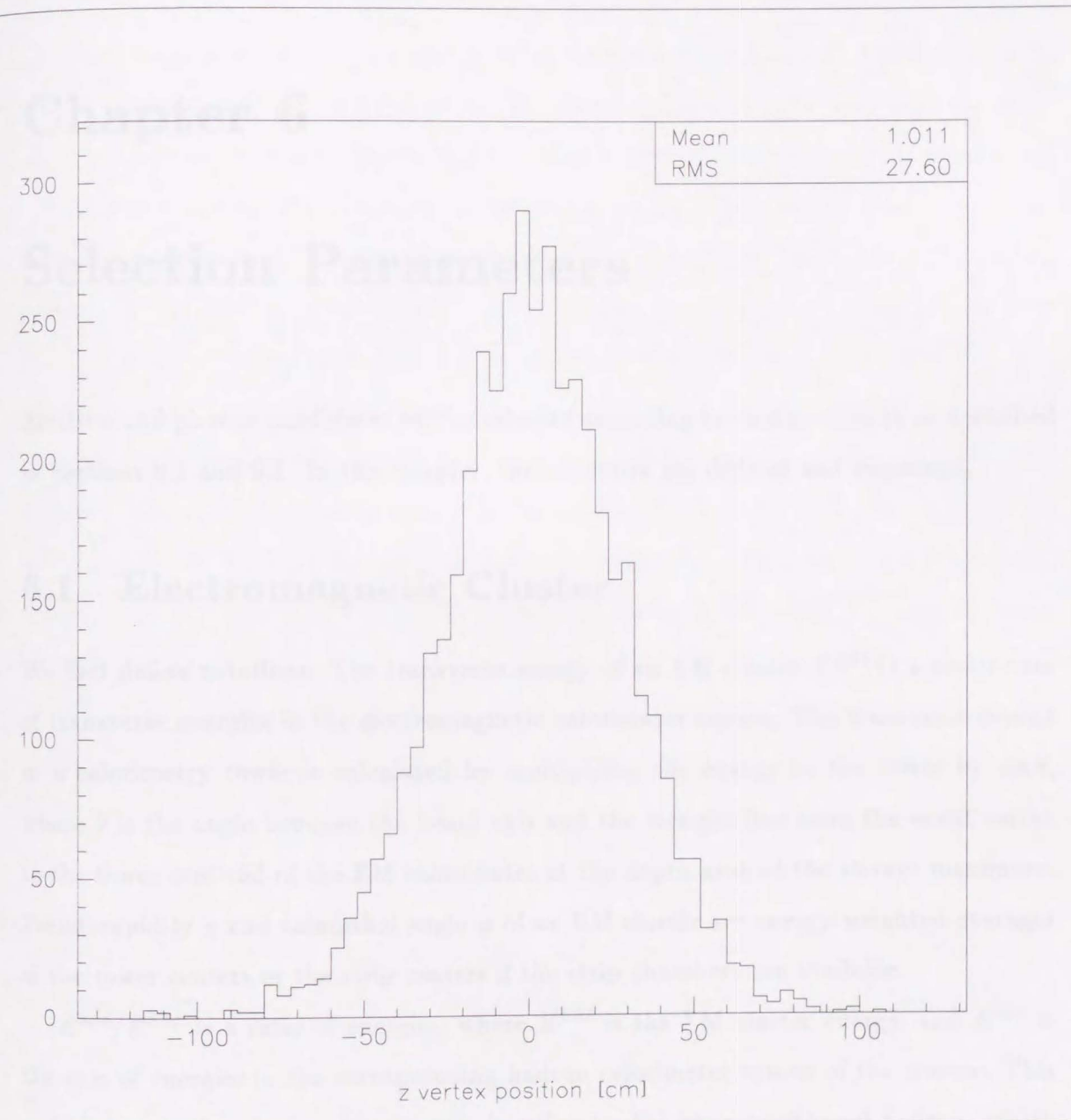


Figure 5.1: Distribution of event vertices along the beam axis for the prompt photon candidates without the vertex requirement.

Chapter 6

Selection Parameters

Electron and photon candidates will be selected according to similar criteria as described in Sections 8.1 and 9.1. In this chapter, these criteria are defined and explained.

6.1 Electromagnetic Cluster

We first define notations. The transverse energy of an EM cluster E_T^{EM} is a scalar sum of transverse energies in the electromagnetic calorimeter towers. The transverse energy in a calorimetry tower is calculated by multiplying the energy in the tower by $\sin \theta$, where θ is the angle between the beam axis and the straight line from the event vertex to the tower centroid of the EM calorimeter at the depth around the shower maximum. Pseudorapidity η and azimuthal angle φ of an EM cluster are energy-weighted averages of the tower centers or the strip centers if the strip chambers are available.

E^{had}/E^{EM} is a ratio of energies, where E^{EM} is the EM cluster energy, and E^{had} is the sum of energies in the corresponding hadron calorimeter towers of the cluster. This ratio is required to be less than a certain value to discriminate charged hadrons which tend to leave more energies in the hadron calorimeters.

The lateral shower profile is used to select a “good” EM cluster. This “goodness” or electron/photon likeliness is quantified by the following χ -squared:

$$\chi_{3 \times 3}^2 \equiv \frac{1}{\mu} \sum \frac{(E_i - E_i^{expected})^2}{(\Delta E_i)^2},$$

where the summation is taken over nine towers around the seed tower of the EM cluster. E_i and $E_i^{expected}$ are measured and expected energies in a tower. ΔE_i represents the energy uncertainty and is assumed to be 10% of E_i . μ is the number of degree of freedom. A linear combination of two gaussian functions is used to estimate the expected lateral shower profile. The function is parametrized from the results with test beam electrons and found to have no energy dependence once the tower energy is normalized by the cluster energy. Note that we assume no differences in the lateral shower shape for electrons and photons. The expected shower profile is calculated by assuming the shower center to be at the seed tower centroid. However, this is not true for showers off-centered in a tower since the pad size of the PEM, which is roughly $3.5 \text{ cm} \times 3.5 \text{ cm}$ to $10 \text{ cm} \times 10 \text{ cm}$, is larger than the Molière radius of the PEM. Thus, the $\chi_{3 \times 3}^2$ definition has been changed, and the new $\chi_{3 \times 3}^2$ algorithm gives the expected shower profile assuming the shower center is at the cluster center. Since we have been using both $\chi_{3 \times 3}^2$ algorithms, we name the old one $\chi_{3 \times 3}^2(\text{old})$ and the new one simply $\chi_{3 \times 3}^2$. Figure 6.2 shows $\chi_{3 \times 3}^2(\text{old})$ distributions for test beam electrons at various energies and incident angles. while Fig. 6.3 for the new $\chi_{3 \times 3}^2$.

VTPC hits can be used to separate photons from electrons. We use only hits of the VTPC instead of reconstructed tracks. The ‘‘VTPC hit occupancy’’ is defined by

$$R_{VTPC} \equiv \frac{N_{hits}}{N_{expected}},$$

where N_{hits} represents the number of sense wire hits in a cylindrical road of a radius of 5 mm between the event vertex and the cluster centroid. $N_{expected}$ is the number of expected hits. Since the active radius of the VTPC is 21 cm measured perpendicular to the beam axis, the road length changes from 40 cm to 100 cm depending on the polar angle, but $N_{expected}$ is around 22 and has only a slight dependence on θ . Figure 6.4 (a) shows an R_{VTPC} distribution for EM clusters with $E_T \geq 25 \text{ GeV}$ in the endplug region of $1.32 < |\eta_{det}| < 2.22$, where η_{det} is pseudorapidity of the particle assuming an event vertex at $z = 0 \text{ cm}$. Two peaks are clearly seen at $R_{VTPC} = 0$ and 1 corresponding to neutral and charged particles, presumably photons/neutral mesons and electrons. Events with R_{VTPC} between the two peaks are mostly expected to be neutral mesons

produced in jets, where charged particles with low energies partially overlap trajectories of the neutral mesons and are swept by the magnetic field. Such events can be reduced significantly by an isolation cut (see later in this section for a definition of isolation) on the EM cluster as shown in Fig. 6.4 (b). The VTPC is sufficiently capable of separating charged and neutral particles if they are isolated.

A cluster is required to be in the “fiducial region” of the PEM. The fiducial cut inhibits clusters of which seeds are in the following towers:

- Outer two and inner two annuli of the towers. The outer two annuli do not have full longitudinal coverage, and the inner two are not fully sensitive because of the chamber edges. Thus, the fiducial region corresponds to seed towers in $1.32 \leq |\eta_{det}| \leq 2.22$, where η_{det} is measured assuming the event vertex at $z = 0$ cm.
- Towers adjacent to the quadrant boundaries. They are the edges of the quadrant modules and not fully sensitive. This removes clusters of which seed towers are in 5° borders of the quadrants, corresponding to 2/18 of the entire φ coverage.
- Dead channels and their adjacent towers. Some electronics channels had problems, and some level 2 trigger channels were inhibited due to high noise rates. A cluster of which seed tower is in a bad tower or one of the eight adjacent towers is removed.
- Miscabled towers. As mentioned in the previous chapter, there were towers with cables incorrectly connected. Since the level 2 trigger tower is a sum of six or nine calorimetry towers, cable connections exchanged between these towers do not affect the level 2 trigger. Others affect the level 2 trigger, and an EM cluster is rejected if its seed is in such towers or their adjacent towers.

The fiducial cut reduces the geometrical acceptance in the PEM by 27%. Figure 6.1 presents the fiducial towers in the PEM.

There are two definitions of the “isolation” cut. They are

$$R^{iso}(\Delta r) \equiv \frac{E_T(\Delta r) - E_T^{EM}}{E_T^{EM}} \quad \text{and}$$

$$E_T^{iso}(\Delta r) \equiv E_T(\Delta r) - E_T^{EM} \cdot \left(1 + \frac{E^{had}}{E^{EM}}\right),$$

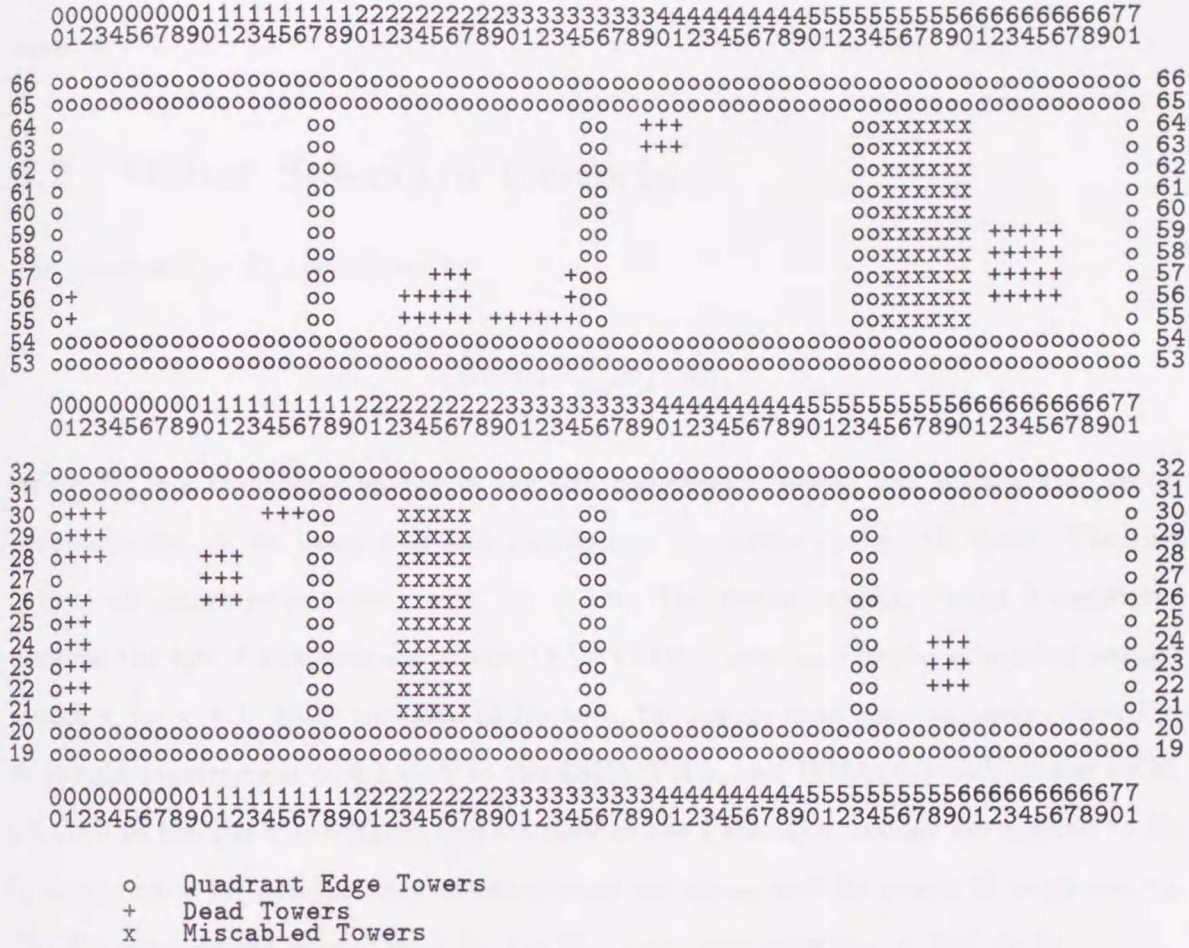


Figure 6.1: PEM fiducial region. Horizontal numbers represent φ towers, and vertical numbers are η in the TOWE numbering (Table 2.3). Blank spaces showing the “fiducial region” of the PEM.

where E_T^{EM} is the transverse energy of an EM cluster. $E_T(\Delta r)$ is a scalar sum of transverse energies of towers whose centers are within Δr from the cluster center. Δr is defined in the η - φ plane as $\Delta r^2 \equiv \Delta \eta^2 + \Delta \varphi^2$. $E_T(\Delta r)$ includes energies measured in both electromagnetic and hadron calorimeters. The former isolation cut is used for the W selection with $\Delta r = 0.4$, and the latter for the prompt photon selection with $\Delta r = 0.7$. The isolation cut reduces a good deal of background events, while only a few prompt photons or electrons from W decays. This is because, at high energies, the background events are mostly neutral mesons in jets or electrons from heavy quark (b or c-quark) decays, and such background mesons/electrons are produced with many other

particles nearby, while the signals are produced rather isolated due to their production natures.

6.2 Other Selection Criteria

The missing E_T (\cancel{E}_T) is defined by

$$\cancel{E}_T \equiv \left| - \sum_i E_T^i \cdot \vec{n}_i \right|,$$

where E_T^i is a transverse energy in the i -th calorimetry tower, and \vec{n}_i is a unit vector perpendicular to the beam axis and pointing at the center of the i -th tower. The sum is over all calorimetry towers with $|\eta| < 3.6$. The pseudorapidity range is restricted because the low- β quadrupoles of the TEVATRON cover part of the azimuthal regions for $3.6 < |\eta| < 4.2$. To be included in the sum, the towers must pass an energy (not E_T) threshold requirement of 0.1 GeV in the CEM, CHA, and WHA, 0.3 GeV in the PEM, 0.5 GeV in the PHA and FEM, and 0.8 GeV in the FHA. Corrections are applied to \cancel{E}_T to compensate for non-linearity of calorimeter responses and for punch through muons. The \cancel{E}_T requirement is only used for the $W \rightarrow e\nu$ event selection in this study.

In addition, the nonexistence of jets is required for the W selection, where jets are defined by the JETCLU algorithm.

The event vertex along the beam axis z_{vertex} is limited in a certain range.

There are three kinds of so called "bad runs" which are removed from the off-line reconstruction. Sources are

- Large \cancel{E}_T means or sigmas found from minimum bias data. This is due to large noise in some particular towers.
- Large number of PEM dead channels (> 30). In some runs, there were more than 30 electronic channels inoperative, and such runs are not used for the study.
- Problems with luminosity. Due to inefficiency of the BBC, luminosity was not properly obtained. Such runs are not used either.

“Spike” events are also removed. The spike is defined as an event with the energy deposit in a wire plane containing 30% or more of the total energy. The spikes come from discharge of the chamber or neutron absorption in gas. We do not use these events, though they are only a few and negligible.

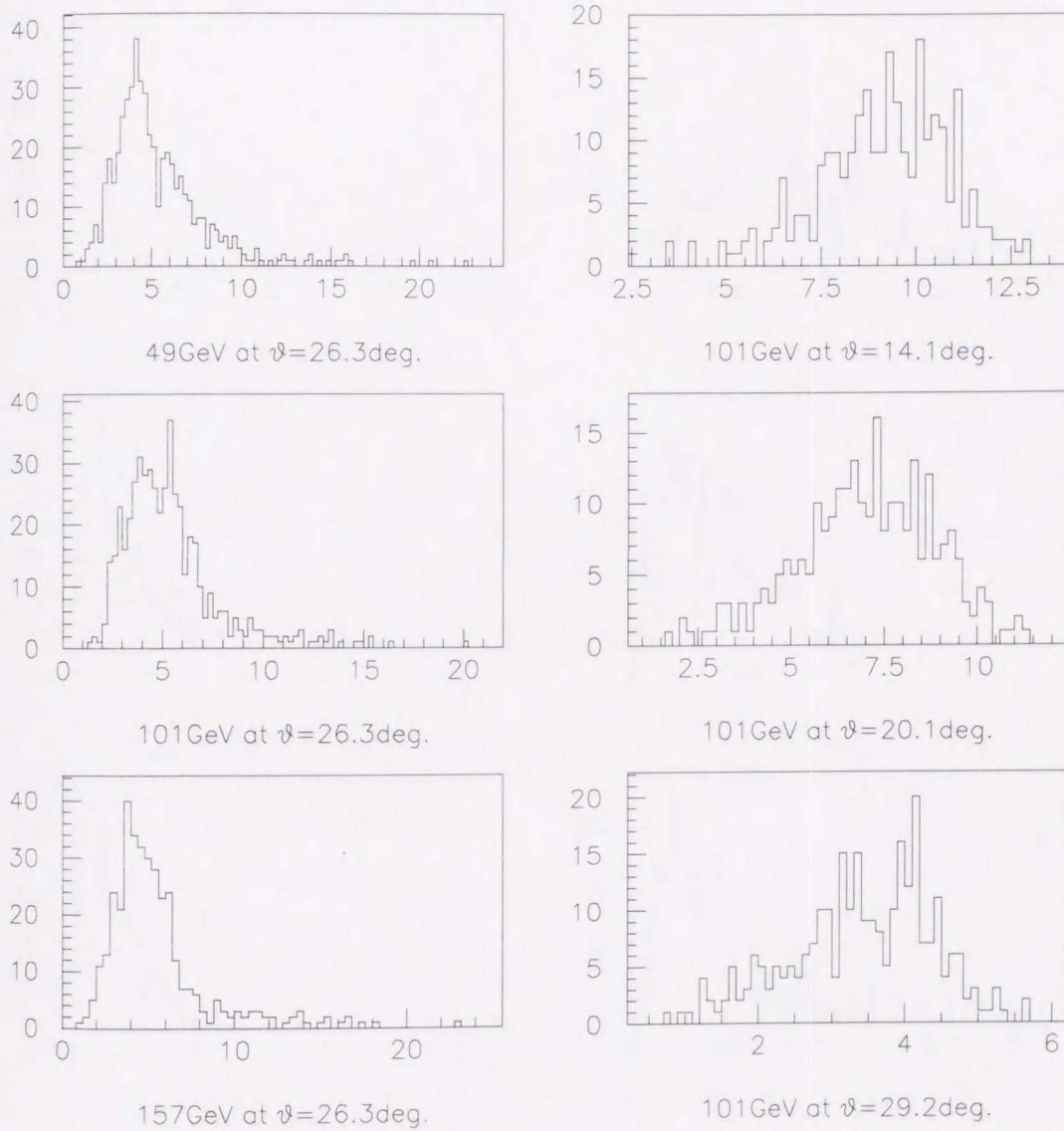


Figure 6.2: Distributions of $\chi^2_{3 \times 3}(\text{old})$ values for test beam electrons at various energies and incident angles. The incident angle is measured perpendicular to the PEM chambers.

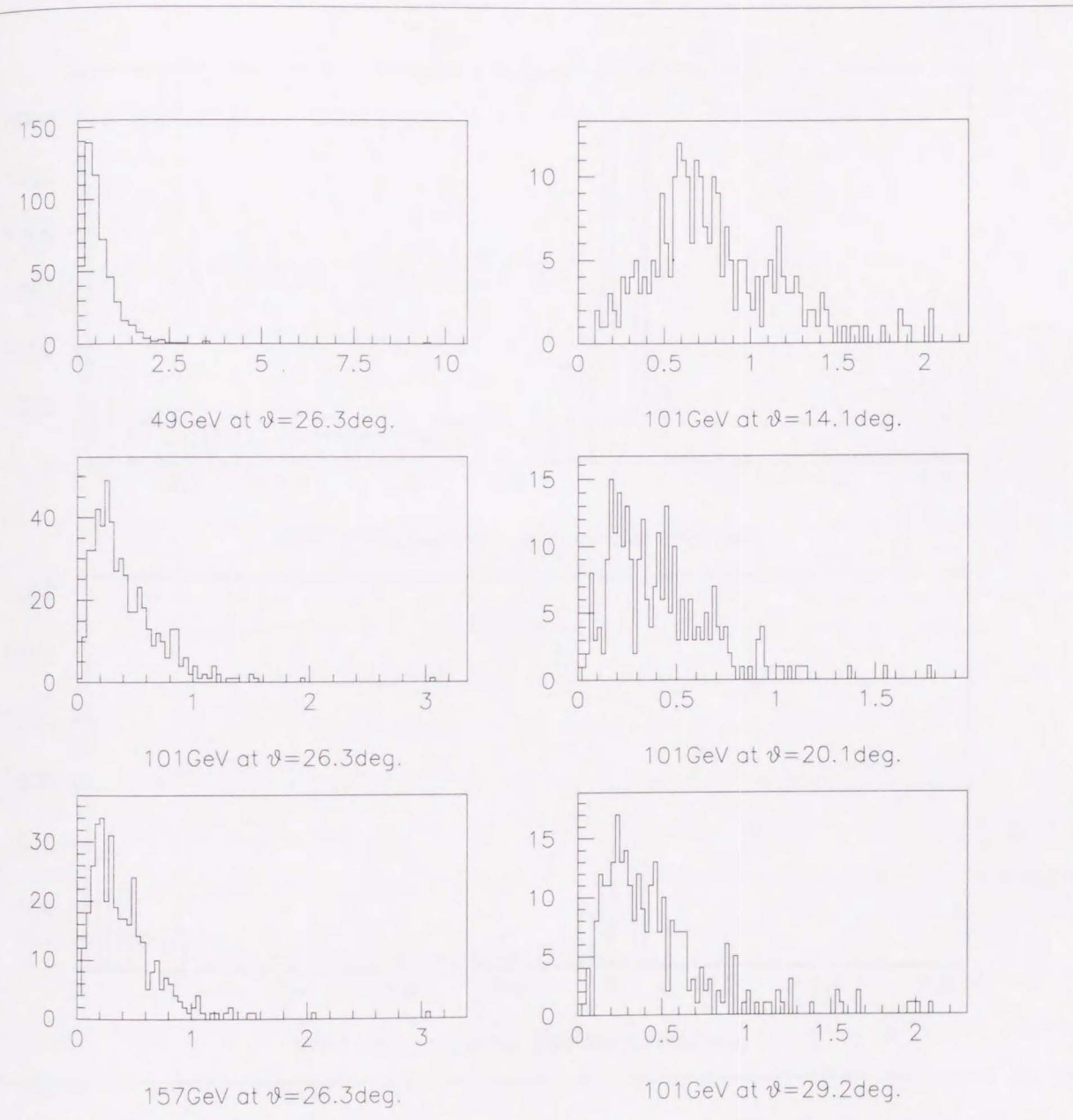


Figure 6.3: Distributions of $\chi^2_{3 \times 3}$ values for test beam electrons at various energies and incident angles. The incident angle is measured perpendicular to the PEM chambers.

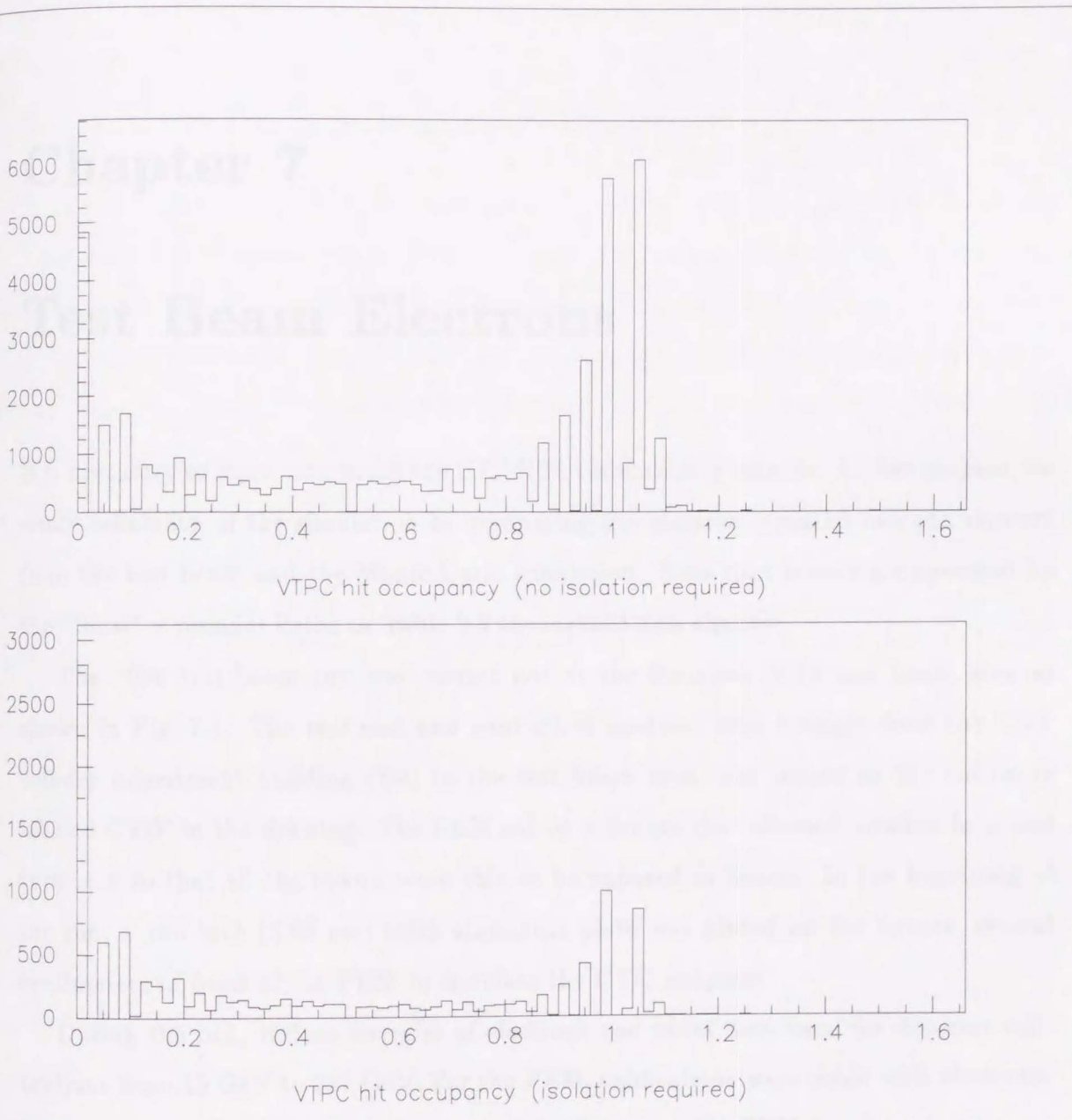


Figure 6.4: Distributions of VTPC hit occupancies for randomly sampled EM clusters with $E_T \geq 25$ GeV in $1.32 < |\eta_{det}| < 2.22$, where η_{det} is pseudorapidity measured from the event vertex assumed $z = 0$ cm. (a) with no isolation cut. (b) $E_T^{iso}(0.7) < 3$ GeV required. The peak at $R_{VTPC} = 1$ is considered electrons from heavy quark decays and reduced by limiting energies around the EM cluster. Events between the two peaks are also reduced significantly by the isolation cut compared to the peak at $R_{VTPC} = 0$.

Chapter 7

Test Beam Electrons

It is necessary to know how much the GEANT3 simulation is reliable. In this chapter, we study reliability of the simulation by comparing the electron-initiated cascade showers from the test beam and the Monte Carlo simulation. Note that towers are specified by the “local” η number listed in Table 2.3 throughout this chapter.

The 1990 test beam run was carried out at the Fermilab MT6 test beam area as shown in Fig. 7.1. The real east and west PEM modules were brought from the CDF collider experiment building (B0) to the test beam area, and placed in the enclosure labeled **CDF** in the drawing. The PEM sat on a fixture that allowed rotation in φ and turn in θ so that all the towers were able to be exposed to beams. In the beginning of the run, a two inch (5.08 cm) thick aluminum plate was placed on the fixture, several centimeters in front of the PEM to simulate the CTC endplate.

During the run, various energies of electrons and pions were used for detector calibrations from 15 GeV to 227 GeV. For the PEM, calibrations were made with electrons. Electrons with the energy of 101 GeV were incident at every PEM tower, and at least a hundred good events were collected to calibrate a tower to tower response variation. In addition, electrons with energies from 25 GeV to 175 GeV were incident at the standard towers ($\eta = 5$) for all eight quadrants. In this study, data of 101 GeV electrons incident at η towers 3, 5, 6, 8, and 12 are used as well as 48, 76, 101, 126, and 157 GeV at a standard tower. An energy of 101 GeV at the centers of η towers 3, 5, 6, 8, and 12 corresponds to the transverse energies of 49, 45, 41, 35, and 25 GeV. Energies of 48, 76,

126, and 157 GeV at the center of η tower 5 are equivalent to E_T of 21, 34, 56, and 70 GeV, respectively.

7.1 Two Inch Aluminum Plate

A two inch (5.08 cm) thick aluminum plate was placed in front of the PEM in the beginning of the test beam run. We have electron cascades for both conditions, with and without the aluminum. Figure 7.2 (a) shows the average longitudinal cascade measured by the anode wires for the “without the aluminum” condition, and Fig. 7.2 (b) is for the “with the aluminum.” For both conditions, 101 GeV electrons are incident at the center of η tower 8. Average showers by the GEANT3 simulation are also shown in both plots. In simulations, electrons with an energy of 101 GeV are generated at $(r,z)=(0,0)$, and the polar angle $\theta = 20.24^\circ$. The cylindrical aluminum blocks around the z axis (Fig. 4.1) are removed. The thickness of the aluminum plate parallel to the PEM is set to 0 (none), 3, and 8 cm.

Comparing (a) with (b), it is clearly seen that the average cascade with the aluminum plate rises up and falls off more quickly than that without the aluminum. The discrepancy between the test beam showers is well reproduced by the GEANT3 simulation except for additional 3 cm aluminum for both conditions. Aluminum of 3 cm thickness along the z axis is equivalent to $0.36 X_0$ at $\theta = 20.24^\circ$.

In the MT6 beamline, dipole magnets, MT5E-1 to MT5E-5, by which particles with a certain momentum are finally selected, are ~ 200 feet upstream the detectors as shown in Fig. 7.1. Between the dipole magnets and the detectors, particles traverse through the air as well as materials such as wire chambers and scintillation counters. Though total amount of materials is not exactly known, the additional material of $0.36 X_0$ can roughly be explained. The air of 200 feet or 60 meters is $0.20 X_0$ and considered to be dominant. Besides, scintillation counters with a thickness of ~ 3 cm, corresponding to $\sim 0.08 X_0^1$, are placed for the event trigger. In addition, there are five gas chambers, MT5SWDC2, MT6SWDC-1, MT6PWC-1, MT6SWDC-2, and MT6PWC-2 located in the beamline

¹Ordinary polystyrene scintillator has $X_0 = 42$ cm

between the dipole magnets and the CDF area. Gas or wires in the chambers are considered negligible, still vessels may not be ignored. It is practically impossible to sum up all the materials along the beamline, however, from this rough estimation, the material of $0.36 X_0$ suggested from the above comparisons is highly possible to exist.

The distributions of FSEF with and without the two inch aluminum plate are presented in Fig. 7.3 together with GEANT3 simulations. Although the test beam distributions are quite different between the two conditions (a) and (b), yet each Monte Carlo distribution shows good agreement with the data. From the above comparisons, the GEANT3 simulation is found to reasonably reproduce the electromagnetic cascade.

We have estimated the total amount of the materials between the dipole magnets and the PEM precisely. Electron cascades are simulated with the aluminum thickness scanned, then a likelihood is calculated for each simulation. The likelihood for the anode profile (Longitudinal Shower Development or LSD) is defined by

$$\chi_{LSD}^2 \equiv \frac{1}{\mu} \sum_{i=0}^{33} \frac{(E_i^{MC} - E_i^{tb})^2}{(5\% E_i^{tb})^2}, \quad (7.1)$$

where E_i^{tb} and E_i^{MC} are energy deposits in the i -th layer for the test beam and the simulation. μ is the number of degrees of freedom. The summation is taken from layer 0 to layer 33 except for two dead layers. 5% systematic uncertainty is assumed for the test beam energy measurement each layer. Statistical errors for both test beam and simulations are small enough to neglect.

Figure 7.4 (a) shows χ_{LSD}^2 values calculated by Eq. 7.1 for simulations with various thicknesses of the aluminum. Quadratic fits are made for both conditions, with and without the aluminum plate. From the fits, the most probable thickness, at which the GEANT3 simulation shows the best agreement with the test beam data, for the "without" condition is found to be 3.2 cm as aluminum, and 3.7 cm (or 8.8 cm including the real two inch aluminum) for the "with" condition. The total amount of the materials between the dipole magnets and the PEM is estimated $\sim 0.4 X_0$.

A likelihood for the FSEF distribution is also define by

$$\chi_{FSEF}^2 \equiv \frac{1}{\mu} \sum_i \frac{(N_i^{MC} - N_i^{tb})^2}{N_i^{MC^2} + N_i^{tb^2}}, \quad (7.2)$$

where N_i^{MC} and N_i^{tb} are the number of entries in the i -th bin, and summation is taken over all bins with finite entries. μ is the number of degrees of freedom. The χ_{FSEF}^2 is calculated and shown in Fig. 7.4 (b) together with quadratic fits to the values. The most probable thicknesses are found to be 3.4 cm and 3.8 cm for both runs, respectively. They correspond to $0.41 \pm 0.02 X_0$ and $0.46 \pm 0.02 X_0$, respectively. These are consistent with those estimated by the longitudinal shower profiles. The discrepancy of the most probable thicknesses suggests there is an ambiguity in the material thickness of $\sim 0.05 X_0$ from this estimation.

7.2 Energy Scan

Electromagnetic cascades for electrons with different energies are compared. Figure 7.5 shows the average longitudinal showers for 48, 76, 101, 126, and 157 GeV test beam electrons at the center of η tower 5 ($\theta = 26.40^\circ$). These energies correspond to 21, 34, 44, 56, and 70 GeV in E_T , respectively, and sufficiently cover the transverse energy range between 27 GeV and 40 GeV of the photon sample as described in Section 9.1. Simulations with the aluminum thickness of 8.1 cm show good agreements with the test beam for all energies. The shower curves show the energy dependence where the maximum changes with the incident energy as explained in Chapter 3.

Scanning the aluminum thickness in the simulation, the most probable thickness for each energy is obtained from a quadratic fit to χ_{LSD}^2 values as shown in Figs. 7.6 (a) to (e). Figure 7.6 (f) shows the most probable thicknesses ranging from 7.2 cm to 8.5 cm with a systematical energy dependence.

FSEF distributions for these electron cascades are also studied. They are shown in Figs. 7.7 (a) to (e) together with simulations. The distributions for lower energy electrons are broader and have large means. Simulations with the aluminum of 8.1 cm are consistent with the test beam.

The most probable thickness is each estimated again by fitting χ_{FSEF}^2 values with a quadratic function as shown in Fig. 7.8. It systematically changes from 8.4 cm to 8.0 cm with the energy and shown in Fig. 7.8 (f).

Including the energy dependence, the uncertainty of the GEANT3 simulation is es-

estimated to be $\sim 0.05 X_0$.

7.3 Position Scan

Electromagnetic showers at different towers are also studied. A different tower means a different incident angle since the CDF calorimeters have the projective tower geometry. Besides, a particle incident at a different tower corresponds to one traversing a different length both in total and individual layers. The maximum of the average longitudinal cascade appears in deeper layers for smaller θ as shown in Fig. 7.9. It shows average longitudinal cascades for 101 GeV test beam electrons incident at η towers 3, 6, and 12 ($\theta=29.29$, 24.13 , and 14.20°) together with simulations. The GEANT3 simulation shows excellent agreements with the test beam data except for the last several layers of the η tower 3 profile. At this large θ , part of the cascade spreads outside fully sensitive regions, especially in the last layers. As seen in Fig. 2.9, the outer neighboring tower does not have the complete coverage in depth. The PEM chambers in the GEANT3 simulation do not have such precise structure to reproduce this quick fall. Though a sum of energies in the last five layers for the test beam is $\sim 2/3$ of the simulation; still, the difference to the total energy becomes only 0.6%.

Test beam mapping data is used in this η position dependence study. The test beam mapping data is a set of runs in which 101 GeV/c electrons are incident at the center of every calorimetry (local) tower in the PEM. A hundred good events per tower are collected over all the towers in the fiducial region², where there are $11(\eta) \times 16(\varphi)$ calorimetry towers per quadrant, or 128 equivalent η towers for both east and west PEM modules. However, the data file of a run in which $\varphi = 69$ towers of the east PEM are scanned has been lost, accordingly data for 127 equivalent η towers are used for the study.

An average shower profile in Fig. 7.9 is obtained essentially by averaging cascades for 100 electrons \times 127 towers except for dead layers. Before we go forth, the tower to tower uniformity in the response of the pad first segment is estimated as well as the absolute

²There were no dead channels in the test beam runs.

energy scale for the pad first segment of the calorimeter. The former is expected to broaden the FSEF distribution, and the latter shifts it.

7.3.1 Absolute Energy Scale

It is considered that the irregularity in the pad response of the PEM comes from a variation of their capacitances rather than the amplifier gain since the gain is calibrated to a tolerance of 1% by the charge injection. Correction factors, known as the “response map,” have been obtained to keep responses uniform. This calibration, however, has been done only to the total response of all the three depth segments, and it is not certain if the first segment response is well calibrated.

It is impossible to determine the absolute energy scale only for the pad first segment directly with high energy electron induced cascades since the first segment *sees* only part of the incident energy (Fig. 7.10). Thus, the anode response is employed as a standard response to calibrate the energy scale for the pad first segment because of a small variation. Figure 7.11 shows deviations in anode responses to 101 GeV electrons. The deviation is defined by

$$d_i \equiv \frac{E_i^{tb} - E_i^{MC}}{E_i^{MC}} \quad (i : \text{layer number} = 0, 33),$$

where E_i^{tb} and E_i^{MC} are average anode responses in the i -th layer to 101 GeV electrons for the test beam and the GEANT3 simulation. The average is taken over 127 same η towers and 100 electrons each tower for the test beam, and 2000 electrons for the simulation. Monte Carlo shower profiles are only employed here as smooth profiles. A layer to layer variation is found to be $\sim 3\%$ with almost no particular trend, and we assume the uniformity in the anode response to be $2.7 \pm 0.5\%$. It is equivalent to the fact that the energy measured by the first 5 layers of the anode, corresponding to the first segment of the pad, is calibrated with an uncertainty of $1.2 \pm 0.2\%$.

The pad energy scale is then calibrated by the ratio of energies measured in the pad and the anode. Figure 7.12 shows the pad to anode ratios for (a) the total energy and (b) the first segment energy. Once the pad to anode ratio for all the three depth segments is scaled to unity as in Fig. 7.12 (a), the mean in (b) represents the absolute

energy scale for the first segment.

We have calculated the absolute energy scale for each tower η and listed in Table 7.1. An energy dependence is found for the absolute energy scale on the size of the cathode pad.

7.3.2 Non-uniformity

The width of the distribution in Fig. 7.12 (b) comes from variations of the pad and anode responses. However, we only need the variation or the uniformity in the response for the pad. Figure 7.13 (a) shows the response in the first segment of a tower to 101 GeV electrons. The distribution of energy deposits comes only from shower fluctuations. Averaging responses for 100 events, we obtain a mean energy deposit in the first segment for a tower. Such mean deposits are plotted for all 127 same η towers in (b). One thing should be noted that the mean energy deposit in the first segment varies with respect to the tower η , and one cannot plot mean energy deposits for different η towers.

The width in Fig. 7.13 (b) represents the uniformity for η tower 8, still containing shower fluctuations of the order of $\sim 3\%$, though. (c) and (d) are the standard deviations and the variances. From these distributions, the uniformity and its statistical uncertainty are estimated and listed in Table 7.1. Detailed formulation is found in Appendix A. The uniformity seems to have a slight η dependence. Ignoring it, the overall uniformity is calculated $9.5 \pm 1.1\%$, where the error is taken as the standard deviation of the uniformities. Hence, we determine the uniformity of the pad first segment to be $10 \pm 1\%$. The absolute energy scale and the uniformity are applied to the GEANT3 simulation.

7.3.3 Comparisons

χ^2_{LSD} values calculated for average showers at towers 3, 5, 6, 8, and 12 ($\theta = 29.29, 26.24, 24.13, 20.24, \text{ and } 14.20^\circ$, respectively) are represented in Fig. 7.14 together with quadratic fits. A reduced uncertainty of 3% in the energy measurement is assumed each layer for the χ^2_{LSD} calculation since a layer to layer irregularity is relatively small as seen in Fig. 7.9 due to the averaging over towers in different φ . In addition, layers 29 to 33 are not used for tower 3. The most probable thicknesses obtained by the quadratic

η	Energy Scale	Uniformity [%]
3	1.000 \pm 0.012	7.96 \pm 0.07
4	1.000	0.012
5	1.005	0.012
6	1.019	0.012
7	1.024	0.012
8	1.028	0.012
9	1.030	0.012
10	1.049	0.013
11	1.051	0.013
12	1.050	0.013
13	1.041	0.012

Table 7.1: Absolute energy scale and uniformity for the first segment of the PEM pad.

fits are summarized in Fig. 7.14 (f). A variation for η scan is smaller than that for the energy scan. The pass length in the aluminum plate of a particle is proportional to $1/\cos\theta$. For an aluminum plate with a thickness of 8.00 cm measured perpendicular to the surface or along the z axis, the pass length or “substantial thickness” becomes 8.25 cm at $\theta = 14.20^\circ$ or 9.17 cm at $\theta = 29.29^\circ$. Considering this fact, a variation in the estimations of the total amount of materials between the dipole magnets and the PEM is rather smaller. Discussions will appear later in the next section.

FSEF distributions for the η position scan are shown in Fig. 7.15 together with the simulation. As regards dead layers in the test beam data, an expected energy deposit in a dead layer is estimated essentially by interpolation with individual wire profile, calculated as the mean of energies in the front and back layers, and this correction is made on an event by event basis. However, another dead layer correction is applied for a quadrant with three or four (depending on the run) dead layers in the last five wire chambers. In this case, multiplicative correction factors are calculated from the average shower profile of 100 GeV electrons for each η tower. The first segment energy and the total energy are individually corrected. Figure 7.16 (a) to (e) show χ_{FSEF}^2 values for η towers 3, 5, 6, 8, and 12 together with quadratic fits to them. The most probable thickness is plotted against η in Fig. 7.16 (f), and it shows only a small variation.

7.4 Uncertainty of the GEANT3 Simulation

The total amount of materials along the beamline between the MT5 dipole magnets and the PEM has been estimated for the energy scan and the η position scan, and the estimations are summarized in Fig. 7.17. Changes in the substantial thickness of the aluminum plate with respect to θ are taken into account. The estimations from the average profiles are all smaller than the corresponding estimations from the FSEF distributions. We take the average over these 20 estimations weighted by the uncertainties, and the total amount of materials is estimated to be $0.382 \pm 0.046 X_0$, where the error is taken as the RMS value of the 20 estimations. Since the electron energies and positions sufficiently cover the ranges of our interest, the error of $\pm 0.046 X_0$ can be considered as an uncertainty for the GEANT3 simulation regardless of a systematic dependence of the cascade on energy. However, it should be overestimated because it is calculated using a larger energy range than that of prompt photon candidates.

At the center of the PEM, $\eta = 1.77$ or $\theta = 19.3^\circ$, $0.046 X_0$ corresponds to 0.39 cm thick aluminum. In practice, we regard the uncertainty for the GEANT3 simulation as changes of the shower shape when the thickness of the aluminum plate is varied by ± 0.39 cm.

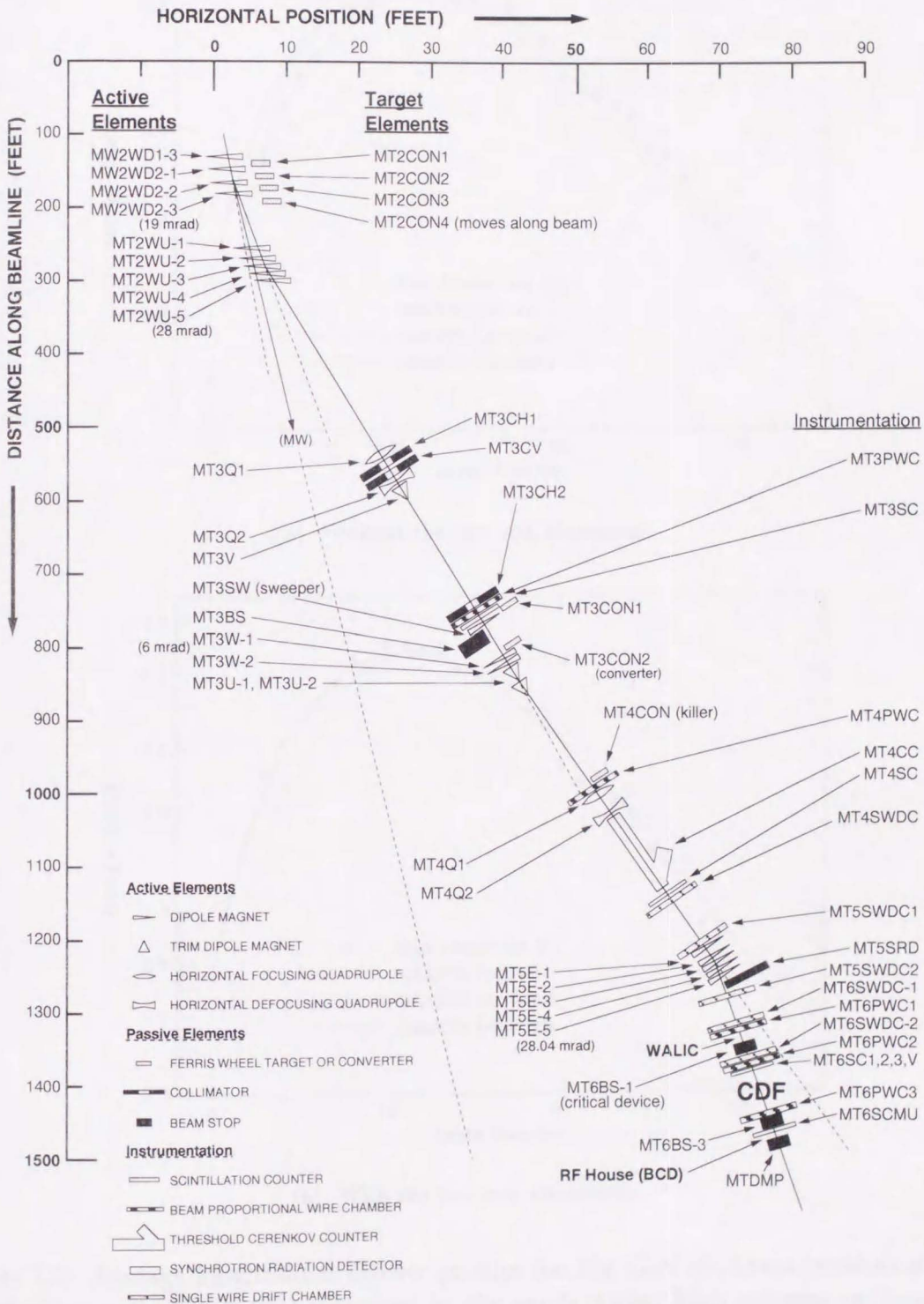
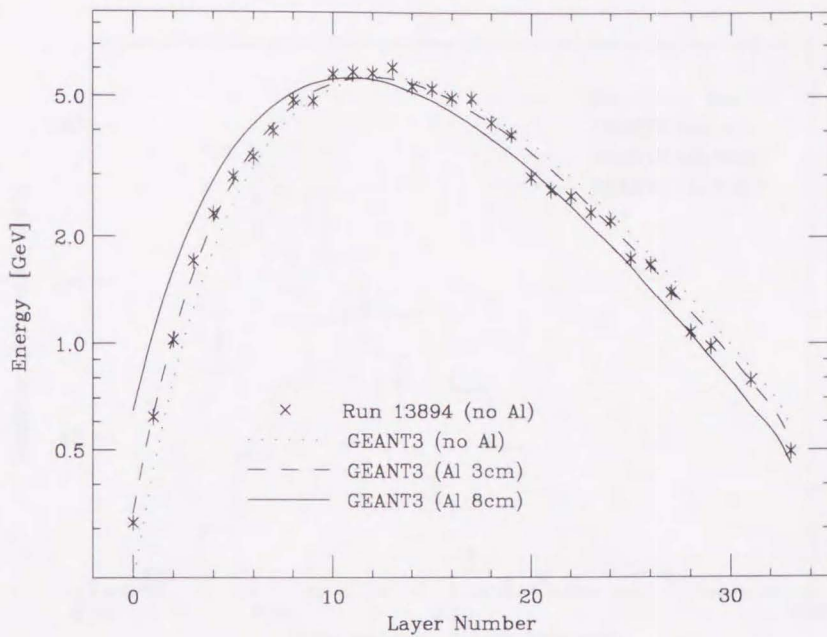
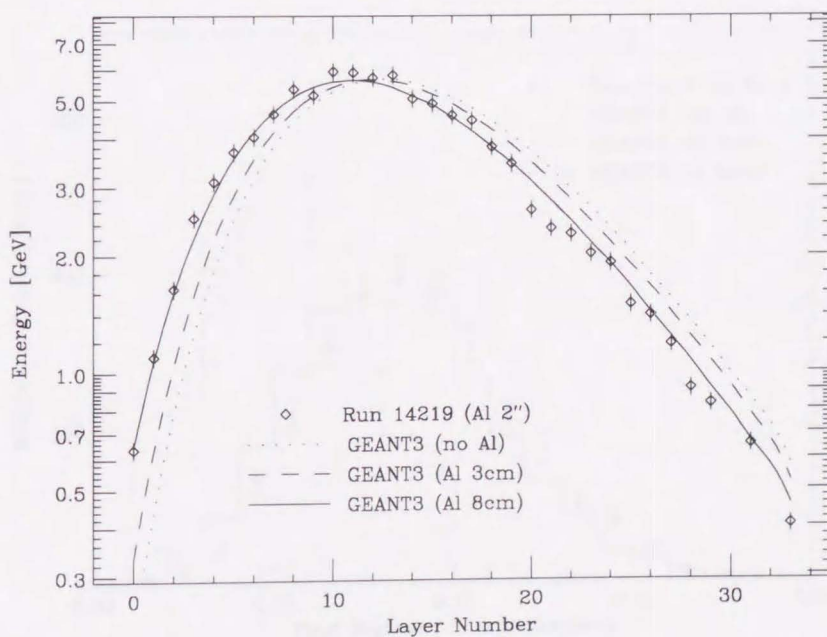


Figure 7.1: MT6 beamline.

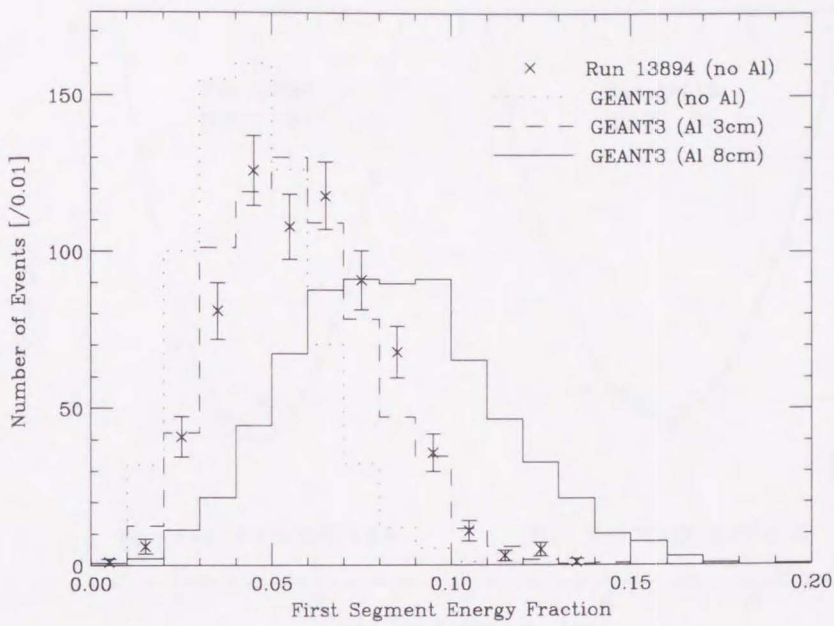


(a) Without the two inch aluminum.

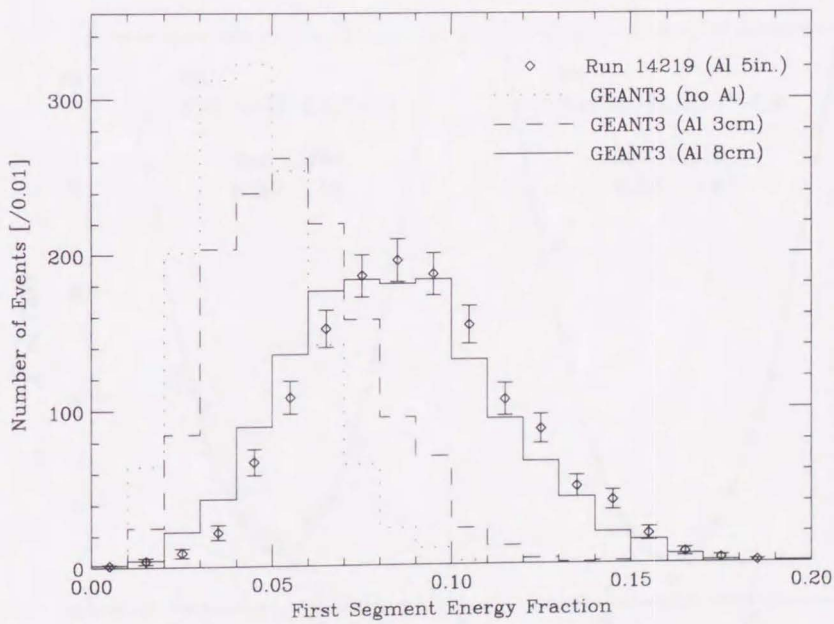


(b) With the two inch aluminum.

Figure 7.2: Average longitudinal shower profiles for 101 GeV electrons incident at the center of tower 8 ($\theta = 20.24^\circ$) measured by the anode wires. High voltages on layers 30 and 32 are off and removed from the plots. An uncertainty is assumed 5% for the data each layer; statistical errors are negligible.



(a) Without the two inch aluminum.



(b) With the two inch aluminum.

Figure 7.3: FSEF distributions for 101 GeV electrons incident at the center of tower 8 ($\theta = 20.24^\circ$). Errors for the test beam are statistical only. 2000 electrons are simulated under each condition, and the number of events is normalized to the test beam data.

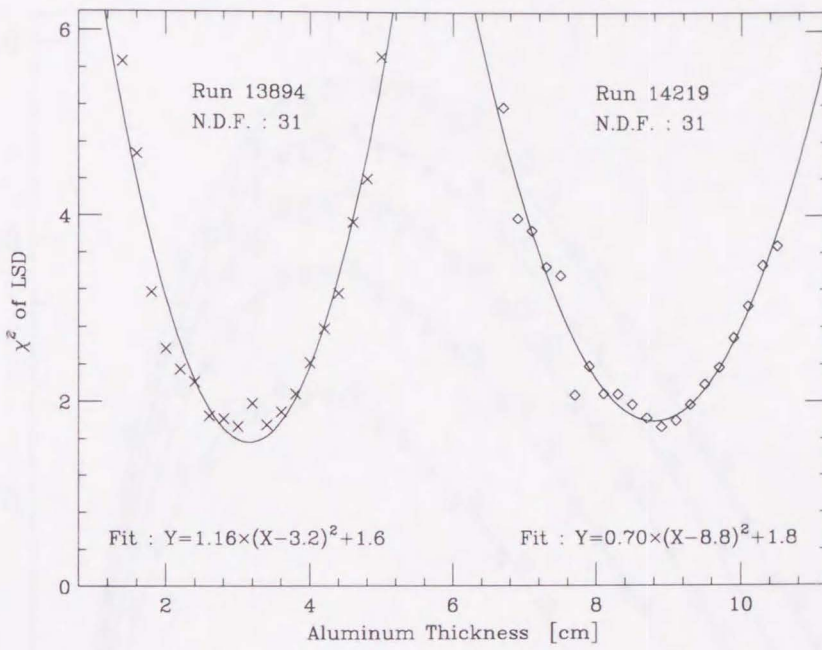
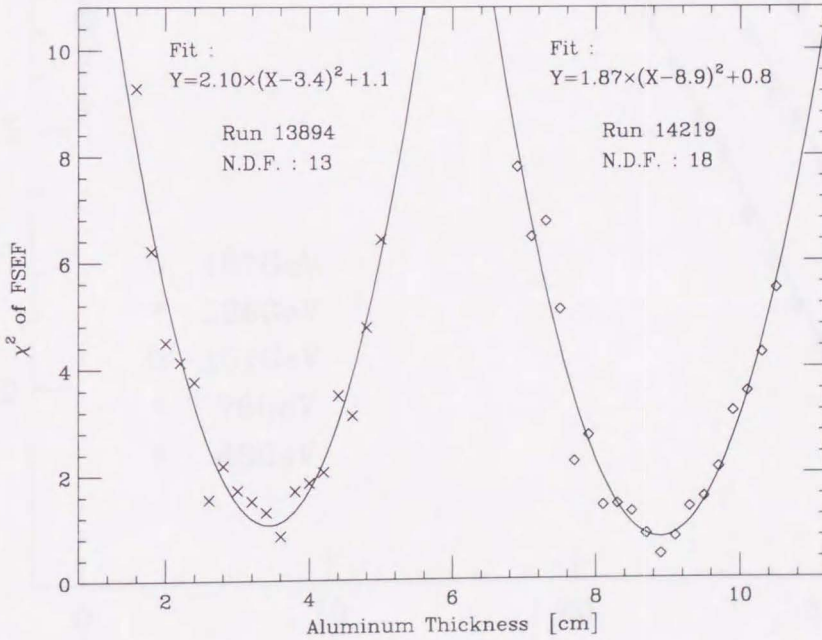
(a) χ_{LSD}^2 (b) χ_{FSEF}^2

Figure 7.4: χ_{LSD}^2 and χ_{FSEF}^2 with respect to aluminum thickness in the GEANT3 simulation. 2000 electrons simulated at each thickness.

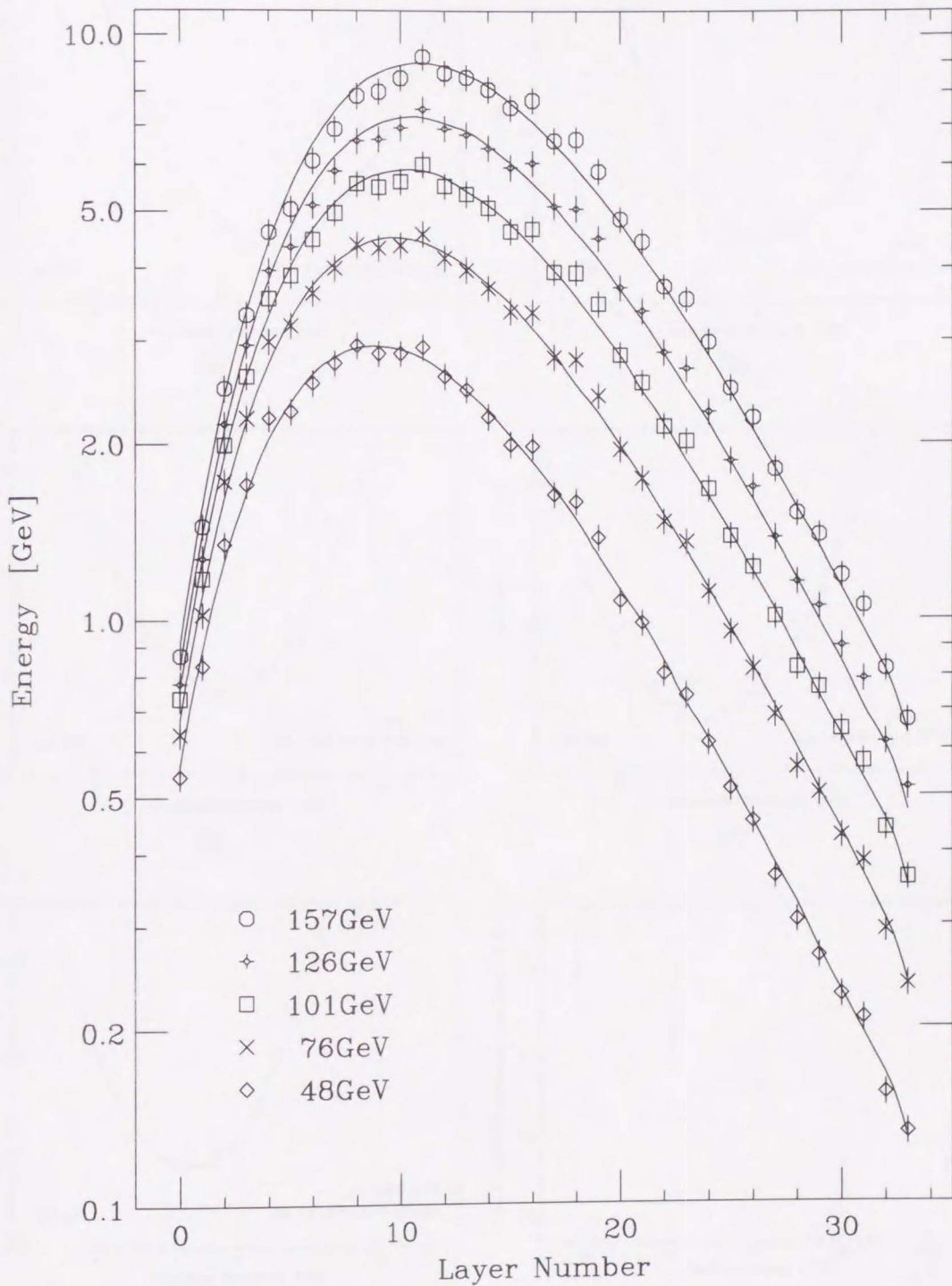
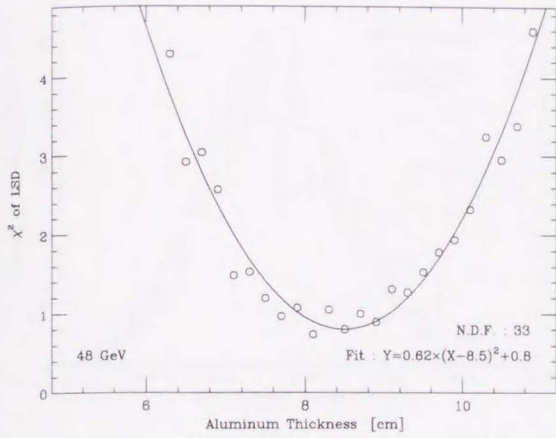
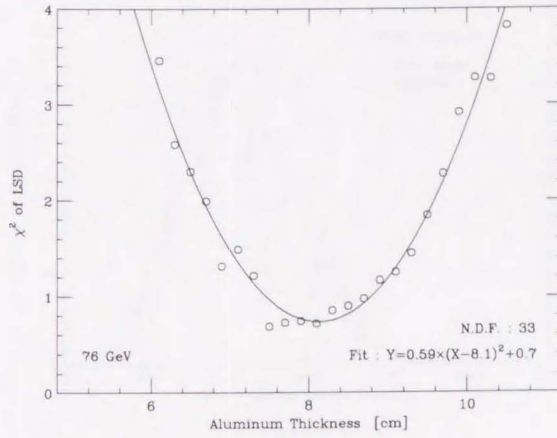


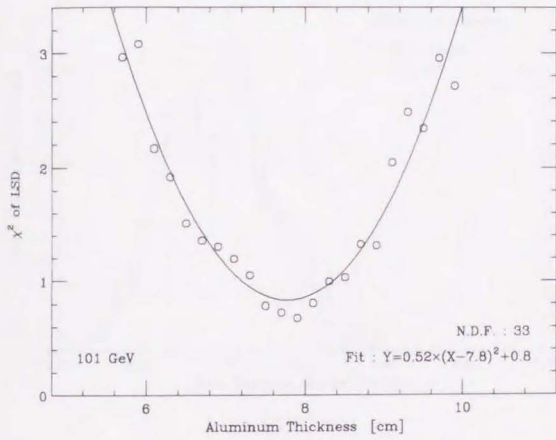
Figure 7.5: Average longitudinal showers for electrons with transverse energies 48, 76, 101, 126, and 157 GeV incident at the center of η tower 5 ($\theta = 26.40^\circ$). The symbols represent the test beam, and curves are the simulations. A uncertainty is assumed 5% for the test beam each layer. The aluminum thickness in the GEANT3 simulation is 8.1 cm.



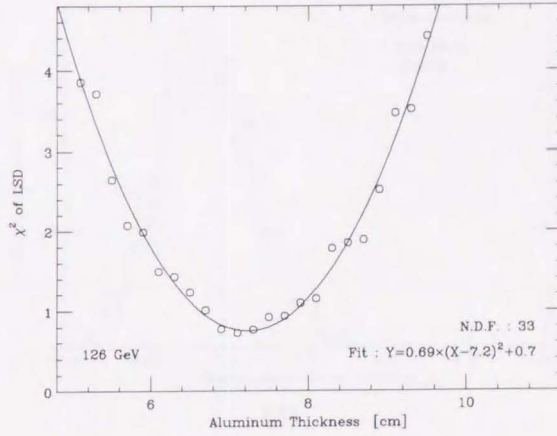
(a)



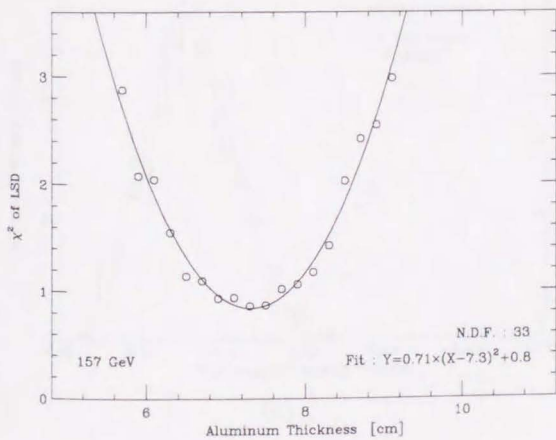
(b)



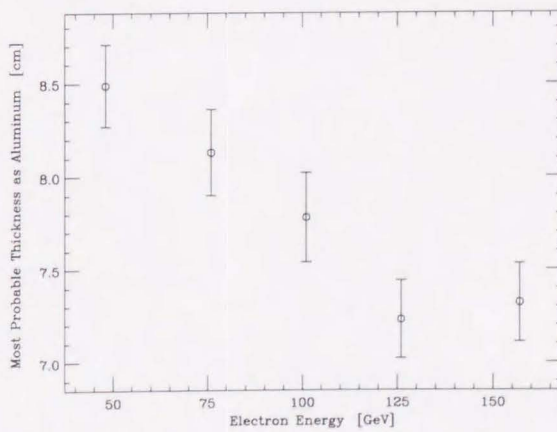
(c)



(d)

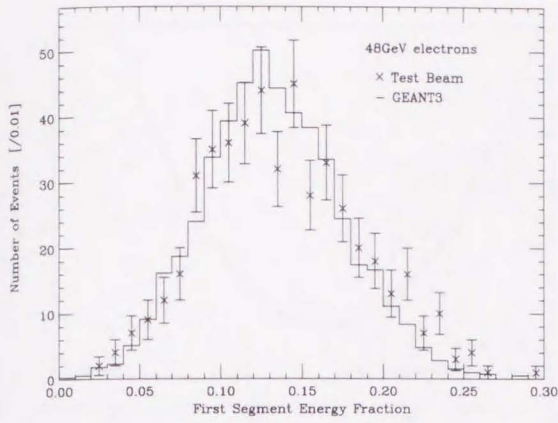


(e)

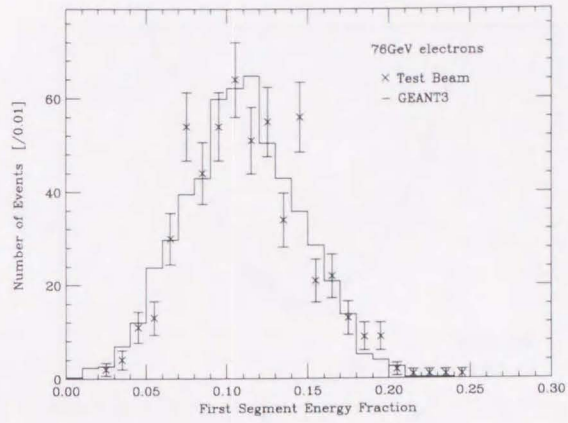


(f)

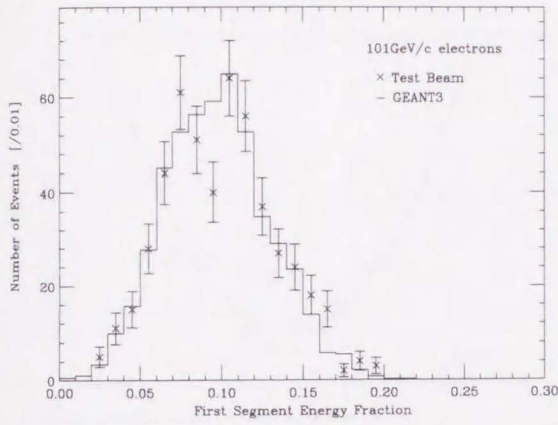
Figure 7.6: (a) - (e) χ^2_{LSD} shown as circles and quadratic fits. (f) Most probable thicknesses from the fits.



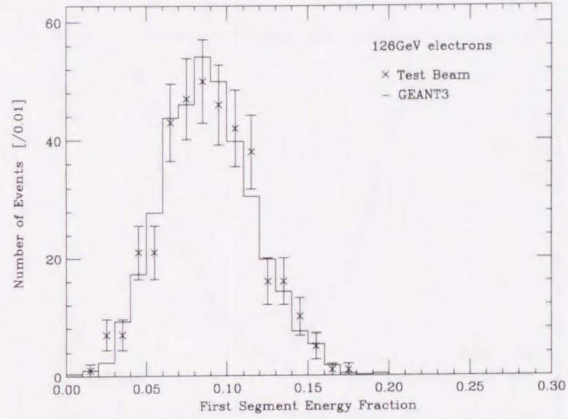
(a)



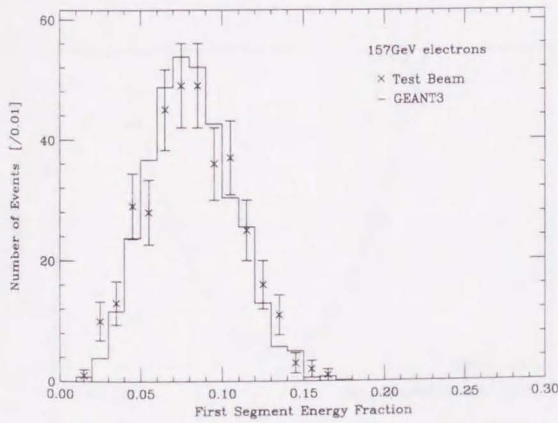
(b)



(c)

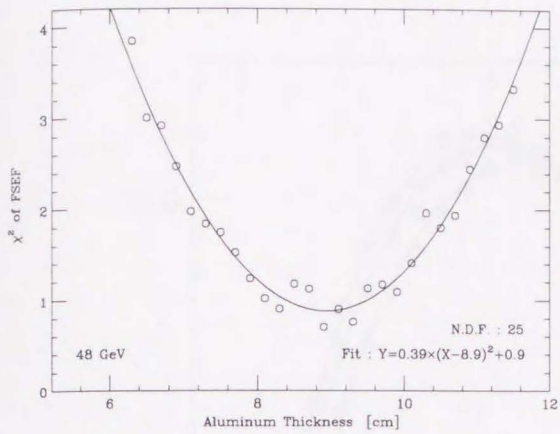


(d)

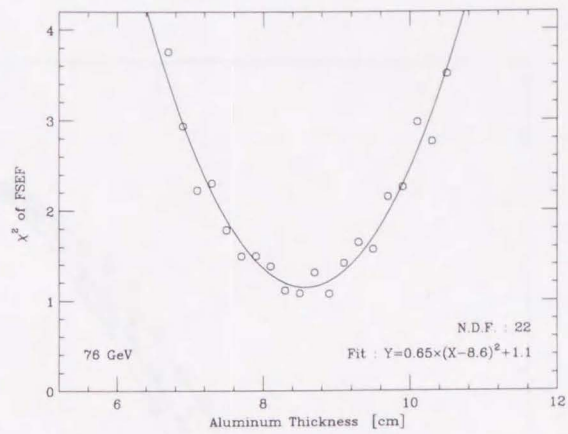


(e)

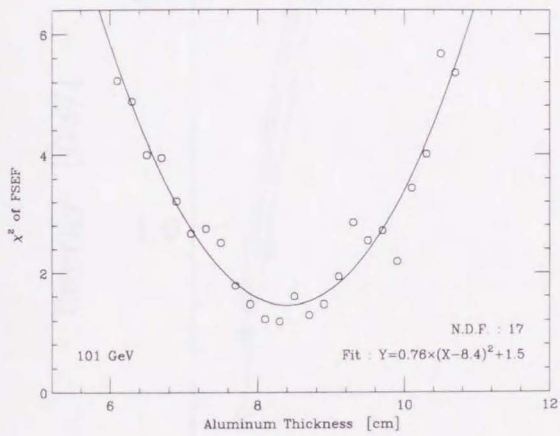
Figure 7.7: Distributions of FSEF for electrons with energies 48, 76, 101, 126, and 157 GeV at the center of η tower 5 ($\theta = 26.40^\circ$). Test beam electrons are shown as crosses, and the histograms are the simulations. The aluminum thickness in the GEANT3 simulation is 8.1 cm.



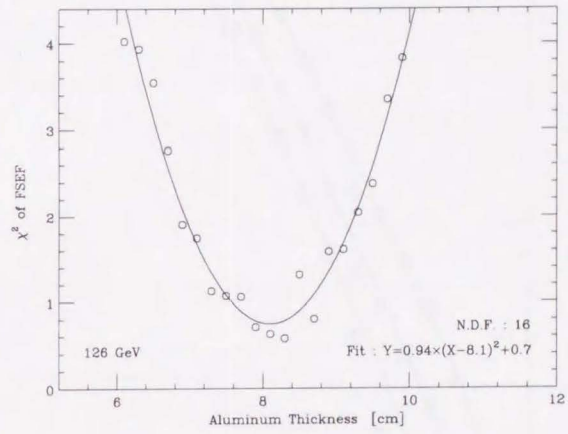
(a)



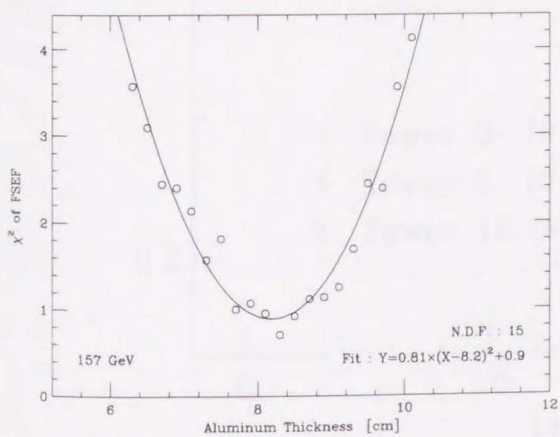
(b)



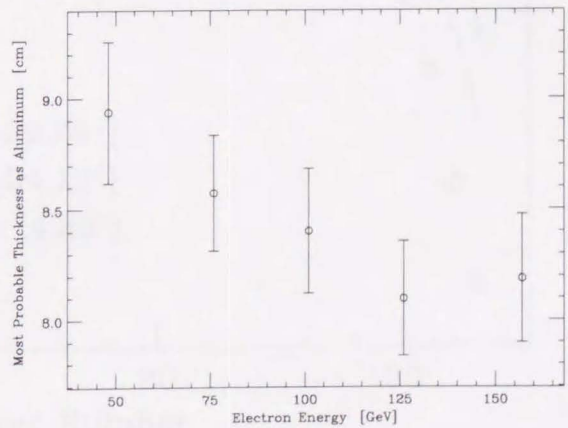
(c)



(d)



(e)



(f)

Figure 7.8: (a) - (e) χ^2_{FSEF} shown as circles and quadratic fits. (f) Most probable thicknesses from the fits.

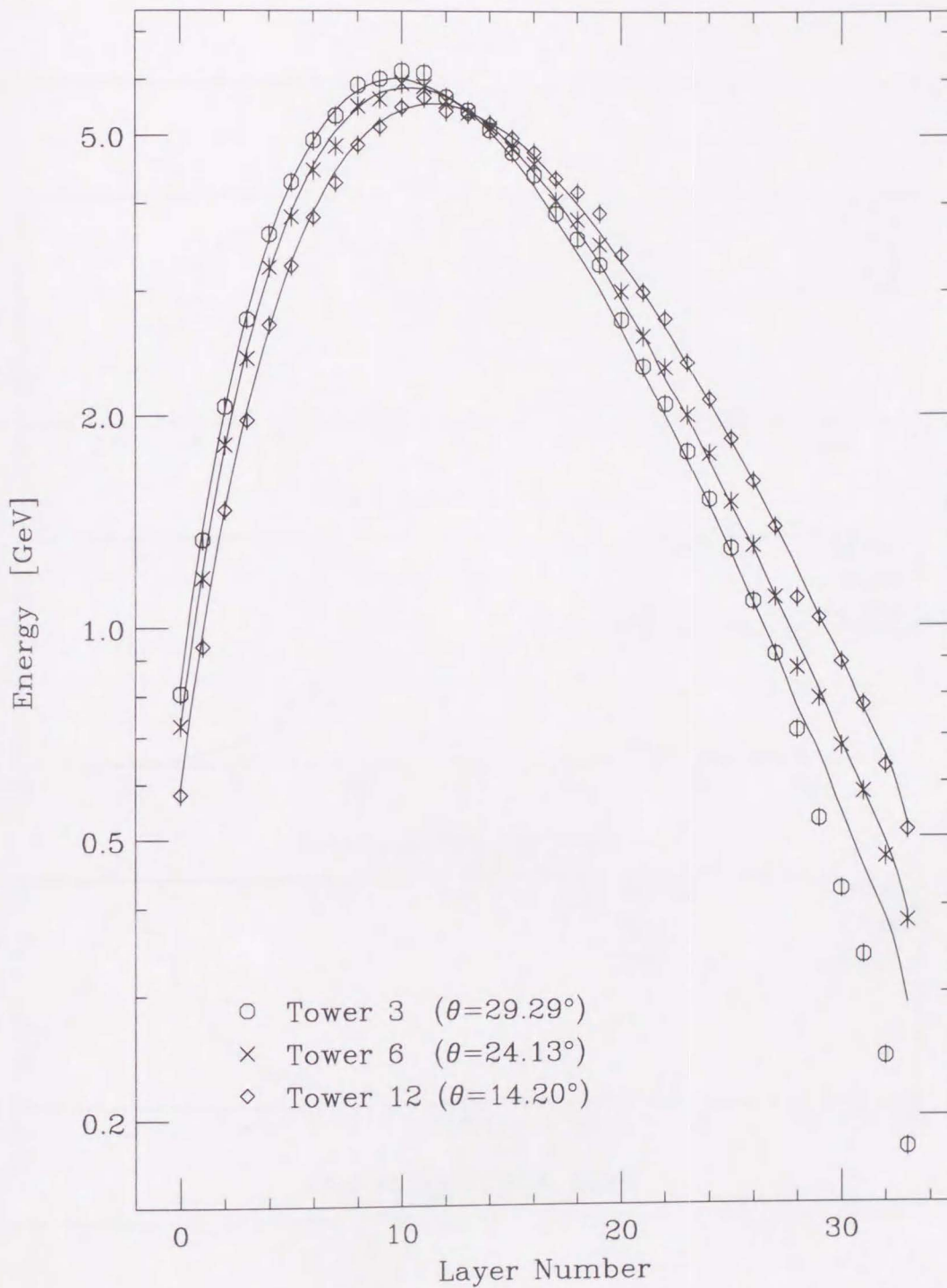


Figure 7.9: Average longitudinal showers for 101 GeV/c electrons incident at the centers of η towers 3, 6, and 12 ($\theta = 29.29, 24.13, \text{ and } 14.20^\circ$). The symbols represent the test beam, and curves are simulations. An uncertainty is assumed 3% for the test beam data each layer. Dead layers are excluded from averaging. The aluminum thickness in the GEANT3 simulation is 8.1 cm.

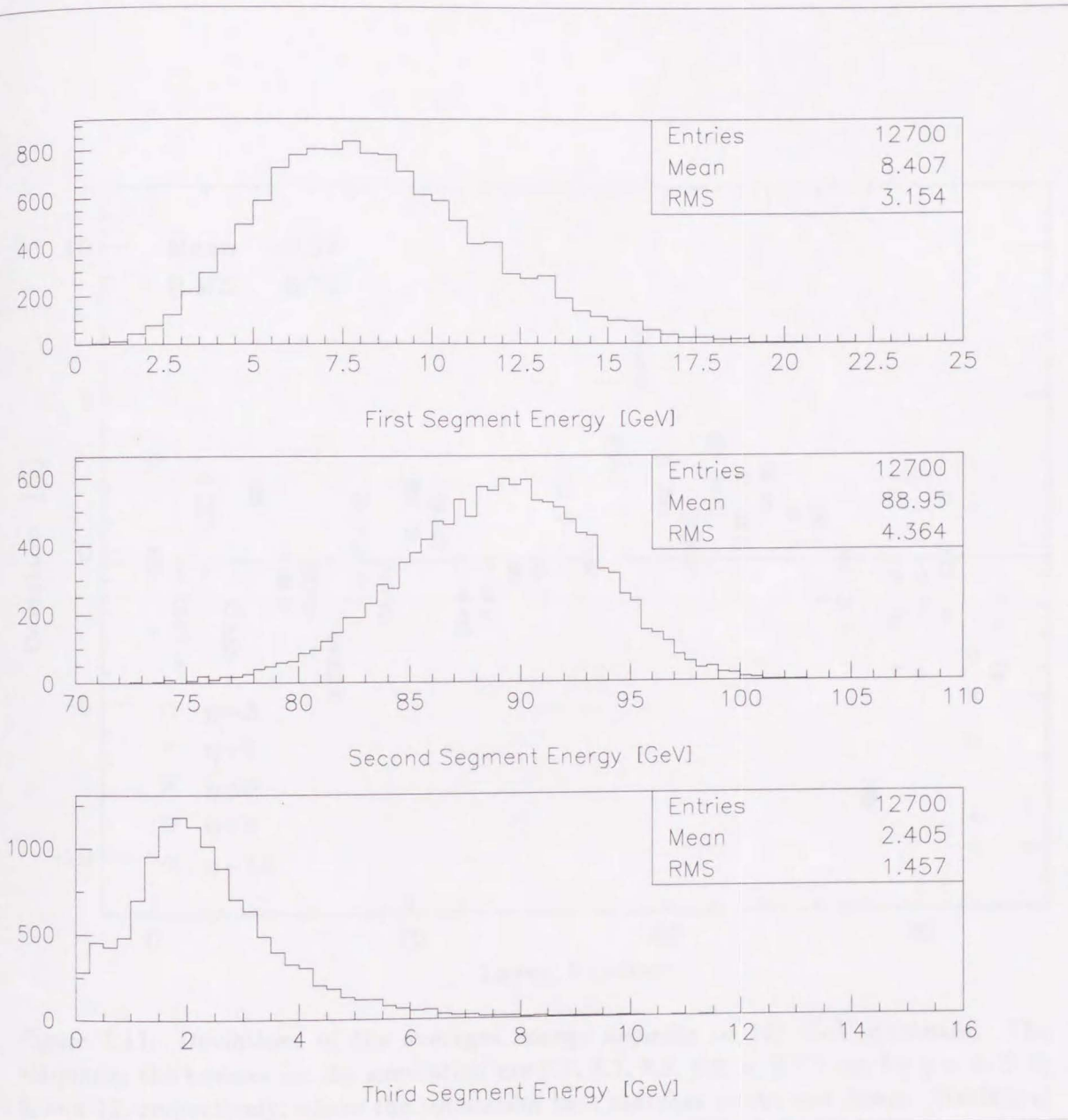


Figure 7.10: Energy deposits in the pad segments to 101 GeV test beam electrons at the center of η 8. No dead layer correction is applied.

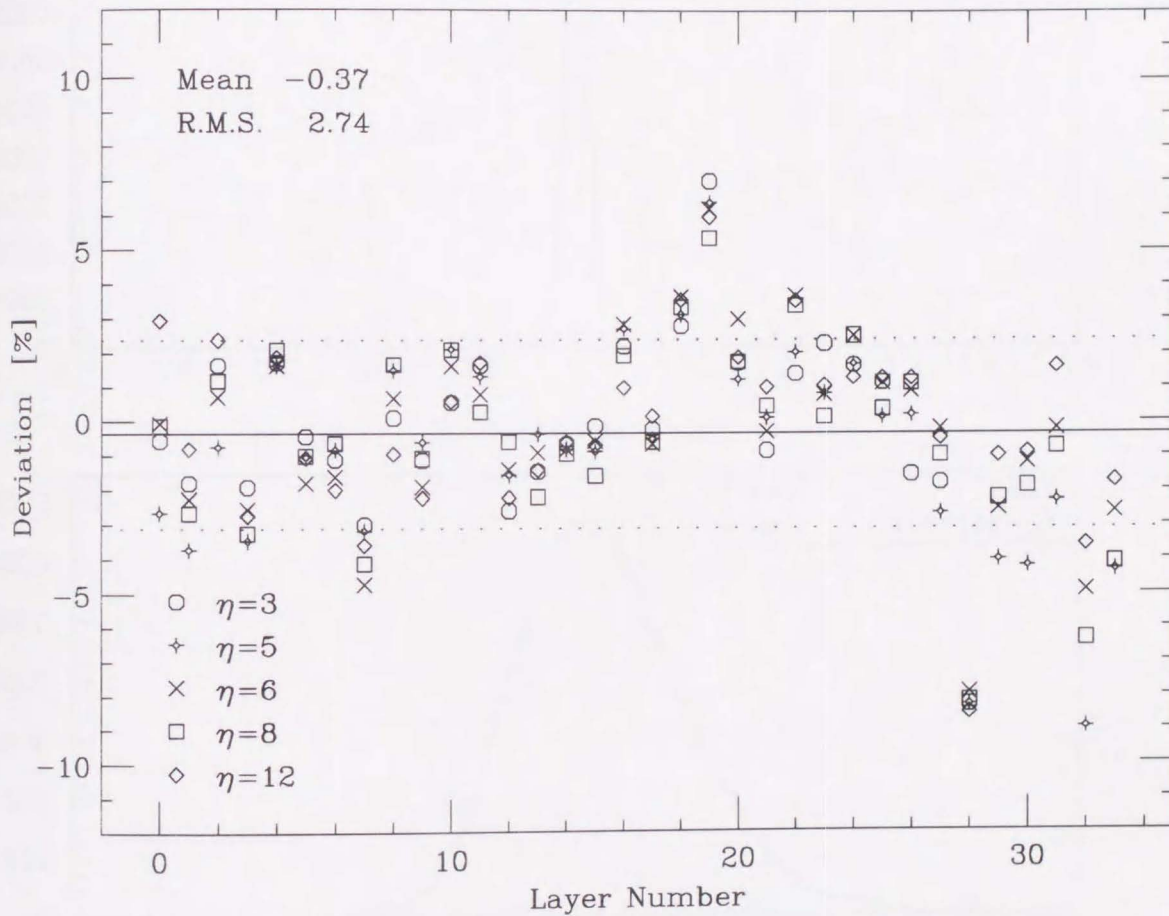


Figure 7.11: Deviations of the averages energy deposits to 101 GeV electrons. The aluminum thicknesses for the simulation are 7.7, 8.1, 8.1, 8.3, and 7.7 cm for $\eta = 3, 5, 6, 8,$ and 12 , respectively, where the simulation best matches to the test beam. Statistical uncertainties are negligible for both test beam data and Monte Carlo.

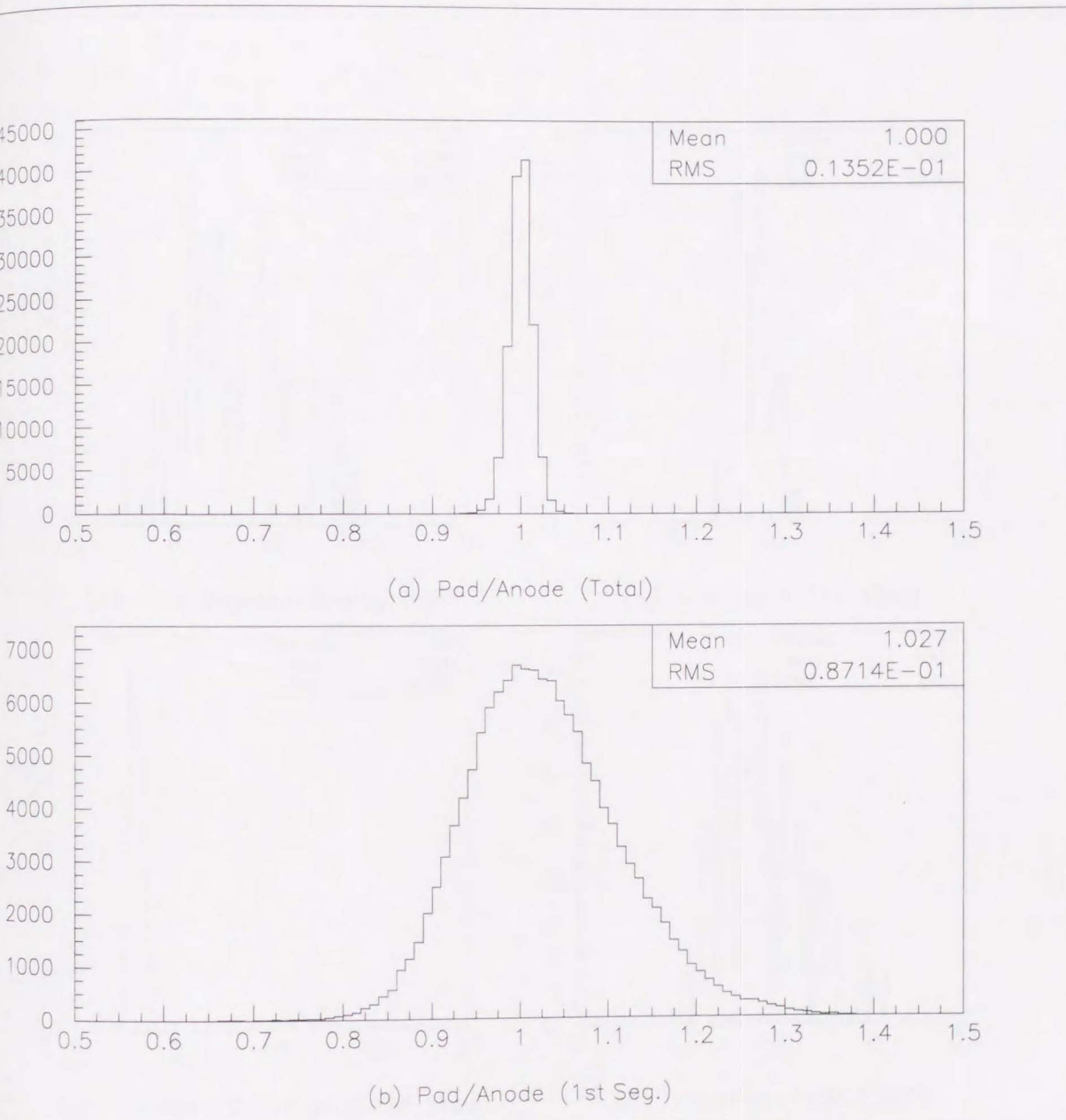
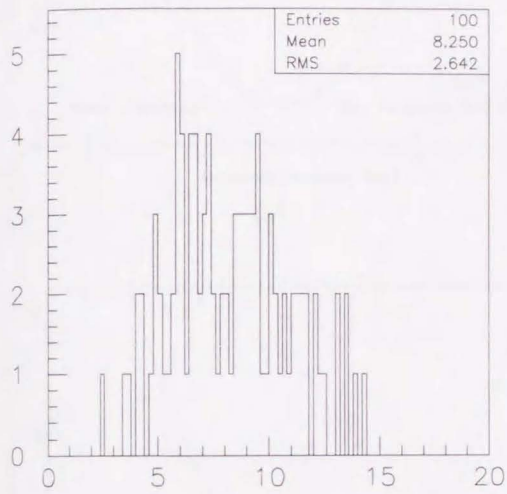
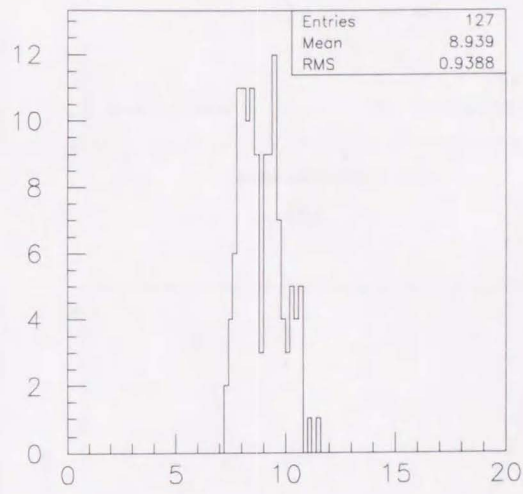


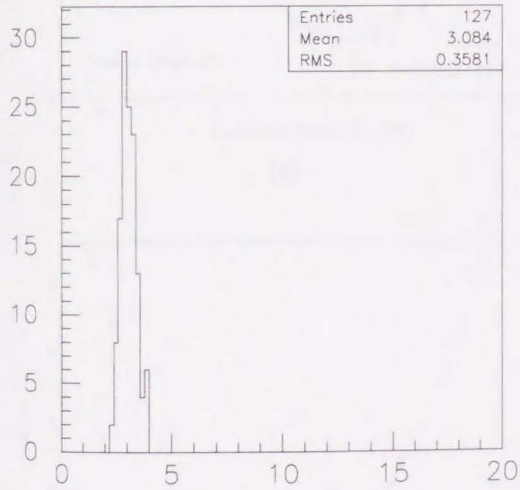
Figure 7.12: Ratios of energies measured by the pad and the anode for (a) the sum of all the three depth segments (all 34 layers) and (b) the first segment (first 5 layers). 101 GeV electrons at all the PEM towers in the fiducial region. 100 events collected from each tower.



(a) First Segment Energy [GeV]



(b) Average of FSE [GeV]



(c) Standard Deviation of FSE [GeV]

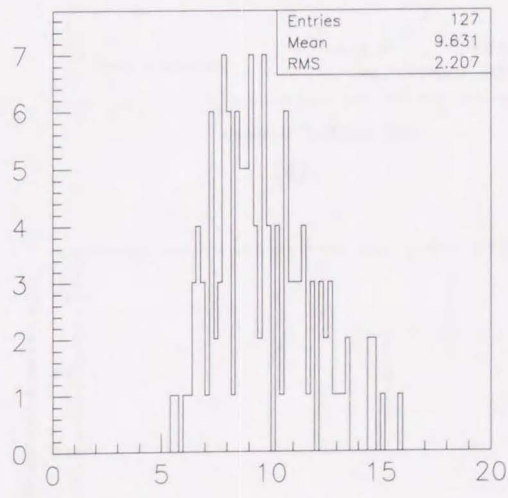
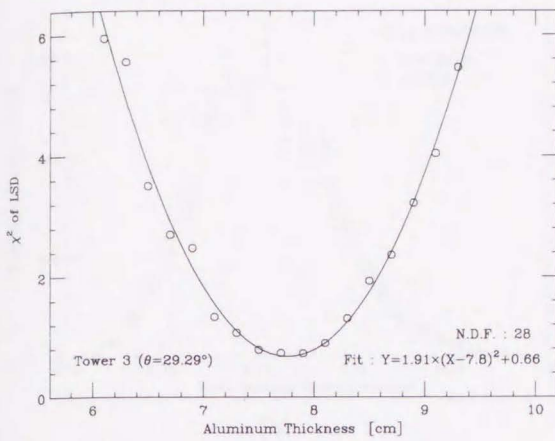
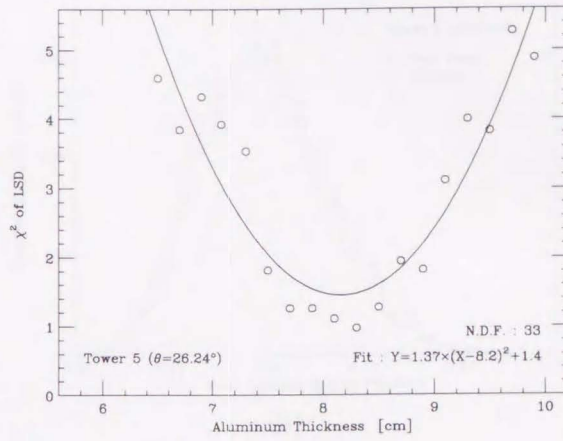
(d) Variance of FSE [GeV²]

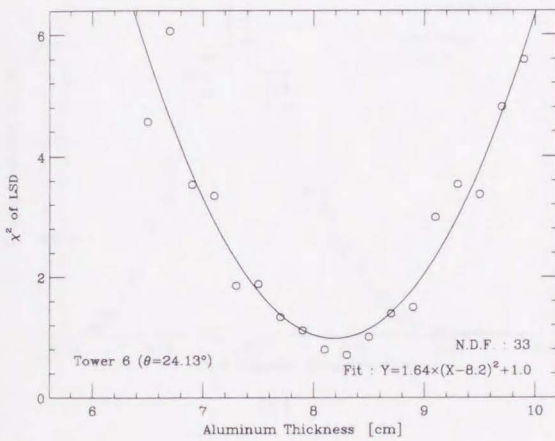
Figure 7.13: First segment responses of the pad to 101 GeV electrons. (a) First segment energy for a tower ($\eta = 8$, $\varphi = 22$). (b) The averages of FSE for 127 same η towers. (c) The standard deviations. (d) The variances.



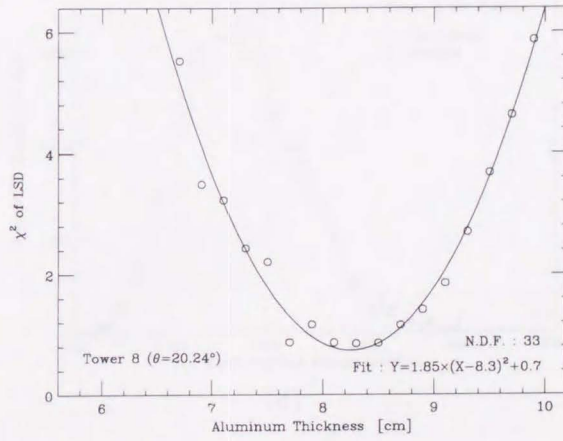
(a)



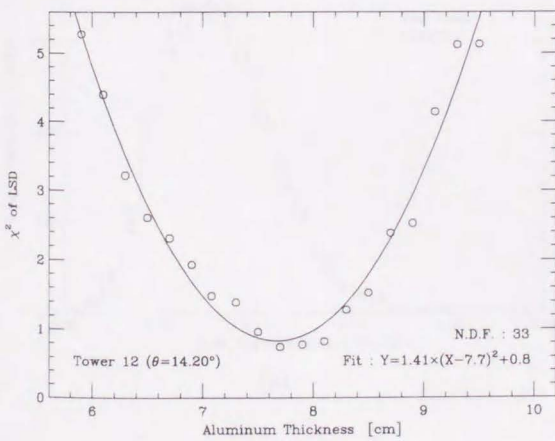
(b)



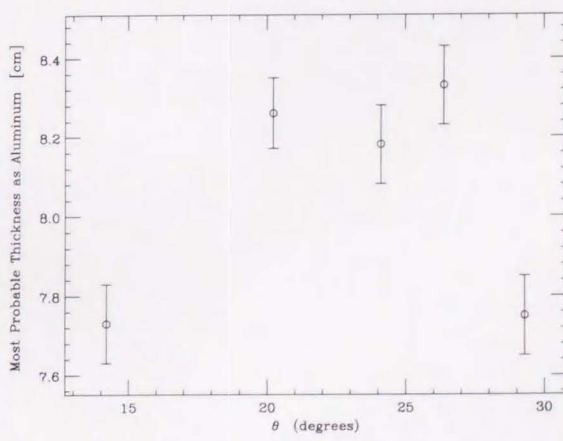
(c)



(d)



(e)



(f)

Figure 7.14: (a) - (e) χ^2_{LSD} and quadratic fits. The last five layers are not used for the χ^2_{LSD} calculation in (a). (f) Most probable thicknesses from the fits.

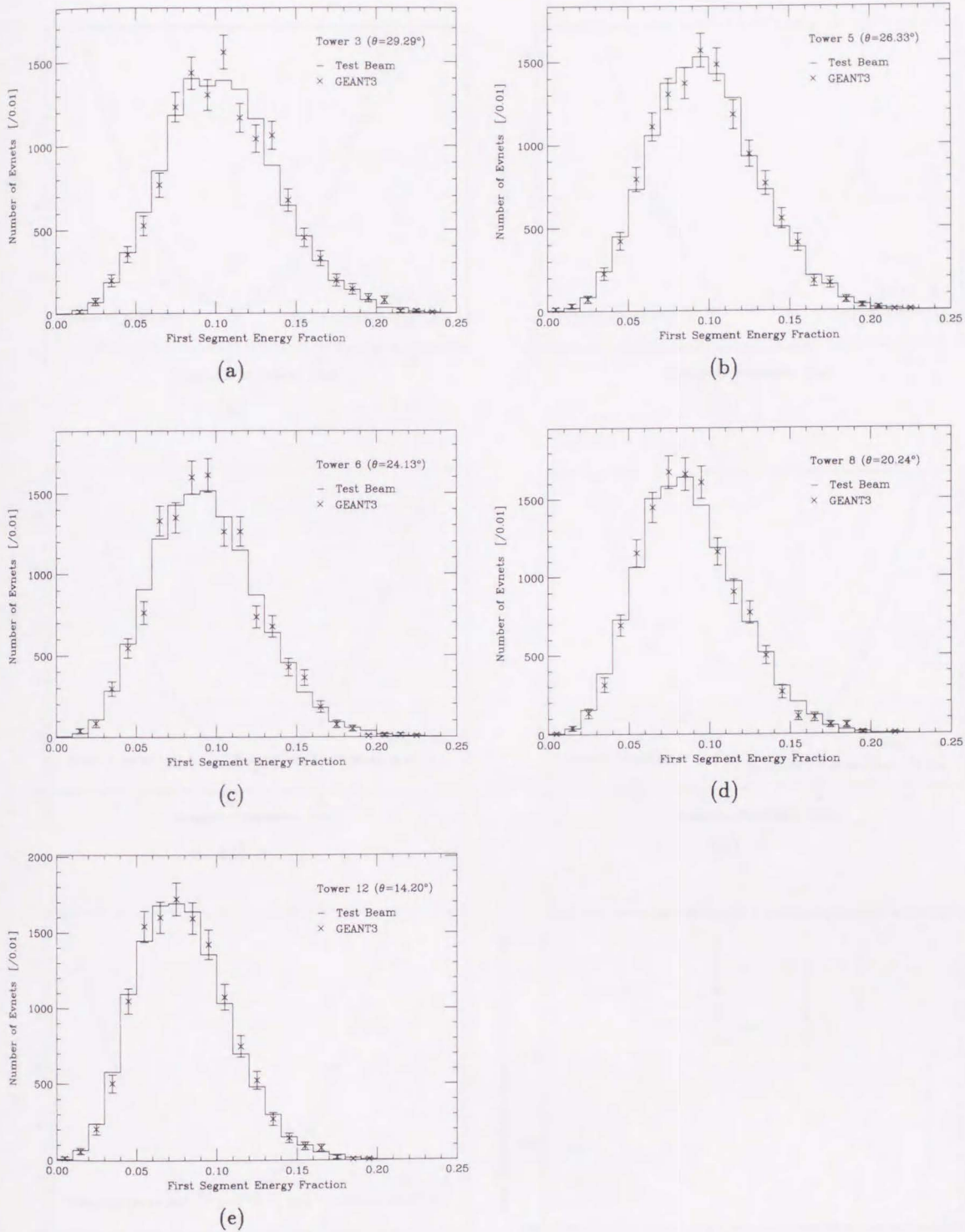
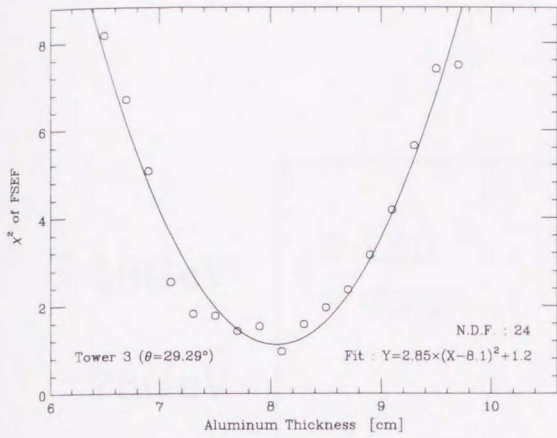
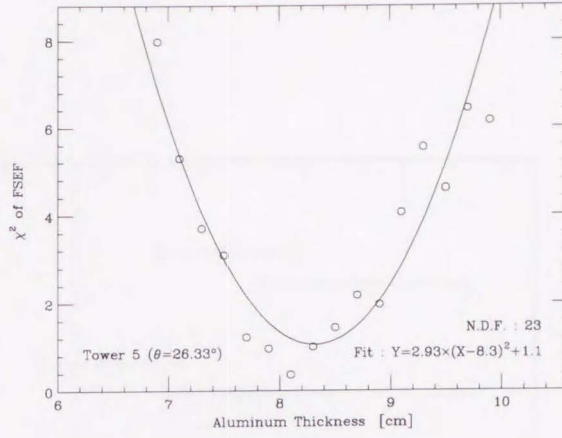


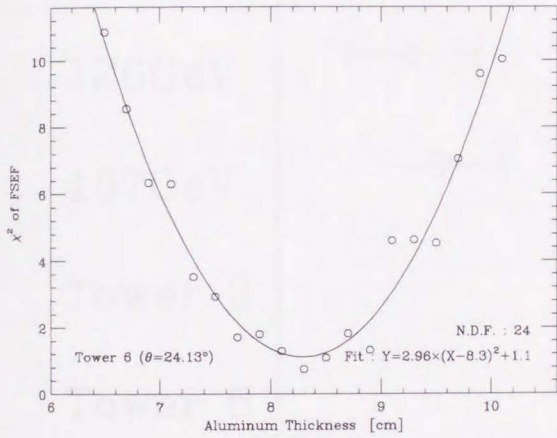
Figure 7.15: Distributions of FSEF for the η position scan. 101 GeV electrons are incident at the centers of η towers 3, 5, 6, 8, and 12 ($\theta = 29.29, 26.24, 24.13, 20.24,$ and 14.20° , respectively). The aluminum thickness in the simulation is 8.1 cm. Note that the test beam is shown in histograms and the Monte Carlo in the symbols since there simulated 2000 electrons for each tower, while the test beam contains 12700 events each.



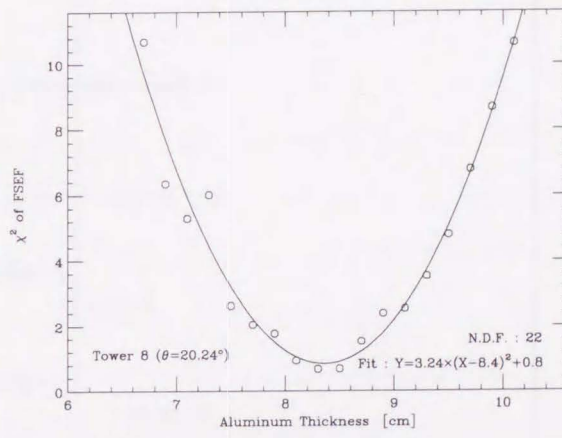
(a)



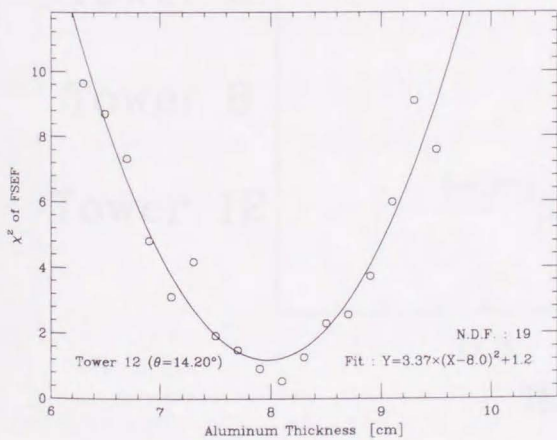
(b)



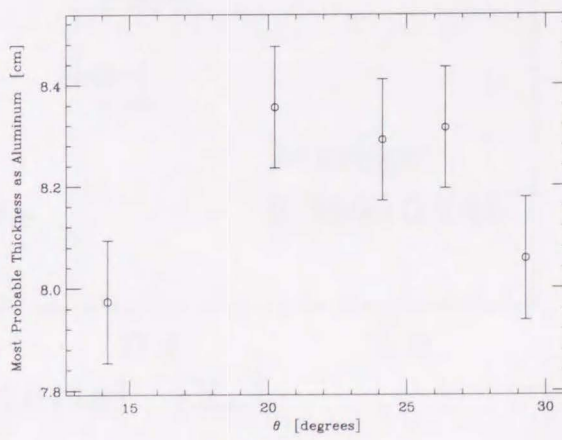
(c)



(d)



(e)



(f)

Figure 7.16: (a) - (e) χ^2_{FSEF} and quadratic fits. (f) Most probable thicknesses from the fits.

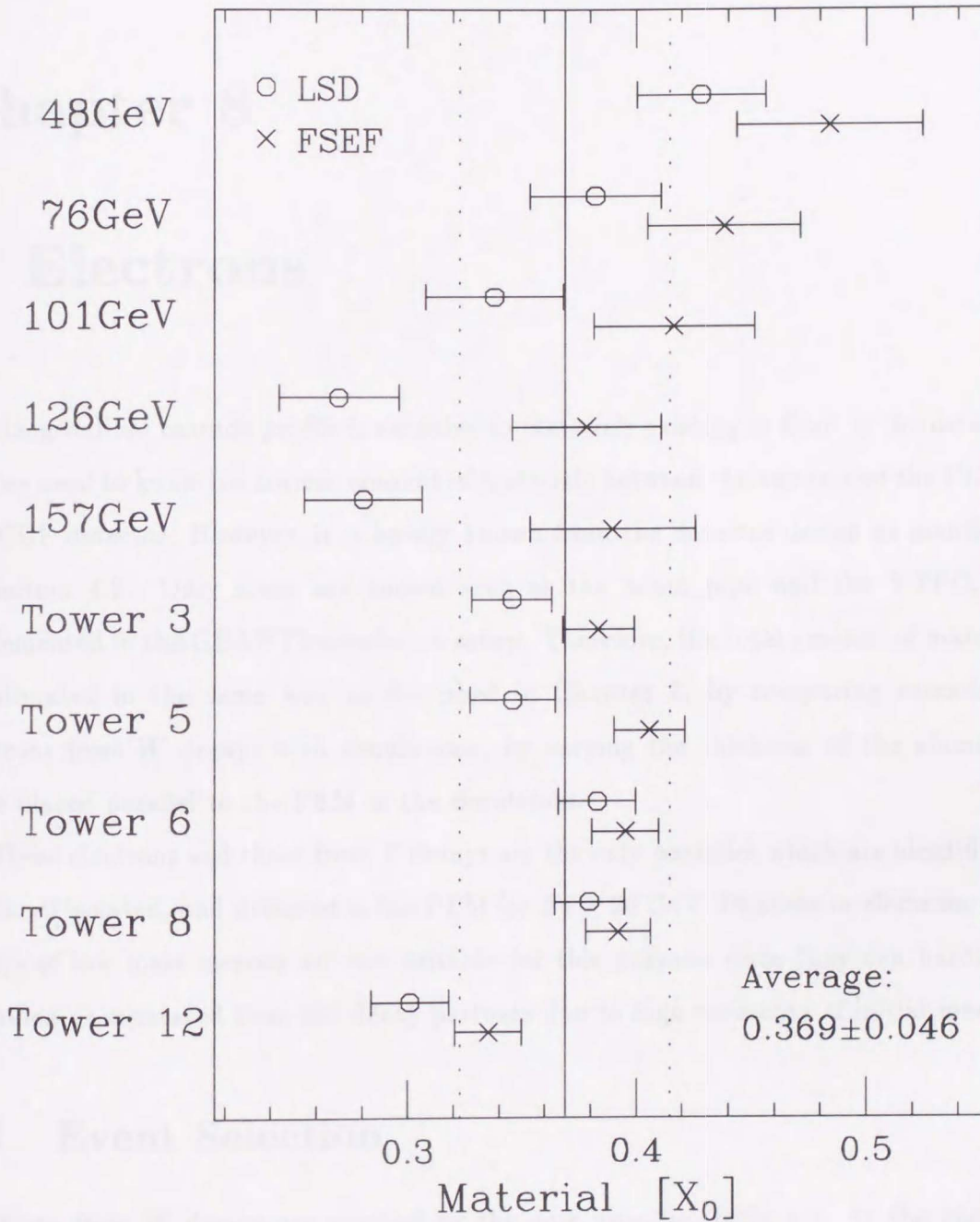


Figure 7.17: Estimations of the total amount of materials between the MT5 dipole magnets and the PEM excluding the real two inch aluminum plate placed in front of the detector. The average is shown in the solid line, and the dots represent the error.

Chapter 8

W Electrons

The longitudinal cascade profile is sensitive to materials existing in front of the detector, and we need to know the correct amount of materials between the vertex and the PEM in the CDF detector. However, it is hardly known from the detector design as mentioned in Section 4.2. Only some are known such as the beam pipe and the VTPC, and implemented in the GEANT3 simulation setup. Therefore, the total amount of materials is estimated in the same way as described in Chapter 7, by comparing cascades of electrons from *W* decays with simulations, by varying the thickness of the aluminum plate placed parallel to the PEM in the simulation.

These electrons and those from *Z* decays are the only particles which are identifiable, produced isolated, and detected in the PEM for $E_T \gtrsim 20$ GeV. Photons or electrons from decays of low mass mesons are not suitable for this purpose since they can hardly be identified or separated from the decay partners due to high momenta of initial mesons.

8.1 Event Selection

Electrons from *W* decays are selected by the cuts listed in Table 8.1. In the endplug region, there was only one level 2 trigger “gas photon 23 GeV” which selected EM clusters with no *prescaling* or no random choice to reduce the event rate. However, the efficiency for this trigger is not enough high in the E_T range of the *W* electrons as we will see in Fig. 9.9, the next chapter. To reduce this trigger bias, off-line E_T thresholds are set at energies where the level 2 trigger efficiencies reach 80%. We have 489 “ $W \rightarrow e\nu$ ”

Level 2 trigger (trigger $E_T \geq 23$ GeV)
$E_T > 31$ GeV for the east PEM
$E_T > 36$ GeV for the west PEM
$E_{had}/E_{EM} < 0.05$
$\chi_{3 \times 3}^2(\text{old}) < 15$
$\chi_{3 \times 3}^2 < 5$
$R^{iso}(0.4) < 0.1$
$R_{VTPC} > 0.5$
$\cancel{E}_T > 20$ GeV
No jet with $E_T^{jet} > 10$ GeV
$ z_{vertex} < 50$ cm
Fiducial region
No bad runs
No miscablings
No spike events

Table 8.1: W selection.

candidates in 3.8 pb^{-1} data. Distributions of E , E_T , and $|\eta|$ for the electron candidates are shown in Fig. 8.1.

8.2 Monte Carlo Simulation

The longitudinal shower shape with respect to the layer number changes with the incident energy and angle. For a direct comparison of cascades every ten electrons are simulated for each real electron, with the same energy, polar angle, and event vertex. The first segment response is, then, smeared by a gaussian function around its mean value of 1, with σ of 0.1 to simulate the uniformity in the response of the pad first segment as described in Section 7.3.2. Dead layers in the test beam data are not corrected. They are rather reproduced in the simulation, i.e., they are also dead in the simulation, or energy summation is taken over layers excluding those inactive during the collider run.

Figure 8.2 shows the FSEF distribution for the W electrons together with the simulation. The thickness of the aluminum plate in the simulation is varied on an event by event basis according to the actual pass lengths of the electrons in the CTC endplate. Since the CTC endplate has an complicated geometry, the aluminum length in the actual CTC endplate of an electron pass is each calculated from the blue print of the CTC

endplate with particle θ , φ , and z_{vertex} for all 489 W electron candidates¹. Figure 8.3 shows the distribution of the pass lengths calculated for the 489 candidates.

The GEANT3 simulation under the above condition does not show good agreement with the W electrons. It suggests that more material is needed to reproduce the data distribution since the first segment energy becomes larger if the aluminum is thicker.

8.3 Estimation of Materials

We estimate the total amount of materials between the vertex and the PEM except for those already implemented in the simulation by comparing the FSEF distribution of the data with those of the simulation. The thickness of the aluminum plate in the simulation is changed randomly on an event by event basis at the real event level, smeared by a gaussian function, to simulate irregularities of the material thickness. Then, we scan both the gaussian mean and σ for the aluminum thickness. The mean is scanned from 4.5 cm to 8.0 cm by a 0.5 cm step, and the σ is scanned from 0.0 cm to 6.0 cm by a 1.0 cm step. χ_{FSEF}^2 is calculated by Eq. 7.2 and listed in Table 8.2 for various mean and σ values.

σ [cm]	mean [cm]							
	4.5	5.0	5.5	6.0	6.5	7.0	7.5	8.0
0.0	2.93	2.10	1.72	1.92	1.67	1.63	2.51	3.11
1.0	2.74	1.95	1.59	1.61	1.45	1.55	2.17	2.34
2.0	2.41	2.04	1.15	1.15	0.86	0.93	1.62	2.28
3.0	2.66	1.89	1.09	1.09	1.07	1.14	1.61	2.45
4.0	2.47	1.48	1.05	1.05	0.87	1.20	1.70	2.46
5.0	2.64	1.54	0.95	0.95	0.74	0.86	1.16	2.03
6.0	2.65	1.56	1.12	1.12	0.99	1.15	1.71	1.69

Table 8.2: χ_{FSEF}^2 for the W electrons. The aluminum thickness is smeared on an event by event basis with a gaussian function in each simulation. The mean and σ are scanned. The aluminum thickness is limited within 0 cm to $2 \times \text{mean}$.

One can notice that χ_{FSEF}^2 is sensitive to changes of the mean not the σ since the aluminum thickness is limited between 0 cm and twice the mean, and the deviation

¹Mikio Takano provided a program for this calculation.

or RMS does not change much for large σ values. However, χ_{FSEF}^2 takes always its minimum value at the mean 6.0 or 6.5 cm for any values of the σ . Thus, it is most likely that there are materials of $\sim 0.7 X_0$ in the CDF detector between the vertex and the PEM measured along the z direction excluding those already implemented in the simulation.

Subtracting the contribution of the CTC endplate, which corresponds to the mean of the substantial thicknesses $0.36 X_0$ in Fig. 8.3, from the estimated $\sim 0.7 X_0$, we expect other materials in the CDF detector to be $\sim 0.35 X_0$. Assuming an irregularity in the thickness of these additional materials is the same with that of the CTC endplate (the RMS value in Fig. 8.3), the overall irregularity is expected $\sim 0.25 X_0$ or ~ 2 cm thick aluminum.

Figure 8.4 shows comparisons of FSEF distributions. In the simulation, the mean of the aluminum thickness is fixed to 6.0 cm, and the gaussian σ is scanned. Any plots for $\sigma \geq 2.0$ cm show excellent agreements. Since FSEF distributions of the simulation for $\sigma \geq 2.0$ cm do not show significant differences, we choose 2.0 cm as an irregularity of the material thickness for simulations of photons and background mesons in Chapter 9.

Figure 8.5 (a) to (e) show FSEF distributions for simulations with various means of the aluminum thickness and the σ of 2.0 cm. The most probable thickness, at which the GEANT3 simulation reproduces the FSEF distribution of the W electrons best, is shown in Fig. 8.5 (f). It is 6.24 ± 0.31 cm thick aluminum along the z axis or $0.701 \pm 0.035 X_0$. We consider there exist, in the average, materials of $0.701 X_0$ with an uncertainty of $0.035 X_0$ in the CDF detector excluding those already implemented in the simulation setup.

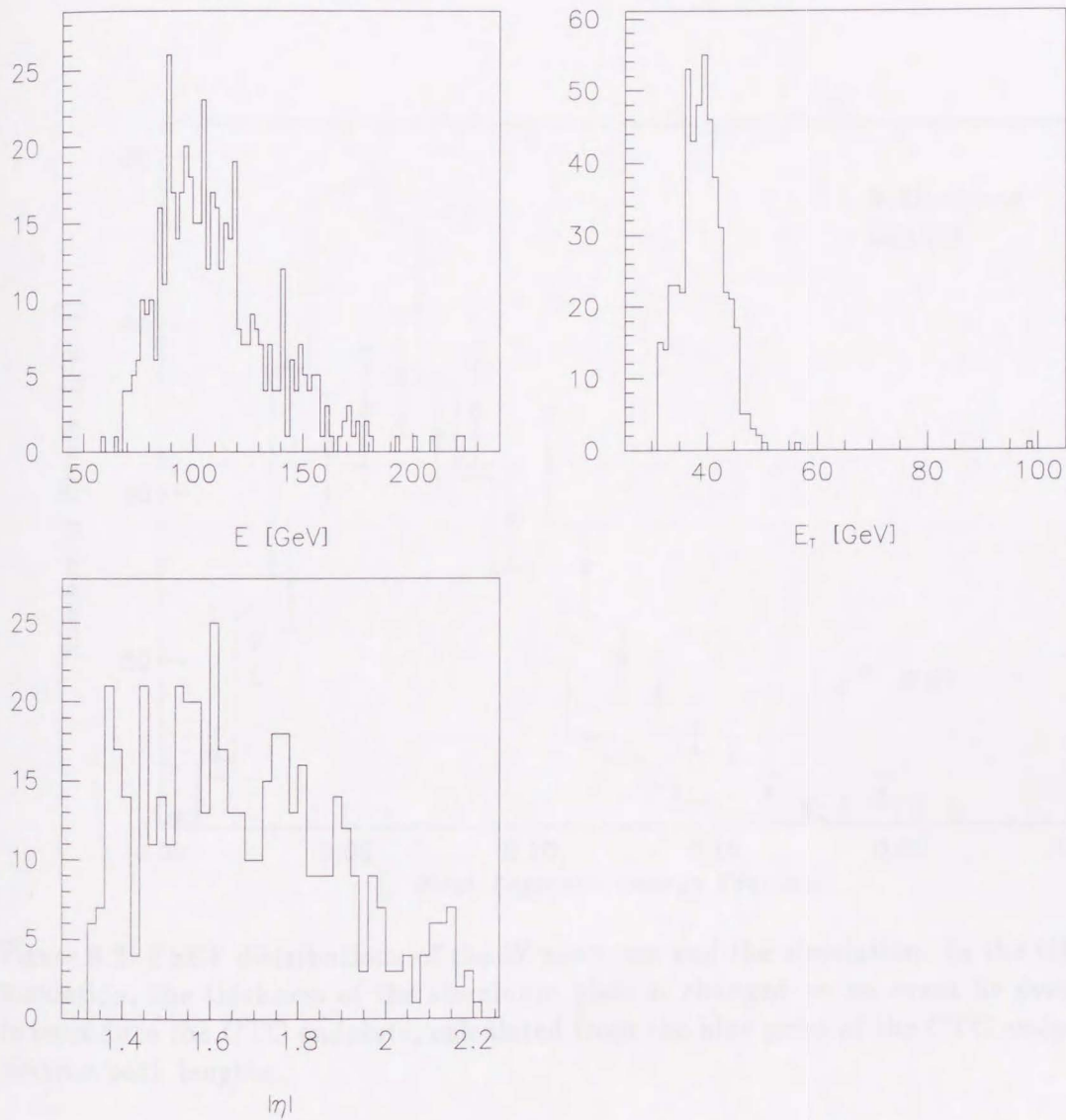


Figure 8.1: Distributions of E , E_T , and $|\eta|$ for the 489 W electrons.

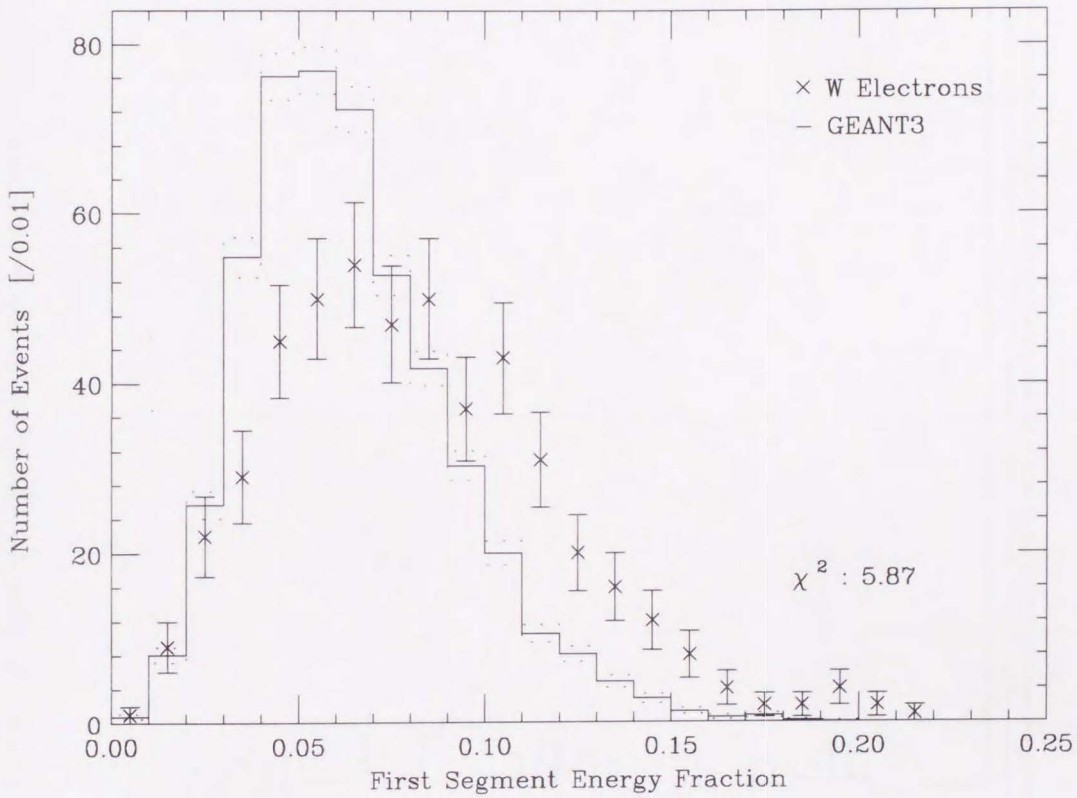


Figure 8.2: FSEF distributions of the W electrons and the simulation. In the GEANT3 simulation, the thickness of the aluminum plate is changed on an event by event basis to reproduce the CTC endplate, calculated from the blue print of the CTC endplate for electron path lengths.

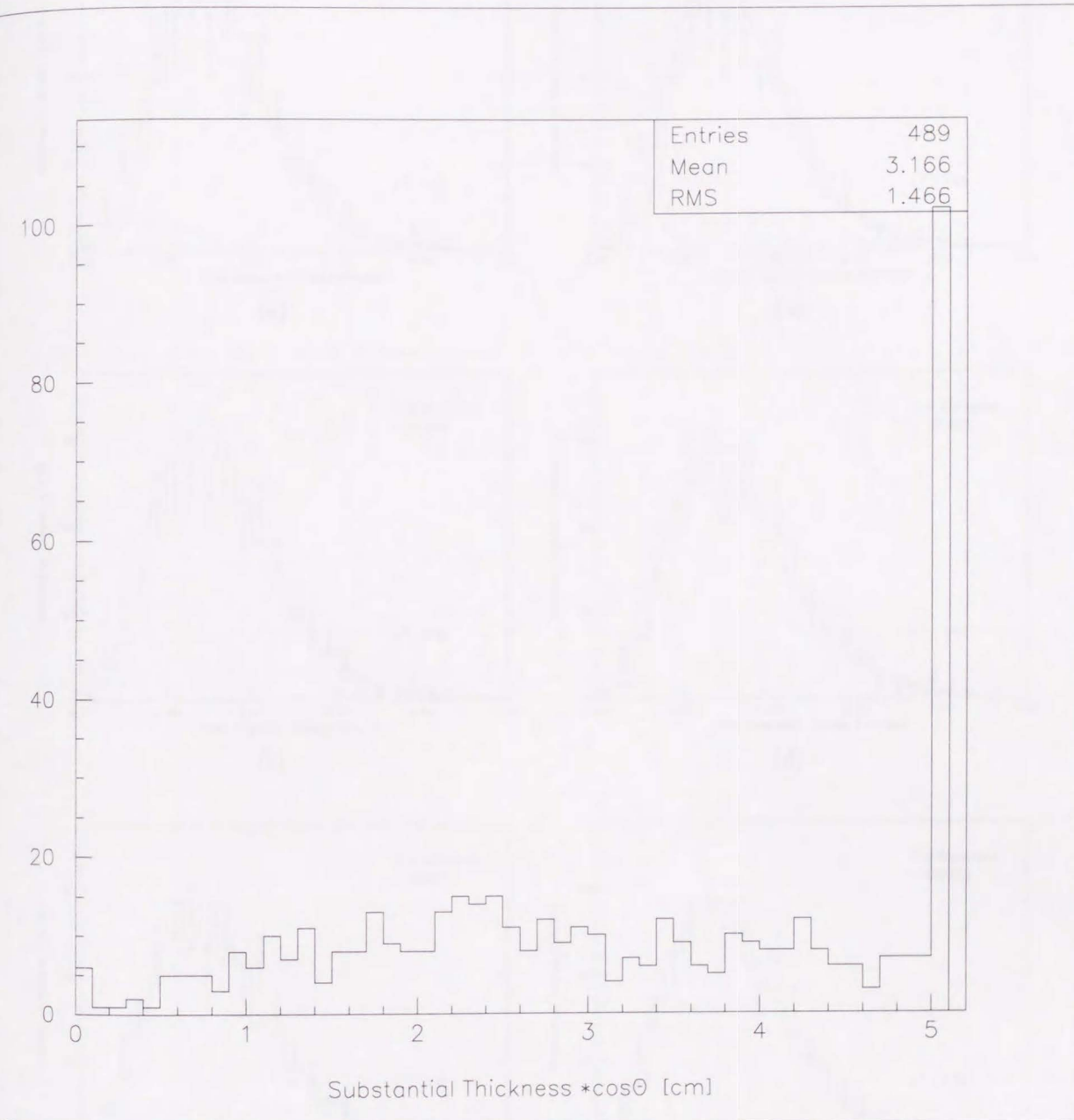
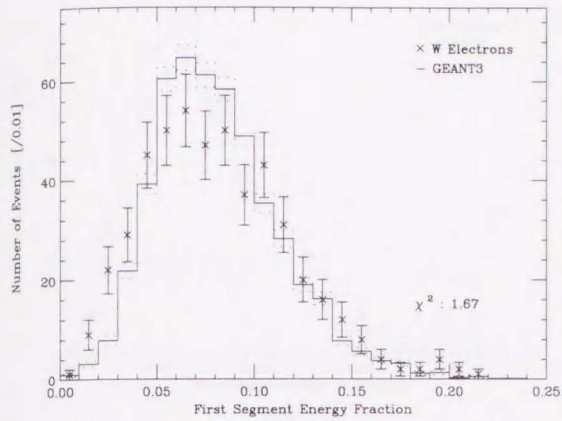
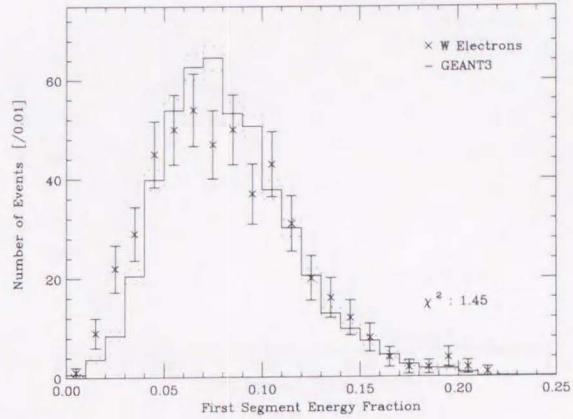


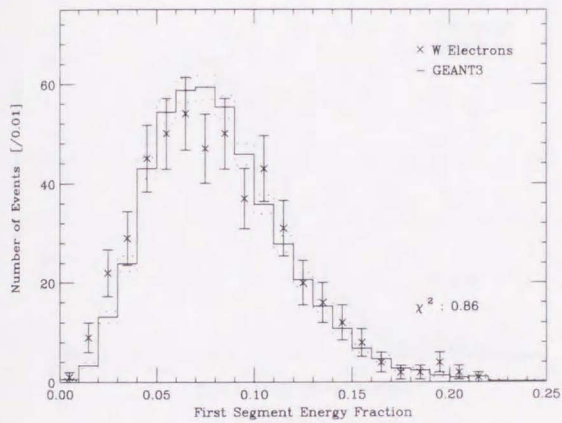
Figure 8.3: Distribution of the electron path lengths in the CTC endplate ($\times \cos \theta$). The path length is defined as a total aluminum length in the CTC endplate along a trajectory of a particle with θ , φ , and z_{vertex} . The mean and the σ correspond to $0.36 X_0$ and $0.16 X_0$, respectively.



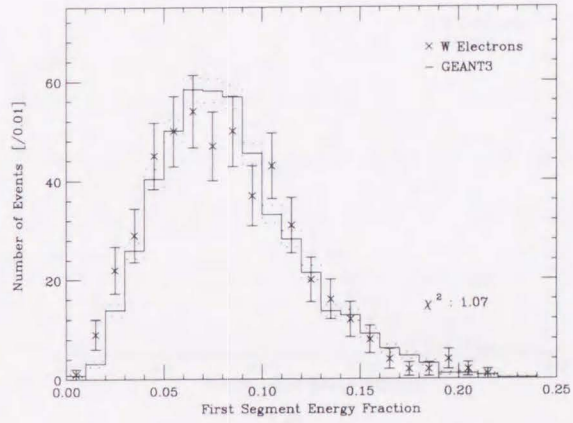
(a)



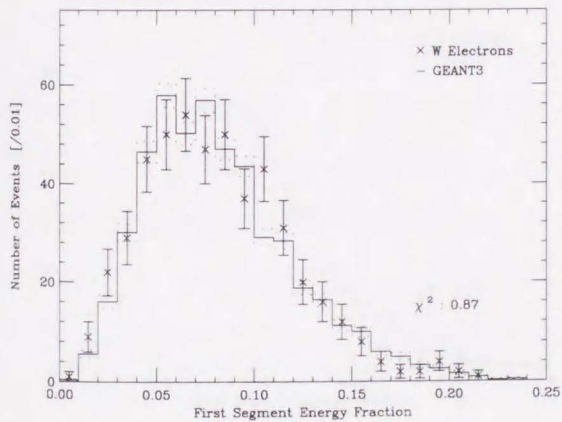
(b)



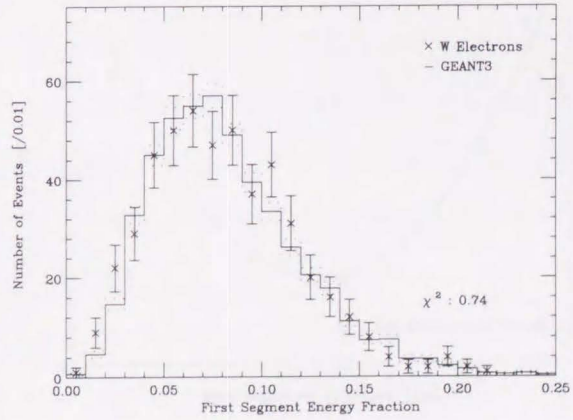
(c)



(d)



(e)



(f)

Figure 8.4: FSEF distributions of the W electrons and simulations. In each simulation, the aluminum thickness is smeared with a gaussian function. The mean is fixed at 6.0 cm, and the σ is scanned.

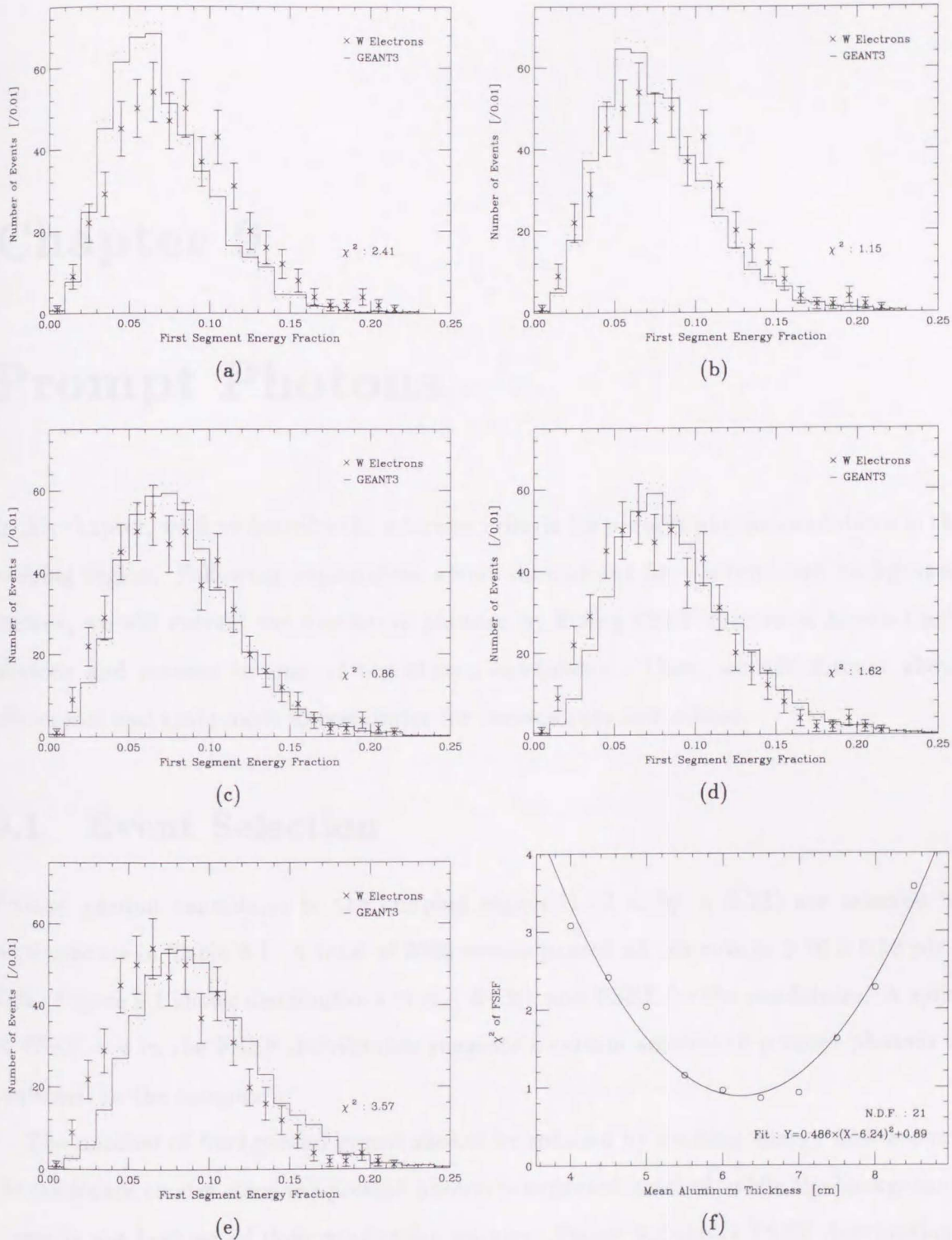


Figure 8.5: (a)-(e) FSEF distributions of the W electrons and simulations. In each simulation, the aluminum thickness is smeared with a gaussian function. The σ is fixed at 2.0 cm, and the mean is scanned. (f) χ^2_{FSEF} values with respect to the mean aluminum thickness.

Chapter 9

Prompt Photons

In this chapter, we first describe the selection criteria for prompt photon candidates in the endplug region. Following explanation about simulations for photons and background mesons, we will extract the number of photons by fitting FSEF spectra of Monte Carlo photons and mesons to that of the photon candidates. Then, we will discuss about efficiencies and systematic uncertainties for various cuts and others.

9.1 Event Selection

Prompt photon candidates in the endplug region ($1.32 < |\eta| < 2.22$) are selected by requirements in Table 9.1. A total of 3995 events passed all the cuts in $3.76 \pm 0.13 \text{ pb}^{-1}$ data. Figure 9.1 shows distributions of E_T , E , $|\eta|$, and FSEF for the candidates. A spike at $\text{FSEF} = 0$ in the FSEF distribution suggests a certain amount of prompt photons is contained in the sample.

The number of background events should be reduced by limiting energy flow around the candidate cluster since the prompt photon is expected isolated, while the background meson is not because of their production natures. Figure 9.2 shows FSEF distributions for various isolation cuts. Changes in the relative height of the spike suggest that the photon to background ratio increases as the cut value is tightened. We have decided the isolation threshold to be 3 GeV as in Table 9.1, while one for the photon analysis in the central region is 2 GeV [4]. A threshold of 3 GeV in the endplug is consistent with 2 GeV in the central for several reasons. They will be explained later in Section 9.4.2.

Level 2 trigger $E_T \geq 23$ GeV
$27 < E_T < 40$ GeV
$E_T^{iso}(0.7) < 3$ GeV
$E^{had}/E^{EM} < 0.05$
$\chi_{3 \times 3}^2(old) < 20$
$\chi_{3 \times 3}^2 < 5$
$R_{VTPC} \leq 0.8$
$ z_{vertex} < 50$ cm
Fiducial region
No bad runs
No miscablings
No spike events

Table 9.1: Photon candidate selection.

A dead layer correction has already been made at the production stage (Section 5.1), multiplying the energy or transverse energy of an EM cluster by a constant. If one of the first five layers is inactive, however, another dead layer correction is applied only for the energy in the first segment of the pads. There is only one such quadrant during 1988-1989 run, and a correction is made accordingly. The correction factor is calculated in the same way as done in the production avoiding a double correction.

9.2 Simulation

As the FSEF spectrum changes with the incident energy and angle, photons and background mesons should be simulated at various energies and angles (θ or η) in accordance with the energy and pseudorapidity distributions of the photon candidates.

The prompt photon sample is divided into 2 E_T and 10 η regions. The number of photon candidates in each region is listed in Table 9.2. In proportion to the numbers in the table, photons, π^0 's, and η 's are each simulated with transverse energies 30 GeV and 37 GeV, and pseudorapidities at the center of each η region. Since the number of candidates in each region is too few to calculate a cross section with a reasonable statistical uncertainty, Monte Carlo events are each summed over all the E_T and η regions on an assumption that the E_T and η spectra of photons, π^0 's, or η 's follow those of the photon candidates.

$ \eta $	$27 < E_T < 33 \text{ GeV}$	$33 < E_T < 40 \text{ GeV}$
1.32-1.41	306	219
1.41-1.50	370	224
1.50-1.59	313	210
1.59-1.68	384	229
1.68-1.77	277	160
1.77-1.86	290	158
1.86-1.95	184	123
1.95-2.04	132	84
2.04-2.13	97	70
2.13-2.22	95	70

Table 9.2: The number of candidates in the prompt photon sample.

Only the following neutral decay modes are simulated for the background mesons:

$$\pi^0 \rightarrow \gamma\gamma,$$

$$\eta \rightarrow \gamma\gamma \quad \text{or} \quad \eta \rightarrow \pi^0\pi^0\pi^0 \rightarrow 6\gamma.$$

Charged decay modes are not simulated because most of such decays are rejected by the VTPC requirement. In magnetic field of 1.5 T, a trajectory of an electron with $P_T = 2 \text{ GeV}/c$ is bent by $\sim 5 \text{ mm}$, corresponding to the road radius for R_{VTPC} , at a distance of 21 cm from the z axis, corresponding to the maximum active radius of the VTPC. In addition, decay particles are measured as single EM clusters if the initial mesons have high momenta. We have studied the “ $\eta \rightarrow \pi^0\pi^0\pi^0 \rightarrow e^+e^-X$ ” decay, in which decay particles are expected to have lowest momenta among the charged decays, with the GEANT3 simulation and a toy Monte Carlo simulation of meson decays. Since the GEANT3 simulation does not equip lateral measurement, we have added the pad readout for the study. A thousand η 's with $E_T = 30 \text{ GeV}$ at $\theta = 20.24^\circ$ are forced to decay into three π^0 's. From the GEANT3 simulation, all of them are found to form single EM clusters. A fraction of 3.6% of the $3\pi^0$ decay has at least a pair of e^+e^- in the final state by the Dalitz decay. We have simulated such decays by a toy Monte Carlo program with $E_T = 30 \text{ GeV}$ and $\theta = 20.24^\circ$ for the initial meson, and found 85% of the $3\pi^0$ charged decay contains at least one electron/positron with $E_T > 2 \text{ GeV}$ and of

which the trajectory is within 5 mm from one of the initial meson at the maximum active radius of the VTPC (21 cm). Considering these estimations, the charged decays of the neutral mesons passing the VTPC cut are expected far less than 1% of the background events, and we neglect such charged decays. Note that the two neutral decays of η are added properly.

It is essential to simulate the level 2 trigger since the trigger efficiencies are not enough high in the E_T range of the photon sample as we will see in Fig. 9.9. The “gas photon 23 GeV” trigger is expected to affect the FSEF distribution due to the fact that the trigger E_T is calculated with energy deposits in the second segment instead of the total energy in all the three depth segments. This makes us trigger more EM clusters with, by shower fluctuations, larger energy deposits in the second segment, especially at lower E_T . Other trigger effects to distort the FSEF spectrum are the dead layers, the different quadrant gains, and an assumption of the event vertex at $z = 0$ cm. All the above effects are implemented in the GEANT3 simulation, and only Monte Carlo events which pass the 23 GeV trigger are collected.

To simulate the uniformity in the response of the first segment, the first segment energy is smeared by a gaussian function with a σ of 10%. The event vertex is also smeared along the z axis by a gaussian function of the mean = 0 cm and $\sigma = 30$ cm with a limitation of $|z_{vertex}| < 50$ cm.

The aluminum plate thickness is smeared by a gaussian function on an event by event basis as done in W electron simulations. Four sets of simulation data are prepared with mean thicknesses of 5.5, 6.0, 6.5, and 7.0 cm, while the gaussian σ is fixed to 2.0 cm. The number of prompt photons in the photon sample is extracted for each set. As we will see later in Section 9.3, the extracted number of prompt photons depends upon the mean thickness, so, by interpolating these, we will evaluate the nominal number of prompt photons and uncertainties.

The isolated production ratio of η and π^0 mesons $(\bar{p}p \rightarrow \eta + X)/(\bar{p}p \rightarrow \pi^0 + X)$ was measured to be 1.02 ± 0.15 (stat.) ± 0.23 (syst.) [4]. We employ this ratio, and FSEF distributions of neutral decays of π^0 and η mesons are put together into one background spectrum at the production rate of $\pi^0 : \eta = 1 : 1.02$.

FSEF distributions of the GEANT3 simulation for single photons, π^0 's, and η 's with

the mean aluminum thickness of 6.5 cm are shown in Fig. 9.3 together with the combined meson background.

9.3 Extraction of Photons

The number of photons in the prompt photon sample is evaluated from its FSEF distribution. Two Monte Carlo spectra of single photons and background mesons in Fig. 9.3 (b) are fitted to the data with free parameters p_1 and p_2 as

$$F_{data} = p_1 \cdot F_{\gamma} + p_2 \cdot F_{background},$$

where F_{data} represents the FSEF distribution of the data, F_{γ} and $F_{background}$ are those of single photons and background mesons. The two parameters p_1 and p_2 are not independent each other because of normalization in the total number of events, but reflect the numbers of photons and background mesons in the data once F_{γ} and $F_{background}$ are each normalized to unity. The fitting is made so as to minimize χ^2 defined below:

$$\chi^2 = \sum_i \frac{1}{\sigma_i^2} (p_1 \cdot n_i^{\gamma} + p_2 \cdot n_i^{b.g.} - N_i^{data})^2,$$

$$\sigma_i^2 = (p_1 \cdot \sigma_i^{\gamma})^2 + (p_2 \cdot \sigma_i^{b.g.})^2 + (\sigma_i^{data})^2,$$

where n_i^{γ} and $n_i^{b.g.}$ are the numbers of photons and background mesons in the i -th bin, representing the Monte Carlo FSEF spectra. N_i^{data} is the number of events in the i -th bin of the data. σ_i^{γ} , $\sigma_i^{b.g.}$, and σ_i^{data} are the statistical uncertainties in n_i^{γ} , $n_i^{b.g.}$, and N_i^{data} , respectively.

Four sets of Monte Carlo simulations are fitted to the data. In each set, the aluminum thickness is smeared around the mean of 5.5, 6.0, 6.5, or 7.0 cm with a σ of 2.0 cm. Entries in FSEF = 0.0 to 0.2 are used for the fitting, and results are shown in Fig. 9.4. The extracted number of prompt photons is found to increase linearly with the aluminum thickness as shown in Fig. 9.5. In Chapter 8, we have estimated the total amount of materials in the CDF detector between the vertex and the PEM to be $0.701 \pm 0.035 X_0$ or 6.24 ± 0.31 cm thick aluminum along the z axis. We have also studied

the reliability of the GEANT3 simulation in Chapter 7 and estimated the reproducibility of the electromagnetic cascade. The accuracy has been evaluated from changes in the shower shape by adding or subtracting material of $0.046 X_0$. It corresponds to 0.41 cm thick aluminum or, at the center of the PEM ($\eta = 1.77$ or $\theta = 19.33^\circ$), 0.39 cm along the z axis. The total uncertainty for both the materials in the detector and the GEANT3 simulation becomes 0.51 cm thick aluminum. From the linear fit in Fig. 9.5, this uncertainty as the aluminum thickness of ± 0.51 cm corresponds to ± 353 of prompt photon events. Thus, the number of prompt photon events in our sample is evaluated to be

$$1972 \pm 353.$$

9.4 Efficiencies and Uncertainties

Efficiencies for the cuts and other requirements listed in Table 9.1 are estimated in this section with the corresponding and other uncertainties.

9.4.1 Level 2 Trigger

As noted in Chapter 5, there are several corrections regarding the energy measurement such as the dead layer corrections and the quadrant gain corrections. Corrections for the gas gain, the tower to tower response variation, and the dead layers are roughly (but not completely) implemented in the level 2 trigger. However, differences in quadrant gains or non-linearity of the calorimeter response is not included. In addition, the level 2 trigger refers only to energies in the second segment of the PEM. Due to the above facts, the level 2 trigger of “gas photon 23 GeV” has inefficiencies at lower transverse energies. It is also expected that the trigger efficiency is different in quadrants since the dead layers and the quadrant gain correction are the most dominant sources on the efficiency. Thus, the trigger efficiency is estimated for eight individual quadrants.

Cluster Selection

We start the estimation with collecting “unbiased” EM clusters, which are free from any influence of the level 2 triggers. Since the level 3 trigger or the off-line production

has essentially no requirement on cluster E_T for ≥ 10 GeV, any EM cluster in an event which passed level 2 triggers other than the “gas photon 23 GeV” or the “di-photon 10 GeV” is considered unbiased.

The “gas photon 23 GeV” trigger requires a level 2 trigger EM cluster with $E_T \geq 23$ GeV in the PEM or FEM, and the “di-photon 10 GeV” requires at least two clusters with $E_T \geq 10$ GeV anywhere in the electromagnetic calorimeters. However, EM clusters found in the PEM are also collected for the study if events satisfy one of the following conditions:

- Containing at least two level 2 EM clusters with $E_T \geq 23$ GeV in the PEM or FEM.
- Containing a level 2 EM cluster with $E_T \geq 23$ GeV in the FEM.
- Containing two level 2 EM clusters with $E_T \geq 10$ GeV in the CEM or FEM.
- Containing at least three level 2 EM clusters with $E_T \geq 10$ GeV found anywhere.
- Satisfying both the “gas photon 23 GeV” and “di-photon 10 GeV” triggers.

Then, level 2 trigger efficiencies are calculated by examining transverse energies of the off-line EM clusters with corresponding level 2 trigger EM clusters.

Clusters are selected by the requirements listed in Table 9.3. No isolation cut is

$10 \leq E_T^{det} < 80$ GeV
$E_{had}/E_{EM} < 0.05$
$z_{vertex} < 50$ cm for a cluster with $\eta_{det} > 0$
$z_{vertex} > -50$ cm for a cluster with $\eta_{det} < 0$
$\chi_{3 \times 3}^2(\text{old}) < 20$
$\chi_{3 \times 3}^2 < 5$
$1.32 < \eta_{det} < 2.22$
Fiducial region
No bad runs
No miscablings
No spike events

Table 9.3: Selection for level 2 trigger study.

required since no isolation dependence of trigger efficiencies is observed. It is already

required essentially by the clustering itself as well as the E_{had}/E_{EM} and $\chi^2_{3 \times 3}$ cuts. The transverse energy E_T^{det} is referred to in the detector coordinates, in which the event vertex is assuming $z = 0$ cm, rather than in the event coordinates since the transverse energy of the level 2 trigger EM cluster is calculated in the detector coordinates. Particles coming from the opposite side of the detector (east-west) are allowed even if $|z_{vertex}| \geq 50$ cm. A notation of η_{det} represents pseudorapidity in the detector coordinates. No track or VTPC hit is required.

There are many off-line clusters without corresponding level 2 clusters found in the trigger study sample. It is expected that some of lower E_T^{det} off-line clusters may not have corresponding level 2 clusters. However, the corresponding level 2 clusters should always exist for high E_T^{det} clusters. Figure 9.6 shows $\eta_{det}-\varphi$ positions for $E_T^{det} \geq 23$ GeV off-line clusters with no corresponding level 2 clusters. Most of such clusters are found in the east PEM module, and especially for $\eta_{det} \gtrsim 1.9$. We have investigated this strange feature and found a correlation between the cluster position and the level 2 trigger tower segmentation.

Figure 9.7 shows $\eta_{det}-\varphi$ positions for off-line clusters passing the “gas photon 23 GeV” trigger. Other requirements are $E_T^{det} > 23$ GeV, $E^{had}/E^{EM} < 0.1$, and $\chi^2(\text{old}) < 20$. The data is essentially a parent sample of the photon candidates. Each east or west distribution is enhanced by overlaying four quadrants in one plot. Two kinds of patterns are recognizable. One is in a small η_{det} region and barely seen in both east and west modules. The other is in a large η_{det} region and found only in the east PEM. The former pattern is due to the tower segmentation since it is rather coarse (typically $10 \text{ cm} \times 10 \text{ cm}$) in this small η_{det} region and the cluster positions localize around the center the tower. The problem is the one in the large η_{det} region. There are virtually no clusters found near the level 2 trigger tower boundaries except for around the four corners in this region. There must have been some kind of problems in the level 2 trigger system, probably in the level 2 trigger clustering algorithm, but we do not know the exact reason. Thus, clusters in this area, $\eta_{det} > 1.9$, are not used for the study. Note that there are observed more events in the east than the west. This is simply due to imbalance of the trigger efficiencies between the two modules.

Efficiency Curves

Ignoring any η_{det} dependence, the level 2 trigger efficiencies are individually calculated for the eight quadrants and shown in Fig. 9.8. The efficiency curves are obtained from fits by the following equation:

$$y = \frac{1 + b}{e^{a/x} + b}$$

Parameters a and b for all the quadrants are listed in Table 9.4. The variation comes

Quadrant #	a	b
0	331.71	202580
1	296.85	25334
2	304.55	31506
3	353.55	15052
4	249.75	23599
5	280.12	83606
6	228.50	7046.8
7	268.97	8088.5

Table 9.4: Parameters a and b obtained from the fits.

mostly from the dead layers and the quadrant gain differences.

Efficiency curves are also obtained for the east and west PEM's and shown in Fig. 9.9.

Parameters a and b are

$$a = 228.58 \quad \text{and} \quad b = 7139.5 \quad \text{for the east PEM} \quad \text{and}$$

$$a = 259.22 \quad \text{and} \quad b = 4796.6 \quad \text{for the west PEM.}$$

Trigger Efficiency

The efficiency curves are applied to the E_T spectrum of the photon candidates in each east or west, and the trigger efficiencies to the photon sample are found to be

$$0.794 \pm 0.022 \text{ (stat.)} + 0.020/-0.022 \text{ (syst.)} \quad \text{for the east } (\eta > 0) \text{ and}$$

$$0.529 \pm 0.025 \text{ (stat.)} + 0.031/-0.031 \text{ (syst.)} \quad \text{for the west } (\eta < 0).$$

Due to many dead layers in the west PEM, the trigger efficiencies for the east and the west are quite different. Averaging both efficiencies weighted by the number of the candidates in each PEM, we have evaluated the level 2 trigger efficiency for prompt photons to be $0.648 + 0.033/-0.034$.

9.4.2 Isolation

Two origins are considered for the cause of energy flow around the prompt photon. The energy flow around the photon or isolation is defined by

$$E_T^{iso}(0.7) \equiv E_T(0.7) - E_T \cdot \left(1 + \frac{E^{had}}{E^{EM}}\right)$$

in Section 6.1, a scalar sum of transverse energies over towers in the EM calorimeters inside a cone of $\Delta r = 0.7$ except those of the photon.

One is the “underlying energy” due to low energy particles produced in soft scatterings of partons other than those making a hard collision. The underlying cone E_T is approximated by the “minimum bias event”, which comes from soft scatterings of partons and produces many low energy hadrons. A minimum bias event is taken with only a trigger requirement of the BBC coincidence; that is why the event is called minimum biased. Figure 9.10 shows distributions of the underlying cone E_T for minimum bias events in the central region of $|\eta_{det}| < 0.9$ and the endplug region of $1.32 < |\eta_{det}| < 2.22$ together with the cone E_T for the photon candidates. The underlying cone E_T is larger in the endplug region than in the central by 0.49 GeV in the average.

Another cause for the energy flow is lateral leakage of the cascade. We have a fair amount of the lateral energy leakage due to the following reasons:

- Large extent of the lateral shower profile.
- The fine segmentation of the PEM.
- The clustering algorithm EMCLST only refers to towers with $E_T^{EM} \geq 0.1$ GeV.
- The cluster size is limited within 5×5 towers around the seed.

This “lateral shower leakage” is estimated with test beam electrons assuming no differences in the lateral shower profile between electrons and photons. Figure 9.11 shows the cone E_T (excluding the cluster E_T) distributions for 101 GeV test beam electrons incident at the center of calorimetry tower 8 ($\theta = 20.24^\circ$ or $\eta = 1.72$). It is noted that the cone E_T includes not only the shower leakage but also calorimeter noise.

The raw data banks (Section 5) only contain channels with at least 10 ADC counts for the calorimetry towers. It considerably reduces the size of raw data as well as calorimeter noise. However, it passes large *positive* noise with 10 or more ADC counts, and such noise is taken as an energy deposit, while *negative* noise is not. Thus, the energy measurement intends to contain only positive not negative noise even if the pedestal value is properly calibrated. Considering this fact, the shower leakage is estimated on the following assumptions:

- Same noise for all calorimetry channels.
- The cascade laterally spreads within $\Delta r = 0.3$.

Thus, a finite value of E_T in an annulus between $\Delta r = 0.3$ and 0.4 in Fig. 9.11 (c) is interpreted to come from the positive noise, and it becomes ~ 0.02 GeV/tower. Subtracting this positive noise from $E_T^{iso}(0.3)$, the lateral shower leakage is obtained as shown in Fig. 9.12 with respect to the electron energy and pseudorapidity η_{det} . The position dependence is estimated with 101 GeV electrons, while the energy dependence by fixing calorimetry tower η at 5. Note that the lateral leakage is almost energy independent since the clustering algorithm does not add towers with $E_T < 0.1$ GeV. Applying the estimated lateral leakage in Fig. 9.12 to the candidate clusters according to the E_T and η_{det} spectra of the photon sample, the lateral shower leakage for prompt photons is estimated as shown in Fig. 9.13 (a).

As we mentioned previously, the isolation threshold is 2 GeV for the prompt photon studies in the central region [4], while one in the endplug region is 3 GeV. We have increased the threshold as the underlying energies and the lateral shower leakage are larger in the endplug region than in the central. The former is estimated to be 0.49 GeV as shown in Fig. 9.10, and the latter becomes 0.49 GeV as shown in Fig. 9.13 (a). Therefore, both cuts in the central and the endplug regions are considered to be consistent

for prompt photons. As we will see later in Chapter 10, there is an uncertainty due to the isolation cut in theoretical calculations, especially in the bremsstrahlung process. If the isolation cuts in both central and endplug regions are common, the measured cross sections for prompt photon production in two regions are equally compared with QCD calculations.

The lateral energy flow $E_T^{iso}(0.7)$ for prompt photons, which is the combination of the underlying E_T and the lateral shower leakage, is obtained as shown in Fig. 9.13 (b). From the expected spectra, the efficiency for the cut " $E_T^{iso}(0.7) < 3$ GeV" is obtained $0.901 \pm 0.007 / -0.008$.

9.4.3 E^{had}/E^{EM}

A small portion of the electromagnetic cascade longitudinally leaks out to the corresponding hadron calorimeter. It carries a finite value of the E^{had}/E^{EM} ratio. An efficiency for the cut " $E^{had}/E^{EM} < 0.05$ " is 0.99 ± 0.01 estimated using electrons from W decays [51]. It should not, however, be the same for photons since the average longitudinal shower shape of photons is different from that of electrons as shown in Fig. 9.14, and larger energy deposits in the hadron calorimeter are expected for photons. The efficiency to the cut " $E^{had}/E^{EM} < 0.05$ " for prompt photons should be smaller than that for electrons.

The GEANT3 simulation is employed for an estimation of the efficiency. Figure 9.15 shows E^{had}/E^{EM} ratios for photons and electrons. The cut efficiencies for photons (electrons) at $\eta = 1.72$ are

$$\begin{array}{lll} 0.989 \pm 0.003 & (0.999 \pm 0.001) & \text{for } E_T = 30 \text{ GeV and} \\ 0.976 \pm 0.005 & (0.995 \pm 0.002) & \text{for } E_T = 37 \text{ GeV.} \end{array}$$

As expected, efficiencies for photons are smaller.

The efficiency should vary not only with the energy but also with the incident angle since the thickness of the PEM changes as $1/\cos\theta$, where a higher efficiency is expected for higher θ , and vice versa. Figure 9.16 shows energy and θ dependences of

the E^{had}/E^{EM} cut. The efficiency is rather dominated by the incident energy than the polar angle θ , and we consider only the energy dependence. Making a linear fit to the efficiency as a function of the photon energy and applying it to the energy spectrum of the photon candidates, the efficiency is estimated to be 0.985 ± 0.010 , where an error of 1% is assumed on the fit. This is somewhat overestimated, but it should safely covers any uncertainties on the simulation.

9.4.4 $\chi_{3 \times 3}^2$ (old) and $\chi_{3 \times 3}^2$

Assuming no difference in the lateral shower profile between photons and electrons, efficiencies for the $\chi_{3 \times 3}^2$ (old) and $\chi_{3 \times 3}^2$ cuts are estimated with test beam electrons.

Figures 9.17 and 9.18 show the old and the new $\chi_{3 \times 3}^2$ for test beam electrons with respect to the beam energy E and the pseudorapidity η , respectively. The beam energy is scanned with the position fixed at the center of calorimetry tower 5 ($\eta = 1.45$ or $\theta = 24.33^\circ$), and the position is scanned with the energy fixed to 101 GeV.

One notices that $\chi_{3 \times 3}^2$ (old) has a slight position dependence, while the new one does not. It comes from the fact that $\chi_{3 \times 3}^2$ (old) is calculated by assuming the shower center to be at the center of the tower. The beam energy dependence is due to the above reason since the beam energy is correlated with the position η , which is 2 – 8 mm/GeV depending on the current of the dipole magnets. The $\chi_{3 \times 3}^2$ distribution changes around η of 1.8. The incontinuity of the distribution at $\eta \sim 1.8$ in $\chi_{3 \times 3}^2$ for the position scan due to the strip chambers (Chapter 2). Since the strip chambers cover $1.2 < \eta < 1.8$, the shower position measurement makes use of the cathode pads for $\eta > 1.8$, and $\chi_{3 \times 3}^2$ values become larger due to relatively poor position measurement.

For the beam energy scan, only 12 events failed the old $\chi_{3 \times 3}^2$ cut out of 2344 with no typical energy dependence, and only one failed the new. For the η position scan, only one failed each cut out of 3192 events. Since no dependence of the cut efficiency is seen with this statistics, we adopt the numbers for both scans and obtain the efficiency to be 5523/5536 for the old cut and 5534/5536 for the new. Statistical errors in the above efficiencies are taken as the corresponding inefficiencies, which are $1-5523/5536$ and $1-5534/5536$, and they should safely cover the true value. No events have failed

both cuts, and we also assumed there is no correlation between the cuts. Finally, we have estimated the efficiency for both $\chi_{3 \times 3}^2$ cuts to be 0.997 ± 0.002 .

9.4.5 VTPC Hit Occupancy

The VTPC requirement rejects prompt photon events when charged particles accidentally overlap the photons. Figure 9.19 (a) shows a distribution of VTPC hit occupancies R_{VTPC} along randomly placed roads between the vertex and the PEM for minimum bias events. This represents an approximate overlap of a charged particle with a prompt photon. The efficiency for the cut " $R_{VTPC} \leq 0.8$ " is calculated 0.972 ± 0.001 .

9.4.6 Vertex

An efficiency for the z vertex cut is estimated using the photon candidates shown in Fig. 5.1. The efficiency for the cut " $|z_{vertex}| < 50$ " cm is found to be 0.931 ± 0.004 .

9.4.7 Geometrical Acceptance

The geometrical acceptance is defined by a ratio of the numbers of good (active) towers to all towers. We have seen in Section 6.1 there were many towers inactive or inoperative in the PEM. The numbers of towers for all, quadrant edges, dead, miscabled, and good are summarized with respect to the TOWE number in Table 9.5 together with acceptances. Applying the acceptance at each tower annulus to the η^{det} spectrum of the prompt photon candidates, the total geometrical acceptance is evaluated to be 0.757 ± 0.015 .

9.4.8 Level 2 Clustering Inefficiency

There was a problem in the level 2 trigger system as shown in Fig. 9.7. We estimate this inefficiency using EM clusters without biased by the level 2 trigger in a similar way as done in Section 9.4.1.

Figure 9.20 shows position distributions of off-line EM clusters with no level 2 trigger requirements. $E_T^{det} > 20$ GeV, $E^{had}/E^{EM} < 0.05$, $\chi_{3 \times 3}^2(\text{old}) < 20$, $\chi^2 < 5$, $|z_{vertex}| < 50$ cm, and the fiducial cuts are required for level 2 trigger unbiased clusters.

Tower #	All	Edge	Dead	Miscabled	Good	Acceptance
64	72	8	3	6	55	0.764
63	72	8	3	6	55	0.764
62	72	8	0	6	58	0.806
61	72	8	0	6	58	0.806
60	72	8	0	6	58	0.806
59	72	8	5	6	53	0.736
58	72	8	5	6	53	0.736
57	72	8	9	6	49	0.681
56	72	8	12	6	46	0.639
55	72	8	12	6	46	0.639

East PEM ($\eta > 0$)

Tower #	All	Edge	Dead	Miscabled	Good	Acceptance
30	72	8	6	5	53	0.736
29	72	8	3	5	56	0.778
28	72	8	6	5	53	0.736
27	72	8	3	5	56	0.778
26	72	8	5	5	54	0.750
25	72	8	2	5	57	0.792
24	72	8	5	5	54	0.750
23	72	8	5	5	54	0.750
22	72	8	5	5	54	0.750
21	72	8	2	5	57	0.792

West PEM ($\eta < 0$)

Table 9.5: Number of bad towers and geometrical acceptances for Towers in the PEM. Tower number is in the TOWE number. See also Fig. 6.1.

No strange pattern is observed at higher η of the east PEM. Figure 9.21 shows those with the existence of the corresponding level 2 trigger EM clusters required. The strange pattern is barely recognizable. Figure 9.22 displays those with the non-existence of the corresponding level 2 clusters required. Cluster positions are hardly seen as the strange pattern. However, the distributions are noticeably different between the east and the west. The level 2 clustering efficiency due to this problem is estimated from the numbers of clusters in the east and the west for $|\eta| > 1.86$.

The numbers of clusters in η_{det} ranges are listed in Table 9.6 with and without a requirement of the existence of the corresponding level 2 EM clusters, together with efficiencies. Neglecting any differences in the η distributions of clusters between the

η range	# of clusters		Clustering efficiency [%]
	not required	L2 required	
1.86 to 2.22	387	252	65.1 ± 2.4
1.32 to 1.86	830	805	97.0 ± 0.6
-1.86 to -1.32	946	932	98.5 ± 0.4
-2.22 to -1.86	449	433	96.4 ± 0.9

Table 9.6: Numbers of clusters in η_{det} ranges with and without requiring the corresponding level 2 clusters.

level 2 trigger unbiased sample and the prompt photon sample, the level 2 clustering efficiency in the region of $1.86 < \eta_{det} < 2.22$ is 0.675 ± 0.026 due to the problem. And, the efficiency to all the prompt photon candidates becomes 0.959 ± 0.008 .

9.4.9 $K_S^0 \rightarrow \pi^0 \pi^0$

The lightest strange meson can be the third source of the background. The K_S^0 meson has a $\pi^0 \pi^0$ decay mode with the branching fraction of $31.39 \pm 0.28\%$ [42]. The pure neutral decay into four photons is $30.6 \pm 0.3\%$. Though it is not small, such decays are not expected as a significant source of the background because of the K_S^0 life time. The mean life time of the K_S^0 meson is $(0.8926 \pm 0.0012) \times 10^{-10}$ s. Since the distance between the vertex and the PEM ~ 185 cm at $\theta = 20^\circ$, only 43% (27%) of K_S^0 mesons with $P = 87$ GeV/c (108 GeV/c), corresponding to $P_T = 30$ GeV/c (37 GeV/c) at

$\theta = 20^\circ$, decay before they reach the PEM.

The production ratio of K_S^0 to π^0 in $\bar{p}p$ collisions at $\sqrt{s} = 1.8$ TeV was measured to be $K_S^0/\pi^0 = 0.4$ by the CDF experiment using charged decay modes [52]. This production ratio is used to estimate the decay of K_S^0 .

From the production rate and the decay fraction including the life time effect, we expect only 2.4% of the background events coming from the K_S^0 decay. Figure 9.23 (a) shows the contribution of K_S^0 to the FSEF spectrum of the background. Note that some of K_S^0 's decay inside the PEM, and such events may leave no energy deposits in the first segment but in the other segments. However, most of these decays are rejected by the E^{Had}/E^{EM} cut. There still remain a few events, and they make a small bump in the first bin of the FSEF distribution as barely seen in Fig. 9.23 (a).

Fitting the Monte Carlo FSEF spectra of single photons and the total background to that of the prompt photon candidates, the number of prompt photon events is extracted 2140 ± 138 as shown in Fig. 9.23 (b). Comparing this with the number in Fig. 9.4 (c), the systematic uncertainty by the K_S^0 decay is obtained to be 0.8%.

9.4.10 η/π^0 Ratio

The isolated production ratio of η and π^0 mesons was obtained to be 1.02 ± 0.15 (stat.) ± 0.23 (syst.) [4]. We estimate systematics due to this uncertainty of the meson production ratio. Varying the ratio by $\pm 1\sigma$, the mesons are mixed at ratios of $1.02 - 1\sigma$, $1.02 - 1/2\sigma$, $1.02 + 1/2\sigma$, and $1.02 + 1\sigma$. Some of the FSEF spectra for the background are presented in Fig. 9.24. With different FSEF spectra for the background, the fitting are made to the data to obtain the systematic error in the number of prompt photons. As shown in Fig. 9.25, only slight changes are observed. Changes in the number of prompt photons are found to be -59 to $+9$ for the nominal number of 2157, and the systematics due to the uncertainty of the π^0/η production ratio is estimated to be $+0.4/-2.7\%$.

9.4.11 Electron Contamination

Since the sensitivity for the VTPC wires is expected to drop near the radial boards, the hit efficiency to a charged particle falls there. Due to this hit inefficiency, some

electrons are misidentified as photon candidates. Such electron contamination in the prompt photon sample is estimated from the hit inefficiency and the production rate of electrons.

The hit inefficiency is estimated with W electrons. Events are selected by the same requirements as used in Section 8.1 except for the VTPC and E_T cuts, no requirement on the VTPC hits and $20 \text{ GeV} < E_T < 60 \text{ GeV}$ required. Figure 9.19 (b) shows the distribution of VTPC hit occupancy for the W electrons, and the hit inefficiency is obtained to be 0.057 ± 0.012 .

The isolated production ratio of electrons and neutral particles (photons, π^0 's, and η 's) is estimated from numbers of events in the two peaks of Fig. 9.19 (c). The plot shows a distribution of the VTPC hit occupancy for isolated EM clusters in the endplug region, which are selected by the requirements in Table 9.1 except for the VTPC cut. Assuming that events with $R_{VTPC} > 0.8$ are all electrons and the rest are all neutral particles, the isolated production ratio of electrons to neutral particles is estimated to be 0.344 ± 0.011 . Hence, the prompt photon sample is expected to contain 80 ± 20 electrons in the 3995 candidates.

The photon sample contains electron events at a rate of $2.0 \pm 0.5\%$. Or, assuming the signal to background ratio is unity, $4 \pm 1\%$ of the background events are expected to be electrons. Following the E_T and η spectra of the prompt photon candidates, electrons are simulated and added to the meson background at the above contamination rate. Figure 9.26 shows FSEF spectra for the background with the electron contamination.

The FSEF spectrum of the data is fitted with those of the single photons and the backgrounds at the electron contamination rates of $e^-/\text{b.g.} = 3, 4, \text{ and } 5\%$ as shown in Fig. 9.27. Though the electron contamination rate is an order of a few percent, change in the number of prompt photons is only -0.8 to $+0.5\%$ to the nominal number in Fig. 9.4 (c). Taking the maximum change, the uncertainty due to the electron contamination is estimated to be 0.8% .

9.4.12 Other Uncertainties

As we have studied in Chapter 7, the systematic uncertainty for the GEANT3 simulation is estimated from changes in the shower shape when the thickness of the aluminum plate is varied by ± 0.39 cm. Applying this uncertainty to the linear fit in Fig. 9.5, we have evaluated the uncertainty for the GEANT3 simulation to be $\pm 13.8\%$.

In the same way, we estimate the systematics due to the uncertainty in the material thickness between the event vertex and the PEM. In Chapter 8, the material thickness was estimated to be 6.24 ± 0.31 cm thick aluminum along the z axis. The variation of ± 0.31 cm corresponds to the systematics of $\pm 11.0\%$.

The luminosity measurement has an uncertainty of 3.5% as described in Section 2.6.

Neutral mesons other than π^0 , η , or K_S^0 possibly give rise to another uncertainties. However, we have studied in this chapter that K_S^0 mesons add an uncertainty of 2.7% , which is still negligible compared to the uncertainties of the GEANT3 simulation and the materials. Thus, we neglect contributions of other neutral mesons such as ω and η' .

The efficiencies and the systematic uncertainties are summarized in Table 9.7.

Requirement / Variable	Efficiency	Uncertainty [%]
Level 2 trigger	0.648 +0.033/-0.034	+5.1/-5.2
$E_T^{iso}(0.7) < 3$ GeV	0.901 +0.007/-0.008	+0.8/-0.9
$E^{had}/E^{EM} < 0.05$	0.985 ± 0.010	± 1.0
$\chi_{3 \times 3}^2(old) < 20$ and $\chi_{3 \times 3}^2 < 5$	0.997 ± 0.002	± 0.2
$R_{VTPC} \leq 0.8$	0.972 ± 0.001	± 0.1
$ z_{vertex} < 50$ cm	0.931 ± 0.004	± 0.4
Geometrical acceptance	0.734 ± 0.015	± 2.0
Level 2 cluster problem	0.959 ± 0.008	± 0.8
η/π^0 ratio		+0.4/-2.7
$K_S^0 \rightarrow \pi^0 \pi^0$		± 0.8
Electron contamination		± 0.8
GEANT3 Simulation		± 13.8
Materials		± 11.0
Luminosity		± 3.5
Total	0.365 +0.057/-0.058	± 19.0

Table 9.7: Efficiencies and systematic uncertainties.

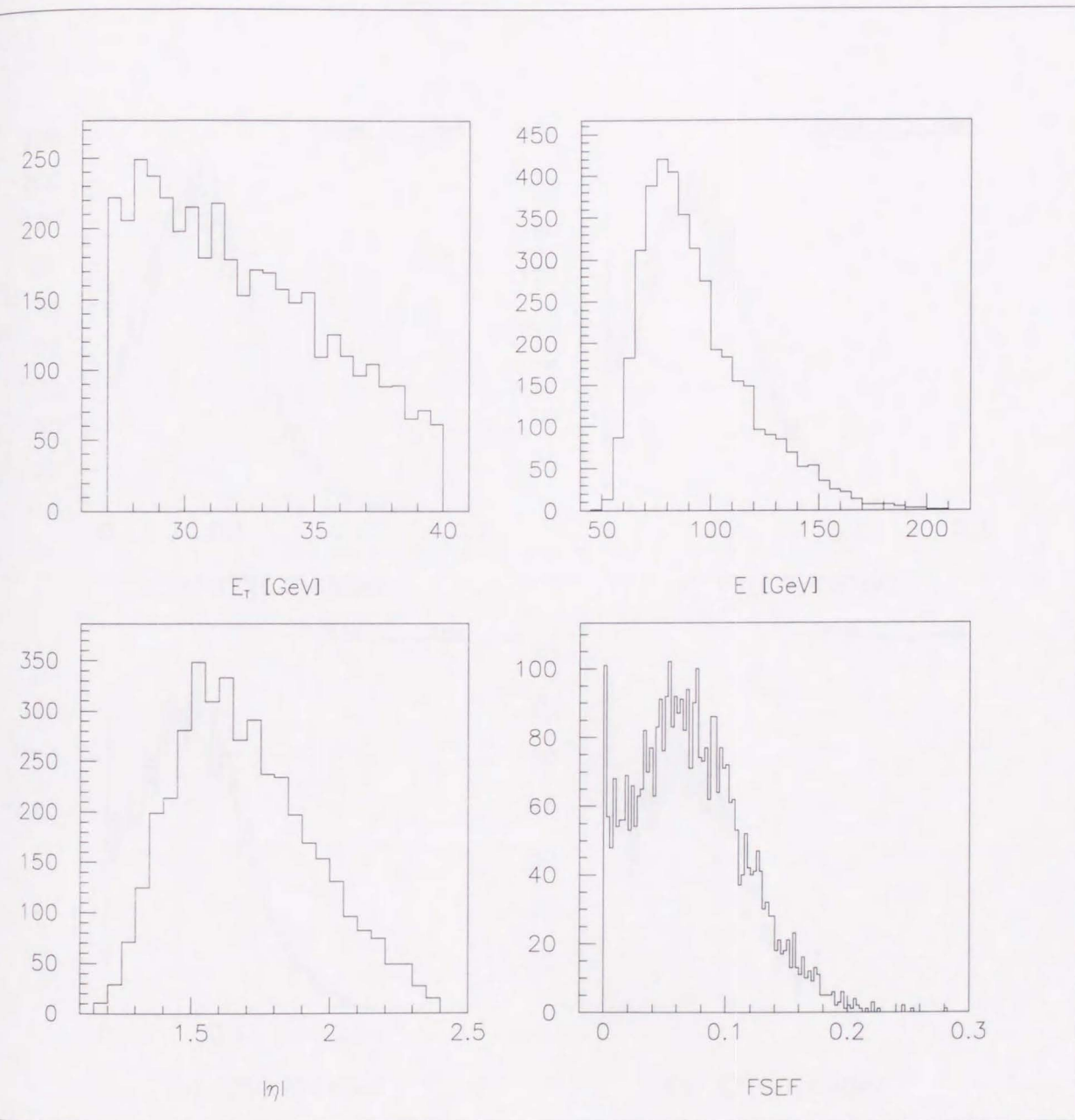


Figure 9.1: Distributions of E_T , E , $|\eta|$, and FSEF of the photon sample.

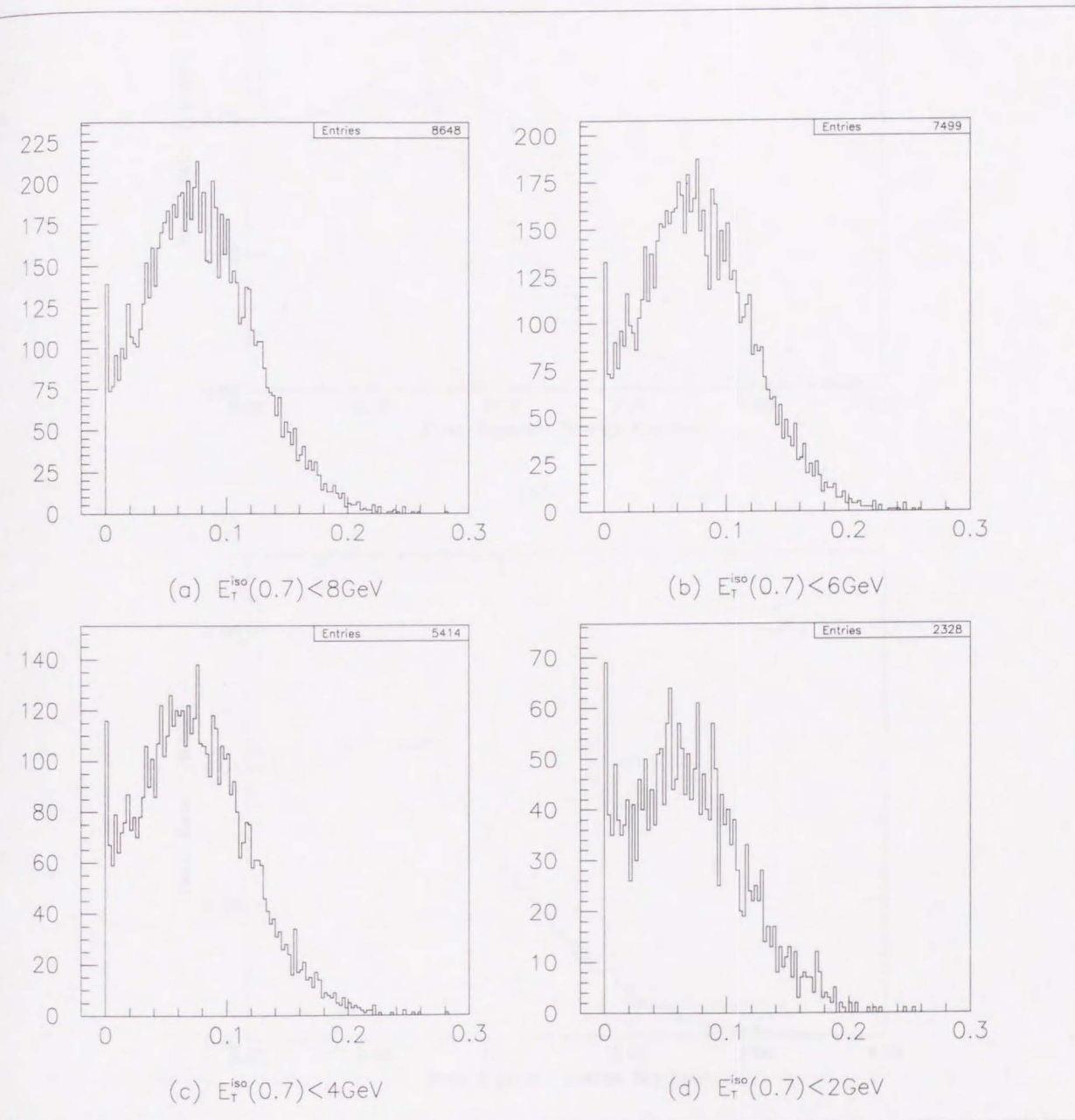
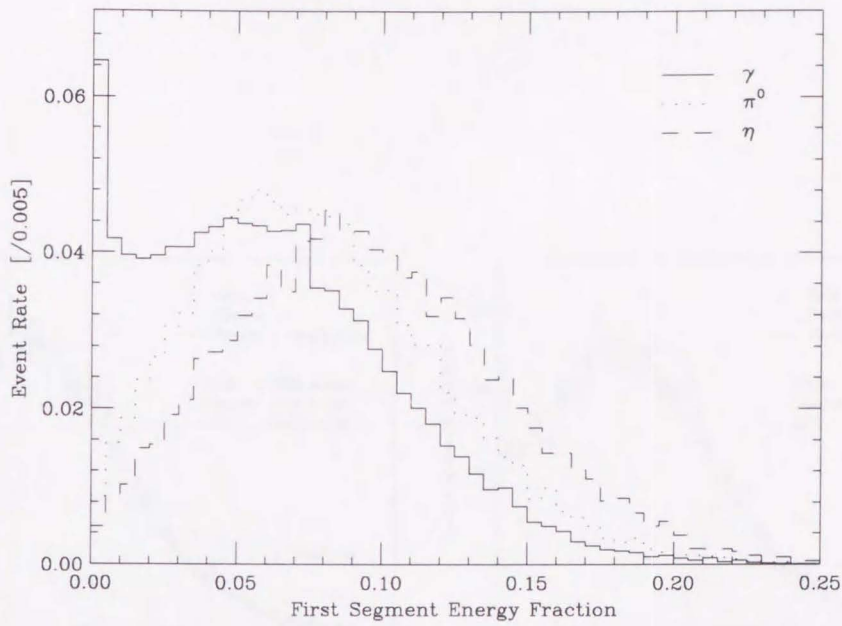
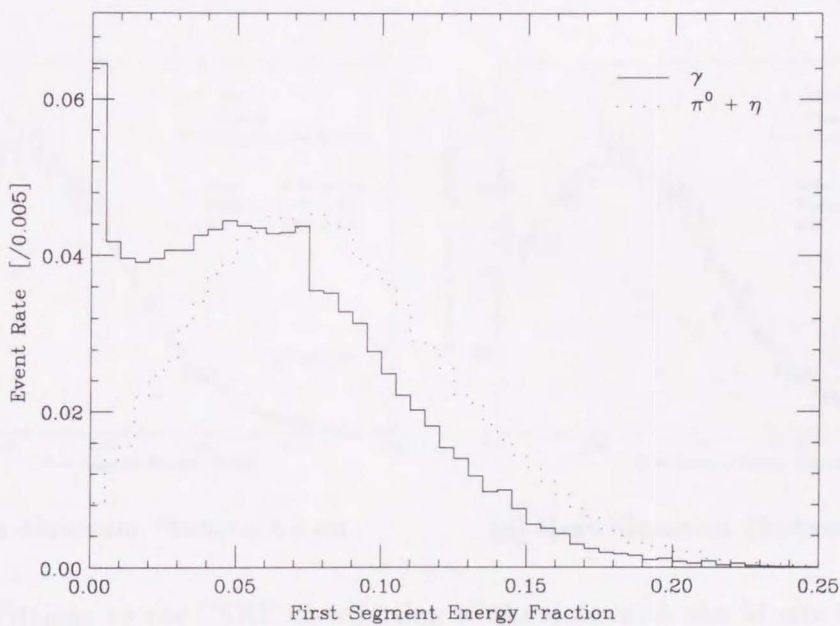


Figure 9.2: FSEF distributions for various isolation thresholds.

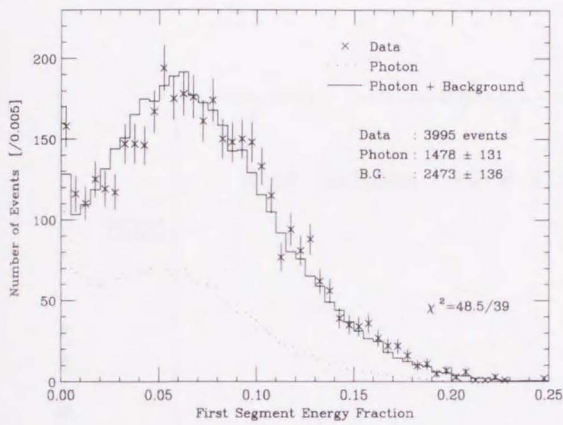


(a)

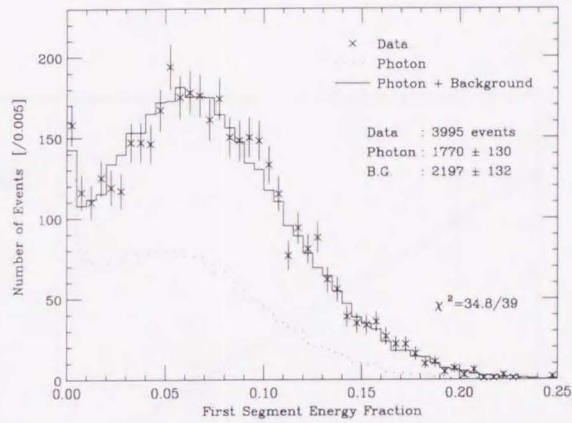


(b)

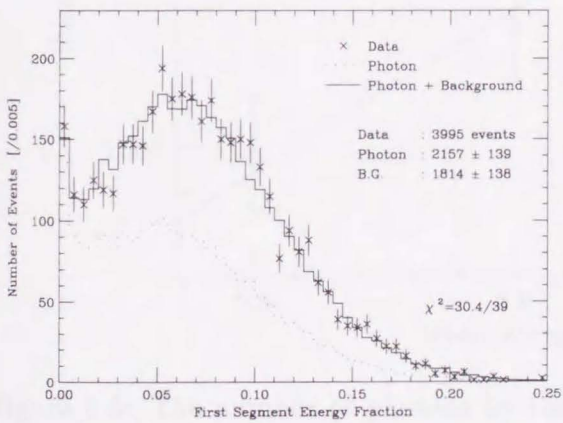
Figure 9.3: FSEF distributions of the GEANT3 simulation for single photons, π^0 's, and η 's. The mean thickness of the aluminum plate is 6.5 cm, and the gaussian σ is 2.0 cm. Only the neutral decay modes are simulated for mesons. Each spectrum is normalized to unity.



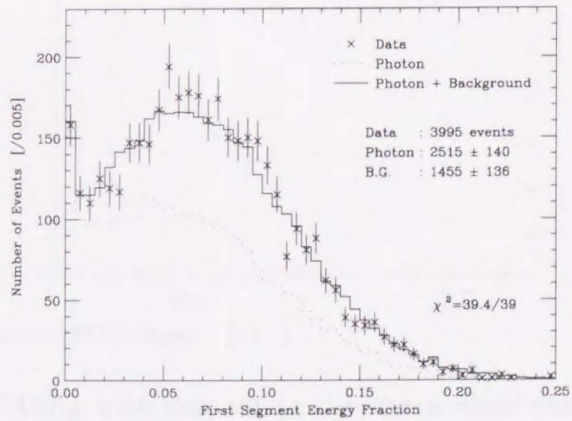
(a) Mean Aluminum Thickness 5.5 cm.



(b) Mean Aluminum Thickness 6.0 cm.



(c) Mean Aluminum Thickness 6.5 cm.



(d) Mean Aluminum Thickness 7.0 cm.

Figure 9.4: Fittings to the FSEF distribution of the data with the Monte Carlo spectra of photons and background mesons. Four sets of the Monte Carlo data with different means of the aluminum plate thickness are used. Bins of FSEF = 0.0 – 0.2 are used for the χ^2 calculation.

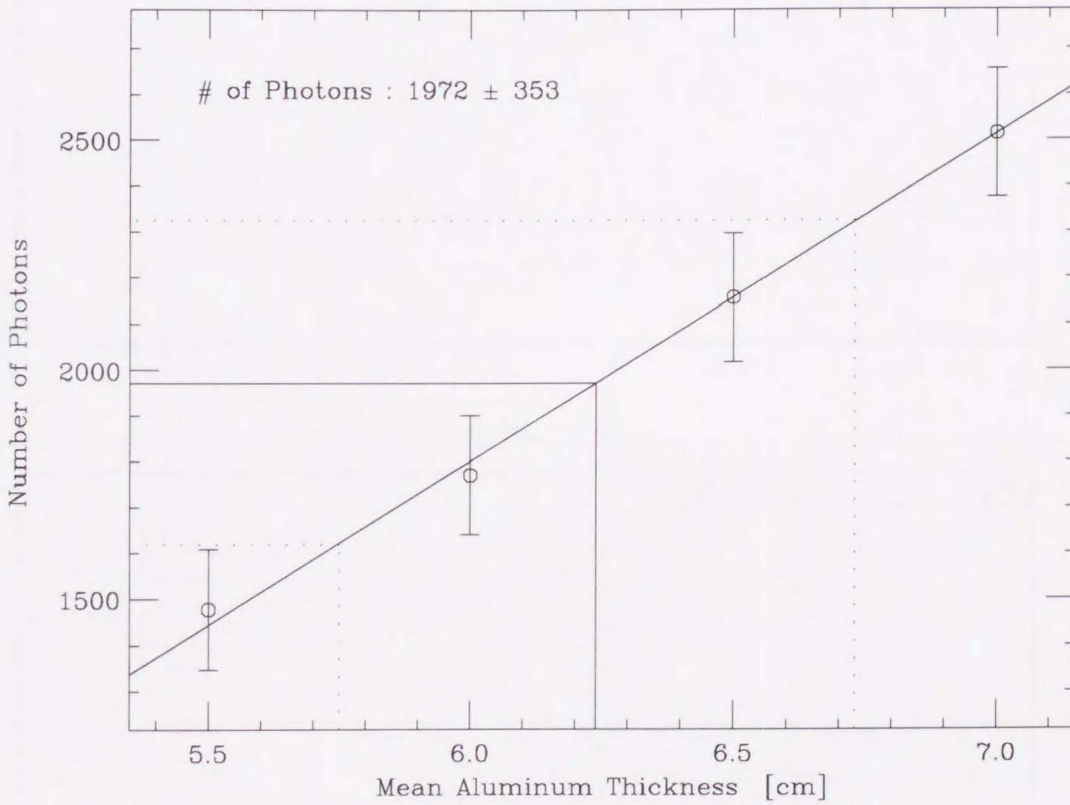


Figure 9.5: The number of photons by the fitting with respect to the mean aluminum thickness. For the nominal thickness (solid vertical line) of 6.24 cm, the number of photons is evaluated 1972. The error (dots) is estimated 353 for ± 0.51 cm, which is the sum of the uncertainties for the GEANT3 simulation, obtained $0.046 X_0$ in Section 7, and for the total amount of materials, obtained 0.31 cm thick aluminum in Section 8.

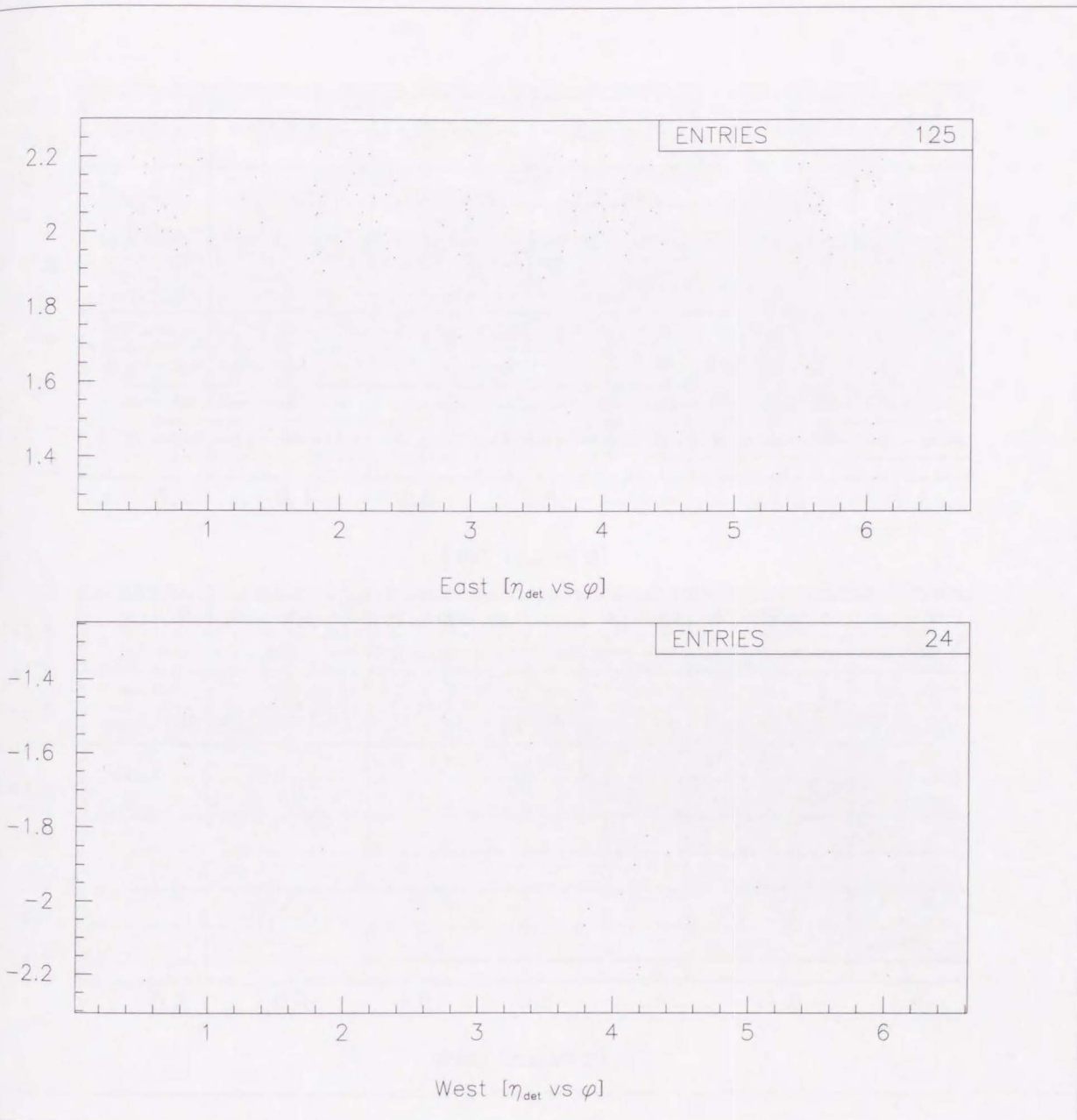


Figure 9.6: η_{det} - φ positions for off-line EM clusters with no corresponding level 2 trigger EM clusters. $E_T^{det} > 23$ GeV required for clusters.

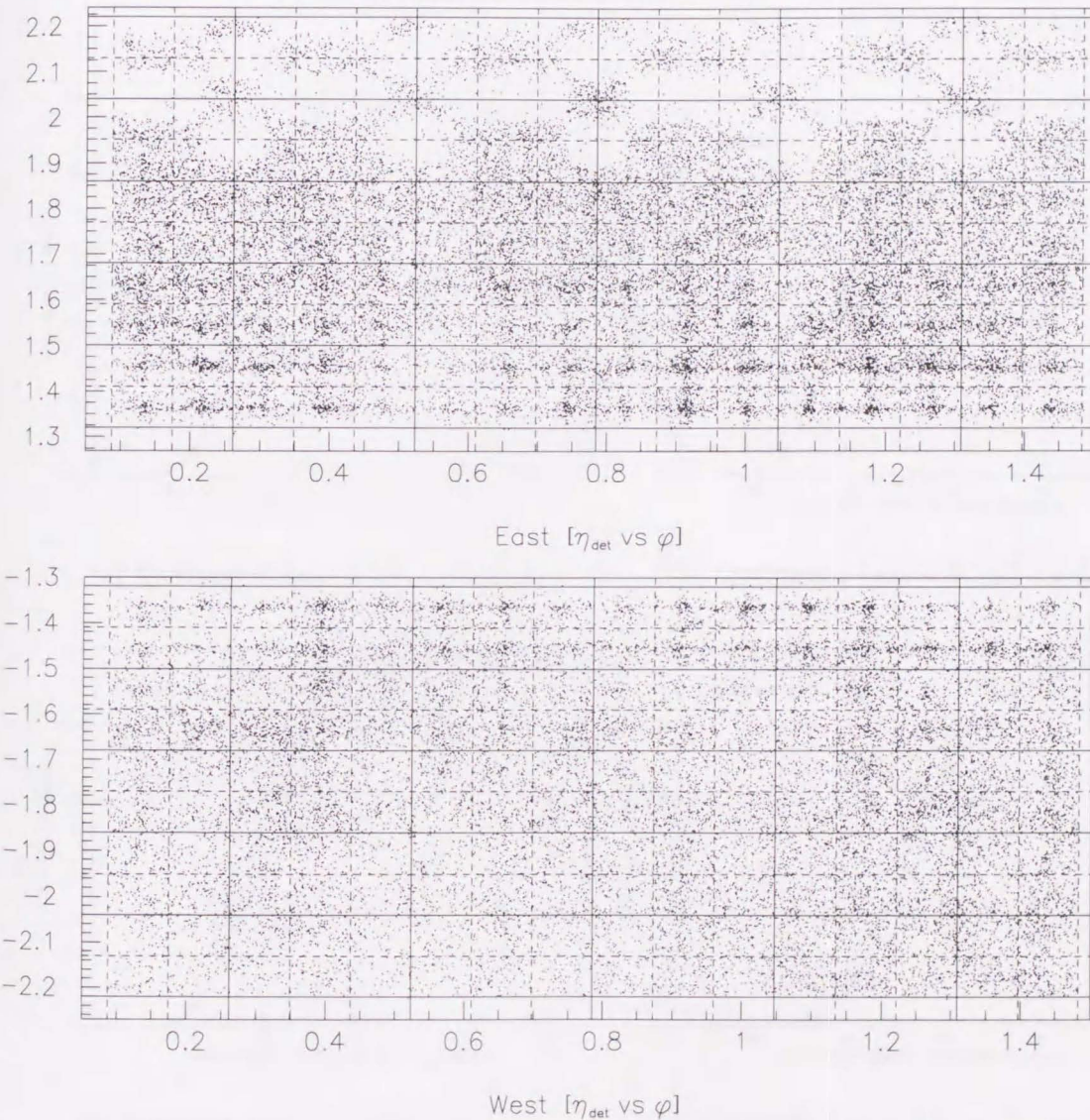


Figure 9.7: $\eta_{\text{det}}-\varphi$ positions for off-line clusters which passed the “gas photon 23 GeV” trigger. $E_T^{\text{det}} > 23$ GeV, $E^{\text{had}}/E^{\text{EM}} < 0.1$, and $\chi^2(\text{old}) < 20$ required. Four quadrants are overlaid for each east or west to enhance the pattern. Solid lines represent the level 2 trigger tower boundaries, and dashed lines are the off-line towers.

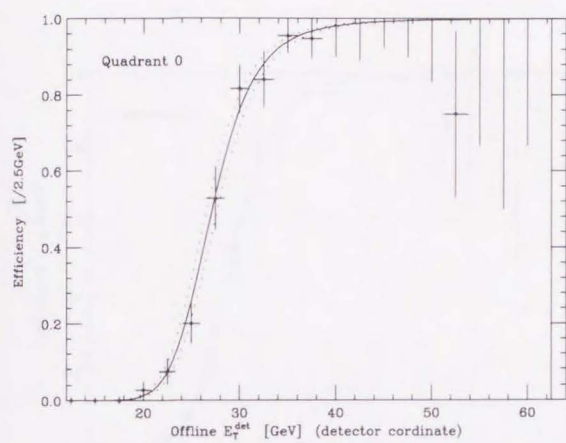
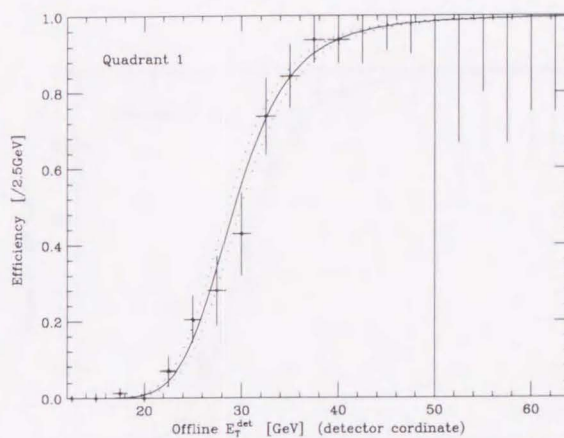
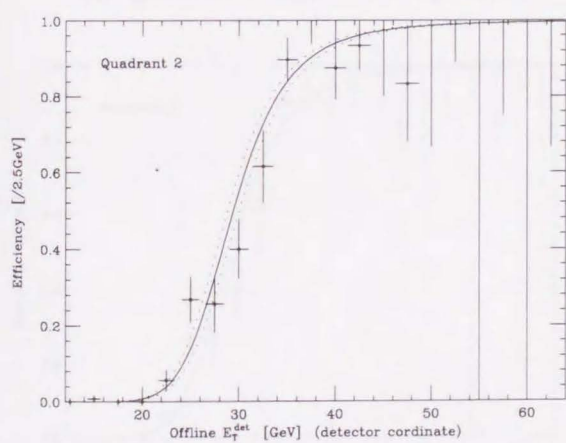
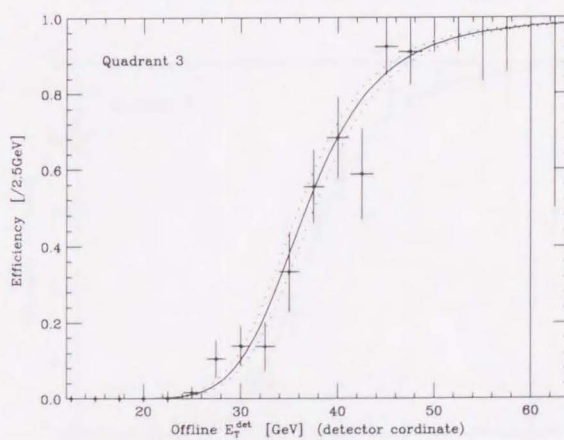
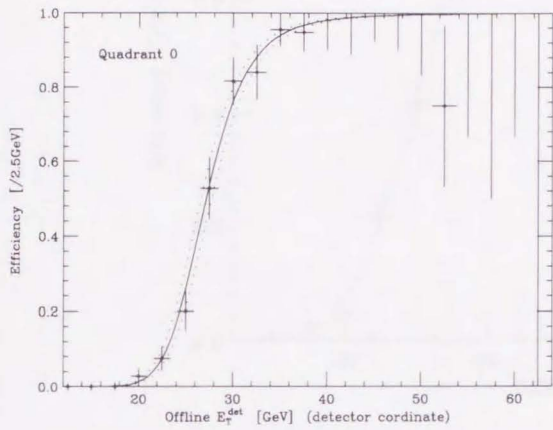
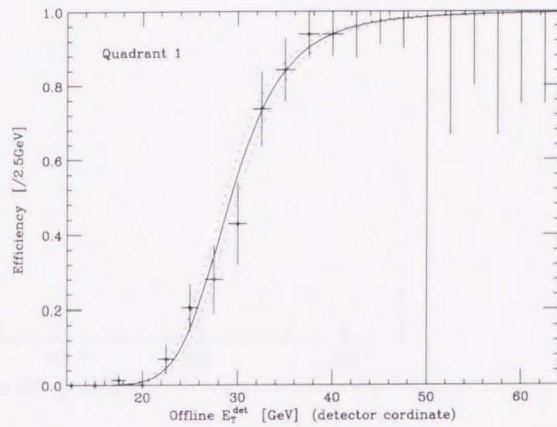
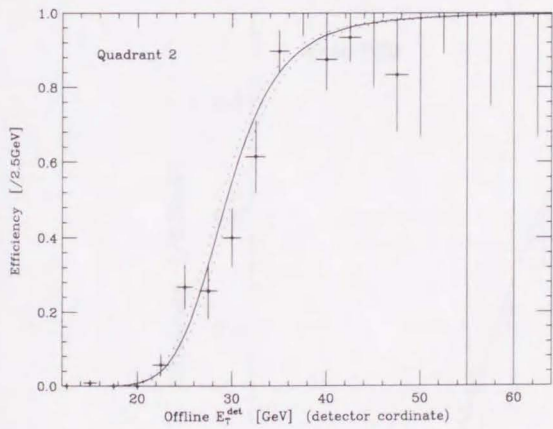
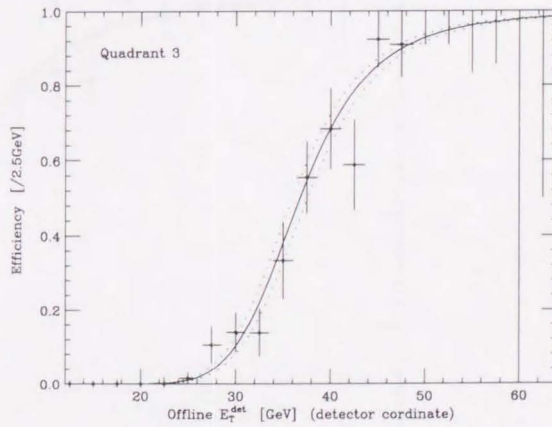
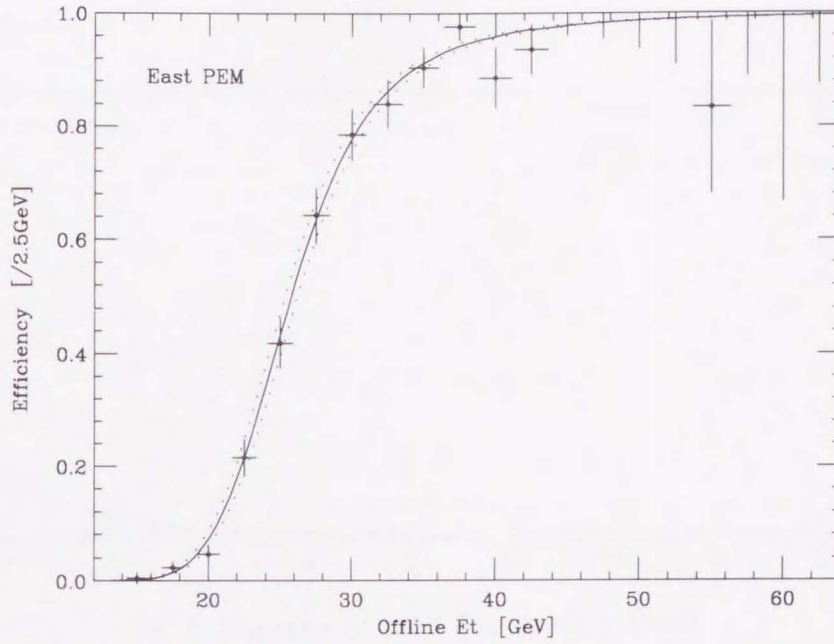
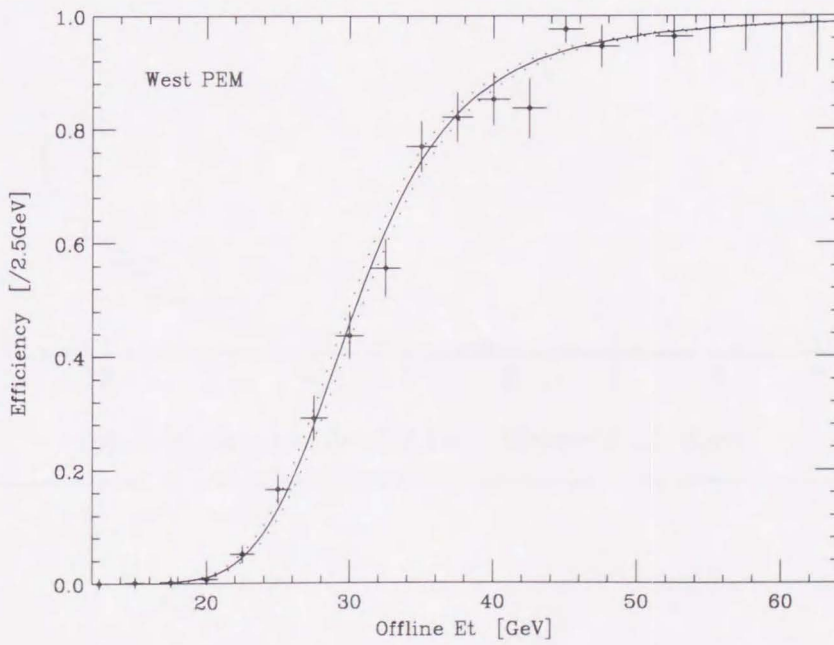
(a) Quadrant 0 ($\eta_{det} < 0, 0 < \varphi < \pi/2$)(b) Quadrant 1 ($\eta_{det} < 0, \pi/2 < \varphi < \pi$)(c) Quadrant 2 ($\eta_{det} < 0, \pi < \varphi < 3\pi/2$)(d) Quadrant 3 ($\eta_{det} < 0, 3\pi/2 < \varphi < 2\pi$)

Figure 9.8: The efficiencies for the level 2 trigger “gas photon 23 GeV.” Continues on the next page.

(e) Quadrant 4 ($\eta_{det} > 0, 0 < \varphi < \pi/2$)(f) Quadrant 5 ($\eta_{det} > 0, \pi/2 < \varphi < \pi$)(g) Quadrant 6 ($\eta_{det} > 0, \pi < \varphi < 3\pi/2$)(h) Quadrant 7 ($\eta_{det} > 0, 3\pi/2 < \varphi < 2\pi$)



(i) East PEM



(j) West PEM

Figure 9.9: The efficiencies for the level 2 trigger "gas photon 23 GeV."

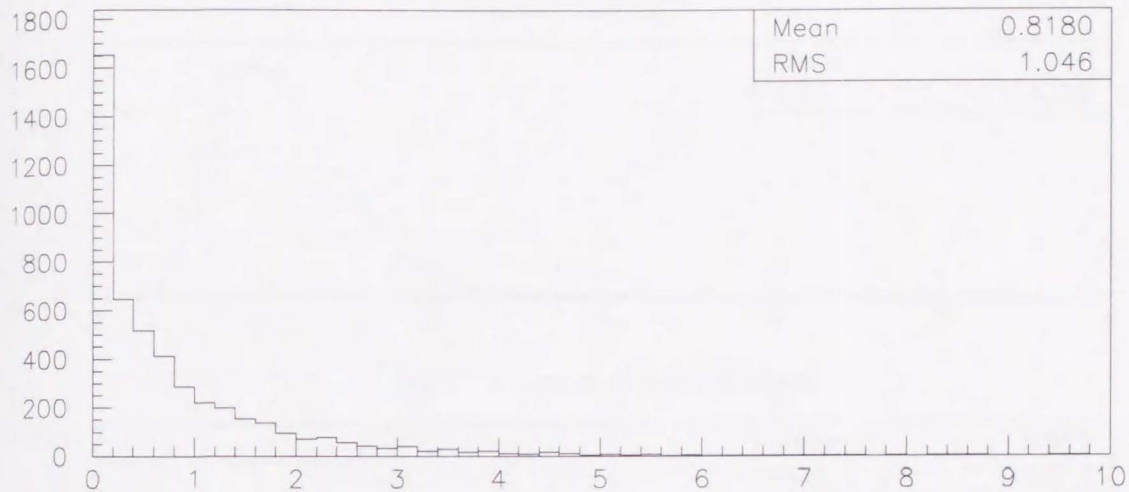
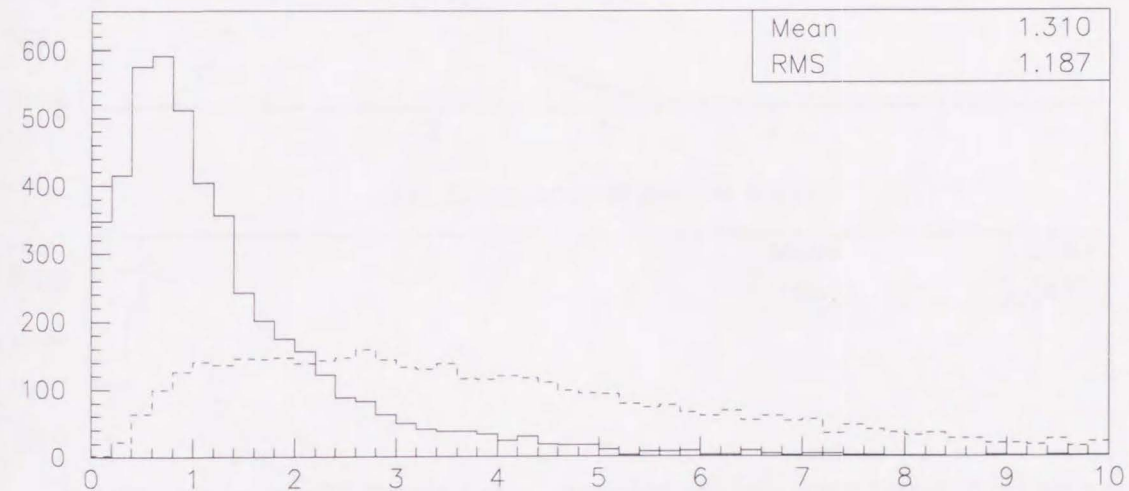
(a) E_T in a cone of $\Delta r=0.7$ for $|\eta|<0.9$ [GeV](b) E_T in a cone of $\Delta r=0.7$ for $1.32<|\eta|<2.22$ [GeV]

Figure 9.10: Distributions of E_T in a randomly placed cone of radius 0.7 for minimum bias events, approximating an underlying E_T distribution expected for prompt photon events in (a) the central region of $|\eta| < 0.9$ and (b) the endplug region of $1.32 < |\eta| < 2.22$. Dashed line in (b) show the $E_T^{iso}(0.7)$ distribution for the prompt photon candidates without the isolation cut, and the number of events are normalized to that of minimum bias events. Mean and RMS shown in (b) are for minimum bias events.

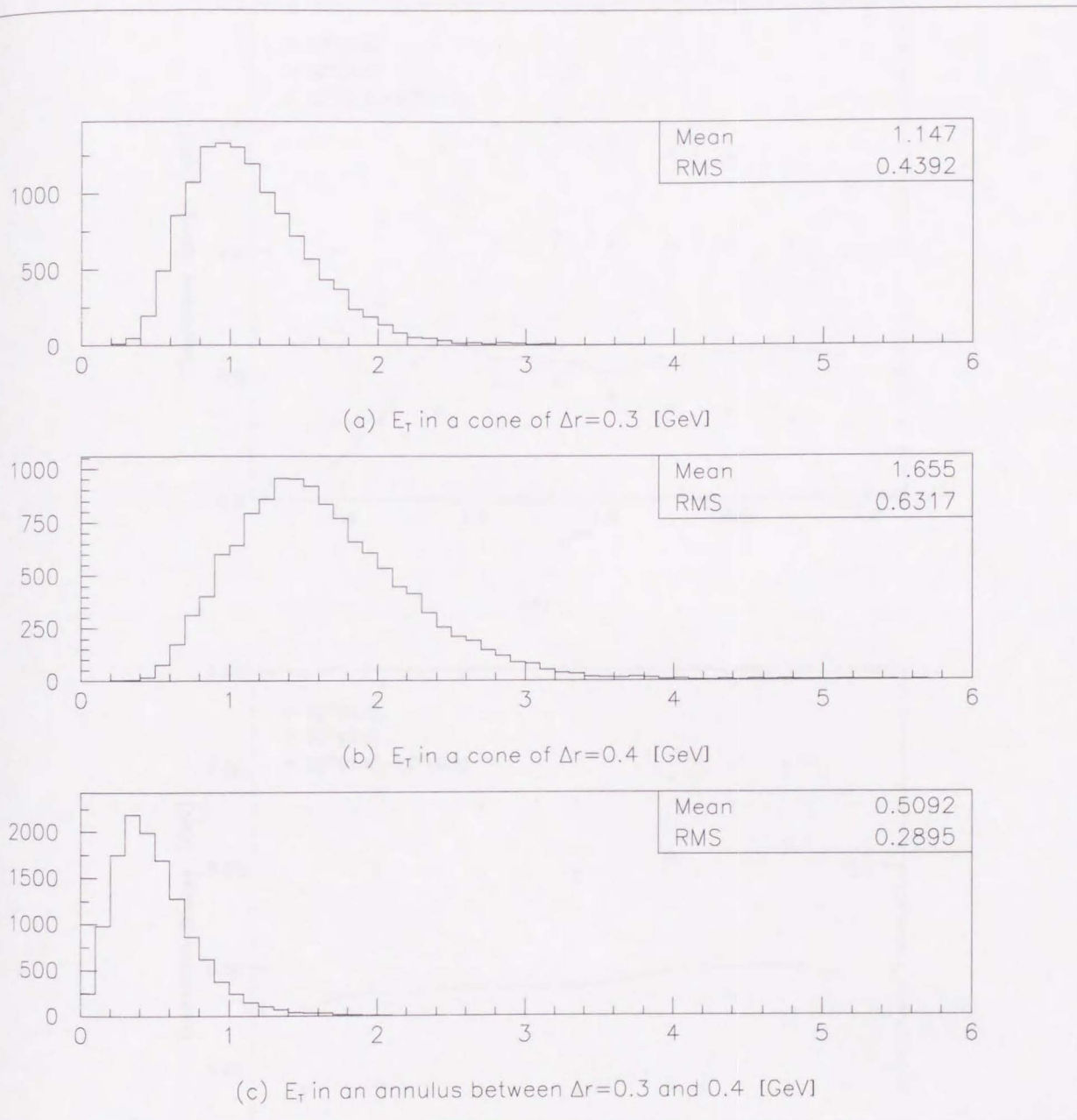
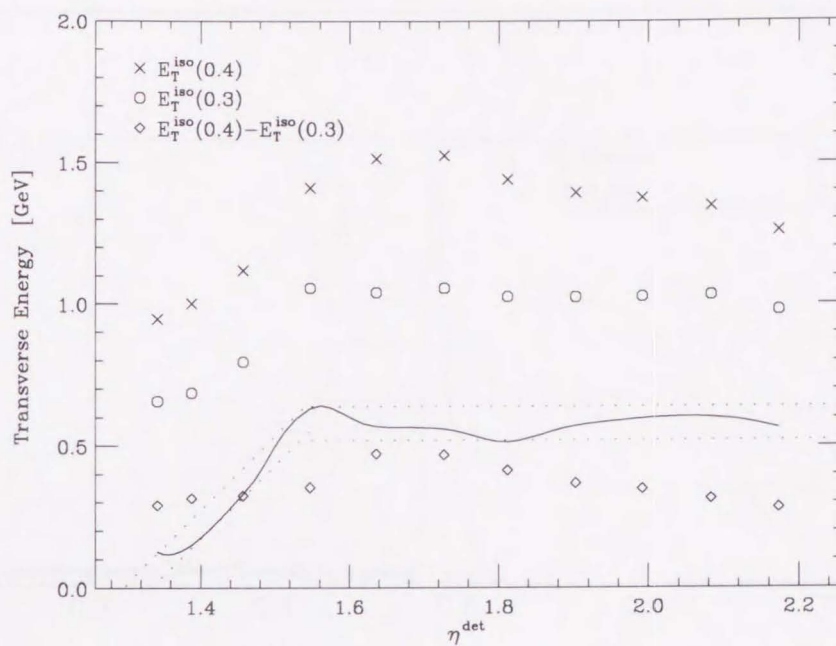
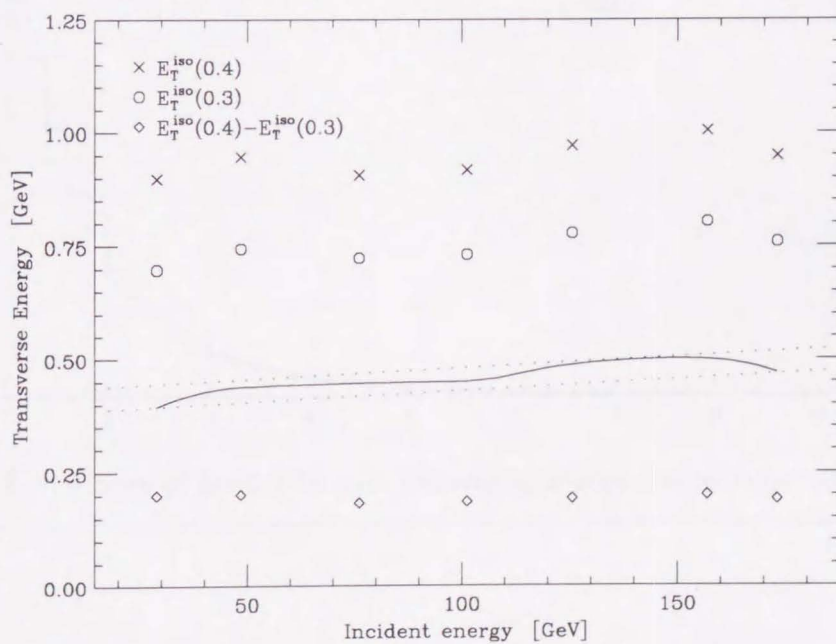


Figure 9.11: Distributions of (a) E_T in a cone of radius 0.3, (b) 0.4, and (c) in an annulus between radius 0.3 and 0.4 centered on test beam electrons of 101 GeV incident at the center of η tower 8 (local number), corresponding to $E_T = 35$ GeV.



(a)



(b)

Figure 9.12: Lateral shower leakage for an EM cluster represented in curves showing (a) η and (b) energy dependences. Note that the typical EM cluster size is $\Delta\eta \times \Delta\varphi \sim 0.1$.

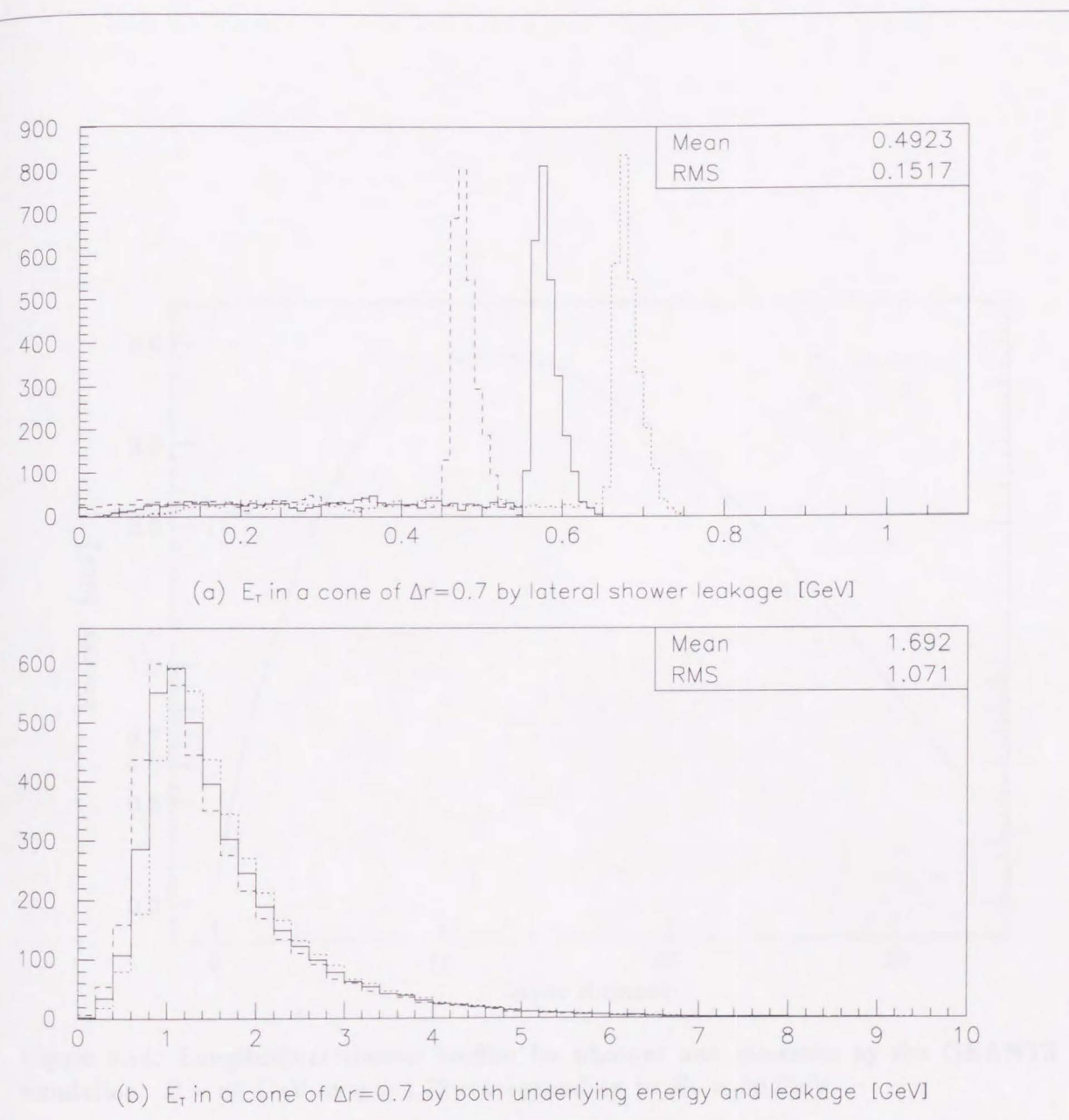


Figure 9.13: (a) E_T in a cone of radius 0.7 due to lateral shower leakage for prompt photon candidates. (b) Underlying E_T with lateral shower leakage. Solid lines represent the nominal value. Dashed lines and dots are the minimum and the maximum, respectively. The mean and RMS are for the nominal.

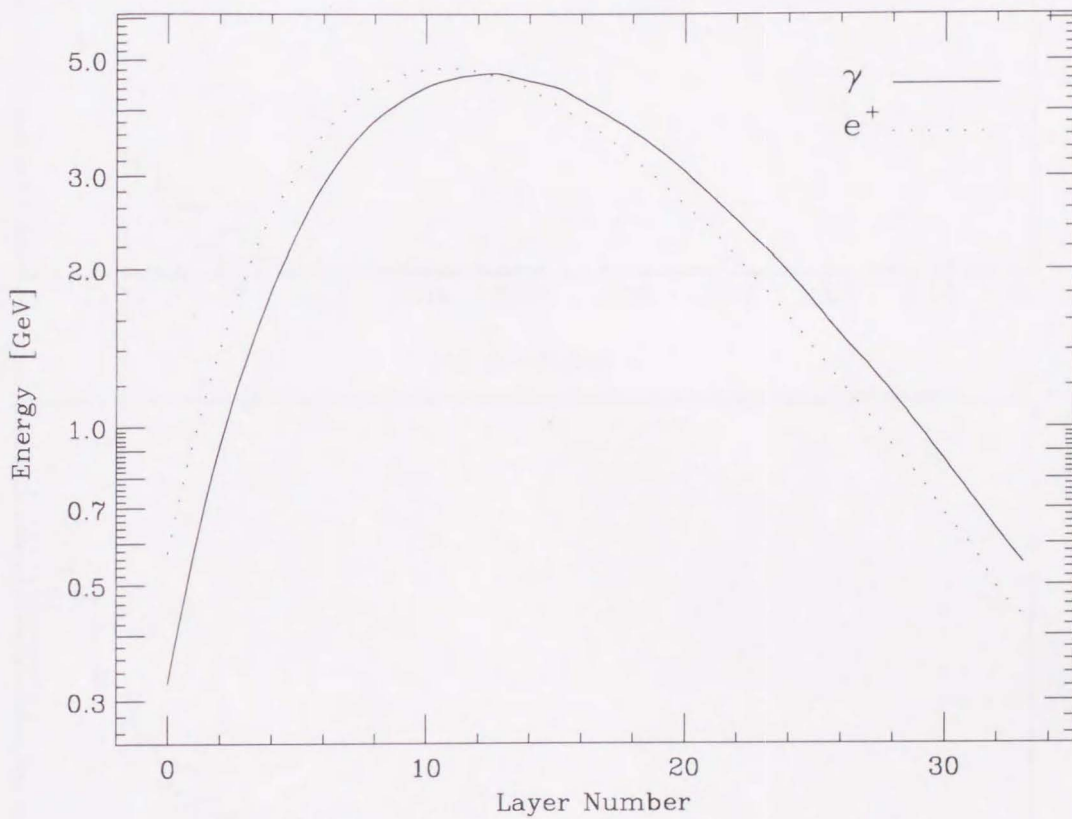


Figure 9.14: Longitudinal shower profiles for photons and electrons by the GEANT3 simulation. $E = 87$ GeV at $\eta = 1.72$ corresponding to $E_T = 30$ GeV.

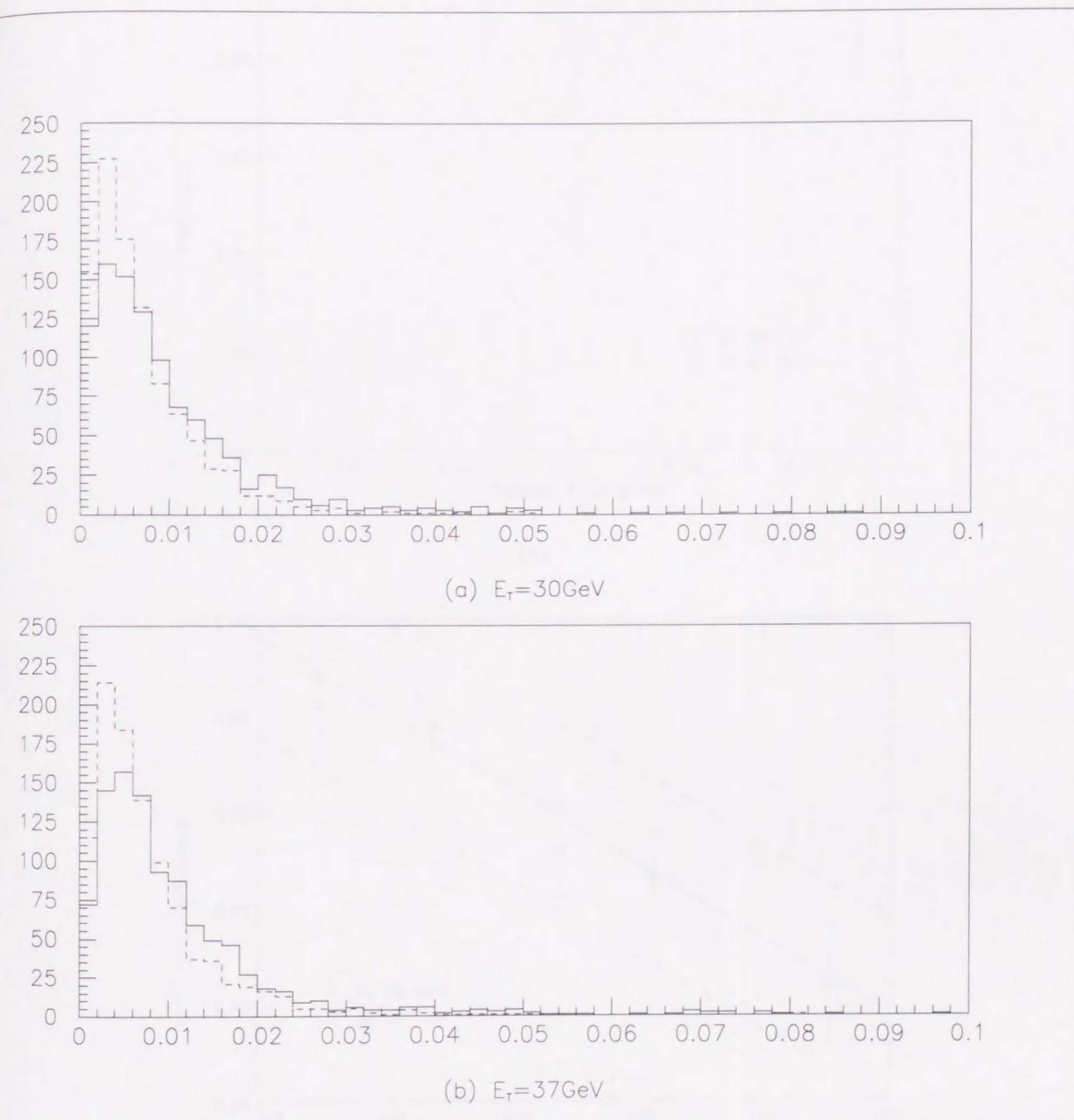
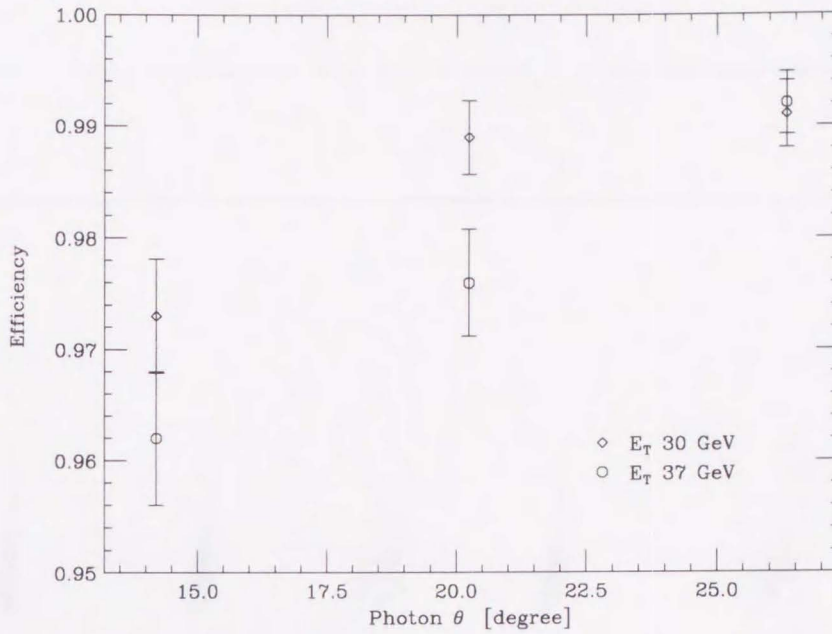
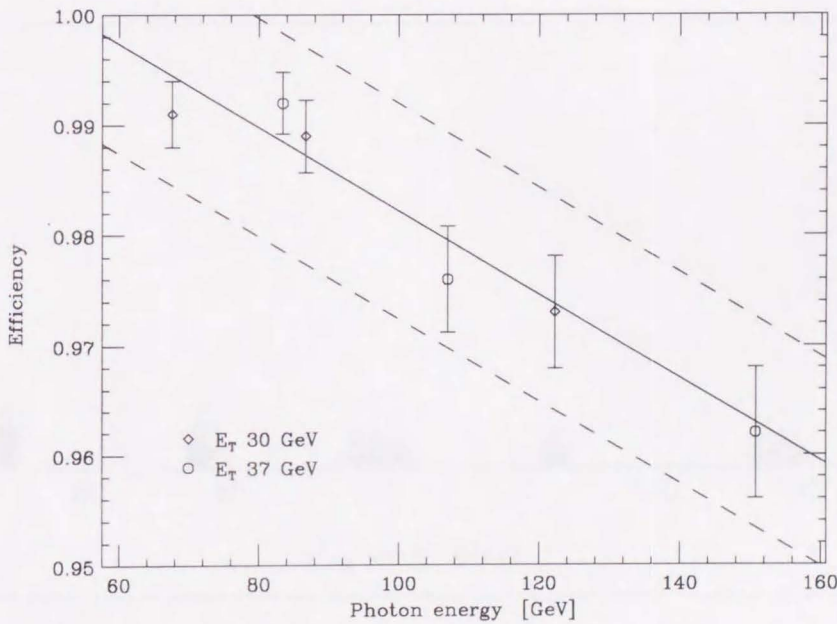


Figure 9.15: E^{had}/E^{EM} ratios for Monte Carlo photons (line) and electrons (dashed line). (a) $E = 87$ GeV at $\eta = 1.72$ ($E_T = 30$ GeV). (b) $E = 107$ GeV at $\eta = 1.72$ ($E_T = 37$ GeV).



(a)



(b)

Figure 9.16: (a) θ dependence of the cut " $E^{had}/E^{EM} < 0.05$." (b) Energy dependence of the cut " $E^{had}/E^{EM} < 0.05$." Solid line showing a linear fit, and dashed lines are 1% errors.

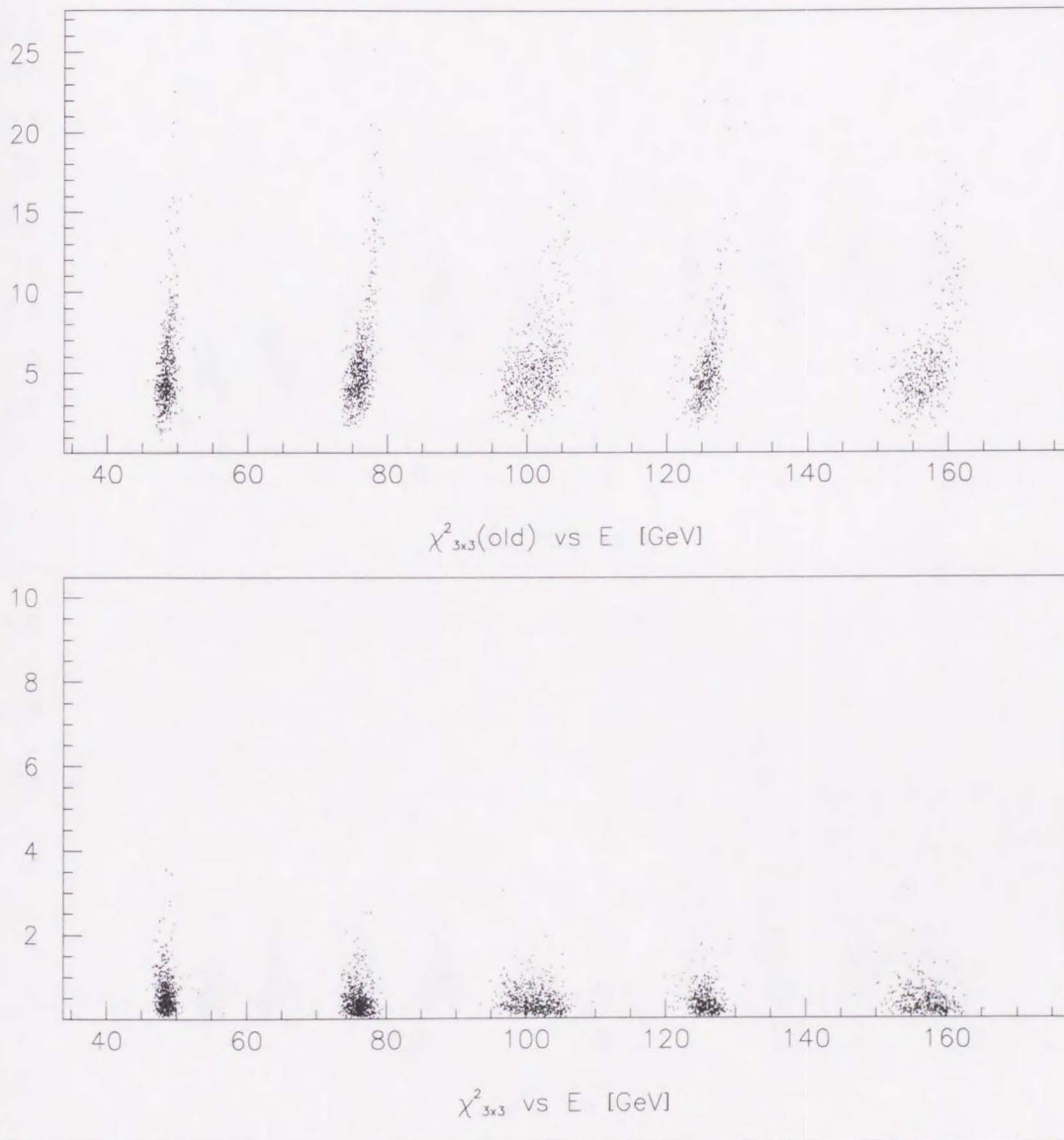


Figure 9.17: $\chi^2_{3 \times 3}$ vs energy for the old and the new. Test beam electrons incident at the center of calorimetry tower 5 ($\eta = 1.45$ or $\theta = 26.33^\circ$). Only 12 events with $\chi^2_{3 \times 3}(\text{old}) \geq 20$ and one with $\chi^2_{3 \times 3} \geq 5$ out of 2344 events. See text for details.

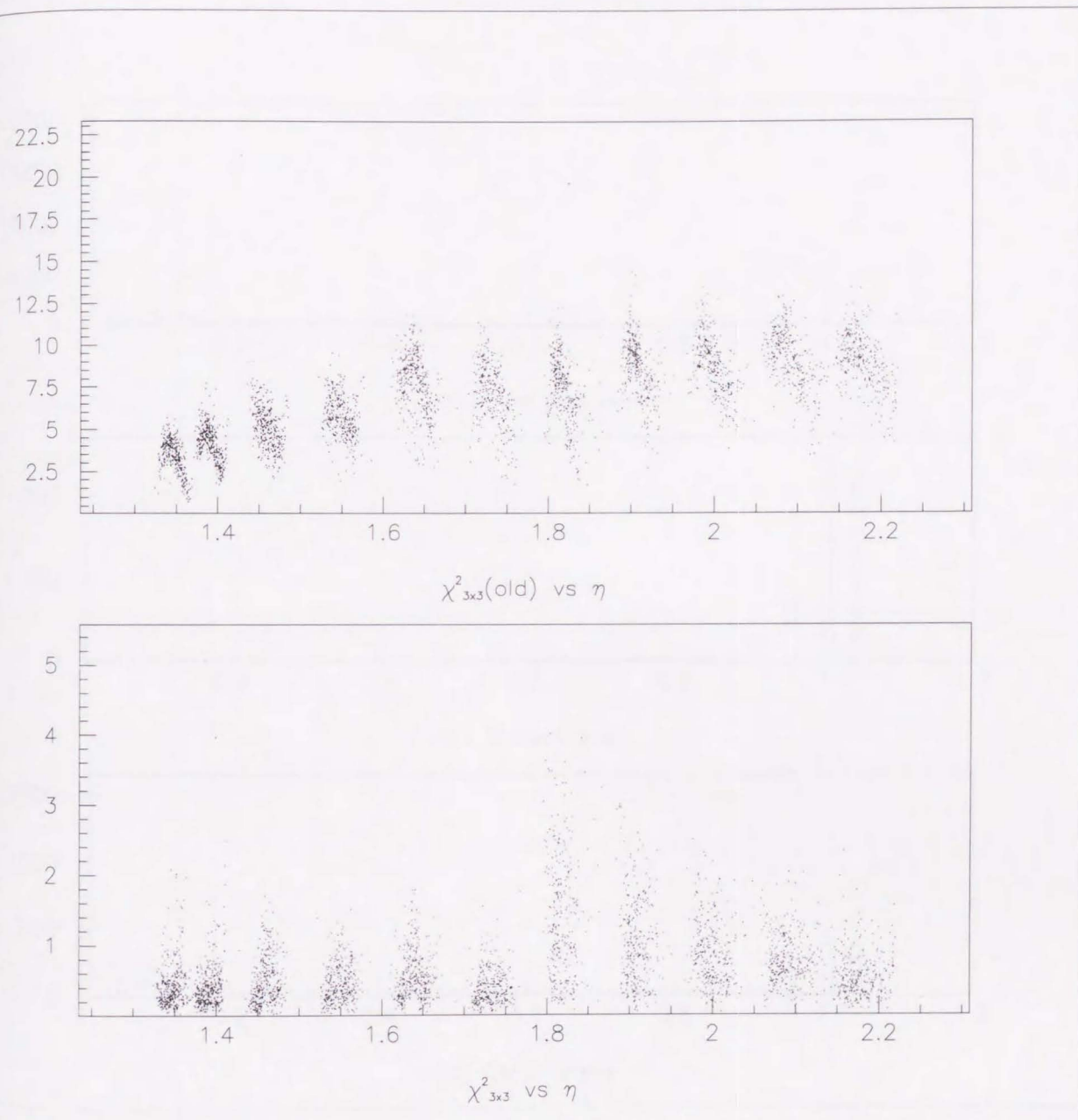


Figure 9.18: $\chi^2_{3 \times 3}$ vs η for the old and the new. 101 GeV test beam electrons used. Only one event with $\chi^2_{3 \times 3}(\text{old}) \geq 20$ and one with $\chi^2_{3 \times 3} \geq 5$ out of 3192 events. See text for details.

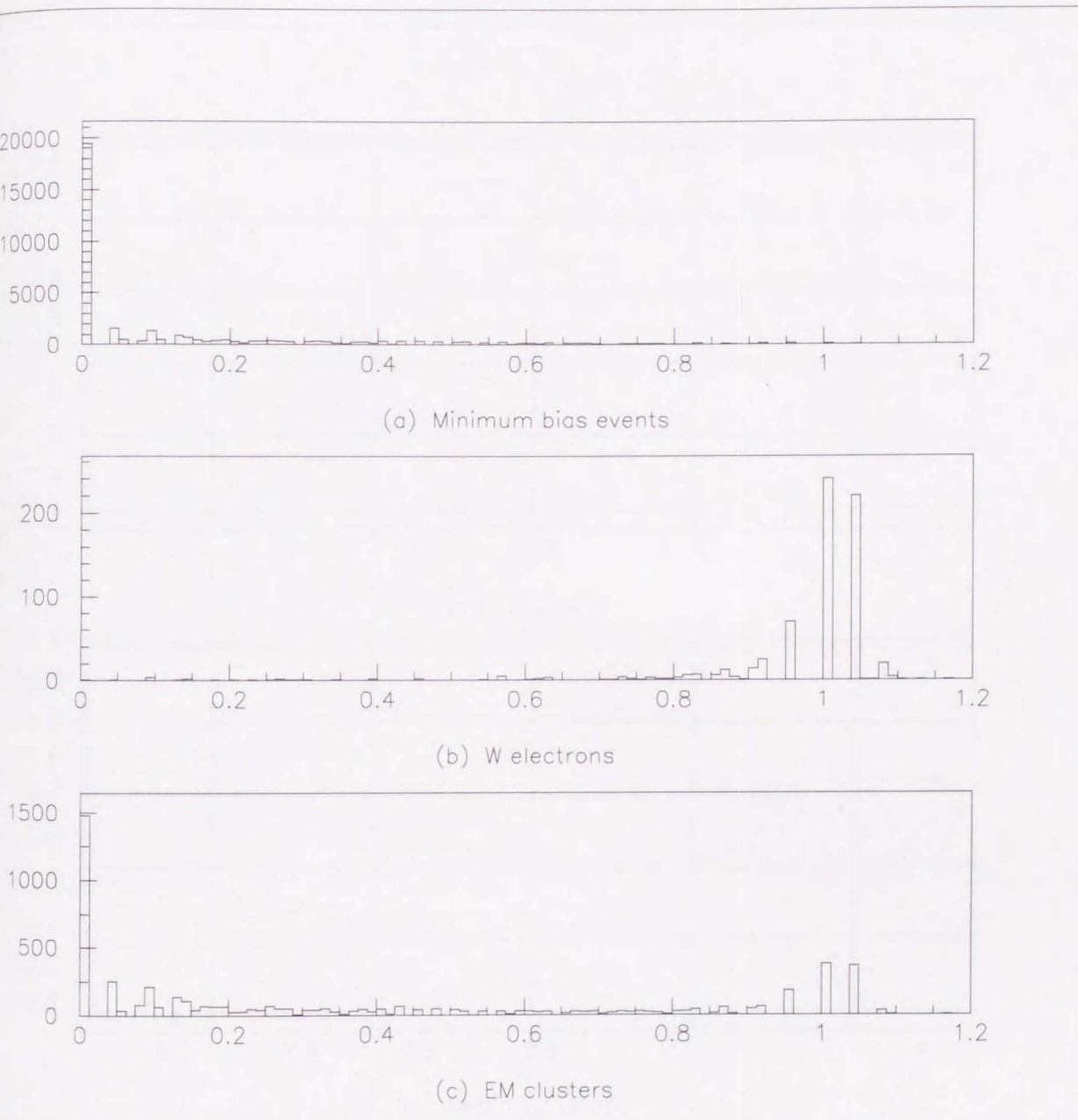


Figure 9.19: Distributions of VTPC hit occupancy R_{VTPC} for (a) minimum bias events along randomly placed roads between the vertex and the PEM, (b) W electron candidates without the E_T and the VTPC requirements, and (c) EM clusters with the same requirements as the prompt photon candidates except the VTPC cut.

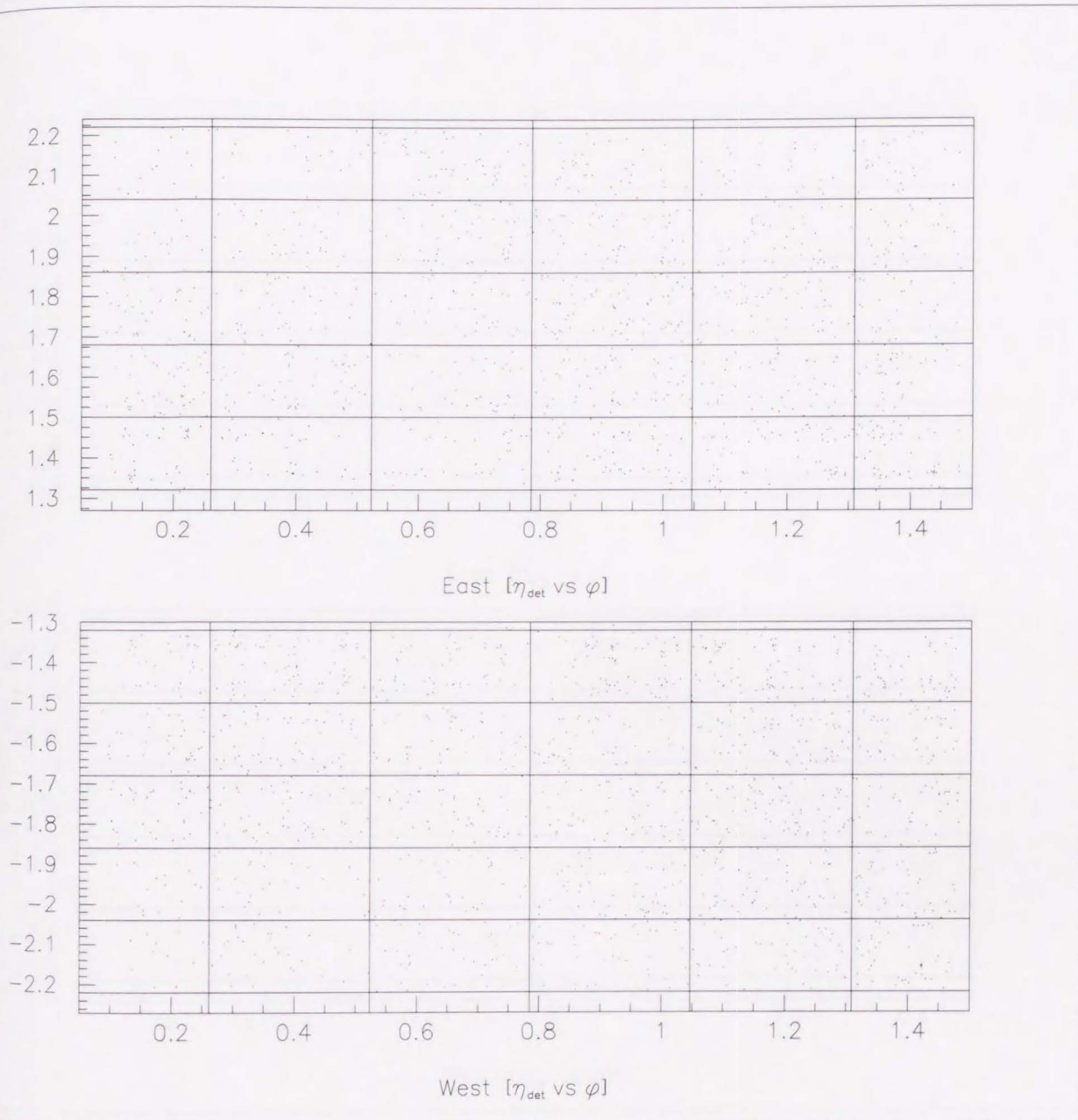


Figure 9.20: Off-line cluster positions for level 2 trigger unbiased clusters with $E_T^{\text{det}} > 20$ GeV. No requirement for level 2 trigger EM clusters. Four quadrants are overlaid each east or west for enhancement. Solid lines represent level 2 trigger tower boundaries.

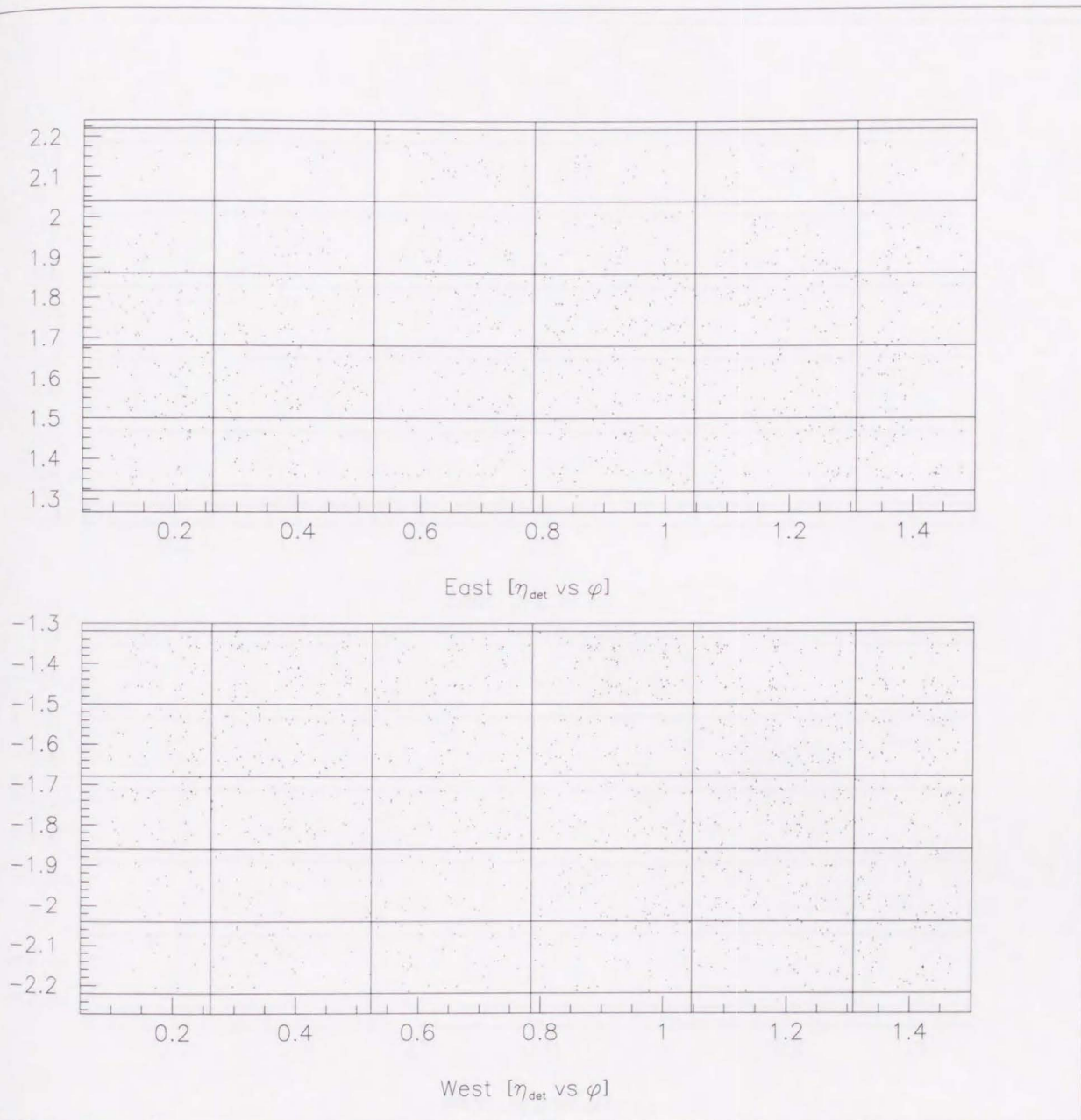


Figure 9.21: Off-line cluster positions for level 2 trigger unbiased clusters with $E_T^{\text{det}} > 20$ GeV. The existence of the corresponding level 2 EM clusters required. Four quadrants are overlaid each east or west for enhancement. Solid lines represent level 2 trigger tower boundaries.

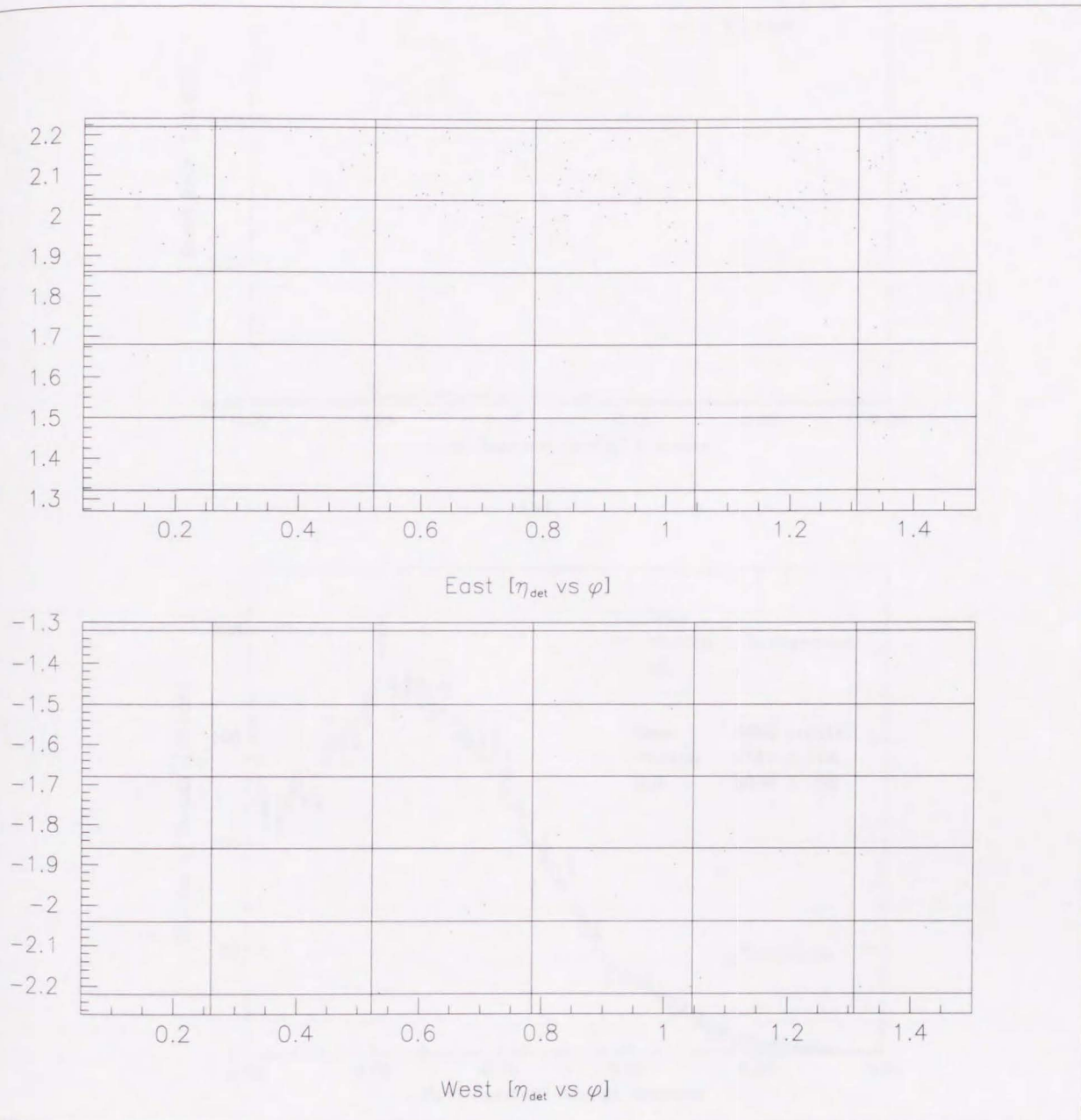
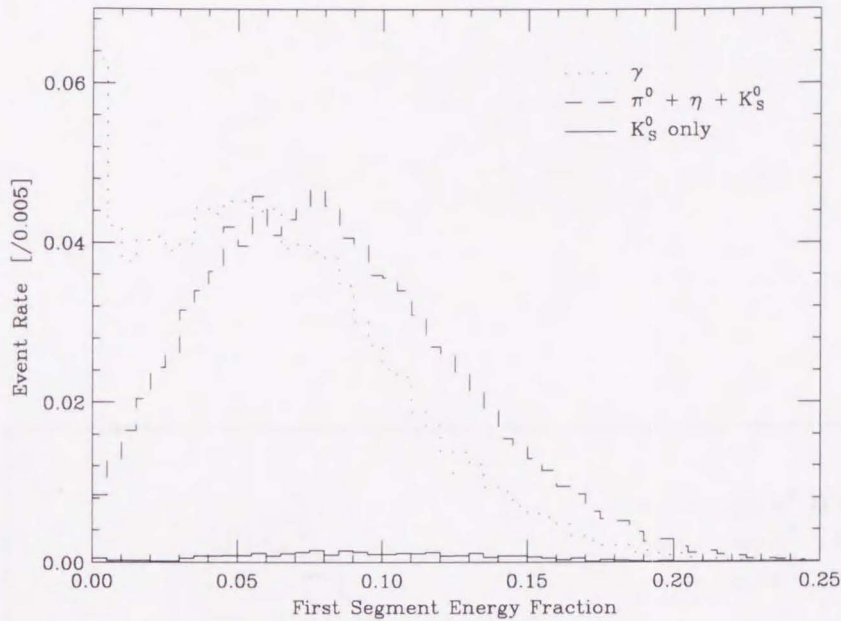
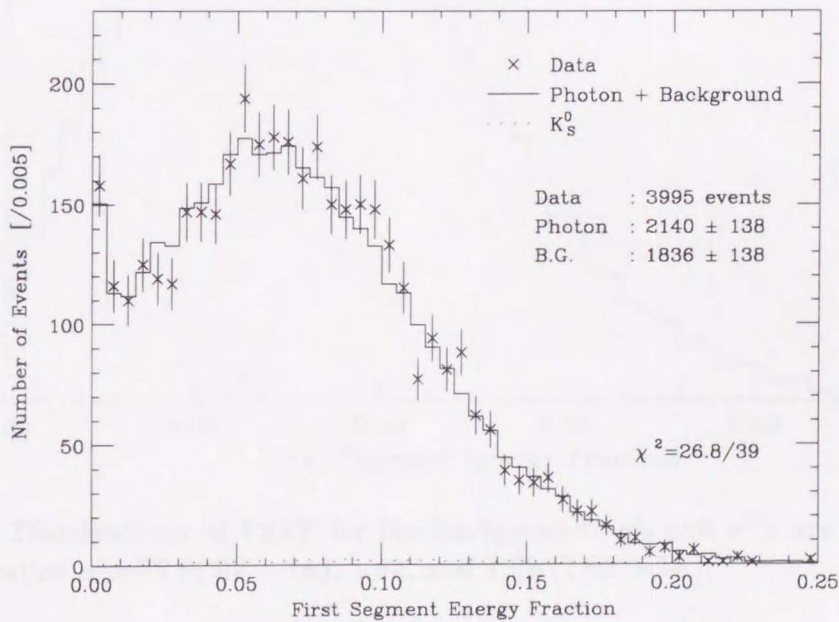


Figure 9.22: Off-line cluster positions for level 2 trigger unbiased clusters with $E_T^{\text{det}} > 20$ GeV having no corresponding level 2 EM clusters. Four quadrants are overlaid each east or west for enhancement. Solid lines represent level 2 trigger tower boundaries.



(a)



(b)

Figure 9.23: (a) Distributions of FSEF for K_S^0 's, the total background, and single photons, showing the K_S^0 contribution. The mean thickness of the aluminum plate is 6.5 cm, and the gaussian σ is 2.0 cm for the GEANT3 simulation. Only the neutral decay modes are simulated for mesons. (b) Fitting with the above spectra to the prompt photon candidates. Bins of FSEF = 0.0 – 0.2 are used for a fitting.

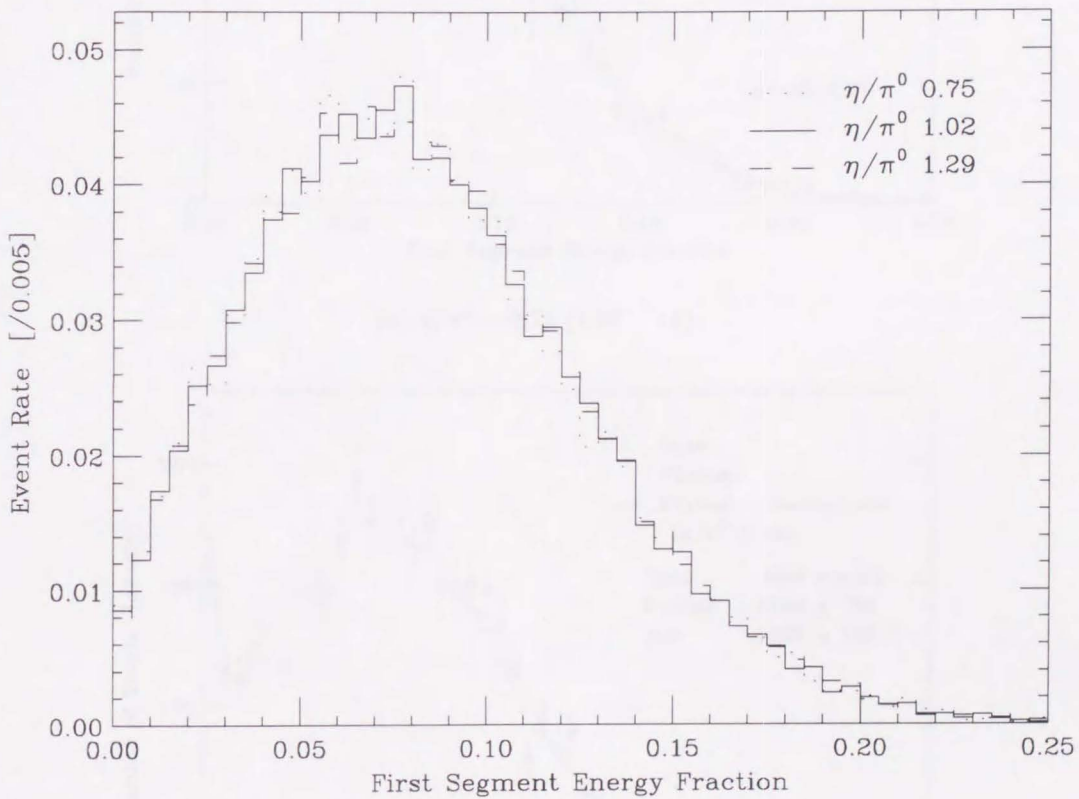
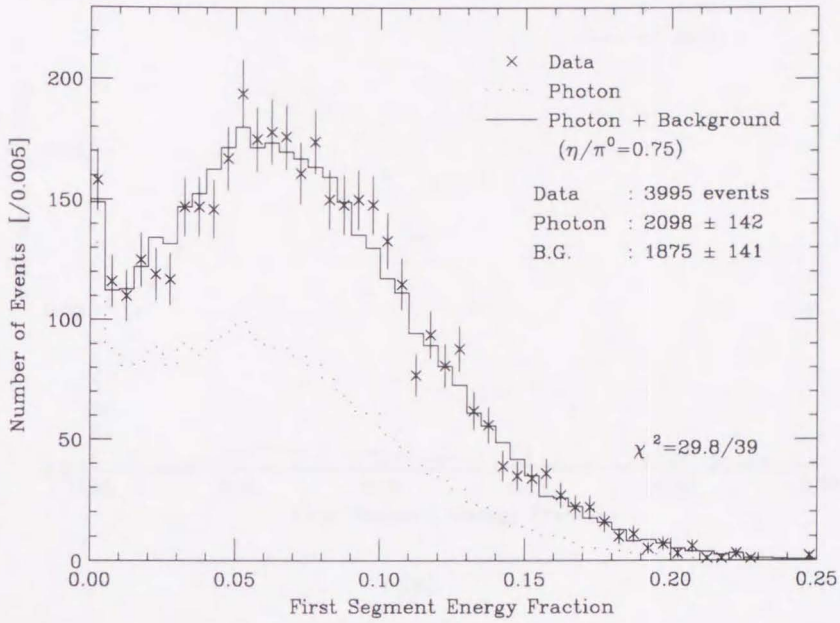
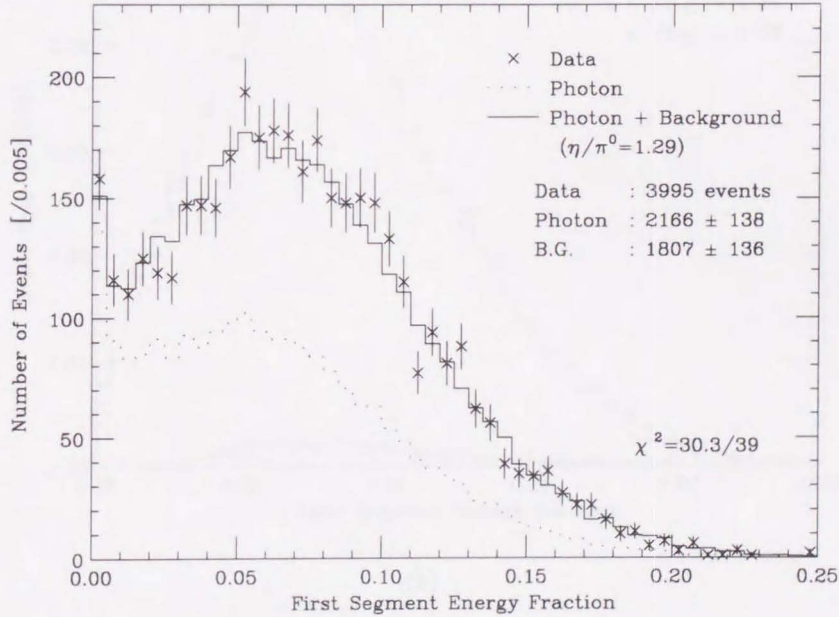
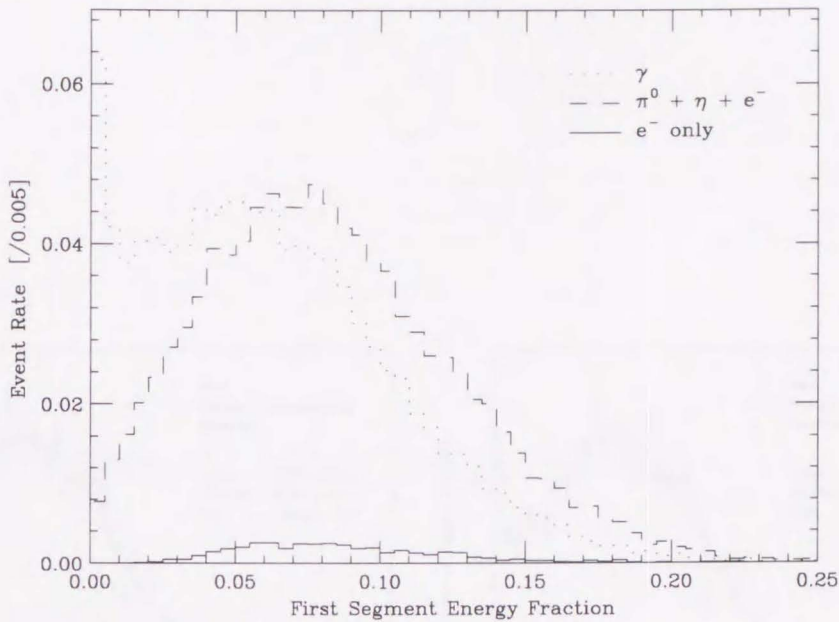
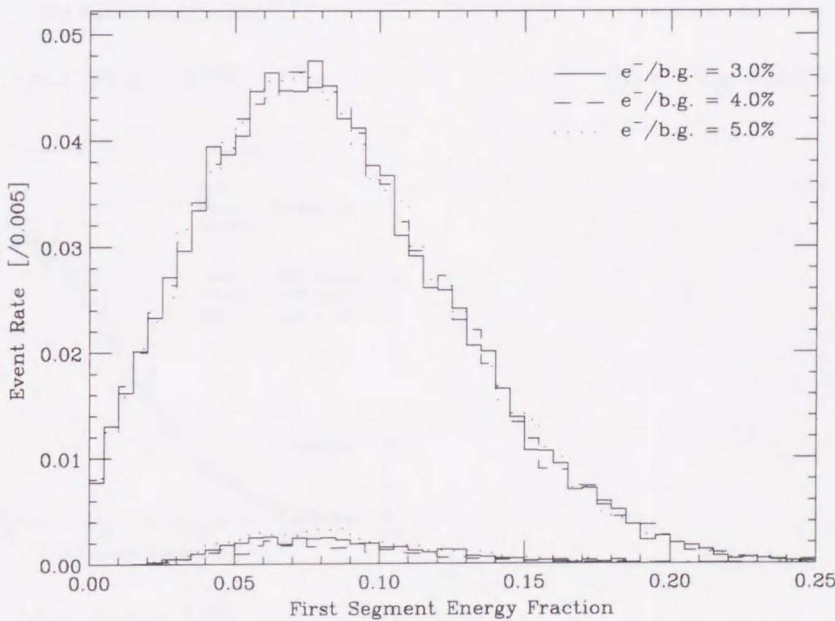


Figure 9.24: Distributions of FSEF for the background. η 's and π^0 's are mixed at the production ratios of 0.75 ($1.02 - 1\sigma$), 1.02, and 1.29 ($1.02 + 1\sigma$).

(a) $\eta/\pi^0 = 0.75$ ($1.02 - 1\sigma$)(b) $\eta/\pi^0 = 1.29$ ($1.02 + 1\sigma$)Figure 9.25: Fittings with the FSEF spectra for the background mesons at the η/π^0 production ratios of 0.75 and 1.29.



(a)



(b)

Figure 9.26: (a) Distributions of FSEF for electrons, the total background, and single photons, showing the electron contamination. The electron spectrum is normalized to the background spectrum at a ratio of 0.04, which is best matched when the prompt photon to background meson ratio is 1. The mean thickness of the aluminum plate is 6.5 cm, and the gaussian σ is 2.0 cm. (b) Distributions of FSEF for the background including electrons at $e^-/\text{b.g.} = 3, 4,$ and 5%, where the prompt photon to background ratio is assumed 1.

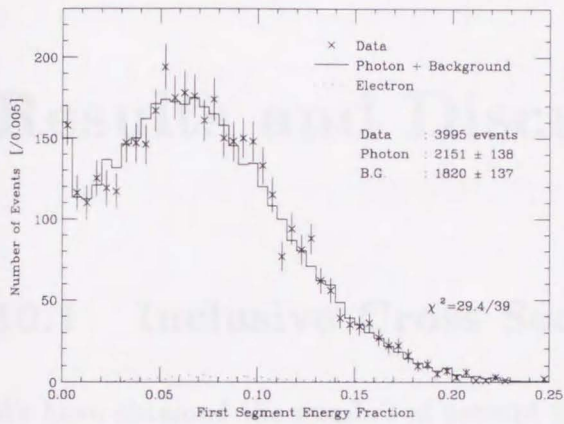
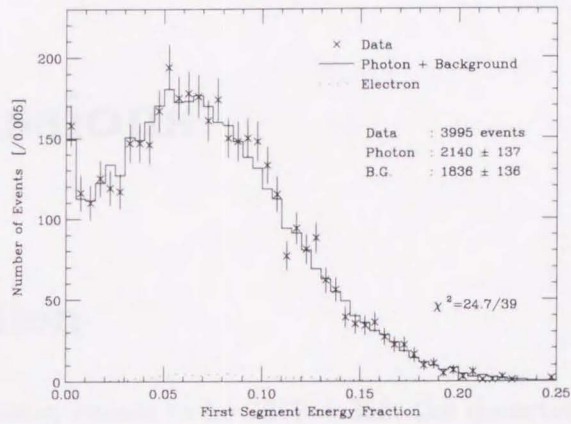
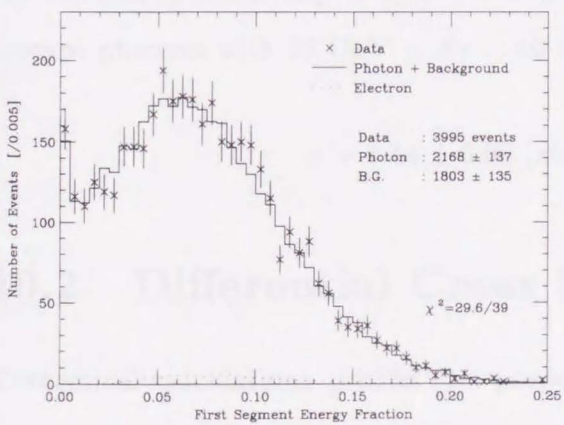
(a) $e^-/\text{b.g.} = 3.0\%$ (b) $e^-/\text{b.g.} = 4.0\%$ (c) $e^-/\text{b.g.} = 5.0\%$

Figure 9.27: Fittings with the electron mixed background. The electron contamination ratio is varied, $e^-/\text{b.g.} = 3, 4,$ and 5% . Bins of FSEF = 0.0 – 0.2 are used for fittings.

Chapter 10

Results and Discussions

10.1 Inclusive Cross Section

We have obtained the number of prompt photon events to be 1972 ± 353 , the detecting efficiency and the systematic uncertainty to be 0.365 and 19.0%, respectively. With the integrated luminosity of $3.76 \pm 0.13 \text{ pb}^{-1}$, the inclusive production cross section of prompt photons with $27 \text{ GeV} < E_T < 40 \text{ GeV}$ in $1.32 < |\eta| < 2.22$ is evaluated to be

$$\sigma = 1.44 \pm 0.09 \text{ (stat.)} \pm 0.27 \text{ (syst.) nb.}$$

10.2 Differential Cross Section

Theoretical calculations predict the production cross section of prompt photons in a certain range of E_T decreases with pseudorapidity at high η as shown in Fig. 1.6. We evaluate the differential cross section with respect to η , $d\sigma/d\eta$, in this section. The differential cross section is calculated for two pseudorapidity ranges, $1.32 < |\eta| < 1.77$ and $1.77 < |\eta| < 2.22$, in the same way as we have done for the inclusive cross section.

The same criteria are used to select prompt photon candidates. We have 1303 candidates in the low η range ($1.32 < |\eta| < 1.77$) and 2692 in the high η range ($1.77 < |\eta| < 2.22$). The FSEF distribution for each η range is shown in Fig. 10.1.

10.2.1 Uncertainty in the Simulation

The systematic uncertainty in the GEANT3 simulation was estimated in Chapter 7 as the uncertainty in the total amount of materials along the beamline between the MT5 dipole magnets and the detector. And, we have observed it has only a small variation with respect to η as shown in Fig. 7.17. Thus, the same uncertainty in the simulation is applied to the differential cross section.

The uncertainty on the material estimation of $0.046 X_0$ corresponds to ± 0.37 cm thick aluminum at the center of the low η range or ± 0.39 cm for the high η range, where the aluminum thickness is measured along the z axis.

10.2.2 Estimation of Material Thickness

Though the total amount of materials between the event vertex and the PEM was estimated in $1.32 < |\eta| < 2.22$, it is expected to change with η since most materials are placed either along or perpendicular to the z direction. Thus, we estimate the amount of materials for the low and high η ranges individually by comparing electron cascades from W decays with the GEANT3 simulation as done in Chapter 8.

We have 397 W electrons in the low η range and 292 in the high η . The FSEF distribution for each η range is shown in Fig. 10.2, and χ_{FSEF}^2 values calculated for simulations with the aluminum thickness smeared around various means and with various gaussian σ are listed in Table 10.1. The χ_{FSEF}^2 in the low η range shows minimum around the aluminum thickness of 6.0 cm – 6.5 cm, which is almost the same as one in all pseudorapidity range. However, in the high η range, χ_{FSEF}^2 takes minimum around 5.0 cm.

To estimate the most probable thicknesses and the corresponding uncertainties, χ_{FSEF}^2 values are fitted with a quadratic function for each η range. Figures 10.3 and 10.4 show some of FSEF distributions of the GEANT3 simulation together with the W electrons in the low and high η ranges, respectively. Quadratic fits to χ_{FSEF}^2 values are shown in Figs. 10.3 (f) and 10.4 (f). Additional sets of Monte Carlo events are simulated with the aluminum thickness smeared around the mean of 2.5 cm to 3.5 cm, and 9.0 cm with the gaussian σ of 2 cm. From the quadratic fits, the total amount of materials

σ [cm]	mean [cm]									
	4.0	4.5	5.0	5.5	6.0	6.5	7.0	7.5	8.0	8.5
0.0	3.46	2.63	1.95	1.37	1.20	0.98	0.92	1.56	1.82	2.23
1.0	3.38	2.50	1.62	1.08	1.06	0.80	0.67	1.32	1.40	2.05
2.0	3.20	2.20	2.04	1.02	0.82	0.62	0.77	1.12	1.69	2.29
3.0	4.04	2.67	1.83	1.20	0.54	0.77	0.63	0.99	1.32	2.14
4.0	3.34	2.16	1.68	1.11	0.96	0.81	0.83	1.14	1.51	2.33
5.0	3.54	2.84	1.37	0.93	0.78	0.74	0.74	1.00	1.52	2.57
6.0	3.99	2.88	1.72	1.17	0.71	1.05	0.93	1.37	1.13	1.90

$$1.32 < |\eta| < 1.77$$

σ [cm]	mean [cm]									
	4.0	4.5	5.0	5.5	6.0	6.5	7.0	7.5	8.0	8.5
0.0	1.60	1.83	1.78	1.88	2.29	2.40	2.07	3.15	3.84	4.28
1.0	2.30	1.69	1.54	1.65	1.96	2.01	2.75	3.05	3.35	2.79
2.0	1.53	1.65	1.14	1.39	1.54	1.59	1.41	2.20	2.44	3.74
3.0	1.18	1.38	1.31	1.18	1.45	1.72	2.13	2.84	3.15	2.79
4.0	2.02	1.47	1.20	1.52	1.48	1.57	2.23	1.79	2.92	2.61
5.0	1.52	1.46	1.36	1.22	1.41	1.73	1.53	1.47	1.50	2.50
6.0	1.38	1.68	1.31	1.11	1.35	1.41	1.42	1.61	1.81	2.51

$$1.77 < |\eta| < 2.22$$

Table 10.1: χ_{FSEF}^2 for the W electrons in each η range. The aluminum thickness in the GEANT3 simulation is smeared around the mean with the gaussian σ , where the mean and the σ are scanned. The thickness is limited within 0 cm to $2 \times \text{mean}$. χ_{FSEF}^2 values for the mean thicknesses from 2.5 cm to 3.5 cm are not shown.

measured along the z axis is estimated

$$6.48 \pm 0.35 \text{ cm thick aluminum or } 0.728 \pm 0.009 X_0 \text{ for } 1.32 < |\eta| < 1.77 \text{ and}$$

$$5.34 \pm 0.47 \text{ cm thick aluminum or } 0.600 \pm 0.012 X_0 \text{ for } 1.77 < |\eta| < 2.22.$$

10.2.3 Extraction of Photons

We need additional sets of simulation data to extract the nominal number of prompt photon events and the corresponding uncertainty in each η range. Considering the amount of materials between the event vertex and the PEM as well as the uncertainties in the simulation and the estimation of materials, simulation data sets with the aluminum thickness smeared around the mean of 5.5 cm to 7.5 cm are necessary to interpolate the numbers of photons in the low η range. And, in the high η range, 4.5 cm to 6.0 cm are essential. Single photons and background mesons are simulated with the aluminum thickness smeared around these means with σ of 2 cm.

Figure 10.5 shows the FSEF spectrum of the prompt photon candidates in the low η range fit with different data sets of the GEANT3 simulation, and Fig. 10.6 in the high η range. FSEF spectra of single photons and background mesons are obtained in the same way as described in Section 9.2 for both η ranges. The number of prompt photons from the fittings are shown against the mean aluminum thickness in Fig. 10.7. From the linear fits in Fig. 10.7, we have evaluated the nominal number of prompt photon events in each η range to be

$$1229 \pm 228 \text{ for } 1.32 < |\eta| < 1.77 \text{ and}$$

$$662 \pm 147 \text{ for } 1.77 < |\eta| < 2.22,$$

where errors are systematics due to the uncertainties in both the simulation and the inside detector materials, corresponding to ± 0.52 cm in the low η range and ± 0.61 cm in the high η range.

Requirement / Variable	1.32 < $ \eta $ < 1.77		1.77 < $ \eta $ < 2.22	
	Efficiency	Uncertainty [%]	Efficiency	Uncertainty [%]
Level 2 trigger	0.662	± 5.3	0.621	+6.8/-6.7
$E_T^{iso}(0.7) < 3$ GeV	0.907	+0.4/-0.8	0.890	+0.9/-1.2
$E^{had}/E^{EM} < 0.05$	0.989	± 1.0	0.975	± 1.0
$\chi^2_{3 \times 3}(\text{old}) < 20$ & $\chi^2_{3 \times 3} < 5$	0.997	± 0.2	0.997	± 0.2
$R_{VTPC} \leq 0.8$	0.978	± 0.1	0.966	± 0.1
$ z_{vertex} < 50$ cm	0.931	± 0.4	0.931	± 0.4
Geometrical acceptance	0.712	± 2.5	0.782	± 3.3
Level 2 cluster problem			0.883	± 2.0
η/π^0 ratio		+0.1/-4.0		+0.1/-2.4
$K_S^0 \rightarrow \pi^0 \pi^0$		± 0.1		± 1.5
Electron contamination		± 1.5		± 1.7
GEANT3 Simulation		± 13.5		± 14.8
Materials		± 12.7		± 17.6
Luminosity		± 3.5		± 3.5
Total	0.384	± 20.2	0.376	± 24.9

Table 10.2: Efficiencies and systematic uncertainties in the pseudorapidity ranges of $1.32 < |\eta| < 1.77$ and $1.77 < |\eta| < 2.22$.

10.2.4 Efficiencies and Uncertainties

Efficiencies of the cuts for prompt photons in each η range are estimated in the same ways as in Section 9.4, and summarized in Table 10.2.

The strange pattern of cluster positions discussed in Section 9.4.8 is only seen in the high η range. Efficiencies for the χ^2 and the vertex cuts are common in both η ranges. The total systematic uncertainty in each η range is slightly larger than one in all pseudorapidity range. This comes mainly from larger systematics due to the uncertainty in the inside detector materials.

10.2.5 Differential Cross Section

The differential cross section for prompt photon production with $27 \text{ GeV} < E_T < 40 \text{ GeV}$ in $1.32 < |\eta| < 2.22$ is evaluated to be

$$\frac{d\sigma}{d\eta} = 0.95 \pm 0.08 \text{ (stat.)} \pm 0.19 \text{ (syst.) nb} \quad \text{in } 1.32 < |\eta| < 1.77 \text{ and}$$

$$\frac{d\sigma}{d\eta} = 0.58 \pm 0.07 \text{ (stat.)} \pm 0.14 \text{ (syst.) nb} \quad \text{in } 1.77 < |\eta| < 2.22,$$

and shown in Fig. 10.8 together with that in the central region.

10.3 Comparison with QCD Predictions

Our measurement is compared with QCD predictions provided by Owens [7] and plotted in Fig. 10.9 together with the leading order and the next-to-leading order calculations. The NLO calculation utilizes all the NLO matrix elements including the bremsstrahlung terms as well as the one-loop graphs.

To compare predictions with the measurement, an equivalent isolation cut is applied to the QCD calculation. It requires E_T in a cone of radius 0.7 around the photon to be less than 1.6 GeV. This requirement is equivalent to the isolation cut at 3.0 GeV used for the prompt photon selection in Section 9.1 because of the following reasons. Due to calorimeter non-linearities, the response to low energy particles is depressed approximately by a factor of 1.4 [53]. In addition, we have the underlying energy of $E_T = 1.31$ GeV in a cone of radius 0.7 around the prompt photon as well as the lateral shower leakage of $E_T = 0.49$ GeV as described in Section 9.4.2.

The measurement in the endplug region shows a good agreement with the NLO QCD calculation rather than the leading order. Despite of large errors, the two measured points suggest the fall of the cross section toward large η , which is significant in the NLO calculation. Note that CTEQ 3M parton distribution function is used here for the theoretical expectations.

Two other PDF sets are compared with the measurement. Figure 10.10 shows the cross section dependence on the PDF sets. Discrepancies are rather noticeable at lower η . In the central region, partons with the fractional momentum x as low as 0.006 contribute to production of prompt photons. For $x \gtrsim 0.006$, the gluon density of GRV 94 HO is always lower than the other two PDF sets as seen in Fig. 1.5, and CTEQ 3M is always the highest. This fact directly reflects on the cross section in the central region of $|\eta| < 0.9$. In the endplug region, however, the cross section reflects the gluon density in a wide range of x , and results in only small discrepancies between the three PDF sets

due to smearing of the distributions.

The statistical errors in the theoretical calculations are, in fact, 0.4% at $\eta = 0$ and increase with pseudorapidity. At $\eta = 2$, they become an order of one percent. The statistical errors of this magnitude are comparable to differences in the cross section due to the choice of the PDF sets.

In addition to the statistical uncertainties, two sources of systematics are considered in the NLO QCD calculation. One is the isolation cut. Figure 10.11 (a) shows changes of the cross section for different isolation thresholds. The cross section is calculated with isolation thresholds of 1.6 GeV (standard), 3.2 GeV, and no isolation requirement. Only a slight increase is observed for double the standard threshold. However, it is found that the bremsstrahlung contribution is significant, and it is strongly suppressed by the isolation requirement. The other source of the systematic uncertainty is the renormalization and factorization scales Q^2 . In the NLO QCD calculation by Owens, a single scale $Q^2 = np_T^2$ is used for both, where $n = 1$ has been employed. The dependence of the cross section on the scale is illustrated in Fig. 10.11 (b) for $n = 1/4$ to 4. The cross section monotonically decreases with increasing n , and the changes are not small. They are an order of 10% and comparable to or larger than the differences due to the choice of the PDF sets.

Considering the error in the measurement as well as that in the calculation, we cannot provide a strong constraint on the PDF sets from the measurement of prompt photon production in the endplug region. However, this new measurement at high pseudorapidity agrees with the NLO QCD calculation and also suggests a rapid decrease in the cross section at large η .

10.4 Photon Fraction

In Section 9.3, the number of prompt photon events was obtained 1972 ± 353 out of 3995 candidate events. It corresponds the photon fraction of 0.49 ± 0.09 . This ratio should change with the isolation requirement because of the production natures of prompt photons and mesons. One may expect a larger fraction of prompt photon events for a tight isolation cut, and vice versa.

Figure 10.12 (a) shows the photon fraction with respect to the isolation threshold. As expected, the photon fraction monotonically decreases with the threshold. At 1 GeV, about 80% of the candidates are expected to be prompt photon events, and the fraction decreases to 20% at 6 GeV.

Events are selected by the criteria listed in Table 9.1 except for the isolation requirement. The number of events is shown by a solid curve in Fig. 10.12 (b) with respect to the threshold. It increases rapidly with the threshold for $\lesssim 8$ GeV, but does not change above 10 GeV because of the E^{had}/E^{EM} requirement. As shown in Fig. 9.13 (b), the energy flow around the prompt photon is estimated as much as 3 GeV. So, the rapid increase in number of Fig. 10.12 (b) for $\gtrsim 3$ GeV is only due to the increase in that of neutral mesons. For unisolated energy clusters, the accompanying hadrons make the E^{had}/E^{EM} ratio so large that they are hardly formed as EM clusters.

The FSEF spectrum of the data for each isolation threshold is fit with those of Monte Carlo photons and meson backgrounds. The same Monte Carlo spectra as shown in Fig. 9.3 (b) are used as well as those of the other three Monte Carlo data sets for all the data spectra. The nominal numbers of prompt photon events and background events are each extracted from linear fits to the numbers obtained from the FSEF fittings in the same way as done in Section 9.3. However, it is improper use of the Monte Carlo spectra to some extent except for the data with the isolation thresholds around 3 GeV because:

- Monte Carlo events are assumed to follow the p_T and η spectra of the prompt photon candidates which satisfy $E_T^{iso}(0.7) < 3$ GeV, and these spectra should be different from those with other isolation cuts.
- Statistics for background events may not be adequate. For each set of simulation data, about 20k events of neutral mesons are collected. It is roughly 10 times of background events in the data for $E_T^{iso}(0.7) < 3$ GeV. However, at an isolation threshold of 10 GeV, nearly 8k events of neutral mesons are expected in the data. and statistics for Monte Carlo events are less than three times of the data.
- The underlying energy should distort the FSEF spectrum of the data for loose isolation cuts. Considering the cone size for the isolation cut of $\Delta\eta \times \Delta\varphi \approx 1.5$

$(\pi \times 0.7^2)$ and the typical EM cluster size of $\Delta\eta \times \Delta\varphi \sim 0.1$, the underlying E_T of 0.16 GeV is expected to overlay on the EM cluster for $E_T^{iso}(0.7) < 3$ GeV assuming the underlying energy is uniform inside the cone. However, it becomes more than 0.6 GeV for $E_T^{iso}(0.7) < 10$ GeV. The underlying energy is mostly measured or detected in the first segment of the PEM since it comes from low energy particles. In addition, the underlying energy for the mesons is not expected uniform inside the cone. It is rather expected larger near the cluster. The above effect broadens the FSEF distribution, and should be subtracted from the data or implemented in the simulation for a proper analysis.

Though the estimations of the numbers of prompt photons and background mesons are not so accurate, especially for loose isolation cuts, they show qualitative tendencies.

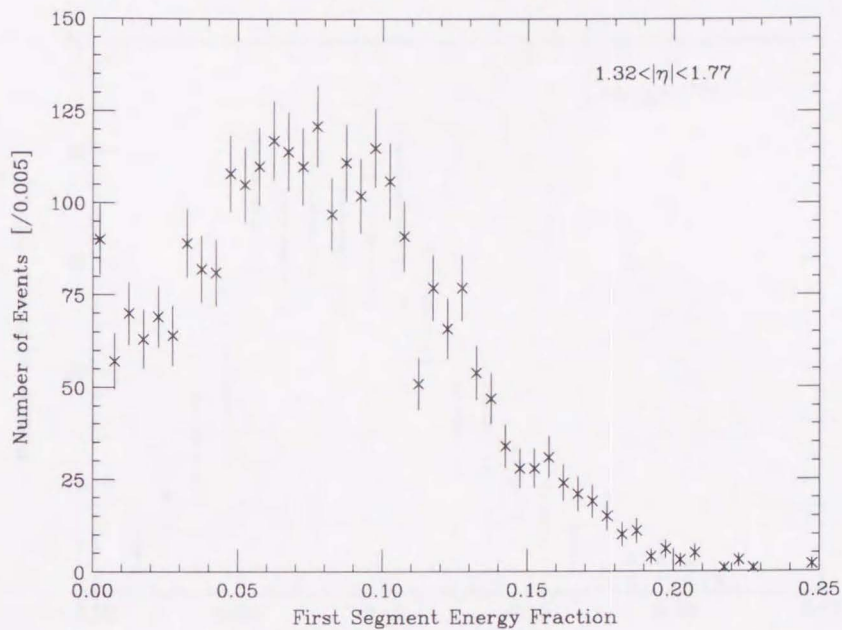
Figure 10.12 (b) shows the numbers of prompt photon events and multi-photon events from neutral meson decays with respect to the isolation threshold. The number of prompt photon events increases with loosening the isolation requirement in the range less than 3 GeV, and then saturates, while that of multi-photon events increases steadily until 10 GeV. A slight decrease in the number of prompt photon events at larger thresholds may come from the improper fittings. However, qualitative trends confirm the isolations of prompt photons and mesons expected from QCD.

The photon fraction is also estimated in two η ranges as shown in Fig. 10.13. The slope looks a little steeper in the high η range. Neglecting large errors, it suggests prompt photons are more produced at large scattering angles than neutral mesons in jets. This is consistent with QCD expectations as well as measurements [54]. QCD predicts the angular distribution of prompt photon production is roughly the form $(1 - \cos\theta^*)^{-1}$, while that of jets is $(1 - \cos\theta^*)^{-2}$, where θ^* is the center-of-mass polar angle. In the lowest order, prompt photon production is dominated by the t -channel quark exchange, and jet production by the gluon exchange.

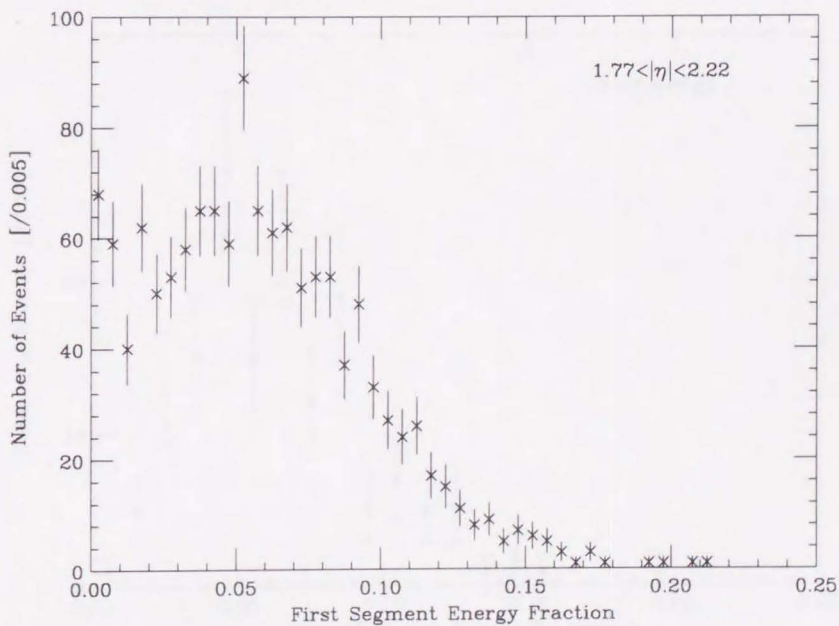
10.5 Stability of Photon Cross Section

Finally, we will see the stability of the cross section to the isolation cut as a test of the fitting method. The numbers of prompt photons have been obtained in Section 9.3

for $E_T^{iso}(0.7) < 3$ GeV, also in the previous section for other isolation thresholds. The efficiencies and uncertainties which depend on the isolation cut are calculated for each threshold. The cross section for production of prompt photons is plotted against the isolation threshold in Fig. 10.14. Although the cross section drops at larger isolation thresholds, the evaluated numbers are constant for $E_T^{iso}(0.7) \lesssim 5$ GeV. This fact steadily supports the reliability of the fitting method.

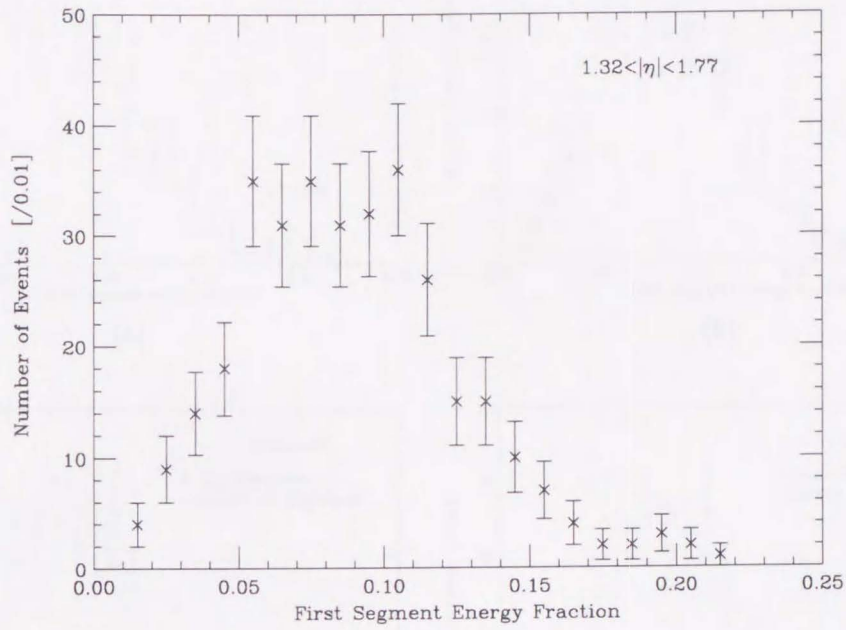


(a)

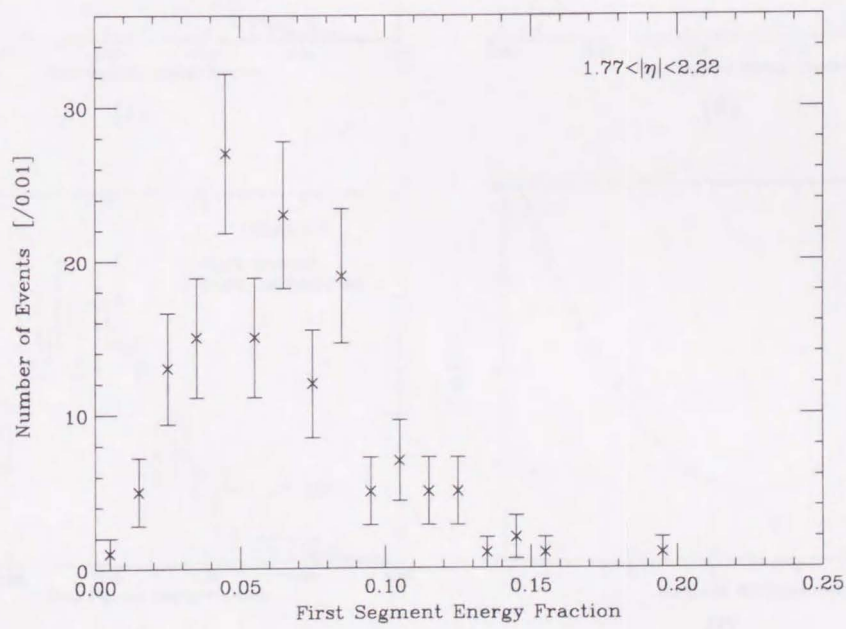


(b)

Figure 10.1: Distributions of FSEF for the prompt photon candidates in two pseudorapidity ranges.



(a)



(b)

Figure 10.2: Distributions of FSEF for the W electrons in two pseudorapidity ranges.

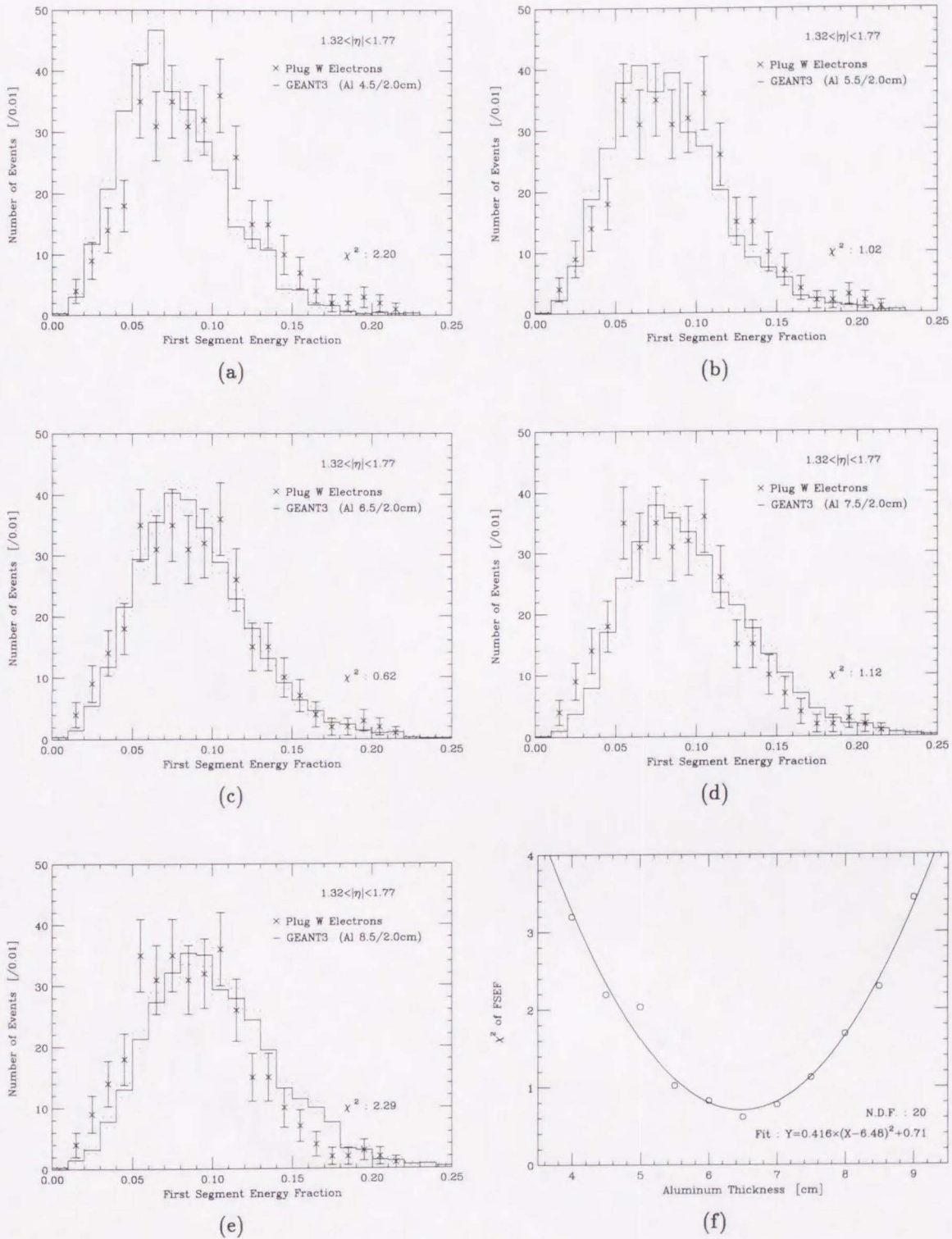


Figure 10.3: (a)-(e) FSEF distributions for the W electrons and the GEANT simulations in $1.32 < |\eta| < 1.77$. In each simulation, the aluminum thickness is smeared with a gaussian function. The σ is fixed to 2.0 cm, and the mean is scanned. (f) χ^2_{FSEF} values with respect to the mean aluminum thickness.

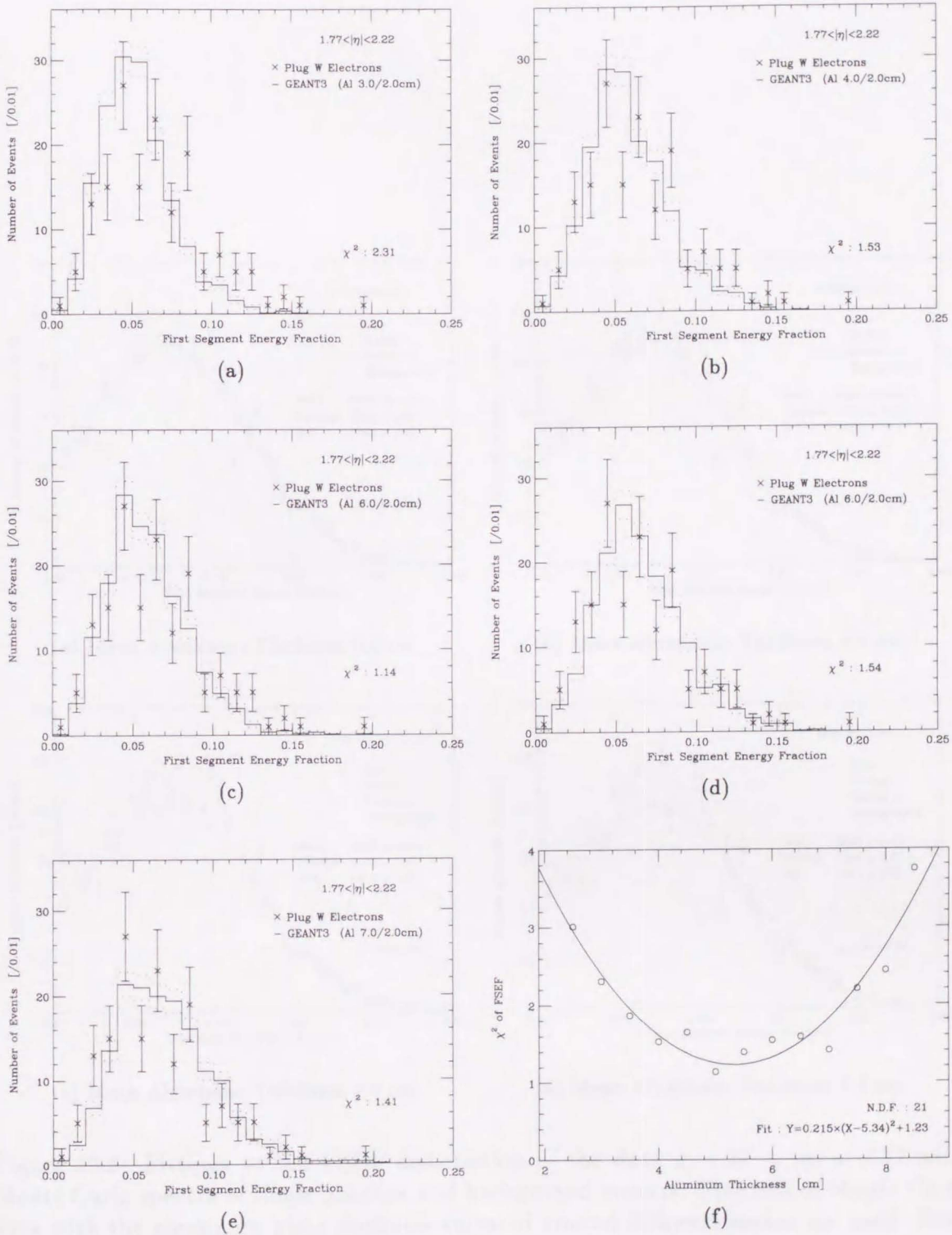
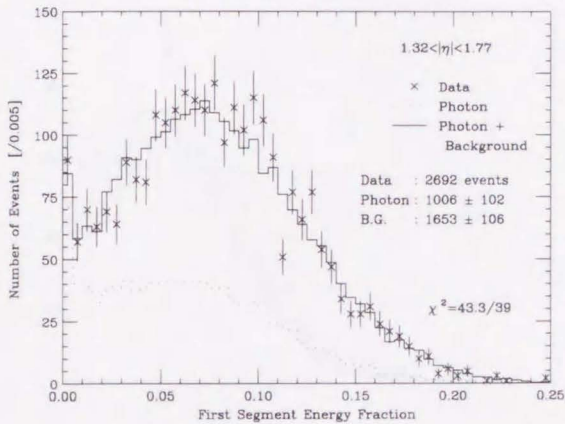
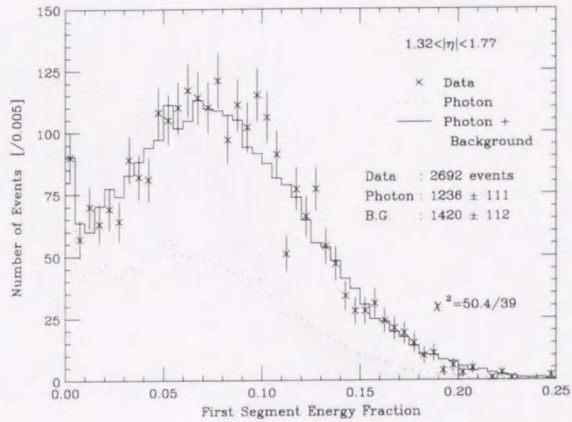


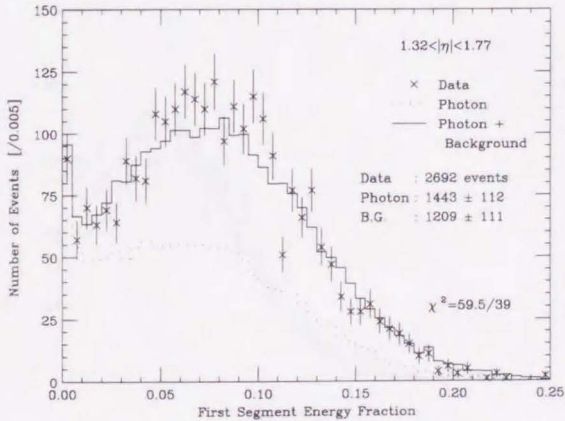
Figure 10.4: (a)-(e) FSEF distributions for the W electrons and the GEANT simulations in $1.77 < |\eta| < 2.22$. In each simulation, the aluminum thickness is smeared with a gaussian function. The σ is fixed to 2.0 cm, and the mean is scanned. (f) χ^2_{FSEF} values with respect to the mean aluminum thickness.



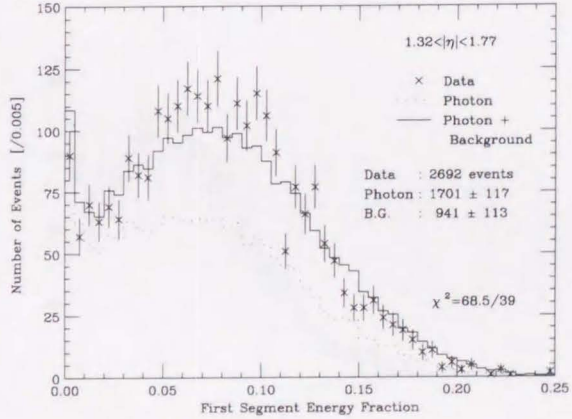
(a) Mean Aluminum Thickness 6.0 cm.



(b) Mean Aluminum Thickness 6.5 cm.

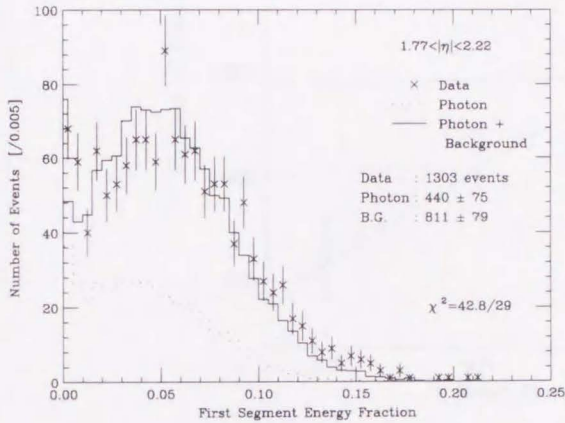


(c) Mean Aluminum Thickness 7.0 cm.

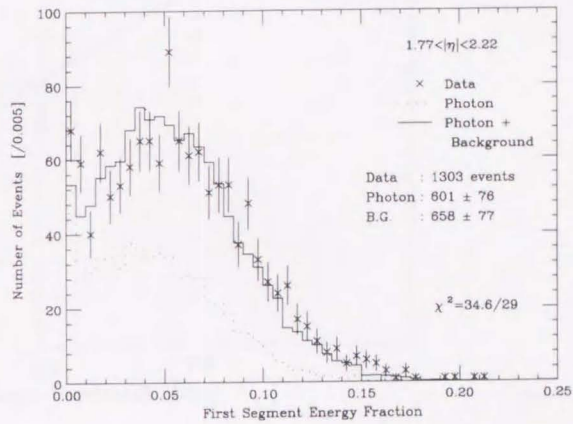


(d) Mean Aluminum Thickness 7.5 cm.

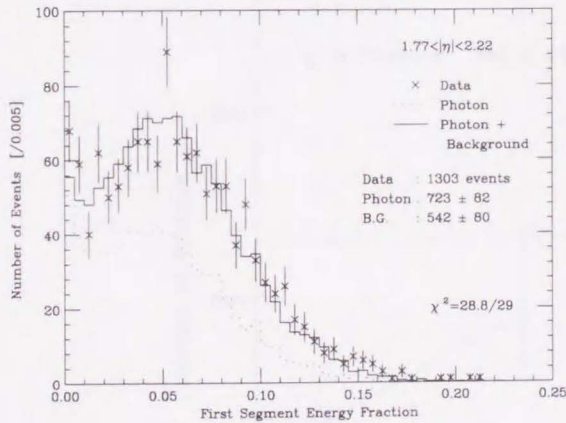
Figure 10.5: Fittings to the FSEF distribution of the data in $1.32 < |\eta| < 1.77$ with Monte Carlo spectra of single photons and background mesons. Five sets of Monte Carlo data with the aluminum plate thickness smeared around different means are used. Four of them are shown here. Bins of $\text{FSEF} = 0.0 - 0.2$ are used for fittings.



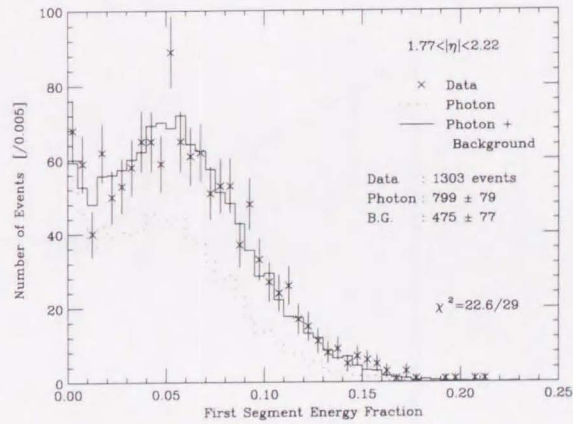
(a) Mean Aluminum Thickness 4.5 cm.



(b) Mean Aluminum Thickness 5.0 cm.



(c) Mean Aluminum Thickness 5.5 cm.



(d) Mean Aluminum Thickness 6.0 cm.

Figure 10.6: Fittings to the FSEF distribution of the data in $1.77 < |\eta| < 2.22$ with Monte Carlo spectra of single photons and background mesons. Four sets of Monte Carlo spectra of single photons smeared around different means are used. Bins of $\text{FSEF} = 0.00 - 0.15$ are used for fittings.

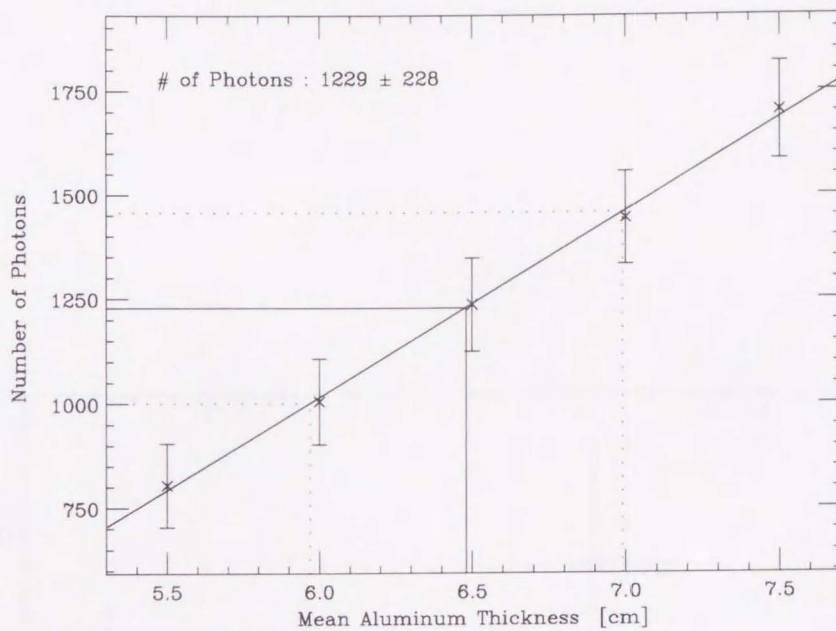
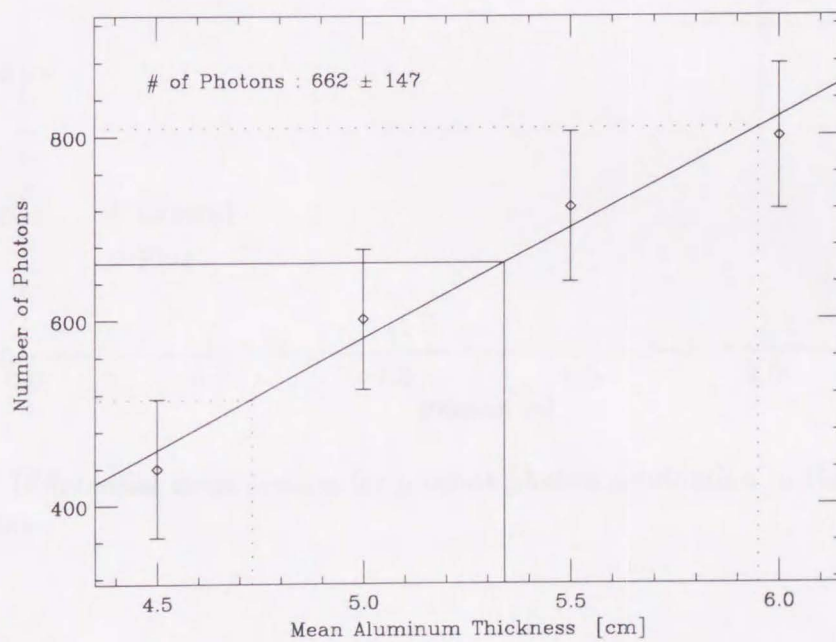
(a) $1.32 < |\eta| < 1.77$ (b) $1.77 < |\eta| < 2.22$

Figure 10.7: Estimations of the nominal numbers of prompt photon events for the low and high η ranges.

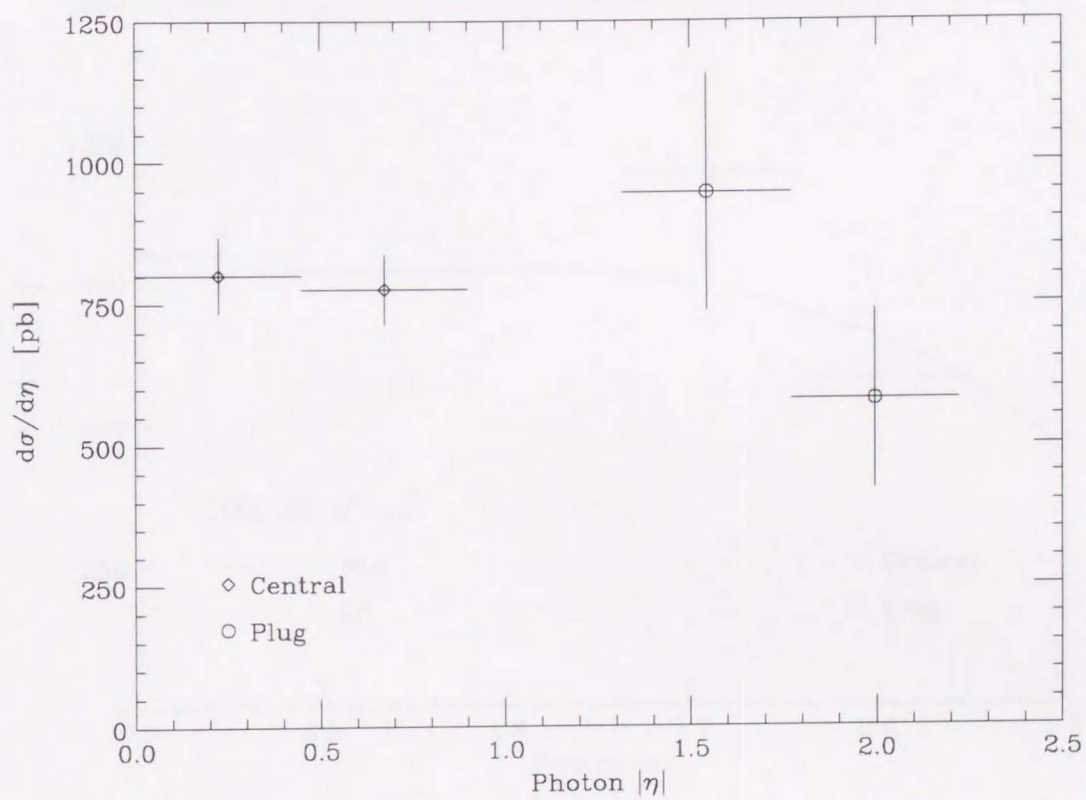


Figure 10.8: Differential cross section for prompt photon production in the endplug and central regions.

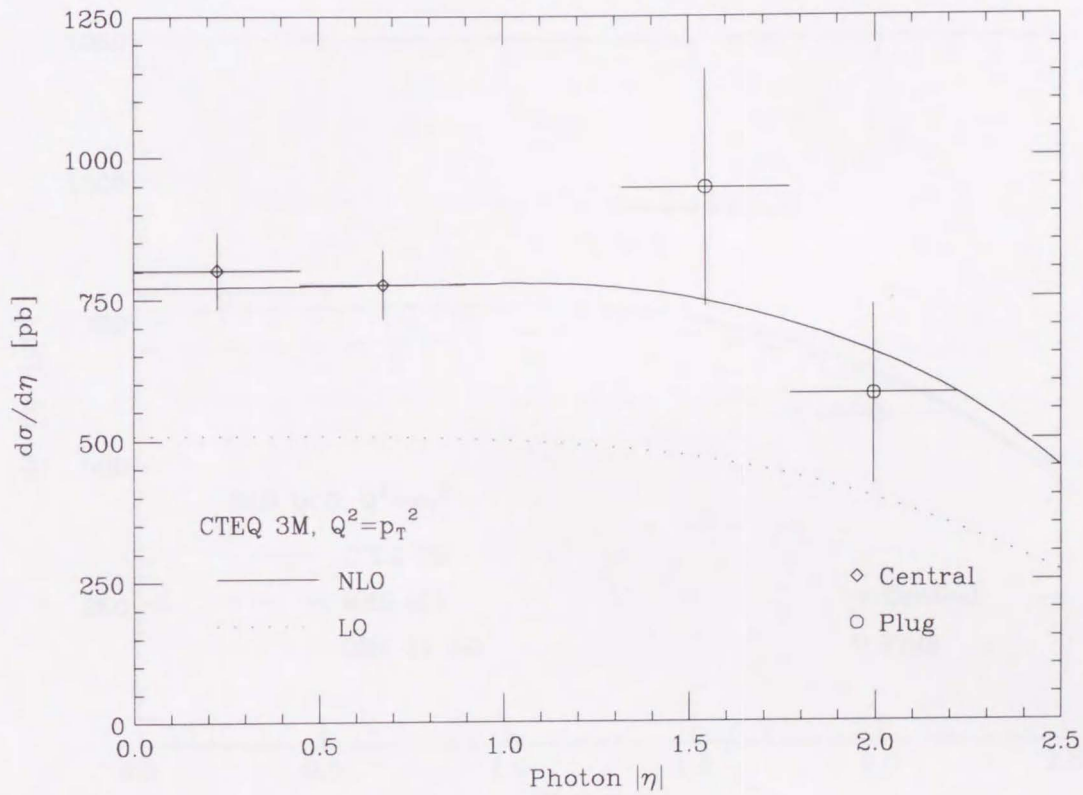


Figure 10.9: Differential cross section for prompt photon production. The next-to-leading order QCD calculation with CTEQ 3M parton distribution function is compared with the measurement. The leading order calculation is also presented.

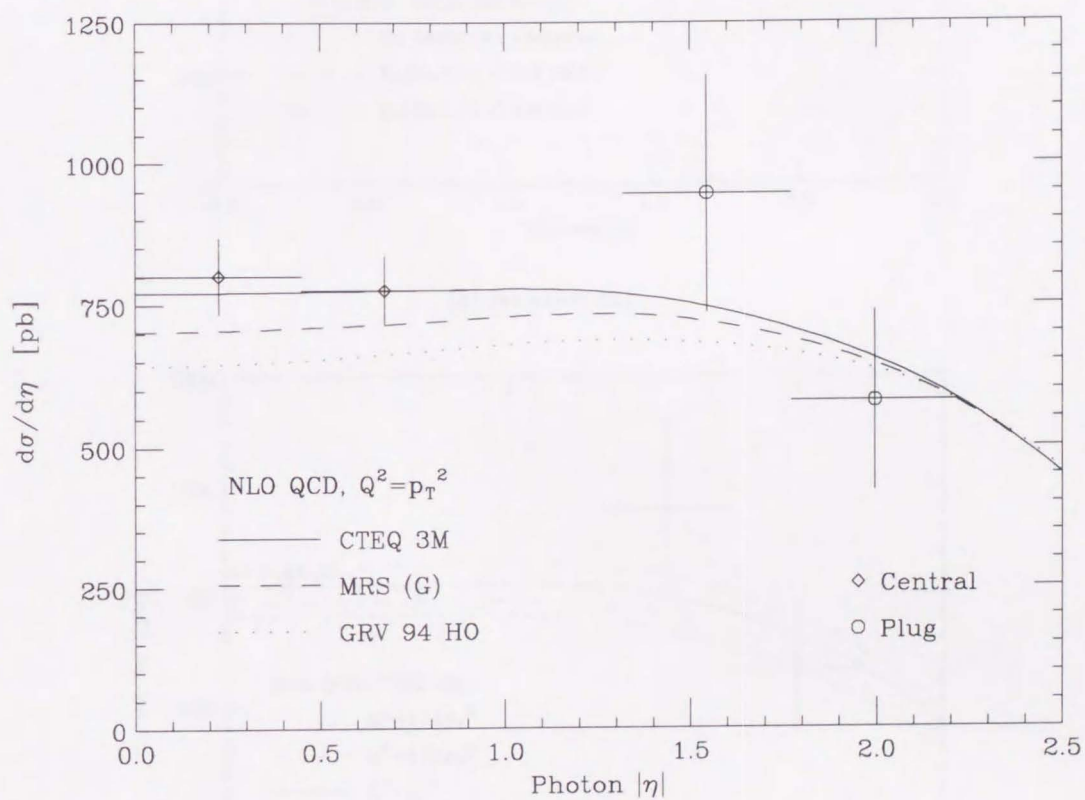
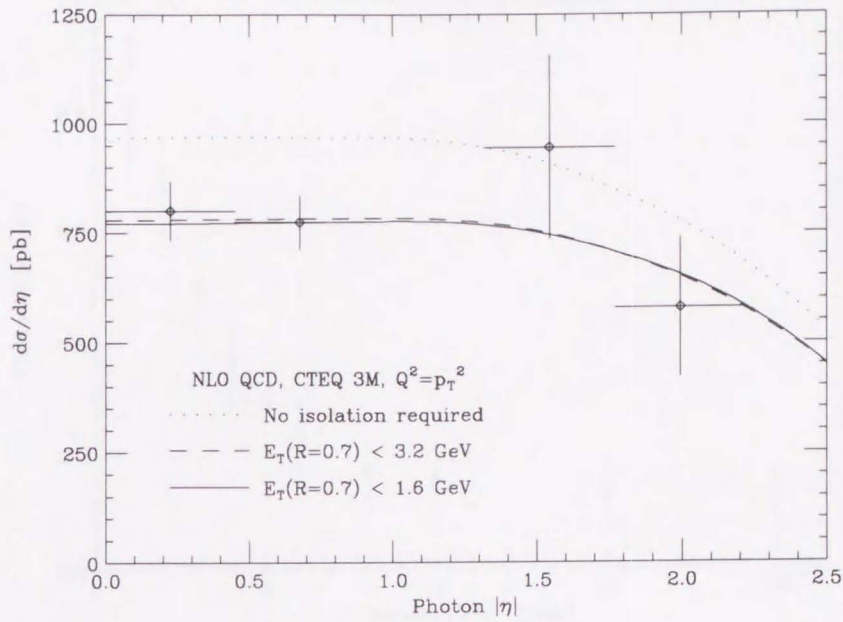
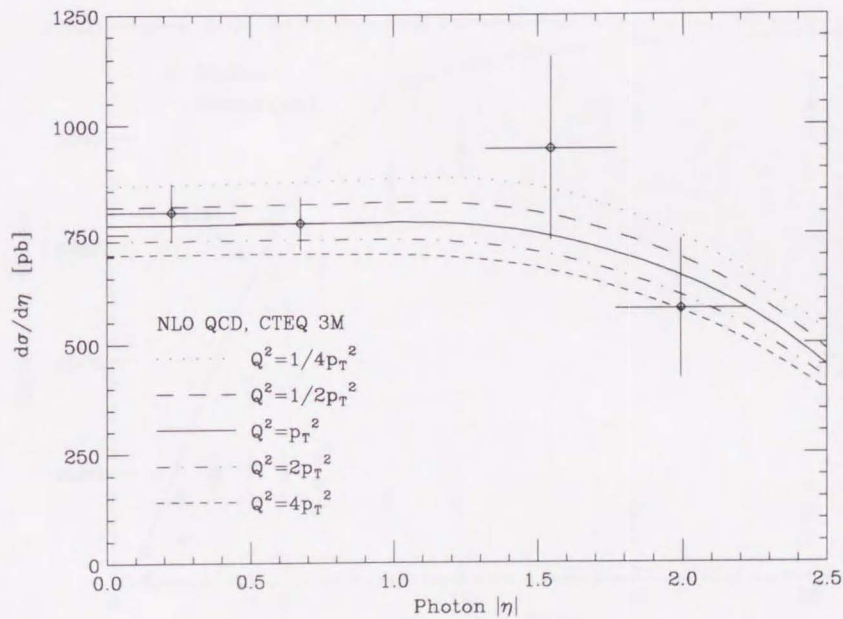


Figure 10.10: NLO QCD calculations with PDF sets, CTEQ 3M, MRS (G), and GRV 94 HO.

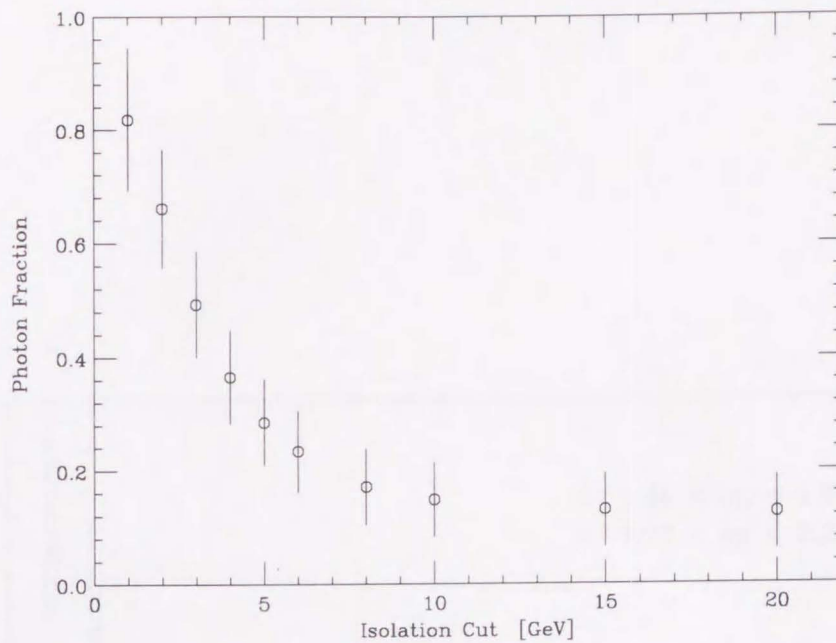


(a) Isolation cut

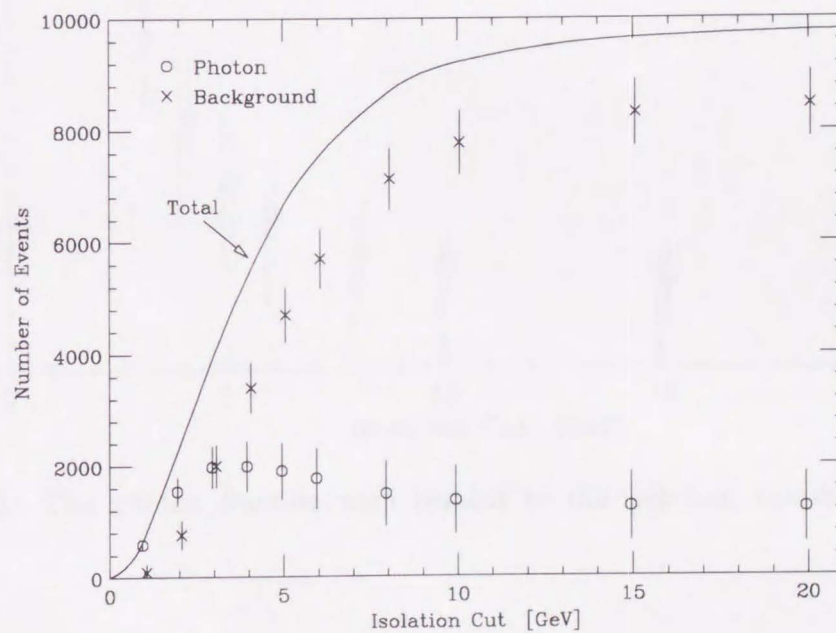


(b) Scale definition

Figure 10.11: Estimations of uncertainties in the NLO QCD calculation. (a) The QCD prediction increases with loosening the isolation cut. (b) The QCD prediction increases with decreasing the factor for the renormalization and factorization scales.



(a) Prompt photon fraction



(b) Numbers of prompt photons and background mesons

Figure 10.12: (a) The photon fraction with respect to the isolation threshold. (b) The numbers of prompt photon events and neutral meson events with respect to the isolation threshold.

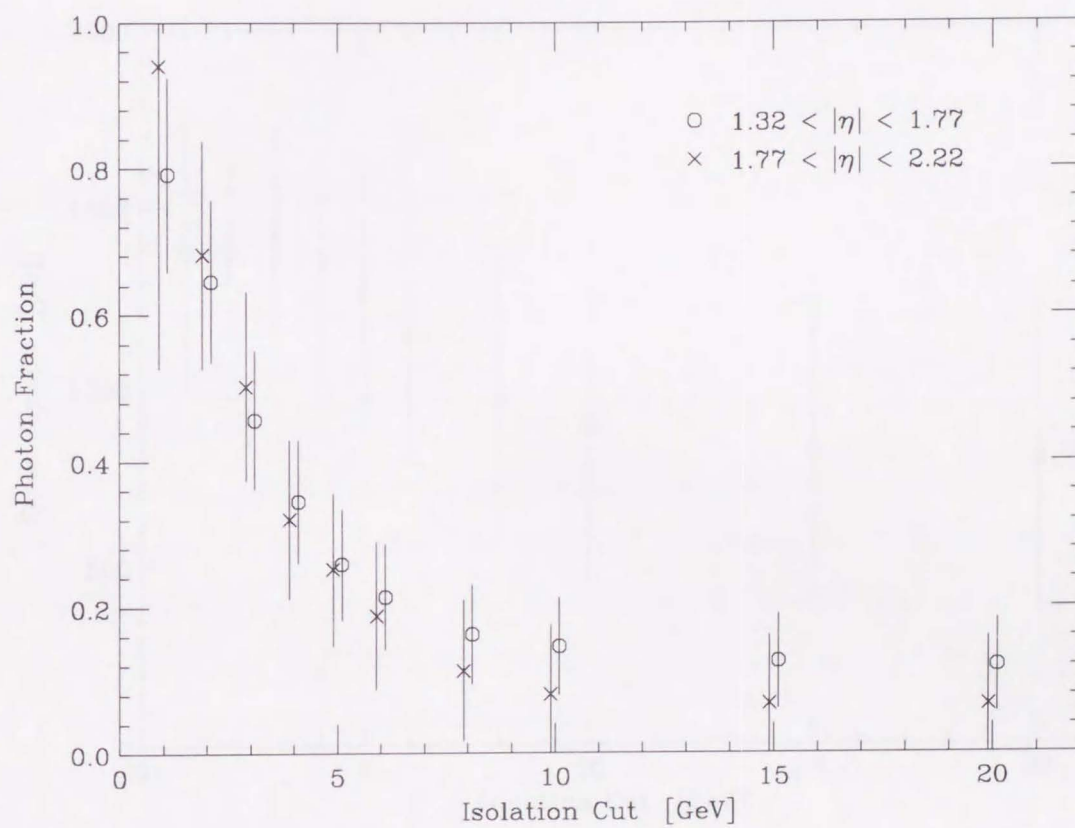


Figure 10.13: The photon fraction with respect to the isolation threshold for two η ranges.

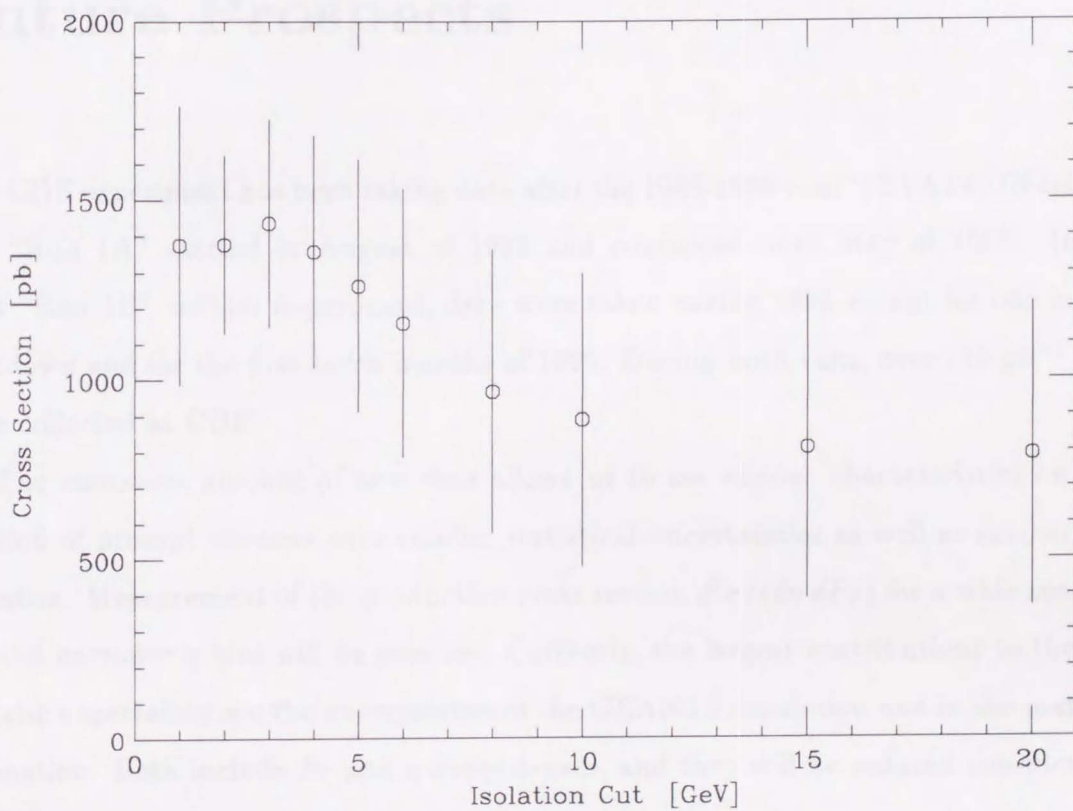


Figure 10.14: The prompt photon cross section with respect to the isolation threshold. The cross section is stable for $\lesssim 5$ GeV.

Chapter 11

Future Prospects

The CDF experiment has been taking data after the 1988-1989 run. TEVATRON collider run "Run 1A" started in August of 1992 and continued until May of 1993. In the next "Run 1B" collider experiment, data were taken during 1994 except for one month shutdown and for the first seven months of 1995. During both runs, over 110 pb^{-1} data were collected at CDF.

The enormous amount of new data allows us to see various characteristics on production of prompt photons with smaller statistical uncertainties as well as smaller systematics. Measurement of the production cross section $d^2\sigma/(d\eta dP_T)$ for a wide range of P_T and narrower η bins will be possible. Currently, the largest contributions to the systematic uncertainty are the uncertainties of the GEANT3 simulation and in the material estimation. Both include P_T and η dependences, and they will be reduced considerably by narrowing the P_T and η bins.

Moreover, with associated jet tag, the center-of-mass angular distribution of prompt photons becomes measurable. Jet tagging also provides information on the parton distribution. In the lowest order, measurement of prompt photons in the endplug region and associated jets gives us exact momenta of the colliding partons, providing precise information on the gluon distribution at small x .

Furthermore, studies on various photon related topics will be possible with a large amount of data. Starting from an identification of other particle, the detection of the associated photon in the endplug region provides not only larger acceptance but also

larger opening angles between the photon and the other particle. For instance, for two prompt photon production, detecting one in the central region and the other in the endplug may double the acceptance of both photons in the central region, and measures wider opening angles of two photons.

11.1 Systematic Uncertainty

Just by limiting the P_T range or the η range, the systematic error in the cross section for prompt photon production is reduced since the P_T and η dependences of the cascade shower which are included in the systematics of the GEANT3 simulation as shown in Fig. 7.17 vanish as well as the inside detector materials (Section 8.3).

In addition, the large statistics also reduce the systematics in the total amount of materials inside the detector. Perhaps, we will see the φ dependence of the inside detector materials with more than thirty times of electrons from W decays in the new data.

We expect that the systematic error can be reduced by a factor of 2 or larger; one for the GEANT3 simulation to be a factor of ~ 1.5 , and one for the estimation of the inside detector materials will be ~ 1.5 or larger.

11.2 Precision Measurement

Figure 11.1 shows NLO QCD calculations of the differential cross section with respect to P_T in the low and high η ranges. For instance, we expect ~ 3000 of prompt photon events in $1.77 < |\eta| < 2.22$ and $50 \text{ GeV}/c < P_T < 60 \text{ GeV}/c$ in the new data. We will be able to measure prompt photons with $P_T = 60 \text{ GeV}/c$ in the endplug region.

It, however, is rather unattractive for a determination of the gluon distribution. Figure 11.2 shows differences between the cross sections with various PDF sets. Only a few to ten percent differences are expected from the NLO QCD calculations. However, the new measurement may provide some hints on the gluon distribution.

11.3 Angular Distribution

It becomes possible to observe the angular distribution of prompt photons with the new data. Just by taking prompt photons in the endplug region with the associated jets produced in the opposite direction, we can measure $\cos \theta^*$ up to ~ 0.98 , where $\cos \theta^*$ is the scattering angle of the photon in the center-of-mass system of the photon and the associated jet. In the LO QCD calculation, prompt photon production is dominated ($\sim 90\%$) by the t -channel quark exchange process (Compton process in Fig. 1.1 (a)). The spin 1/2 quark propagator produces a photon angular distribution roughly of the form $(1 - \cos \theta^*)^{-1}$.

However, due to large distribution of small x gluons, a photon and the associated jet are mostly produced in the same side (east or west). Figure 11.3 is a scatter plot showing the correlation between prompt photon η associated jet η for $P_T > 20$ GeV/c. The distribution is obtained by the HERWIG (Hadron Emission Reactions With Interfering Gluons) Monte Carlo generator [55] which calculates all the LO QCD processes for prompt photon production. Still, we are able to see prompt photons produced in the opposite direction of associated jets. In the lowest order, the cross section for production of prompt photons in $20 \text{ GeV}/c < P_T < 30 \text{ GeV}/c$ and $1.32 < |\eta| < 2.22$ with associated jets at the opposite is ~ 35 pb. Hence, approximately 40k such events are expected in the new data. We will be able to add a few measurement points around $\cos \theta^* = 0.93$ to the angular distribution of prompt photons in the central region [54].

11.4 Small x Gluons

There are two ways to see small x gluons. One is lowering the photon energy. The other is to go to higher η .

In the new runs, electromagnetic clusters with $E_T > 20$ GeV were triggered in the endplug region without prescaling. To see a specific range of x , one needs to tag the associated jets. For instance, in the lowest order Compton process, x will be limited between 0.0015 and 0.0030 if photons are required to be in $20 \text{ GeV} < E_T < 30 \text{ GeV}$ and $2.04 < |\eta| < 2.22$ with the associated jets in $3.0 < |\eta| < 3.6$, where the gluon x

is assumed to be smaller than that of the quark. From the NLO QCD calculation, the production cross section for prompt photons and jets in the above ranges is ~ 24 pb. Therefore, in the new data, we must have ~ 2500 prompt photon events in the above ranges, and it will be possible to see only gluons with $0.0015 < x < 0.0030$ by tagging the associated jets.



Figure 11: NLO QCD ratio of the differential cross-section for the prompt photon production with respect to A_s .

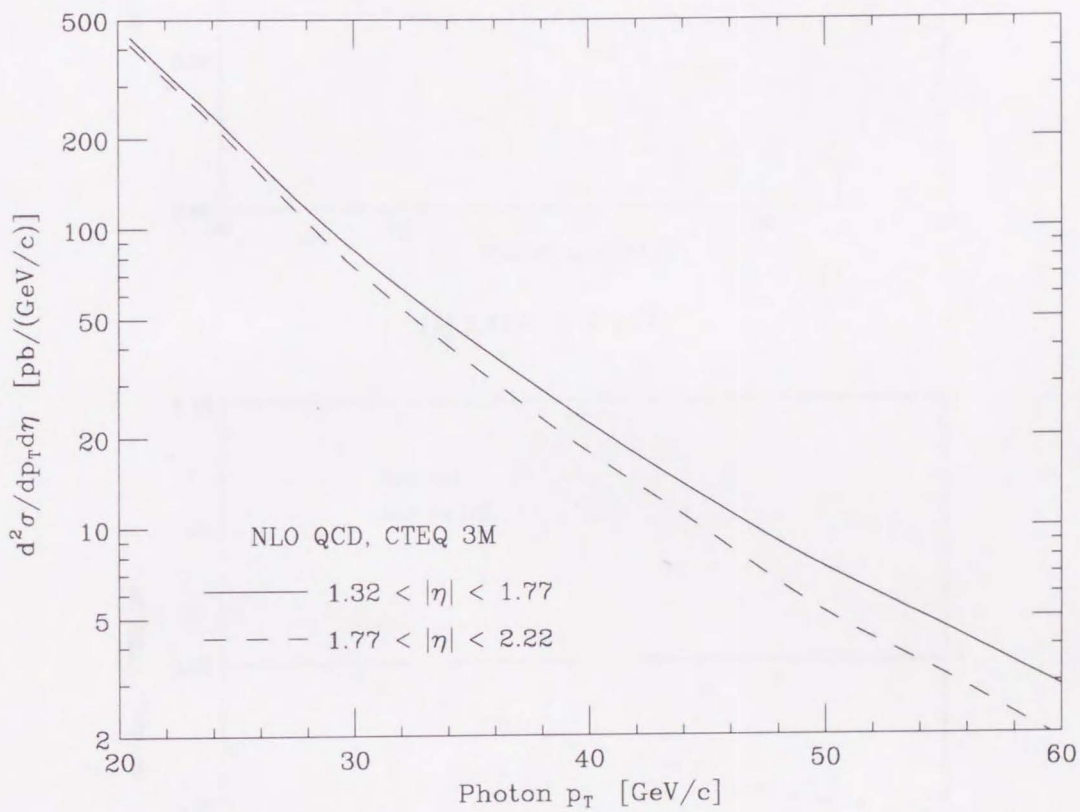


Figure 11.1: NLO QCD calculations of the differential cross section for prompt photon production with respect to P_T .

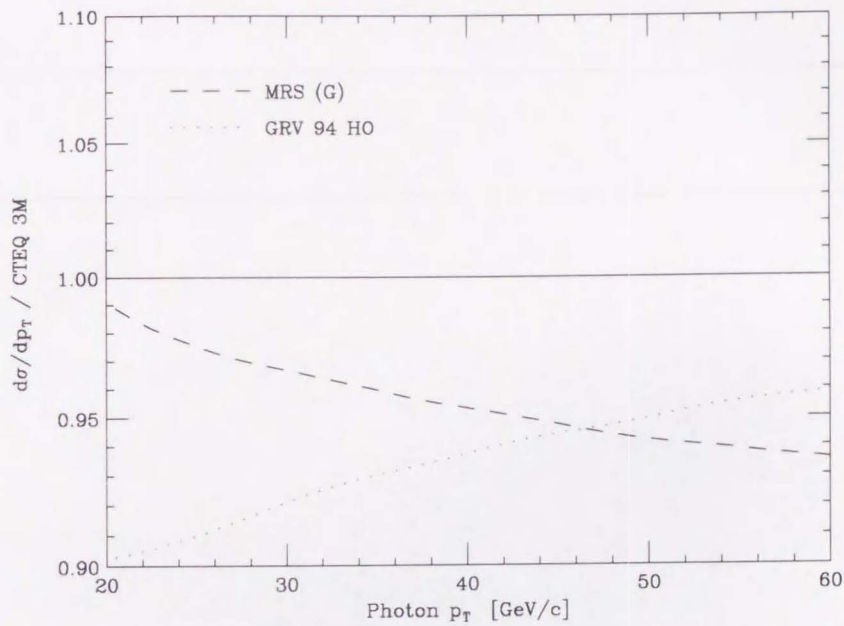
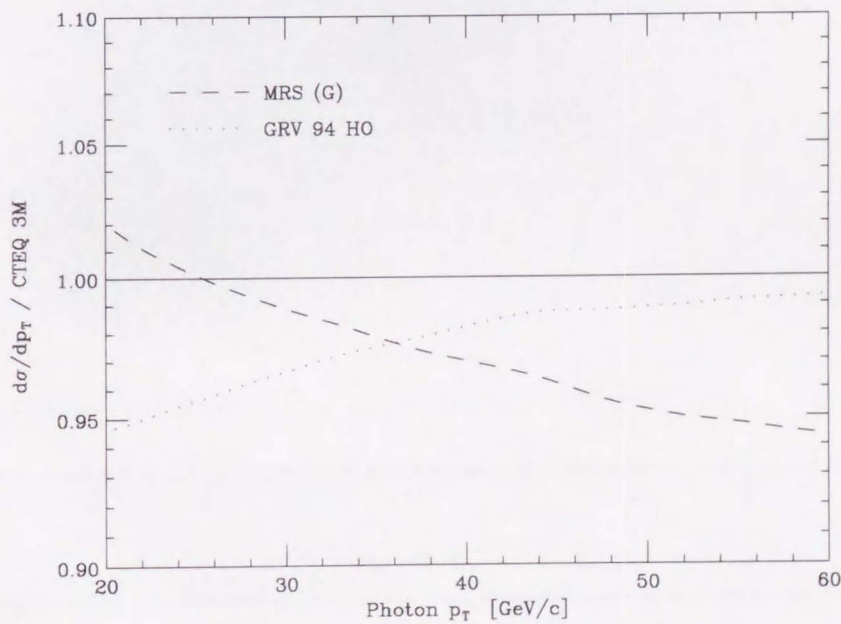
(a) $1.32 < |\eta| < 1.77$ (b) $1.77 < |\eta| < 2.22$

Figure 11.2: NLO QCD calculations showing difference in the differential cross section for prompt photon production. The cross section is normalized by CTEQ 3M.

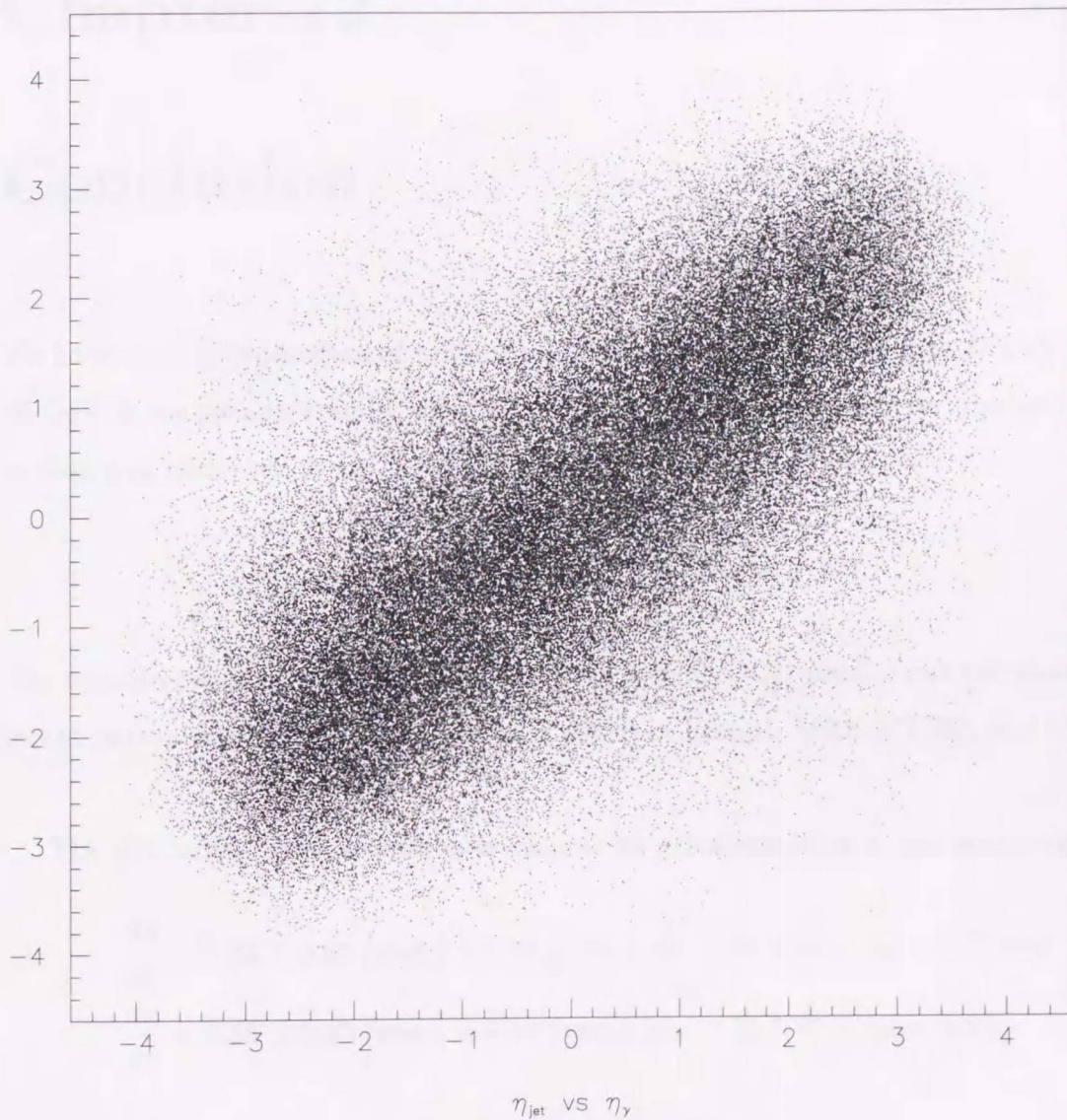


Figure 11.3: Scatter plot showing an η distribution of prompt photons and the associate jets by the HERWIG Monte Carlo generator.

Chapter 12

Conclusion

We have studied production of prompt photons with transverse energies $27 \text{ GeV} < E_T < 40 \text{ GeV}$ in the pseudorapidity range of $1.32 < |\eta| < 2.22$. The inclusive production cross section was measured to be

$$\sigma = 1.44 \pm 0.09 \text{ (stat.)} \pm 0.27 \text{ (syst.) nb.}$$

The measurement is in good agreement with the NLO QCD predictions calculated using recent parton distribution functions from different groups, MRS, CTEQ, and GRV.

The differential cross section with respect to pseudorapidity η was measured to be

$$\begin{aligned} \frac{d\sigma}{d\eta} &= 0.95 \pm 0.08 \text{ (stat.)} \pm 0.19 \text{ (syst.) nb} && \text{in } 1.32 < |\eta| < 1.77 \text{ and} \\ \frac{d\sigma}{d\eta} &= 0.58 \pm 0.07 \text{ (stat.)} \pm 0.14 \text{ (syst.) nb} && \text{in } 1.77 < |\eta| < 2.22. \end{aligned}$$

They are also consistent with the NLO QCD calculations.

Appendix A

Formulation for the Uniformity

Estimation

It¹ is assumed that a tower has a gain a_k (k : tower number = 1, 127) whose mean $\langle a \rangle$ is normalized to unity. Thus, the standard deviation σ_a represents the uniformity of the towers. A bare (excluding the effect of a gain a_k) response to an electron at tower k is defined as ε_k^i (i : event number = 1, 100). Then, Fig. 7.13 (a) is interpreted as a distribution of $a_k \cdot \varepsilon_k^i$ for $i = 1, 100$. The mean and the variance of bare responses to 100 electrons at tower k are written as

$$E_k \equiv \bar{\varepsilon}_k = \frac{1}{100} \sum_{i=1}^{100} \varepsilon_k^i,$$

$$e_k^2 \equiv s_{\varepsilon_k}^2 = \frac{1}{100 - 1} \sum_{i=1}^{100} \varepsilon_k^{i^2} - \bar{\varepsilon}_k^2.$$

¹In this section, the parent mean (the parent standard deviation) and the sample mean (the sample standard deviation) are used as the same words. However, variables are defined as follows.

The parent mean and the parent standard deviation of variable x are

$$\langle x \rangle \equiv \lim_{n \rightarrow \infty} \frac{1}{n} \sum_{i=1}^n x_i, \quad \sigma_x^2 \equiv \lim_{n \rightarrow \infty} \left(\frac{1}{n} \sum_{i=1}^n x_i^2 - \langle x \rangle^2 \right).$$

The sample mean and the sample standard deviation are

$$\bar{x} \equiv \frac{1}{N} \sum_{i=1}^N x_i, \quad s_x^2 \equiv \frac{1}{N - 1} \sum_{i=1}^N x_i^2 - \bar{x}^2,$$

where N is finite.

Then, Fig. 7.13 (b) shows the distribution of $a_k \cdot E_k$ for $k = 1$ to 127, and (c) is $a_k \cdot e_k$.

The mean and the variance of E_k are calculated

$$\begin{aligned}\bar{E} &= \frac{1}{127} \sum_{k=1}^{127} E_k \quad \simeq \langle \varepsilon \rangle, \\ s_E^2 &= \frac{1}{127-1} \sum_{k=1}^{127} E_k^2 - \bar{E}^2 \quad \simeq \frac{1}{100} \sigma_\varepsilon^2,\end{aligned}$$

where $\langle \varepsilon \rangle$ and σ_ε are the mean and the standard deviation of ε_k^i . On the other hand, the RMS value divided by the mean in Fig. 7.13 (b), which is ~ 0.1 , describes the uniformity the statistical fluctuations from the limited numbers of electrons and towers. Therefore,

$$\left(\frac{s_{a \cdot E}}{a \cdot \bar{E}} \right)^2 \simeq \left(\frac{s_a}{\bar{a}} \right)^2 + \left(\frac{s_E}{\bar{E}} \right)^2,$$

where $\overline{a \cdot E}$ and $s_{a \cdot E}$ are the mean and the standard deviation of $a_k \cdot E_k$; \bar{a} and s_a are those for a_k . Taking the mean of e_k^2 ,

$$\begin{aligned}\bar{e}^2 &= \frac{1}{127} \sum_{k=1}^{127} e_k^2 \\ &= \frac{1}{127} \sum_{k=1}^{127} \left(\frac{1}{100-1} \sum_{i=1}^{100} \varepsilon_k^{i2} - E_k^2 \right),\end{aligned}$$

and comparing with s_E^2 , it is found that

$$s_E^2 + \bar{e}^2 \simeq \sigma_\varepsilon^2$$

or

$$s_E^2 \simeq \frac{1}{99} \bar{e}^2.$$

Employing the above relation, $\overline{a \cdot E} \simeq \bar{a} \cdot \bar{E}$, and $\overline{a^2 \cdot E^2} \simeq \bar{a}^2 \cdot \bar{E}^2 \simeq (\sigma_a^2 + \bar{a}^2) \cdot \bar{E}^2$, the uniformity becomes

$$\begin{aligned}\sigma_a^2 &\simeq s_a^2 \\ &\simeq \bar{a}^2 \cdot \left(\frac{s_{a \cdot E}^2}{a \cdot \bar{E}^2} - \frac{s_E^2}{\bar{E}^2} \right)\end{aligned}$$

$$\simeq \bar{a}^2 \cdot \left(\frac{s_{a \cdot E}^2}{a \cdot E^2} - \frac{\overline{a^2 \cdot E^2}}{99(\sigma_a^2 + \bar{a}^2)} \right).$$

Considering $\sigma_a \sim 0.1$ and $\bar{a} \simeq \langle a \rangle = 1$, the uniformity is obtained as

$$\sigma_a^2 \simeq \frac{1}{a \cdot E^2} (s_{a \cdot E}^2 - \frac{1}{100} \overline{(a \cdot E)^2}),$$

where $\overline{a \cdot E^2}$, $s_{a \cdot E}^2$, and $\overline{(a \cdot E)^2}$ are calculable directly from data. Assuming $\overline{a \cdot E^2}$, $s_{a \cdot E}^2$, and $\overline{(a \cdot E)^2}$ are independent each other, the uncertainty $\Delta\sigma_a$ is given by

$$\begin{aligned} 4\sigma_a^2 \cdot (\Delta\sigma_a)^2 &= \left\{ 2 \frac{1}{a \cdot E^3} (s_{a \cdot E}^2 - \frac{\overline{(a \cdot E)^2}}{100}) \right\}^2 \cdot (\Delta\overline{a \cdot E})^2 \\ &+ \left\{ \frac{2s_{a \cdot E}}{a \cdot E^2} \right\}^2 \cdot (\Delta s_{a \cdot E})^2 \\ &+ \left\{ \frac{1}{100a \cdot E} \right\}^2 \cdot (\Delta\overline{(a \cdot E)^2})^2. \end{aligned}$$

Here, $\Delta\overline{a \cdot E}$, $\Delta s_{a \cdot E}$, and $\Delta\overline{(a \cdot E)^2}$ are the uncertainties on $\overline{a \cdot E^2}$, $s_{a \cdot E}^2$, and $\overline{(a \cdot E)^2}$, respectively. Note that the first and the third terms are negligible small compared to the second term.

Bibliography

- [1] CDF collaboration, F. Abe *et al.*, Phys. Rev. Lett. **75**, 613 (1995).
- [2] CDF collaboration, F. Abe *et al.*, Phys. Rev. Lett. **72**, 3004 (1994).
- [3] CDF collaboration, F. Abe *et al.*, Phys. Rev. Lett. **74**, 1936 (1995);
CDF collaboration, F. Abe *et al.*, Phys. Rev. Lett. **74**, 1941 (1995).
- [4] CDF collaboration, F. Abe *et al.*, Phys. Rev. Lett. **73**, 2662 (1994);
CDF collaboration, F. Abe *et al.*, Phys. Rev. D **48**, 2998 (1993);
CDF collaboration, F. Abe *et al.*, Phys. Rev. Lett. **71**, 679 (1993).
- [5] CDF collaboration, F. Abe *et al.*, Phys. Rev. Lett. **70**, 2232 (1993).
- [6] J.F. Owens, Rev. Mod. Phys. **59**, 465 (1987);
P. Aurenche, R. Baier, M. Fontannaz, and D. Schiff, Nucl. Phys. **B297**, 661 (1988);
Edmond L. Berger and Jian-wei Qiu, Phys. Rev. D **44**, 2002 (1991);
M. Gluck, L.E. Gordon, E. Reya, and W. Vogelsang, Phys. Rev. Lett. **73** 388 (1994);
CTEQ Collaboration, Raymond Brock *et al.*, Rev. Mod. Phys. **67**, 157 (1995).
- [7] H. Baer, J. Ohnemus, and J.F. Owens, Phys. Rev. D **42**, 61 (1990).
- [8] Bruno Rossi, *High-Energy Particles*, Prentice-Hall, Incorporated, 1952.
- [9] D.W. Duke and J.F. Owens, Phys. Rev. D **30**, 49 (1984).
- [10] E. Eichten, I. Hinchliffe, K. Lane, and C. Quigg, Rev. Mod. Phys. **56**, 579 (1984).
- [11] M. Diemoz, F. Ferroni, E. Longo, and G. Martinelli, Z. Phys. C **39**, 21 (1988).

- [12] A.D. Martin, W.J. Stirling, and R.G. Roberts, Phys. Lett. B **354**, 155 (1995) and references therein.
- [13] Jorge G. Morfin, Wu-Ki Tung, Z. Phys. C **52**, 13 (1991).
- [14] CTEQ Collaboration, James Botts *et al.*, Phys. Lett. B **304**, 159 (1993);
H.L. Lai, J. Botts, J. Huston, J.G. Morfin, J.F. Owens, J.W. Qiu, W.K. Tung, and
H. Weerts, Phys. Rev. D **51**, 4763 (1995) and references therein.
- [15] M. Gluck, E. Reya, and A. Vogt, Z. Phys. C **67** 433 (1995) and references therein.
- [16] P. Aurenche, R. Baier, M. Fontannaz, J.F. Owens, and M. Werlen, Phys. Rev. D
39, 3275 (1989).
- [17] Edmond L. Berger and Rui-bin Meng, Phys. Lett. B **304** 318 (1993).
- [18] L.N. Gribov and L.N. Lipatov, Sov. J. Nucl. Phys. **15**, 438 and 675 (1972);
G. Altarelli and G. Parisi, Nucl. Phys. **B126**, 298 (1977).
- [19] E.A. Kuraev, L.N. Lipatov, and V.S. Fadin, Sov. Phys. JETP **45**, 199 (1977);
Ya.Ya. Balitsky and L.N. Lipatov, Sov. J. Nucl. Phys. **28**, 822 (1978).
- [20] ZEUS Collaboration, M. Derrick *et al.*, Z. Phys. C **65**, 379 (1995);
ZEUS Collaboration, M. Derrick *et al.*, Z. Phys. C **69**, 607 (1996).
- [21] H1 Collaboration, T. Ahmed *et al.*, Nucl. Phys. **B439**, 471 (1995);
H1 Collaboration, S. Aid *et al.*, Nucl. Phys. **B449**, 3-24 (1995);
H1 Collaboration, S. Aid *et al.*, Phys. Lett. B **354**, 494 (1995);
H1 Collaboration, S. Aid *et al.*, "A Measurement and QCD Analysis of the Proton
Structure Function $F_2(x, Q^2)$ at HERA," DESY-96-039 (1996), unpublished.
- [22] A.J. Askew, J. Kwiecinski, A.D. Martin, and P.J. Sutton, Phys. Rev. D **49**, 4402
(1994); Mod. Phys. Lett. **A8**, 3813 (1993); Phys. Rev. D **47**, 3775 (1993).
- [23] A.D. Martin, W.J. Stirling, and R.G. Roberts, Phys. Rev. D **50**, 6734 (1994).

- [24] C.O. Escobar, Nucl. Phys. **B98**, 173 (1975);
G.R. Farrar and S.C. Frautschi, Phys. Rev. Lett. **36**, 1017 (1976);
H. Fritzsch and P. Minkowski, Phys. Lett. B **69**, 316 (1977);
F. Halzen, M. Dechantszeiter, and D.M. Scott, Phys. Rev. D **22** 1617 (1980);
R. Baier, J. Engels, and B. Petersson, Z. Phys. C **6**, 309 (1980).
- [25] J. Huston, E. Kovacs, S. Kuhlmann, H.L. Lai, J.F. Owens, and W.K. Tung, Phys. Rev. D **51**, 6139 (1995).
- [26] FERMILAB-E706 Collaboration, G. Alverson *et al.*, Phys. Rev. D **48**, 5 (1993);
FERMILAB-E706 Collaboration, (G. Alverson *et al.*, Phys. Rev. D **49**, 3106 (1994).
- [27] E. Anassontzis *et al.*, Z. Phys. C **13**, 277 (1982).
- [28] UA1 Collaboration, C. Albajar *et al.*, Phys. Lett. B **209**, 385 (1988).
- [29] UA2 Collaboration, J. Alitti *et al.*, Phys. Lett. B **263**, 544 (1991).
- [30] DØ Collaboration, S. Abachi *et al.*, FERMILAB-PUB-96-072-E, (1996), submitted to Phys. Rev. Lett.
- [31] CDF collaboration, F. Abe *et al.*, Nucl. Instrum. Methods **A271**, 387 (1988).
- [32] CDF collaboration, F. Abe *et al.*, Phys. Rev. Lett. **63**, 720 (1989).
- [33] Y. Fukui *et al.*, Nucl. Instrum. Methods **A267**, 280 (1988).
- [34] W.C. Carithers *et al.*, "Performance and Calibration Studies of the C.D.F. Endplug Hadron Calorimeter," CDF internal note 368 (1985).
- [35] E. Barsotti *et al.*, Nucl. Instrum. Methods **A269**, 82 (1988).
- [36] K. Byrum *et al.*, Nucl. Instrum. Methods **A268**, 46 (1988).
- [37] G. Aascoli *et al.*, Nucl. Instrum. Methods **A269**, 63 (1988).
- [38] H. Areti *et al.*, Proc. 23rd Conf. on High Energy Physics, Berkeley, California (July 1986).

- [39] C.D. Moore *et al.*, "Single Bunch Intensity Monitoring System Using an Improved Wall Current Monitor," Proc. of the 1989 IEEE Particle Accelerator Conference, Chicago (1989).
- [40] UA4 collaboration, M Bozzo *et al.*, Phys. Lett. B **147**, 392 (1984);
UA4 collaboration, M Bozzo *et al.*, Phys. Lett. B **198**, 513 (1987).
- [41] CDF collaboration, F. Abe *et al.*, Phys. Rev. D **44**, 29 (1991);
Paul Derwent, "Updating 88-89 Cross Section Measurements," CDF internal note 2761 (1994).
- [42] Particle Data Group, L. Montanet *et al.*, Phys. Rev. D **50**, 1193 (1994).
- [43] David Quarrie and Brian Troemel, "YBOS Programmers Reference Manual Version 4.00," CDF internal note 156 (1995).
- [44] Jay Hauser, "Guide to the Triggers Used in the 1988-1989 CDF Data Run," CDF internal note 966 (1989).
- [45] S. Kim, *et al.*, "Spike Noises in PEM," CDF internal note 997 (1989).
- [46] M. Ninomiya *et al.*, "PEM miscabling in '88-89 run," CDF internal note 914 (1989).
- [47] S. Kim and S. Ogawa, "PEM Quadrant Gain Factors," CDF internal note 1021 (1989).
- [48] T. Kamon and S. Kim, "Electron Energy Correction in PEM Dead Layers," CDF internal note 869 (1989).
- [49] R. Brun *et al.*, "GEANT3," CERN DD/EE/84-1.
- [50] CERN program Library Long Writeup W5013.
- [51] Satoru Ogawa, "Measurement of Electron-Positron Asymmetry in W Decays from 1.8 TeV Proton-Antiproton Collisions," Ph.D. thesis, University of Tsukuba, UTPP-38 (1992).
- [52] Martin Schub, Ph.D. thesis, Purdue University, 1989.

- [53] CDF collaboration, F. Abe *et al.*, Phys. Rev. D **43**, 2070 (1991).
- [54] CDF collaboration, F. Abe *et al.*, Phys. Rev. Lett. **71**, 679 (1993).
- [55] G. Marchesini, B.R. Webber, G. Abbiendi, I.G. Knowles, M.H. Seymour, and L. Stanco, Comp. Phys. Commun. **67**, 465 (1992).